ON THE MICROSCALE MODELING OF FRACTURE PROPAGATION IN ROCK: APPLICATIONS TO LANDSLIDES

By

Ge Gao

Department of Civil Engineering and Applied Mechanics

McGill University
Montréal, Québec, Canada

August 2020

A thesis submitted to McGill University in partial fulfillment of
the requirements for the degree of Doctor of Philosophy

Dedication

To the spirit of my **Grandma (Nainai)**
Shuzhen Wang (1939 - 2019)

To the spirit of my **Uncle**
Liai He (1960 - 2017)

To my favourite **Parents**
Xuguang Gao and Naixia Wang

To my esteemed and beloved **Grandpa**
Sifu Gao

To my amiable **Grandma (Laolao)**
Fenglan Sun

Abstract

The study of rock fracturing is a fundamental research topic in rock mechanics and engineering. Discrete element methods are proven to be very capable for describing fracturing and fragmentation processes because, much like real rocks, the numerical materials are composed of assemblages of particles. Nonetheless, correlation macromechanical behaviour to the corresponding origin at the microscale is scarce in the literature. In this study, a systematic analysis is carried out to investigate failure mechanisms taking place in rock mass with special emphasis put on macroscopic deformation processes and the micromechanical origin. Detailed inspection of fracturing behavior of jointed rock mass at the laboratory-scale can allow the implication of the acquired fundamental knowledge of rock fracturing development and failure mechanism extend to the large-scale rock slope instability problems. This thesis is devoted to gain a comprehensive understanding regarding the rock deformation from laboratory-scale experiments to large-scale geodynamic processes that leads to an improved design for rock engineering projects.

The research results have been submitted or published in refereed journals amounting to 3 journal papers. These papers are compiled to produce 6 chapters in this manuscript-based thesis. The investigation of damage evolution and failure characteristic of rock mass with increased density of initial jointing subjected to confined stress state is first conducted using discrete element method (DEM) to provide a micromechanical description of the mechanisms involved and foster an accurate interpretation and prediction on rock instabilities for advancing the understanding of rock fracturing process during landslide propagation. The rest of the thesis is devoted to modeling the progressive slope failure under seismic loading via discrete element method, aiming to provide new insights into the detailed microresponses and macroresponses of coseismic landslides. Replication of the natural system, the calibration procedure to determine the properties of the discrete elements is in essence for a reasonable numerical simulation, in particular, boundary condition. Thus, quite boundary is used to ensure the seismic wave cannot reflect back to the model. The developed discrete element framework is used to investigate complex dynamic responses of rock slopes, including internal rock damage, energy conversion, dynamic disintegration, and fragment runout. The results of the numerical analysis are compared with field data. The characteristics of dynamic rock fragmentation and the mechanism governing the postfailure fragmented landsliding

motions is investigated and displacements, stresses, fracturing behaviour, solid fraction, and fragmentation and fragment shape developing within the transport of rock mass are analyzed. Conclusions and recommendations are made regarding the dynamic rock fragmentation and the mechanisms governing the transport kinematics of seismic-induced landslides.

RÉSUMÉ

L'étude de la fracturation des roches est un sujet de recherche fondamental en mécanique et ingénierie des roches. Les méthodes des éléments discrets se sont avérées très capables de décrire les processus de fracturation et de fragmentation car, tout comme les vraies roches, les matériaux numériques sont composés d'assemblages de particules. Néanmoins, la corrélation du comportement macromécanique avec l'origine correspondante à l'échelle microscopique est rare dans la littérature. Dans cette étude, une analyse systématique est réalisée pour étudier les mécanismes de rupture se produisant dans la masse rocheuse avec un accent particulier mis sur les processus de déformation macroscopique et l'origine micromécanique. Une inspection détaillée du comportement de fracturation de la masse rocheuse articulée à l'échelle du laboratoire peut permettre l'implication des connaissances fondamentales acquises sur le développement de la fracturation rocheuse et le mécanisme de rupture jusqu'aux problèmes d'instabilité des pentes rocheuses à grande échelle. Cette thèse est consacrée à acquérir une compréhension globale de la déformation des roches, des expériences à l'échelle du laboratoire aux processus géodynamiques à grande échelle, ce qui conduit à une conception améliorée des projets d'ingénierie des roches.Les résultats de la recherche ont été soumis ou publiés dans des revues à comité de lecture pour un total de 3 articles. Ces articles sont compilés pour produire 6 chapitres dans cette thèse manuscrite. L'étude de l'évolution des dommages et des défaillances caractéristiques de la masse rocheuse avec une densité accrue de joints initiaux soumis à un état de contrainte confiné est d'abord réalisée en utilisant la méthode des éléments discrets (DEM) pour fournir une description micromécanique des mécanismes impliqués et favoriser une interprétation et une prédiction précises sur la roche. instabilités pour faire progresser la compréhension du processus de fracturation des roches pendant la propagation des glissements de terrain. Le reste de la thèse est consacré à la modélisation de la rupture progressive de la pente sous charge sismique via la méthode des éléments discrets, dans le but de fournir de nouvelles perspectives sur les microresponses et macroresponses détaillées des glissements de terrain coseismiques. Réplication du système naturel, la procédure d'étalonnage pour déterminer les propriétés des éléments discrets est essentiellement pour une simulation numérique raisonnable, en particulier, la condition aux limites. Ainsi, une frontière assez étroite est utilisée pour garantir que l'onde sismique ne peut pas se refléter sur le modèle. Le cadre d'élément discret développé est utilisé pour étudier les réponses dynamiques complexes des pentes rocheuses, y compris les dommages internes aux roches, la conversion d'énergie, la désintégration dynamique et le ruissellement des fragments. Les résultats de l'analyse numérique sont comparés aux données de terrain. Les caractéristiques de la fragmentation dynamique de la roche et le mécanisme régissant les mouvements de glissement de terrain fragmentés après la rupture sont étudiés et les déplacements, les contraintes, le comportement de fracturation, la fraction solide et la fragmentation et la forme des fragments se développant dans le transport de la masse rocheuse sont analysés. Des conclusions et des recommandations sont formulées concernant la fragmentation dynamique des roches et les mécanismes régissant la cinématique de transport des glissements de terrain induits par les séismes.

Acknowledgments

First and foremost, I want to thank my PhD advisor Prof. Mohamed A. Meguid, for his invaluable professional guidance and unflagging encouragement, and effective mentorship throughout this research. Prof. Meguid challenged me to always aim higher than I initially thought I could since I joined the GeoGroup as a fresh graduate student, and his unfaltering faith in my capabilities gave me the unwavering confidence to overcome all challenges in the research process. I am forever grateful for his positivity and for the knowledge and wisdom he instilled in me for both my life and my career. I would like to acknowledge my co-supervisor Prof. Luc E. Chouinard for graciously lending his time to provide helpful feedback and invaluable insights to furthering the progression of this work. My many conversations with him always left me with new ideas and considerations for this research.

I am grateful to the geotechnical engineering, rock mechanics and mining engineering, mechanical engineering, and mathematics faculty at McGill who educated me in the background and skills needed to even begin the work of this dissertation. Furthermore, I thank Jorge Sayat, Dr. William Cook, John Bartczak for preparing me to enter the Scientific World in the first place.

My friends in MacDonald Engineering Building truly made my graduate school experience unforgettable. For all the good times shared, I would like to thank my fellow PhD students. In addition, I thank my friends outside of Canada for their moral support, especially Peng linglin for his many "remote" visits and many conversations from China through social media. Of course, I owe a profound thanks to my idols in life, Zuxian Wang, Manyu Zhang, Fei Wang, Yixing Zhang, and Yanzi Sun for giving me the faith to be my better self.

I cannot overstate how important the encouragement of my entire family has been to me during my time at McGill. I especially thank my parents Xuguang Gao and Naixia Wang for being my role models and for supporting all of my endeavors my whole life. To my grandparents Sifu Gao, Shuzhen Wang, and Fenglan Sun, my uncle Liai He: You have always been my inspiration.

Finally, in this day and age, I really need to say a huge thank-you to all the superheroes (doctors, nurses, scientists, etc.) all over the globe who are putting themselves at risk and spending their days and nights fighting the coronavirus pandemic wreaking havoc over our entire society

List of Publications Arising from this Thesis

Refereed Journal Papers

[J1] Gao G, Meguid MA, Chouinard L. "On the role of pre-existing discontinuities on the micromechanical behavior of confined rock samples: A numerical study." ***Acta Geotechnica*** (In Press).

[J2] Gao G, Meguid MA, Chouinard L, Xu C. (2020) "Insights into the Transport and Fragmentation Characteristics of Earthquake-Induced Rock Avalanche: A Numerical Study." ***ASCE Int J Geomech***, 20(9), 1-23.

[J3] Gao G, Meguid MA, Chouinard L, Zhan WW. "Dynamic disintegration processes accompanying transport of an earthquake-induced Landslide." ***Landslides*** (In Press).

TABLE OF CONTENTS

Abstract .... **i**

RÉSUMÉ iii

Acknowledgments v

List of Publications Arising from this Thesis vi

TABLE OF CONTENTS vii

LIST OF FIGURES xi

LIST OF TABLES xvi

LIST OF SYMBOLS xvii

Chapter 1 Introduction 1

1.1. Background 1

1.2. Research Motivation 1

1.3. Objective and Scope 2

1.4. Contributions of authors 3

1.5. Thesis Organization 3

Chapter 2 Literature review 5

2.1. Discrete element method 5

2.1.1. Basic formulation 5

2.1.2. Bonded particle contact model for rock 6

2.2. DEM modeling of fracture development in a rock mass 12

2.3. DEM analysis of fracturing in geodynamic processes 13

2.4. Conclusion for the Literature Review 16

Chapter 3 On the role of pre-existing discontinuities on the micromechanical behavior of confined rock samples: A numerical study 17

3.1. Introduction 18

3.2. Model Description 20

3.2.1. The discrete element method (DEM) 20

3.2.2. Model Calibration 23

3.3. Numerical results and discussion 29

3.3.1. Deformation and Failure Processes 29

3.3.2. Failure mode and orientations of microscopic cracks 32

3.3.3. Particle-level kinematics and contact force information 34

3.3.4. Spatial correlation and contact force heterogeneity 39

3.3.5. Energy budget during deformation 43

3.4. Micro-mechanism and Macro-response 46

3.4.1. Evolution of fabric and coordination number 46

3.4.2. Microstructure Anisotropy 51

3.4.3. Anisotropic distribution 56

3.5. Discussion .... **Error! Bookmark not defined.**

3.5.1. Marcoscale Response & Microscopic Origin 61

3.5.2. Limitation and Future Outlook 63

3.6. Conclusion 64

Preface to Chapter 4 65

Chapter 4 Insights into the Transport and Fragmentation Characteristics of Earthquake-Induced Rock Avalanche: A Numerical Study 66

4.1. Introduction 67

4.2. The Tangjia Valley Rock Avalanche 69

4.2.1. Geological and Geomorphologic Setting 69

4.2.2. Failure mechanism and dynamic process 72
4.3. Discrete Element Modeling 75
4.3.1. Numerical Model 75
4.3.2. Physical and Mechanical Parameters 77
4.3.3. Earthquake Loading and Boundary Conditions 78
4.3.4. Joint Characteristics 79
4.3.5. Damping 81
4.4. Simulation Results 81
4.4.1. Kinematics of the Rock Avalanche 81
4.4.2. Stress evolution and Solid Concentration 85
4.4.3. Energy Regime and Rock Damage 87
4.4.4. Lubrication Mechanism and Friction Reduction 92
4.4.5. Fragmentation and Fragment Distribution 97
4.5. Conclusion 107
Preface to Chapter 5 109
Chapter 5 Dynamic disintegration processes accompanying transport of an earthquake-induced landslide 110
5.1. Introduction 111
5.2. Geological and Geomorphologic setting 114
5.2.1. Landforms and Topography 114
5.2.2. Geological and Structural Settings 116
5.3. Wangjiayan landslide 118
5.4. The Discrete Element Model 121
5.4.1. DEM bonded particle model 122
5.4.2. Boundary conditions 125

5.4.3. Damping 130
5.4.4. Model setup 132
5.5. Results and Discussions 136
5.5.1. Deformation evolution 136
5.5.2. Disintegration process 138
5.5.3. Granular temperature and dispersive stress 143
5.5.4. Morphology and structure of fragmented deposits 150
5.5.5. Fragmentation Degree and Landslide Runout 156
5.6. Conclusions 160
Chapter 6 Conclusions and Recommendations 162
6.1. Conclusions 162
6.2. Recommendations for Future Work 164
References 165

LIST OF FIGURES

Figure 2 - 1. Behavior and rheological components of the linear parallel bond model with inactive dashpots (Itasca Consulting Group. 2015). 8
Figure 2 - 2. The bond removal method (Bahaaddini et al. 2015). 9
Figure 2 - 3. Behavior and rheological components of the smooth-joint model 10
Figure 2 - 4. Force-displacement law for an unbonded joint: (a) normal force versus normal displacement; (b) shear force versus shear displacement; (c) strength envelope; and (d) normal displacement versus shear displacement during sliding. 11
Figure 2 - 5. Illustrations of progressive failure in the rock slopes of the Xiaowan hydroelectric station, China (Huang et al. 2014). 14
Figure 2 - 6. Field evidences from the landslide deposit for occurrence of dynamic fragmentation (Wang et al. 2018). 15
Figure 3 - 1. Behavior and rheological components of (a) the linear parallel bond model; (b) the smooth-joint model. 22
Figure 3 - 2. Stress–strain responses of (a) BS granite and DEM model; (b) BS jointed granite and DEM jointed model for validation micro-parameters. 28
Figure 3 - 3. Stress–strain responses of (a) intact (b) 1V + 2H (c) 2V + 3H (d) 3V + 5H and (e) 6V + 9H rock samples; (f) Volumetric strain versus axial strain in numerical confined compression experiments. 30
Figure 3 - 4. (a) Micro-crack distribution within the rock mass samples; (b) Fragment size distributions presented by the logarithmic hue scale; (c) Polar histogram for tensile failure; (d) Polar histogram for shear failure at the final damage stage. 33
Figure 3 - 5. Schematic illustrations of (a) definition of the neighborhood of a particle; (b) association of grid node to particle, and (c) displacement of grid node and its associated particle. 36
Figure 3 - 6. (a) distribution of translational granular temperature, T_V^i; (b) distribution of rotational granular temperature, T_R^i; (c) contour of void ratio; (d) contour of localized shear strains; (e) contact force chain at the final damage stage. 38

Figure 3 - 7. (a) Spatial force correlation function $G(r)$ for normal contact force plotted as a function of distance r normalized by mean particle diameter d_{50} for intact and jointed samples; 41
Figure 3 - 8. Evolution of energy in (a) intact (b) 1V + 2H (c) 2V + 3H (d) 3V + 5H and (e) 6V + 9H rock samples; (f) Energy partitioning into elastic energy and plastic energy during numerical confined compression experiment. 45
Figure 3 - 9. The deviatoric fabric in the intact and jointed rock samples: (a) considering all engaged contacts; (b) considering only contacts transmitting compressive forces; (c) considering only contacts transmitting tensile forces; (d) considering bonded contacts. 48
Figure 3 - 10. The coordination number in the intact/jointed rock samples: (a) considering all engaged contacts; (b) considering all bonded contacts.. 50
Figure 3 - 11. (a) – (c) Evolution of geometrical anisotropy a_c, mechanical anisotropy a_n, and mechanical anisotropy a_t as a function of cumulative axial strain in intact and jointed rock samples. 55
Figure 3 - 12. Distribution of anisotropies of contact normal, normalized average contact normal force ($\bar{f}^n(\Theta)/\bar{f}^0$) and normalized average contact shear force ($\bar{f}_i^t(\Theta)/\bar{f}^0$) of the intact and two jointed rock samples at initial stress state. 58
Figure 3 - 13. Distribution of anisotropies of contact normal, normalized average contact normal force ($\bar{f}^n(\Theta)/\bar{f}^0$) and normalized average contact shear force ($\bar{f}_i^t(\Theta)/\bar{f}^0$) of the intact and two jointed rock samples at peak stress state. 59
Figure 3 - 14. Distribution of anisotropies of contact normal, normalized average contact normal force ($\bar{f}^n(\Theta)/\bar{f}^0$) and normalized average contact shear force ($\bar{f}_i^t(\Theta)/\bar{f}^0$) of the intact and two jointed rock samples at 50% post-peak stress state. 60
Figure 4 - 1. (a) The tectonic setting of the 2013 Lushan earthquake (SDF: Shuangshi-Dachuan fault; WSF: western Shangli fault; DF: Dayi fault; YWF: Yanjing-Wulong fault; JAF: Jintang Arc fault; (b) A geological map of landslide area.. 70
Figure 4 - 2. Overview of local geomorphologic conditions of the Tangjia Valley rock avalanche. 71

Figure 4 - 3. (a) Detailed topography of the Tangjia Valley rock avalanche along the main movement direction; (b) geological section map of the left stream of the avalanche along line A-A'; (c) geological section map of the right stream of the avalanche along line B-B'. 72

Figure 4 - 4. Characteristics of the Tangjia Valley rock avalanche: (a) the mountain ridge controls the landslide initiation; (b) The upper part of the Chunjianwo valley towards the source area; (c) The upper part of the Gangoutou valley towards the source area; (d) Deposits in the Chunjianwo Valley; (e) The two streams converge into the Tangjia Valley. 74

Figure 4 - 5. Two-dimensional discrete element model of the rock avalanche: (a) Left stream; (b) Right stream. 76

Figure 4 - 6. Modeling the unconfined compression test. 77

Figure 4 - 7. Seismic time history curves: (a) Horizontal acceleration for the left stream; (b) Horizontal velocity for the left stream; (c) Horizontal acceleration for the right stream; (d) Horizontal velocity for the right stream; (e) Vertical acceleration; (f) Vertical velocity. 80

Figure 4 - 8. (a) Maximum and average velocities of the mass during motion; (b) Velocities of the monitoring points along a vertical section with the time; (c) Velocity trajectories of the monitoring particles along a vertical section. 83

Figure 4 - 9. Evolution of the landslide process at different time stamps. 84

Figure 4 - 10. Evolution of the interpolated (a) average stress and (b) solid concentration fields within the avalanche at different time stamps. 85

Figure 4 - 11. Energy transfers resulting from the analysis of the rock avalanche. 89

Figure 4 - 12. (a) Changes in fragmentation energy with the time; (b) Fragmentation energy versus damage ratio; (c) Degree of fragmentation versus damage ratio; (d) Number of fragments evolution. 91

Figure 4 - 13. The distribution of translational granular temperatures $T_V^i(t)$ at different time stamps. 95

Figure 4 - 14. The distribution of rotational granular temperatures $T_R^i(t)$ within the avalanche at different time stamps. 96

Figure 4 - 15. Changes in fragment size at different time stamps. 98

Figure 4 - 16. (a) Relationship between cumulative mass fractions and fragment sizes for increasing loading time; (b) Fractal distributions of fragment sizes for increasing loading time. 101

Figure 4 - 17. Fragment size frequency distributions with corresponding log-normal approximations for the four investigated timestamps. 102
Figure 4 - 18. Distributions of the square root of the ratio of the larger and smaller eigenvalues of the tensor inertia of the fragment shape for checking shape isotropy at different loading times. 105
Figure 4 - 19. Aspects of the fragmented deposits for the right stream of Tangjiayan avalanche: (a) Discrete element numerical observation; (b) Field investigation; (c) Large rock blocks observed only in deposits of the right stream. 106
Figure 5 - 1. (a) Airborne remote sensing image of Wangjiayan landslide; (b) Overview of the Wangjiayan landslide. 115
Figure 5 - 2. Geological and structural Settings of the Wangjianyan landslide area. (a) The fault belt location; (b) Details of the geological structural features. 117
Figure 5 - 3. (a) An illustration of the downslope route of the Wangjiayan landslide; (b) Longitudinal profile of the Wannjiayan landslide. 119
Figure 5 - 4. Characteristics of the Wangjiayan landslide: (a) The earthquake damaged buildings ruined into pieces by the turbulence generated by the rapid-moving rock mass; (b) The impact marks commonly existed in the deposited rock blocks; (c) The scarp of the rupture surface; (d) The scratches left on the bedrock; (e) Features of hummocky deposits; (f) A view of accumulation body still retaining original rock structures. 121
Figure 5 - 5. Micro-parameters calibration: (a) Modeling the unconfined compression test; (b) Modelling the Brazilian test. 124
Figure 5 - 6. Calculation model for a rock column using Ricker wavelet to demonstrate the different boundaries reacting. 128
Figure 5 - 7. Ricker wavelet time history calculated at five points along the rock column using DEM. (a) absorbing boundary; (b) free boundary; (c) fixed boundary. 129
Figure 5 - 8. Relationships between velocity and drop height with different local damping coefficients obtained from DEM free falling tests and theoretical calculation. 131
Figure 5 - 9. (a) Two-dimensional discrete element model of the landslide; (b) The corresponding fragment network due to the presence of the rock discontinuities.. 134

Figure 5 - 10. Seismic time history curves: (a) EW acceleration; (b) NS acceleration; (c) Horizontal acceleration; (d) Horizontal velocity; (e) Vertical acceleration; (f) Vertical velocity. 135

Figure 5 - 11. The emplacement evolution of the Wangjiayan landslide at the selected timestamps: (a) 7.11 s; (b) 18.46s; (c) 20.43 s; (d) 24.48 s; (e) 27.06 s; (f) 28.57 s; (g) 32.69 s;........ 137

Figure 5 - 12. The disintegration process of the Wangjiayan landslide at selected timestamps: 140

Figure 5 - 13. (a) Evolution of rock damage in each slope layer and ground seismic shaking; (b) Evolution of volumetric fraction of fine fragments and growth rate of fragment number. 142

Figure 5 - 14. Evolution of the vibrational (T_V) and rotational (T_R) granular temperatures within the translating slope mass. 146

Figure 5 - 15. The distribution of granular temperatures within the Wangjiayan landslide at the selected timestamps: (a), (b) 15.74 s; (c), (d) 24.5s; (e), (f) 35.02 s; (g), (h) 43.29 s; (i), (j) 53.21 s. 148

Figure 5 - 16. (a) Variations of the deviator stress of the Wangjiayan landslide; the distribution of the deviator stress within the landslide at the selected timestamps: (b) 7.11 s; (c) 16.5s; (d) 22.69 s; (e) 30.51 s; (f) 46.75 s; (g) 71.59 s. 149

Figure 5 - 17. (a) Mass distribution of fragments using the power law distribution; (b) Mass distribution of fragments using the Gates–Gaudin–Schuhmann distribution; (c) Volume-based size distributions of fragments. 153

Figure 5 - 18. (a) Fragment size frequency distributions of the deposit with corresponding log-normal approximations. (b) Distributions of the square root of the ratio of the larger and smaller eigenvalues of the tensor inertia of the fragment shape for checking shape isotropy of the deposit. 155

Figure 5 - 19. Numerical investigation of final landslide deposit for tests with various particle bonding strengths: (a) 11 MPa; (b) 16 MPa; (c) 21 MPa; (d) 26 MPa; (e) 31 MPa; (f) 36 MPa. 157

Figure 5 - 20. (a) Variations of degree of fragmentation and damage ratio with the particle bonding strength; (b) The travel distance of the center of slope mass and the displacement of the front of the deposits with the degree of fragmentation. 159

LIST OF TABLES

Table 3 - 1. Numerical parameters used in the discrete element analysis 25
Table 3 - 2. Comparison of target and achieved macro-mechanical parameters of intact and jointed rock samples 25
Table 3 - 3. Numerical Configurations of Rock Blocks 27
Table 3 - 4. Strength and deformability of intact and increasingly jointed samples 29
Table 3 - 5. *Gini* coefficient 43
Table 3 - 6. Tensile and shear fracture energy 62
Table 4 - 1. Field information of source area 73
Table 4 - 2. Micromechanical parameters used for the DE model 78
Table 5 - 1. Physical and mechanical properties of the rock mass 123
Table 5 - 2. Numerical parameters used in the discrete element analysis 125

LIST OF SYMBOLS

Roman Symbols

2D	Two-dimensional analysis
3D	Three-dimensional analysis
i	The particle i
j	The particle j
m_i	The mass of particle i
x_i	The location of particle i
I_i	The moment of inertia of particle i
$F_{n,ij}^{l}$	The normal component of the elastic forces
$F_{s,ij}^{l}$	The shear component of the elastic forces
$F_{n,ij}^{d}$	The normal component of the damping force
$F_{s,ij}^{d}$	The shear component of the damping force
H_i	The angular momentum of the particle
$\mathbf{F}^{\mathbf{l}}$	The linear elastic force
$\mathbf{F}^{\mathbf{d}}$	The dashpot force
$\bar{\mathbf{F}}$	The parallel-bond force
$\bar{\mathbf{M}}$	The parallel-bond moment
$\hat{\mathbf{n}}_{\mathbf{c}}$	The unit vector that defines the contact plane

$\bar{A}$	The area of the parallel bond cross section
$\bar{I}$	The moment of inertia the parallel bond cross section
$\bar{J}$	The polar moment of inertia of the parallel bond cross section
$\bar{F}_n$	The normal parallel-bond force
$\bar{\mathbf{F}}_{\mathbf{s}}$	The shear parallel-bond force
$\bar{M}_t$	The twisting parallel-bond moment
$\bar{\mathbf{M}}_{\mathbf{b}}$	The bending parallel-bond moment
$R^{(1)}$	The radii of the contacting entity (disk/sphere)
$(F_n)_0$	The smooth joint normal force
$(\mathbf{F_s})_0$	The smooth joint shear force
k_n / k_s	The ball stiffness ratio
$\bar{k}_n / \bar{k}_s$	The parallel bond stiffness ratio
k_n^{sj}	The smooth joint normal stiffness
k_s^{sj}	The smooth joint shear stiffness
v_x^i	The translational velocity component of the selected i -th particle
$\overline{v_x^i}$	The mean translational velocity component of the selected i -th particle

$v_x^i{}'$	The fluctuating part of translational velocity component of the selected i -th particle
T_V^i	The translational granular temperature
T_R^i	The rotational granular temperature
r_i	The radius of particle i
d_i	The distance between the centroid of particle i and the considered grid nod
N_P	The number of particles
d_{50}	The median particle diameter
u_x^g	The displacement component of the grid point
u_x^p	The displacement component of the particle centroid respectively
d	The distance between the grid point and the particle centroid
$u_{i,j}$	The displacement gradient tensor over the grid
E_{ij}	The Green – St Venant strain tensor
$G(r)$	The spatial correlation function
N	The total number of contact points
f_i	The normalized normal contact force acting at contact i
r_{ij}	The distance between contacts i
r	The distance of two particles

G	The *Gini* coefficient
dE_W	The boundary work of the granular system
dE_b	The body work done by gravity force
dE_s	The elastic strain energy dE_s stored at particle contacts
dE_{pb}	The bond energy stored in parallel bonds
dE_k	The kinetic energy of the granular system
dE_f	The frictional dissipation of the granular system
dE_d	The damping dissipation of the granular system
E_{frac}	The fracture energy of the granular system
E_W^j	The total accumulated work done by all walls on the assembly at the current time step
E_W^{j-1}	The total accumulated work done by all walls on the assembly at the previous time step
F_W	The resultant force acting on the wall
ΔU_W	The applied displacement occurring during the current time step
dE_p	The plastic energy dissipation dE_p of the granular system
C_n	The coordination number
$E(\mathbf{n})$	The probability density function
a_c	The contact normal anisotropy
a_n	The normal force anisotropy

a_t	The tangential force anisotropy
T_3x	The Xujiajointe Group
Q_4^{del}	The Quaternary deposits
$T_1 j$	The Jialingjiang Group
T_2l	The Leikoupo Group
$r_{\max} / r_{\min}$	The size ratio
UCS_m	The unconfined compressive strength of the rock mass
d	The fragment size
V_f	The volume of a fragment
V_0	The volume of the rock mass
n_v	The non-convex envelope of neighboring particles
S	The solid fraction
V_{tot}	The total representative volume within the non-convex envelop
V_m	The volume of granular material inside the total representative volume
N	The number of fragments with a characteristic linear dimension larger than fragment size
D	The fractal dimension
erf	The complementary error function
δ_{ij}	The Kronecker delta

C_v	The coefficient of variations
N_d	The number of base disks in each fragment
m^d	The mass of base disk of each fragment
$\mathbf{x}^d$	The vector of constituent disk and fragment centroids
$\mathbf{X}^{fragment}$	The vector of fragment centroids
$I_{ij}^{fragment}$	The interial tensor of fragment shape
$\mathbf{I}^d$	The inertial tensor relative to the disk local Cartesian axis
V_p	The P wave velocity
V_s	The S wave velocity
v_n	The instantaneous normal velocity of the boundary particles
v_s	The instantaneous shear velocity of the boundary particles
v_n^{equ}	The applied velocity decomposed in the vertical direction
v_s^{equ}	The applied velocity decomposed in the horizontal direction
E	The Young's modulus
K	The Bulk modulus
G	The shear modulus
ν	The Poisson's ratio
ρ	The density
A	The amplitude of the signal

f	The central frequency of the signal
v	The rock block velocity
h	The drop height
$x_i^{(p)}$	The locations of the particle centroid
$x_i^{(c)}$	The locations of the contact
$n_i^{(c,p)}$	The unit normal vector directed from a particle centroid to its contact location
$F_j^{(c)}$	The force acting at a contact
q'	The deviator stress
$p(m)$	The mass distribution of fragments
$N(d > d_i)$	The number of fragments with size greater than a certain size
C	The number of elements at a unit length scale
$M(d < d_i)$	The cumulative mass of fragments smaller than a certain size
M_T	The total mass of all of the fragments
$d_{\max}$	The size of the largest fragment
F_D	The degree of fragmentation
$M_{\max}$	The mass of the largest fragment at initial static state
$m_{\max}$	The mass of the largest fragment at final deposition
L	The center of the sliding mass
L_f	The travel length of the front of the deposits

Greek Symbols

$\bar{\sigma}$	The tensile strength of the parallel bond
$\bar{\sigma}_c$	The tensile strength limit of the parallel bond
$\bar{\tau}$	The shear strength of the parallel bond
$\bar{\tau}_c$	The shear strength limit of the parallel bond
$\Delta\widehat{\delta}_n^e$	The elastic portions of the normal displacement increment
$\Delta\widehat{\delta}_s^e$	The elastic portions of the shear displacement increment
μ^{sj}	The smooth joint friction coefficient
σ_t^{sj}	The smooth joint tensile strength
c^{sj}	The smooth joint cohesion
ψ	The smooth joint dilation angle
ω^i	The angular velocity component of the selected i -th particle
$\overline{\omega^i}$	The mean angular velocity component of the selected i -th particle
$\omega^{i}{'}$	The fluctuating part of translational velocity component of the selected i -th particle
Ω_i	The selected spherical region Ω_i
θ_0	The initial phase angle of the grid point location relative to the particle centroid
ω	The accumulated rotation of the particle
Φ_{ij}	The second-order fabric tensor

Φ_1	The principal fabric
δ_{ij}	The Kronecker delta
Φ'_{ij}	The deviatoric fabric tensor
σ	The standard deviation
μ	The mean
σ_n	The time-dependent normal stress at the base boundary
σ_s	The time-dependent shear stress at the base boundary
$\sigma'_{1,f}$	The eigenvalues of the stress tensor $\bar{\sigma}_{ij}^{(P)}$
σ_{disp}	The dispersive stress
$\bar{\sigma}_{ij}^{(P)}$	The input average normal and shear stress tensor of a particle

Chapter 1

Introduction

1.1. Background

The mechanical loading of rocks results in local inelastic processes that produce microcracks. The cooperative interaction of these cracks leads to the formation of macroscopic fractures (Lockner, 1993). The growth of fractures results in the loss of cohesion and a reduction in rock strength, imparting permanent changes to the material. In particular, the introduction of pre-existing weak planes within a rock can aggravate inhomogeneity and anisotropy, affecting the mechanical properties of these materials. The formation of microcracks during rock deformation, and their evolution into macrofractures is a complex process that includes initiation, propagation, extension, and coalescence of cracks through rock matrix. Coalescence is defined as the connection of freshly formed broken faces and pre-existing discontinuities in a rock material via propagation. This progressive fracturing process is mainly at the origin of the rock mass destabilization. The same crack propagation and coalescence processes observed in laboratory-scale experiments and numerical models occur in a fractured rock slope.

1.2. Research Motivation

Numerical modeling of damage and failure development involving crack localization and coalescence is known to be challenging, especially in the presence of pre-existing discontinuities (e.g. joint sets, schistosity, bedding planes, and faults). Different from a continuum approach, discrete element simulations always contain an intrinsic microstructural heterogeneity (Cundall 2001; Koyama and Jing 2007), which is an important premise for localization of deformation. This is especially important when simulating complex processes arising during fracturing deformation of rocks (Virgo et al. 2013). Additionally, DEM can be extended to access the phenomena that are otherwise difficult, even impossible, to obtain directly from laboratory experiments, such as intergranular interactions and fracture interaction and coalescence.

Thus, the goal of this study is to develop a DE framework that is appropriate for solving this class of problems. This framework is able to investigate the micromechanisms underlying the deformation behavior of rocks and to predict and interpret the macroscopic behavior occurring in a rock mass. Essentially, model predictions are analyzed at the scale of a rock slope with an emphasis on its capacity to reproduce two of the keys mechanisms that contribute the development of progressive failure, namely, static and dynamic fragmentations.

1.3. Objective and Scope

The research presented in this thesis has two major objectives. The first is to validate the use of discrete element method in investigating the overall behaviour of rock mass involving multiple interconnected weak planes. This objective is achieved by addressing the following:

1) The progressive development of microfracture is clearly presented in DE simulations.
2) The numerical model is validated by comparing the numerical results with experimental data.
3) Particle kinematics, contact force chains, void ratios, and shear strains are utilized to understand the response of the granular media.
4) In-depth micromechanical analysis of the fracturing process and the associated energy budget.

The second objective of this research is to extend the discrete element methodology to analyze the destabilization of a large-scale natural rock slope that involves dynamic fragmentation process. This objective is achieved by addressing the following:

5) Illustrate the progressive damage in the rock slope.
6) Investigate the kinematics and energy conversion associated with the movement of the granular system.
7) Perform statistical analysis to examine the fragmentation characteristics as a result of the rock fracturing during the solid mass emplacement.
8) Quantify the influence of fragmentation on the rock slope instability and subsequent runout.

1.4. Contributions of authors

This thesis has been prepared in a manuscript format in accordance with the regulations and stipulations of the Faculty of Graduate Studies at McGill University. Papers J1, J2, J3 outlined in the publication list are all the candidate's original work and are included in the thesis. Chapter 3 contains manuscript J1, which is currently undergoing a second round of review in Acta Geotechnica Journal. Chapter 4 reflects the content of manuscript J2 that has been accepted for publication in the ASCE International Journal of Geomechanics. Chapter 5 contains manuscript J3, which is being requested for revision for final submission to Landslides Journal. General conclusions from the research work are included in Chapter 6.

The discrete element model, micromechanical analysis, fragmentation statistic, as well as spatial interpolation technique presented in the thesis have been achieved using the numerical platforms of PFC (particle flow code) and MATLAB. The required coding has been written using MATLAB intrinsic language, and Fish or Python scripting languages in PFC.

All the formulation, program coding, and the preparation of the manuscripts were completed by the candidate, under the supervision of Prof. Mohamed Meguid and Prof. Luc Chouinard, his thesis supervisors

1.5. Thesis Organization

The thesis consists of six chapters. After this introduction, Chapter 2 reviews the literature on the discrete element modeling of fracture growth mechanisms in rock. The theoretical background required to formulate the fragmentation behaviour of rock material during landsliding process is also outlined. Chapters 4, 5, and 6 are versions of journal papers J1, J2 and J3 in the publication list, respectively.

Chapter 3 presents the results of a numerical study that has been performed to investigate the deformability and failure behaviour (progressive fracture growth, material damage, failure mode) of rock samples containing two sets of persistent joints with increased initial joint frequency through confined compression tests using discrete element analysis. The numerical results are compared with previously published experimental data. The chapter is a modified version of paper J1 in the publication list.

Chapter 4 delineates the development of DE analyses that incorporates spatial interpolation technique and statistical analyses to provide new insights into the characteristics of dynamic rock fragmentation and the mechanisms governing the fracture growth mechanism and transport kinematics of a co-seismic landslide, including trajectory motion, internal damage accumulation, the evolution of stresses, and the solid concentration. Additionally, the observed features from field investigations are used to verify the validity of the numerical model. Thus, the proposed framework for the analysis of rock avalanches can be used to understand the physics of similar geological hazards.

Chapter 5 illustrates a dynamic discrete element simulation to analyze a landslide triggered by the 2008 Ms 8.0 Wenchuan earthquake aiming to understand the dynamic disintegration and transport behaviour of an earthquake induced landslide. Original application of absorbing boundary condition to avoid the adverse effect of seismic wave transmission and reflection at the slope base. The numerical results demonstrate that under seismic loadings, internal rock damage initiates, propagates, and coalesces progressively along the weak solid structure and subsequently leads to fragmentation and pulverization of the slope mass. The fragment network before movement initiation and the final fragmented depositions after rapid transport have been investigated using fragment statistics (fragment size distribution, fragment mass distribution, and fractal dimension) and morphometric characters (fragment shape isotropy) to offer new insights into the disintegration characteristics of the earthquake-induced catastrophic mass movements.

The thesis ends with Chapter 6 that contains a set of conclusions and recommendations for future work.

Chapter 2

Literature review

2.1. Discrete element method

2.1.1. Basic formulation

The DEM was introduced by Cundall (1971) for the analysis of rock-mechanics problems and then applied to soils by Cundall and Strack (1979).

In the DEM, the interaction of particles is treated as a dynamic process with states of equilibrium developing whenever the internal forces balance. The contact forces and displacements of a stressed assembly of particles are found by tracing the movements of the individual particles. Movements result from the propagation through the particle system of disturbances caused by wall and particle motion, externally applied forces and body forces.

Translational and rotational motion of particles are determined using Newton's second law and the contact forces caused by the relative motion of particles are updated using force-displacement law at each contact point (Potyondy and Cundall, 2004). The translational and rotational motions can be generally described using the following equations:

$$m_i\left(\frac{d^2x_i}{dt^2} - g_i\right) = \sum_{j=1}^{n_i}\left(F_{n,ij}^l + F_{s,ij}^l + F_{n,ij}^d + F_{s,ij}^d\right) \quad (1)$$

and

$$I_i\,\frac{d^2\theta_r}{dt^2} = \sum_{j=1}^{n_i}\frac{dH_i}{dt} \quad (2)$$

where m_i, x_i, I_i are, respectively, the mass, location, and the moment of inertia of particle i. Gravitational and inter-particle forces between particles i and j in equation (1) involve normal and shear components of the elastic forces $F_{n,ij}^l$ and $F_{s,ij}^l$, and similar components of the damping forces $F_{n,ij}^{d}$ and $F_{s,ij}^{d}$. In equation (2), θ_r represents the relative rolling angles between two contacting particles i and j and H_i is the angular momentum of the particle.

2.1.2. Bonded particle contact model for rock

The bonded-particle model for rock (referred to hereafter as the BPM) exhibits a rich set of emergent behaviors that correspond very well with those of real rock. The BPM provides both a scientific tool to investigate the micromechanisms that combine to produce complex macroscopic behaviors and an engineering tool to predict these macroscopic behaviors (Potyondy and Cundall 2004).

The inherent characteristics in the BPM are listed below:

1. Particles are circular or spherical rigid bodies with a finite mass.

2. Particles move independently of one another and can both translate and rotate.

3. Particles interact only at contacts; because the particles are circular or spherical, a contact is comprised of exactly two particles.

4. Particles are allowed to overlap one another, and all overlaps are small in relation to particle size such that contacts occur over a small region (i.e., at a point).

5. Bonds of finite stiffness can exist at contacts, and these bonds carry load and can break. The particles at a bonded contact need not overlap.

6. Generalized force–displacement laws at each contact relate the relative particle motion to the force and moment at the contact.

The BPM mimics the mechanical behavior of a collection of grains joined by cement where each grain is considered as a particle and each cement entity is treated as a parallel bond. The linear parallel bond model provides the behavior of two interfaces: (i) an infinitesimal, linear elastic (no-tension) and frictional interface that carries a force; and (ii) a finite-size, linear elastic and bonded interface that carries a force and moment (see Figure 2-1). The first interface is equivalent to the linear model: it does not resist relative rotation, and slip is accommodated by imposing a Coulomb limit on the shear force. The second interface is called a parallel bond, because when bonded, it acts in parallel with the first interface. When the second interface is bonded, it resists relative rotation, and its behavior is linear elastic until the strength limit is exceeded and the bond breaks making it unbonded. When the second interface is unbonded, it carries no load. The unbonded linear parallel bond model is equivalent to the linear model.

The linear parallel bond model updates the contact force and moment as follows:

$$\mathbf{F_c} = \mathbf{F^l} + \mathbf{F^d} + \bar{\mathbf{F}} \tag{3}$$

$$\mathbf{M_c} = \bar{\mathbf{M}} \tag{4}$$

where $\mathbf{F^l}$ is the linear elastic force, $\mathbf{F^d}$ is the dashpot force, $\bar{\mathbf{F}}$ is the parallel-bond force, and $\bar{\mathbf{M}}$ is the parallel-bond moment. The parallel-bond force is resolved into a normal and shear force, and the parallel-bond moment is resolved into a twisting and bending moment:

$$\bar{F} = -\bar{F}_n \hat{\mathbf{n}}_\mathbf{c} + \bar{\mathbf{F}}_s \tag{5}$$

$$\bar{\mathbf{M}} = \bar{M}_t \hat{\mathbf{n}}_\mathbf{c} + \bar{\mathbf{M}}_\mathbf{b} \ \text{(2D model: } M_t \equiv 0\text{)} \tag{6}$$

where $\hat{\mathbf{n}}_\mathbf{c}$ is the unit vector that defines the contact plane.

The increments of elastic force and moment are given by

$$\bar{F}^n := \bar{F}^n + \bar{k}^n \bar{A} \Delta\delta_n \tag{7}$$

$$\bar{\mathbf{F}}^\mathbf{s} := \bar{\mathbf{F}}^\mathbf{s} - \bar{\mathbf{k}}^\mathbf{s} \bar{A} \Delta\delta_s \tag{8}$$

$$\bar{M}_t := \begin{cases} \bar{M}_t - \bar{k}_s \bar{J} \Delta\theta_t, & \text{3D} \\ 0, & \text{2D} \end{cases} \tag{9}$$

$$\bar{\mathbf{M}}_\mathbf{b} := \bar{\mathbf{M}}_\mathbf{b} - \bar{k}^n \bar{I} \Delta\theta_b \tag{10}$$

where $\bar{A}$, $\bar{I}$ and $\bar{J}$ are the area, moment of inertia and polar moment of inertia of the parallel bond cross section, respectively. In two dimensions, $\bar{A} = 2\bar{R}t$, $\bar{I} = \frac{2}{3}\bar{R}^3 t$, and $J = 0$.

In a bonded discrete element system, each element is bonded to its neighboring elements with which it is in contact using springs and linear elastic beams of circular cross-section (see Fig. 2 - 1).

The maximum tensile and shear stresses acting on the parallel-bond periphery are calculated from the beam theory as

$$\bar{\sigma} = \frac{\bar{F}_n}{\bar{A}} + \frac{\left\|\bar{M}_b\right\| \bar{R}}{\bar{I}} \tag{11}$$

$$\bar{\tau} = \frac{\left\|\bar{\mathbf{F}}_{\mathbf{s}}\right\|}{\bar{A}} + \begin{cases} \dfrac{\left|\bar{M}_t\right| \bar{R}}{\bar{J}}, & \text{3D} \\ 0, & \text{2D} \end{cases} \tag{12}$$

where $\bar{F}_n$, $\bar{\mathbf{F}}_{\mathbf{s}}$ are normal and shear parallel-bond force, $\bar{M}_t$, $\bar{\mathbf{M}}_{\mathbf{b}}$ denote twisting and bending parallel-bond moments;

If the tensile strength limit is exceeded $\bar{\sigma} > \bar{\sigma}_c$, then the bond breaks in tension. If the bond does not break in tension, then the shear strength limit is enforced. The shear strength $\bar{\tau}_c > -\sigma \tan \bar{\phi} + \bar{c}$, where $\sigma = \dfrac{\bar{F}_n}{\bar{A}}$ is the average normal stress acting on the parallel bond cross section. If the shear strength limit is exceeded ($\bar{\tau} > \bar{\tau}_c$), then the bond breaks in shear.

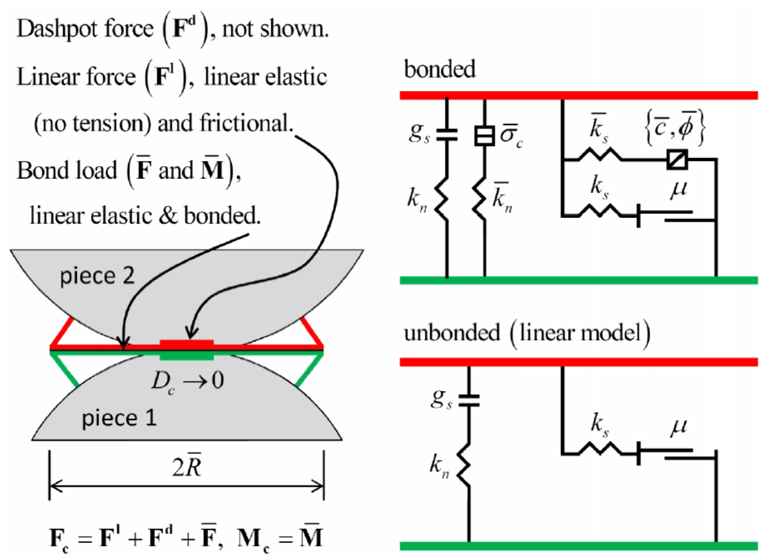

Figure 2 - 1. Behavior and rheological components of the linear parallel bond model with inactive dashpots (Itasca Consulting Group. 2015).

The bond removal method and the smooth joint (SJ) model are two common approaches for generating joints in PFC. The smooth joint model was developed by Cundall (Pierce et al. 2007) to resolve the shortcomings of the bond removal approach and has been used largely in numerical simulations of jointed rock masses (Bahaaddini et al. 2013; Mas Ivars et al. 2011).

Bond Removal Method

The most common method for simulating joints in PFC is the bond removal method. With this approach, particles lying on a joint track are left unbonded, as shown in Fig. 2 - 2. A number of studies have used this approach to study the mechanical behaviour of rock joints (Asadi et al. 2012, 2013; Cundall 2000; Park and Song 2009&2013; Rasouli and Harrison 2010).

For joint representation, interfaces in numerical models consisting of assemblies of bonded particles have been traditionally represented by debonding contacts along a line or plane and assigning low strength and stiffness microproperties to them (Kulatilake et al. 2001). This way of representing interfaces is problematic because of the inherent roughness of the interface surfaces (Fig. 2-2). Even the assignment of very low friction to the contacts on the interface will not generally lead to realistic sliding because of the roughness or bumpiness induced by the particles.

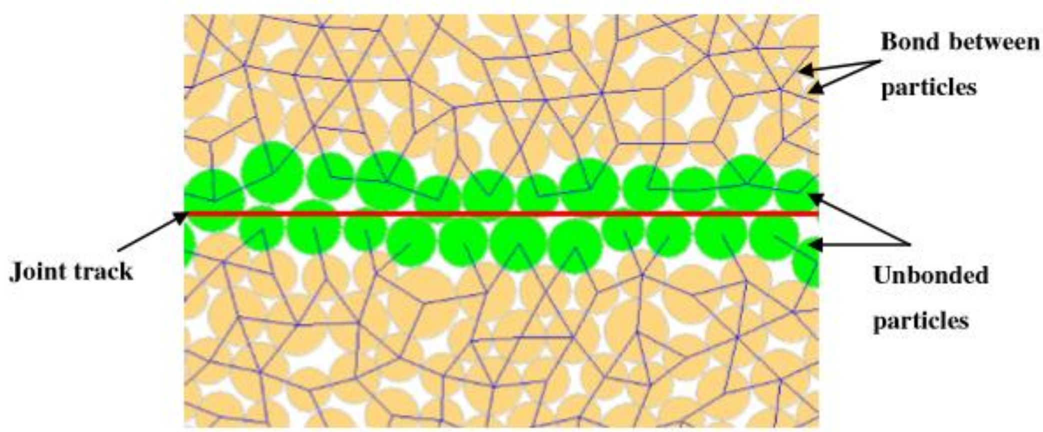

Figure 2 - 2. The bond removal method (Bahaaddini et al. 2015).

To overcome the shortcomings of this approach, the smooth joint (SJ) model was introduced into DEM simulation (Pierce et al. 2007).

Smooth-Joint Contact Model

A smooth-jointed interface can be inserted into the bonded materials by identifying the contacts near the interface and replacing their contact models with the smooth-joint contact model. New grain grain contacts that may form during subsequent motion are assigned the linear contact model, with the exception of the new contacts associated with the interface, which are assigned the smooth-joint contact model and aligned with the interface direction.

A smooth joint can be envisioned as a set of elastic springs uniformly distributed over a circular cross-section (Fig. 2 - 3), centered at the contact point and oriented parallel with the joint plane. The area of the smooth-joint cross-section is given by:

$$A = \pi R^2 \qquad (13)$$

with $R = \lambda \min(R^{(1)}, R^{(2)})$

where $R^{(1)}$ and $R^{(2)}$ are the radii of the two contacting entities (disk/sphere).

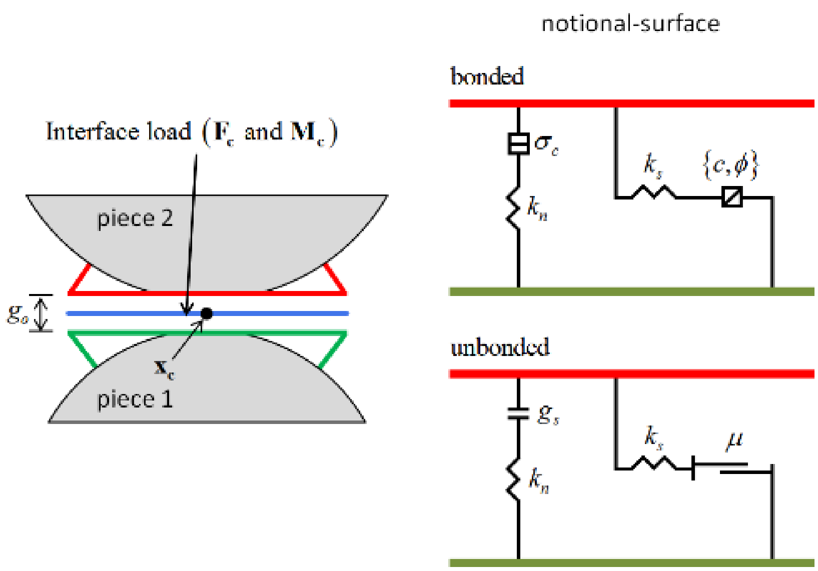

Figure 2 - 3. Behavior and rheological components of the smooth-joint model

(Itasca Consulting Group. 2014)

The force-displacement law (see Figure 2 - 4) for the smooth-joint model updates the contact force as given by:

$$\mathbf{F_c} = \mathbf{F}, \quad \mathbf{M_c} \equiv 0 \tag{14}$$

where $\mathbf{F}$ is the smooth-joint force. The force is resolved into normal and shear forces:

$$\mathbf{F} = -F_n \hat{\mathbf{n}}_\mathbf{j} + \mathbf{F_s} \tag{15}$$

Updating the normal and shear forces:

$$F_n = (F_n)_0 + k_n A \Delta \hat{\delta}_n^e \tag{16}$$

$$\mathbf{F_s^*} = (\mathbf{F_s})_0 - k_s A \Delta \hat{\delta}_s^e \tag{17}$$

where $(F_n)_0$ and $(\mathbf{F_s})_0$ are the smooth joint normal and shear forces, respectively, at the beginning of the time step; $\Delta\hat{\delta}_n^e$ and $\Delta\hat{\delta}_s^e$ are the elastic portions of the normal and shear displacement increments.

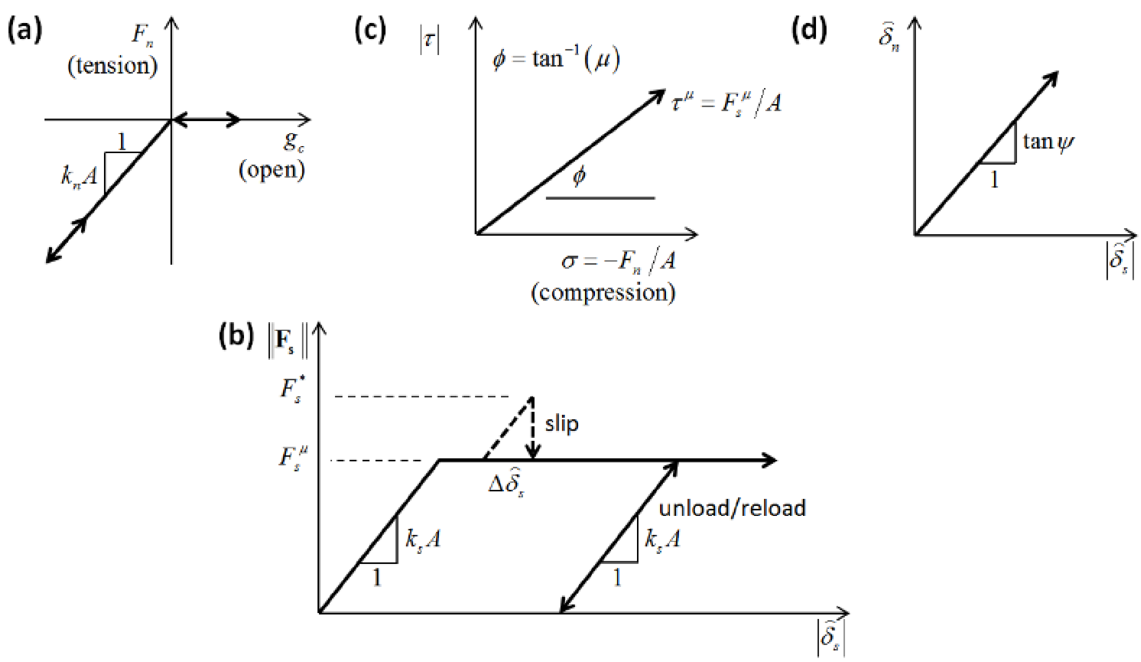

Figure 2 - 4. Force-displacement law for an unbonded joint: (a) normal force versus normal displacement; (b) shear force versus shear displacement; (c) strength envelope; and (d) normal displacement versus shear displacement during sliding.

The shear strength is also computed as: $F_s^\mu = -\mu F_n$

In the unbonded smooth joint model, the shear force will then be updated by:

$$F_s = \begin{cases} \mathbf{F_s^*}, & \left\| \mathbf{F_s^*} \right\| < F_s^{\mu} \\ F_s^{\mu} (\mathbf{F_s^*} / \left\| \mathbf{F_s^*} \right\|) \end{cases} \tag{18}$$

When the $\left\| \mathbf{F_s} \right\| = F_s^{\mu}$, the slip state is active, and then the contact is sliding. While slipping, shear displacements produce an increase in normal force due to dilation:

$$F_n = F_n + (\frac{\mathbf{F_s^*} - F_s^{\mu}}{k_s}) k_n \tan \psi \tag{19}$$

2.2. DEM modeling of fracture development in a rock mass

The discrete element method has proven to be a promising approach to capture the response of rock material to applied external forces. Potyondy et al. (1996) first proposed a synthetic PFC model that could reproduce modulus, unconfined compressive stress, and crack initiation stress of the Lac du Bonnet Granite. Extended results were illustrated by Potyondy and Cundall (2004) with the simulation of the stress–strain behavior during biaxial compression tests for varying confining pressures. Several features of the rock behavior emerged from the BPM, including elasticity, fracturing, damage accumulation producing material anisotropy, dilation, post-peak softening and strength increase with confinement (Lisjak and Grasselli 2014). Duan et al. (2017), and Zhang et al. (2019) used DEM simulations to explore aspects of the deformation and strength characteristics under true triaxial stress states.

Application of acoustic emission in DEM that complements the micromechanical studies to analyze fracture growth mechanisms was reported by Hazzard and Young (2000, 2002 & 2004), and van der Baan and Chorney (2019). BPM was employed as a numerical tool to study the initiation and propagation of fracks caused by pre-existing flaws. Lee and Jeon (2011), and Yang et al. (2014) performed a numerical simulation to examine the coalescence characteristics in rock samples containing two unparallel fissures using DEM, and the simulated peak strength, crack initiation stress and ultimate failure mode of rock samples were compared with experimental results.

Cao et al. (2015) utilized DEM to explore the peak strength and failure characteristics of rock-like materials with multi-fissures. Manouchehrian and Marji (2012) investigated numerically the influence of confining pressure on the crack propagation behavior in rock-like materials using DEM, which showed that wing cracks initiate perpendicular to the flaw and propagate toward the direction of major stress. Manouchehrian et al. (2014) studied the effect of the fissure orientation on the crack propagation mechanism in brittle materials such as rocks under various compressive loads by using DEM.

Analyses of failure and deformation mechanisms during compressive loading of rock joints were also carried out to obtain insights into rock fracture coalescence behaviour and integrity degradation. De Silva and Ranjith (2020) carried out a discrete element analysis on rock formations with complex joint geometries to study the rock mass fracturing mechanisms. Yang et al. (2016) studied uniaxial compression tests for non-persistent jointed rock samples by analyzing the effects of joint gap, dip angle, and persistency. Scholtès et al. (2011) used the discrete element method to investigate the effect of discontinuities on fracturing development in rock-like material.

Substantial insights have been gained from the above studies regarding rock deformation under different loading conditions. Nonetheless, there is still a need for an in-depth knowledge of the macroscopic deformation processes of jointed rock mass by identifying the mechanisms involved at the microscopic scale during compression test simulations performed under confined loading conditions.

2.3. DEM analysis of fracturing in geodynamic processes

Rockslides or rock avalanches start out as a quasi-intact rock mass that can disintegrate during transport. Generally, one separates the disintegration into two types (Pollet and Schneider 2004): **(1) Primary (static) fragmentation:** where the rock mass separates by breaking rock bridges connecting fragments of more competent rock together (Eberhardt et al., 2004). Indeed, on the bases of in situ observations, most rock slope failures involve a complex interaction between pre-existing discontinuities and brittle fracture propagation through intact rock bridges, resulting in a step-path failure mode involving both sliding on existing discontinuities and brittle fracturing of intact rock (Brideau et al. 2009). Clearly, the potential step-path failure surfaces are related to the spatial distribution of the joints and modes of their coalescence. Then, instability finally occurs along an adverse step-path slip surface under the action of external forces, e.g., gravity, and seismic loading.

Figure 2 - 5 shows the step-path failure in two gneiss slopes in natural system. In the preceding chapters, a large body of literature that thoroughly present the process of rock bridge failure/crack coalescence in laboratory-scale experiments is reviewed. Likewise, the application of fracture growth mechanism leading to failure in rock slopes is demonstrated.

From basic laboratory scale simulations to complex slope stability case study, Scholtès and Donzé (2012) showed that DEM models can simulate the progressive nature of failure occurring in jointed rock and provided a validation of the method on the basis of referenced experiments and in situ observations. Utili and Nova (2008), Jiang and Murakami (2012), and Jiang et al. (2015) modeled the failure processes of idealized rock slopes by increasing the gravitational acceleration or strength reduction in DEM.

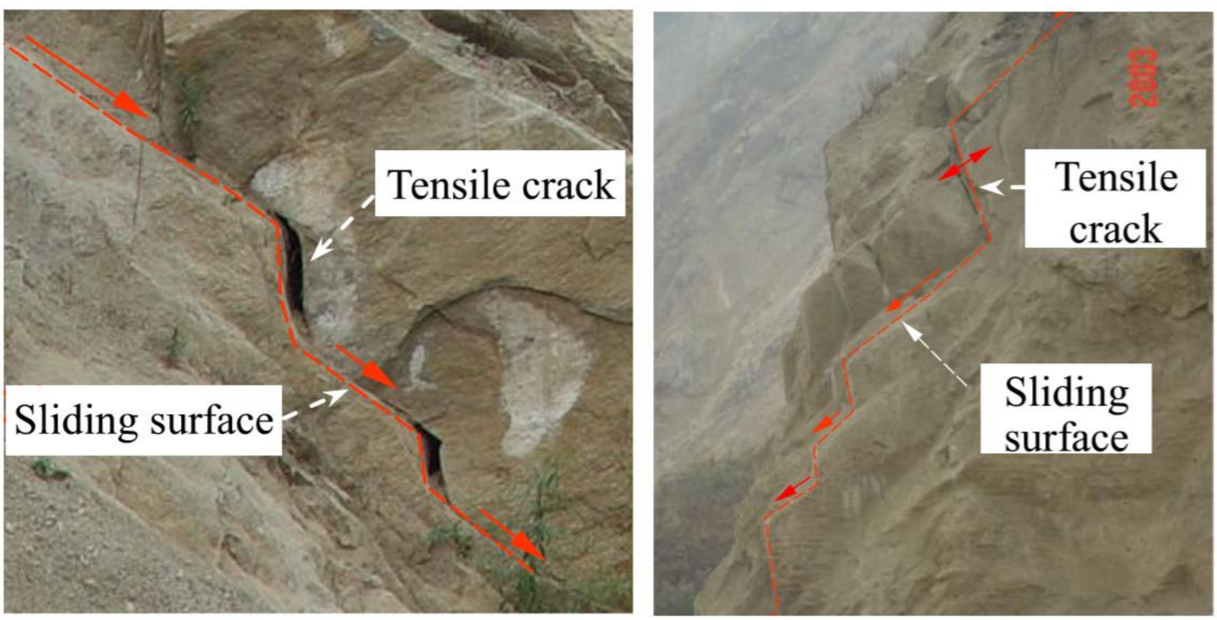

Figure 2 - 5. Illustrations of progressive failure in the rock slopes of the Xiaowan hydroelectric station, China (Huang et al. 2014).

(2) Dynamic fragmentation: where particles are continuously reduced in size by grinding and comminution (Pollet and Schneider 2004; Imre et al. 2010). Despite the face that this sequence of fragmentation is based on observation of rock avalanches, it is assumed here that the fragmentation of rockslides occurs in a similar manner (Haug et al. 2016). Even though the entire deposit of rockslides may be fragmented, zones of more intense fragmentation can be observed in localized shear zones, such as at the base of rockslides (Pollet and Schneider 2004; Imre et al. 2010). The

Figure 2 - 6. Field evidences from the landslide deposit for occurrence of dynamic fragmentation (Wang et al. 2018).

For numerical modeling of dynamic fragmentation within landslide emplacement, De Blasio and Crosta (2015) employed a simple two-dimensional DEM model to study the fragmentation behavior of rock mass along a slope break profile. They suggested that for slope angles greater than 70^{o}, the fragmentation process can produce uniformly distributed fragments, with significantly enhanced momentum and runout distance. Discrete element analyses performed by Langlois et al. (2015) have shown that fragmentation can increase the travel length of the front of rockslide deposits. Numerical simulations with discrete element methods conducted by Zhao et al. (2017) highlighted that high kinetic energy associated with steep slopes increases the intensity of fragmentation.

Following the experimental studies designed by Bowman et al. (2012), Zhao et al. (2018) created more complex joint sets to investigate the dynamic fragmentation of jointed rock blocks during rockslides by discrete element method simulations. The results indicate that jointed rock blocks influence the elastic wave propagation and energy dissipation when the blocks collide with the horizontal plane and finally affect the degree of fragmentation in the deposit.

The numerical investigations have further confirmed and explained the observations from natural systems that the deposits of rock avalanches are highly fragmented, and fragmentation has been demonstrated to cause the long travel lengths in some rock avalanches. For example, fragmentation produces fine materials that may have a lubricating effect (e.g., Kilburn 2001; Pollet and Schneider 2004), or dispersive stresses from exploding fragments may effectively reduce the normal stress at the base (e.g., Davies and McSaveney 2009).

2.4. Conclusion for the Literature Review

Based on this literature review and the review presented in other chapters, it can be seen that modeling progressive fracture development either at the laboratory-scale or at the large-scale geodynamic system is a very complex numerical exercise. Notwithstanding the aforementioned advancements, comprehensive studies on the microscale characterization of fracture growth in laboratory-scale rock samples and the progressive disintegration of rock slopes during landsliding are scarce in the literature. Therefore, there is a need for more numerical studies to simulate and validate the related problems using a robust framework that accounts for the progressive deformational behavior of the rock system, which is not possible to achieve using conventional continuum-based or experimental approaches. Such development will be presented in this thesis using both experimental studies and numerical simulations of large-scale problems.

Chapter 3

On the role of pre-existing discontinuities on the micromechanical behavior of confined rock samples: A numerical study

Abstract

The deformation process and failure mechanism of rock mass with increased density of initial joints subjected to confined stress state is investigated in this study using discrete element method (DEM). A numerical model of standard size granite samples is developed and validated using experimental data for both intact and jointed rocks. The micro parameters of the rock material are first determined and the effects of the rock discontinuity on strength, deformability, stress–strain relationship and failure modes are then investigated at the macro scale level. Analyses are also performed to examine the tensile and shear crack distributions, fragmentation characteristics, particle kinematics, and energy dissipation to advance the current understanding of the deformation processes and failure mechanisms of jointed rock masses. The microscopic evolutions in the fabric and force anisotropy during loading and distributions of contact forces provide insights into the influence of increasing initial jointing on the macroscopic deformational behaviour of the rock. The results show how the deceleration in the growth of fabric and contact force anisotropies develop and confirm that the increase in initial jointing and the associated changes in microstructure can restrain the development of anisotropy, thereby reducing significantly the strength of the rock samples.

Keywords: Rock failure processes; Discrete element method; Rock discontinuity; Micromechanics; Fabric evolution and anisotropy

∗ A version of this chapter has been accepted in ***Acta Geotechnica*** *Journal*.

3.1. Introduction

One of the main characteristics of rock mass is the presence of discontinuities, such as fractures, joints, bedding planes, and faults. These discontinuities can have dominant effects on the deformability and strength of a rock mass. In particular, a discontinuity can have a critical effect on the stability of rock slopes and underground structures. Therefore, for stability analysis of rock slopes or support design of underground excavations, it is of crucial importance to acquire a thorough understanding of the geometrical and mechanical properties of rock discontinuities.

Laboratory experiments on rock samples are usually performed to understand crack evolution as well as the complex mechanical behavior of joints. Uniaxial compression tests conducted on samples with pre-existing discontinuities (Kulatilake et al. 1997 & 2001; Singh et al. 2002; Feng et al. 2019) revealed that the most significant factors controlling the strength, deformation, and failure mechanism of jointed rock include joint length and density, and joint orientation. However, rock masses are generally subjected to in-situ confinement and, therefore, it is important to investigate the effect of pre-existing joint sets on the strength and failure behaviour of rock under confining pressure. Brown and Trollope (1970) carried out a series of triaxial compression tests under five different confinements on an idealized rock-like material with four arrangements of joint sets orientation. They concluded that the predicted strength was much lower than that of the intact material, except for the case of vertical-horizontal orientation. Prudencio and Van Sint Jan (2007) performed biaxial compression tests on jointed rock samples and indicated that the geometry of the joint systems, the orientation of the principal stresses, and the ratio between intermediate principal stress and intact material compressive strength have significant effects on the failure modes and strengths of jointed rock masses.

Although laboratory experiments can shed some lights on the significance of joint configuration on the mechanical behavior of jointed rock masses (Yang et al. 2016), the entire failure progression from crack initiation, propagation and coalescence up to failure is hard to visualize inside the samples during testing (Quiñones et al. 2017; Li et al. 2019). Moreover, the fracture of some brittle rock materials is very rapid, which makes it difficult to trace the process with currently available monitoring devices (Glynn et al. 1978; Zhang et al. 2006). In addition, experimental results are sensitive to sample preparation and boundary conditions; a small change in the contact condition between the sample and loading platen may result in a different failure mode (Ghazvinian et al.

2012). Therefore, given the mechanical and geometrical complexities of jointed rock blocks, there is a need to develop suitable numerical models that are capable of capturing the progression of fracture growth and the associated material damage.

Continuum (e.g. FEM and FDM) and discontinuum (e.g. DEM) methods are among the main methods used to model rock failure. Continuum methods generally assume continuous, isotropic, homogeneous, and linearly elastic medium. However, jointed rocks are usually heterogeneous and anisotropic such that fractures developing in the intact rock interact with the pre-existing joints (Chiu et al. 2013). In addition, the presence of weak planes, being sources of large deformation and low shear strength, contributes significantly to the anisotropic behavior of rocks (Park and Min 2015; Eshiet and Sheng 2016; Fu et al. 2018).

By contrast to continuum methods, the application of the discrete element method to simulate jointed rock mass has the following advantages: (i) the failure and fracture development caused by a joint face can be simulated free from the limits of the mesh deformation; and (ii) the distribution of actual joint faces can be considered. Thus, the discrete element method (DEM) is a promising approach to capture the heterogeneous and anisotropic nature of rock mass and assess the failure process and the strength of jointed rock-masses. Bahaaddini et al. (2013, 2016) simulated uniaxial compression tests for non-persistent jointed samples and investigated the dependence of different failure modes on the joint dip and overlap angles, and joint spacing by analyzing contact force distribution and bond breakage. Yang et al. (2016) studied uniaxial compression tests for non-persistent jointed rock samples by analyzing the effects of joint gap, dip angle, and persistency. They concluded that the contact and interaction of joint surfaces have significant effects on the mechanical behavior of jointed rock blocks. Chen et al. (2018) showed that the effect of joint strength mobilization includes not only multi-peak deformation behavior but also strength reduction and increasing deformability features.

In the aforementioned experimental work and the corresponding discrete element modeling, only block-jointed samples and samples with medium or small non-persistent joints were studied. Indeed, very few experiments have been performed for samples under confined compression with multiple sets of large persistent joints, which can be considered as a natural representative of a rock mass characterized by discontinuity, heterogeneity, anisotropy, and non-elasticity.

The objective of this study is to investigate the micro-scale behaviour of brittle rock material under confined compressive loading with different joint configurations. A two-dimensional bonded particle model (BPM) is developed to model the behavior of brittle rock. Model validation is carried out by comparing the numerical results with laboratory tests performed on Blanco Mera (BM) granite material. Joint intensity related phenomena such as fracture patterns and modes, the shape of the stress–strain curve, and the post peak strength reduction (degradation) are studied. Detailed analyses are performed to investigate the evolutions of the microstructure of the rock mass for different joint set configurations in terms of the occurrence, propagation, and coalescence of micro-cracks. In addition, several important aspects are also examined including, evolution of energy transition, coordination number, fabric and anisotropies of contact normal (a unit vector perpendicular to the direction of contact between two particles) and contact forces, modes of microcracks in terms of shear or tensile failure of parallel bonds.

3.2. Model Description

3.2.1. The discrete element method (DEM)

The Discrete Element Method, or DEM, (Cundall and Strack 1979) has been used extensively to model the mechanical behavior of rocks and soils (Cho et al. 2007; Wang and Tonon 2009, 2010; Zhang and Wong 2012; Scholtès and Donzé 2012; Wang and Yan 2012; Shen et al. 2017; Gao and Meguid 2018 a&c; Yang and Qiao 2018; Shang et al. 2018a; Zhao et al. 2018; Garcia and Bray 2018). In rock mechanics, the bonded particle model (BPM) (Potyondy and Cundall 2004) allows for the rock to be simulated using a statistically generated assembly of bonded particles at the micro-scale level. The BPM reflects the macro characteristics by assigning different micro-parameters to particles and bonds to reproduce realistic features and to capture the response of brittle rocks. The smooth-joint contact model in bonded-particle systems provides the DEM model with the ability to simulate fracture propagation within a rock mass with persistent or non-persistent joints under selected loading conditions.

Discrete element modeling of jointed rock masses essentially comprises four components (Potyondy and Cundall 2004; Mas Ivars et al. 2011; Varela Valdez et al. 2018):

(1) *Discrete spherical/disk elements*: of a finite radius r, mass density ρ, and a friction coefficient μ. These discrete particles obey Newton's laws of motion and can interact when they are either in contact or bonded.

(2) *The force-displacement law*: for the linear parallel bond model updates the contact force and moment (Itasca Consulting Group 2014):

$$\mathbf{F_c} = \mathbf{F^l} + \mathbf{F^d} + \bar{\mathbf{F}} \tag{1}$$

$$\mathbf{M_c} = \bar{\mathbf{M}} \tag{2}$$

where $\mathbf{F^l}$ is the linear elastic force, $\mathbf{F^d}$ is the dashpot force, $\bar{\mathbf{F}}$ is the parallel-bond force, and $\bar{\mathbf{M}}$ is the parallel-bond moment. The parallel-bond force is resolved into a normal and shear force, and the parallel-bond moment is resolved into a twisting and bending moment (Itasca Consulting Group 2014):

$$\bar{F} = -\bar{F}_n \hat{\mathbf{n}}_\mathbf{c} + \bar{\mathbf{F}}_s \tag{3}$$

$$\bar{\mathbf{M}} = \bar{M}_t \hat{\mathbf{n}}_\mathbf{c} + \bar{\mathbf{M}}_\mathbf{b} \text{ (2D model: } M_t \equiv 0) \tag{4}$$

where $\hat{\mathbf{n}}_\mathbf{c}$ is the unit vector that defines the contact plane. Detailed information regarding the increments of elastic force and moment can be found in Potyondy and Cundall (2004).

(3) *Parallel Bonds*: In a bonded discrete element system, each element is bonded to its neighboring elements with which it is in contact using springs and linear elastic beams of circular cross-section (see Fig. 3 - 1a). The maximum tensile and shear stresses acting on the parallel-bond periphery are calculated from the beam theory as (Potyondy and Cundall 2004):

$$\bar{\sigma} = \frac{\bar{F}_n}{\bar{A}} + \frac{\left\|\bar{M}_b\right\| \bar{R}}{\bar{I}} \tag{5}$$

$$\bar{\tau} = \frac{\left\|\bar{\mathbf{F}}_\mathbf{s}\right\|}{\bar{A}} + \begin{cases} \dfrac{\left|\bar{M}_t\right| \bar{R}}{\bar{J}}, & \text{3D} \\ 0, & \text{2D} \end{cases} \tag{6}$$

where $\bar{F}_n$, $\bar{\mathbf{F}}_\mathbf{s}$ are normal and shear parallel-bond force, $\bar{M}_t$, $\bar{\mathbf{M}}_\mathbf{b}$ denote twisting and bending parallel-bond moments;

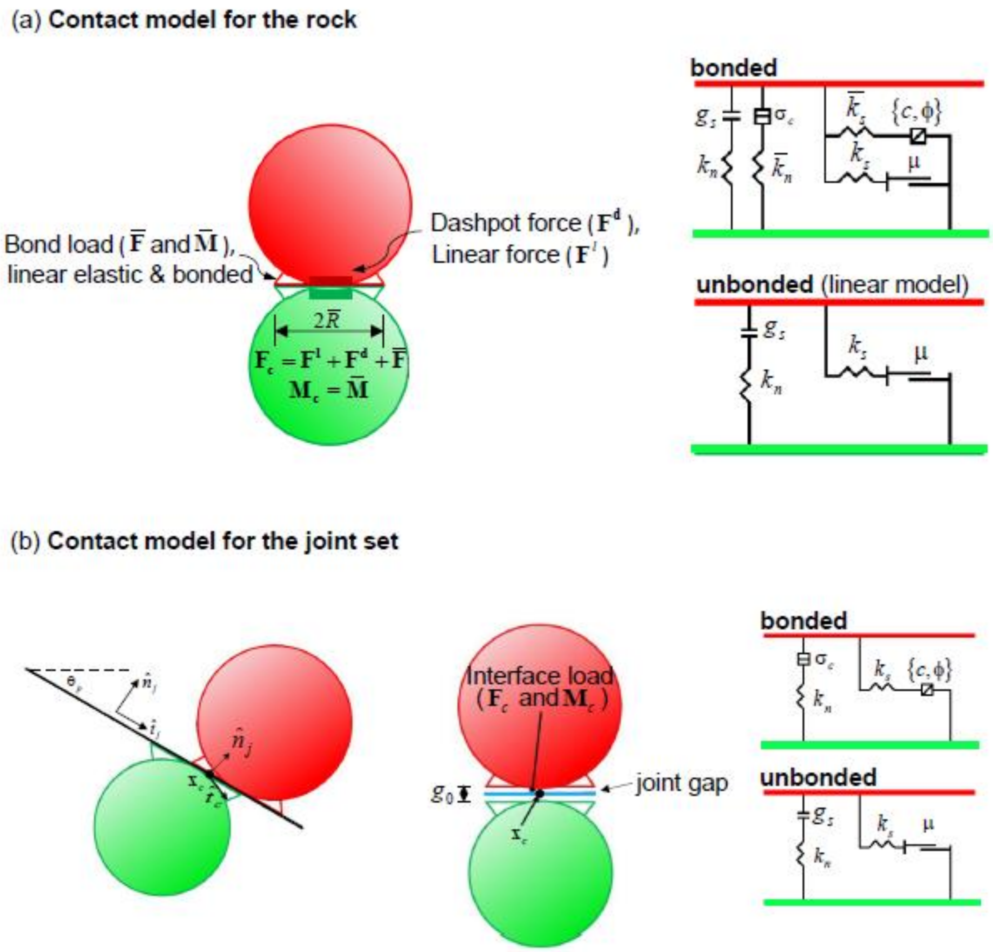

Figure 3 - 1. Behavior and rheological components of (a) the linear parallel bond model; (b) the smooth-joint model.

If the tensile strength limit is exceeded $\bar{\sigma} > \bar{\sigma}_c$, then the bond breaks in tension. If the bond does not break in tension, then the shear strength limit is enforced. The shear strength $\bar{\tau}_c > -\sigma \tan \bar{\phi} + \bar{c}$, where $\sigma = \frac{\bar{F}_n}{\bar{A}}$ is the average normal stress acting on the parallel bond cross section. If the shear strength limit is exceeded ($\bar{\tau} > \bar{\tau}_c$), then the bond breaks in shear.

(4) *Joints*: With the introduction of the smooth joint contact model, the bonded-particle DEM model with embedded smooth joints allows for the generation of an equivalent anisotropic jointed rock mass. After generation of the joint plane, a smooth joint is assigned at the contacts of particles with centres located on the opposite sides of the joint plane. At these contacts, the bonds are removed and smooth joints are defined in a direction parallel to the joint plane (see Fig. 3 - 1b).

Particles intersected by a smooth joint may overlap and pass through each other rather than be forced to move around one another.

A smooth joint can be envisioned as a set of elastic springs uniformly distributed over a circular cross-section, centered at the contact point and oriented parallel with the joint plane. The area of the smooth-joint cross-section is given by (Itasca Consulting Group 2014):

$$A = \pi R^2 \tag{7}$$

with $R = \lambda \min(R^{(1)}, R^{(2)})$

where $R^{(1)}$ and $R^{(2)}$ are the radii of the two contacting entities (disk/sphere).

The force-displacement law for the smooth-joint model updates the contact force (Fig. 3 - 1b) as given by (Itasca Consulting Group 2014):

$$\mathbf{F_c} = \mathbf{F}, \quad \mathbf{M_c} \equiv 0 \tag{8}$$

where $\mathbf{F}$ is the smooth-joint force. The force is resolved into normal and shear forces:

$$\mathbf{F} = -F_n \hat{\mathbf{n}}_\mathbf{j} + \mathbf{F_s} \tag{9}$$

The shear strength is also computed as: $F_s^{\mu} = -\mu F_n$ (10)

More information related to the computation of the normal and shear forces can be found in Itasca Consulting Group (2014).

3.2.2. Model Calibration

In DEM, the macro behaviour of the material is derived from the interaction of micro components where the input properties of these micro constituents are usually unknown. Therefore, these micro-properties have to be determined through a calibration process (Bahaaddini et al. 2015; Xu et al. 2018; Gao and Meguid 2018c; Zhang and Evans 2019). In the calibration process, the appropriate micro-properties are chosen in which the mechanical behaviour of the model is directly compared against the measured response of a physical material (Potyondy and Cundall 2004; Itasca Consulting Group 2014).

Calibration of Intact Rock Models

Laboratory experiments of Alejano et al. (2017) on intact rocks were first simulated to calibrate the material parameters of the parallel-bonded model and the contact of particles. This starts with the generation of a dense packing of non-uniform and well-connected grain assembly with a specified non-zero material pressure, and the installation of parallel bonds at grain-grain contacts. A polyaxial vessel consisting of frictionless walls with a mean width of 54.0 mm and a mean height of 96.7 mm is constructed to match the dimensions of laboratory sample. Subsequently, an assembly of grains with diameters satisfying a uniform size distribution ($R_{\max} / R_{\min}$ = 1.66) is generated, and then allow them to rearrange into a packed state under conditions of zero friction until static-equilibrium is obtained. The material friction coefficient is set to the particles, and a confinement pressure of 4MPa is applied to be consistent with the experimental conditions. The confinement is applied by moving the vessel walls under control of the servomechanism until the wall pressures are within the specified pressure tolerance of the material pressure and static-equilibrium is established. The parallel bonds then are implemented and final material properties are assigned to the grain-grain contacts.

However, these material properties cannot be measured directly from laboratory experiments; thus, extensive calibration process is unavoidable, which requires an iterative process to reproduce the mechanical properties of intact rocks at the laboratory scale of Alejano et al. (2017). Particle contact modulus (E_c), particle normal/shear stiffness ratio ($\overline{k}_n / \overline{k}_s$), parallel bond modulus ($\overline{E}_c$) and parallel bond normal/shear stiffness ratio ($\overline{k}_n / \overline{k}_s$) are first varied to match the Young's modulus and the Poisson's ratio of the intact rocks. Peak strength is then matched by varying the parallel bond normal and shear strength. The calibrated values of microscopic parameters are listed in Table 3 - 1. The stress–strain behavior of the DEM model compared with that obtained from laboratory test on intact rocks under confining pressure of 4 MPa is illustrated in Fig. 3 - 2a. It can be seen that the adopted parameters can reasonably simulate the mechanical behaviors of BM granite under confined compression. A comparison of macro-properties of the intact sample by the numerical test and physical test is presented in Table 3 - 2.

Table 3 - 1. Numerical parameters used in the discrete element analysis

Item	Micromechanical properties
Rock	
Ball-ball contact effective modulus	27.0 GPa
Ball stiffness ratio (k_n / k_s)	2.0
Ball friction coefficient	0.5
Parallel bond effective modulus	27.0 GPa
Parallel bond stiffness ratio ($\bar{k}_n / \bar{k}_s$)	2.0
Parallel bond tensile strength	148 MPa
Parallel bond cohesion	148 MPa
Joint set	
Smooth joint normal stiffness (k_n^{sj})	420 GPa
Smooth joint shear stiffness (k_s^{sj})	210 GPa
Smooth joint friction coefficient (μ^{sj})	0.839
Smooth joint tensile strength (σ_t^{sj})	0 MPa
Smooth joint cohesion (c^{sj})	0 MPa
Smooth joint dilation angle (ψ)	0º

Table 3 - 2. Comparison of target and achieved macro-mechanical parameters of intact and jointed rock samples

	Intact rock sample		Jointed rock sample	
	Experiment	DEM	Experiment	DEM
Deformation modulus (GPa)	28.67	31.74	11.74	14.08
Peak strength (MPa)	185.87	187.06	129.13	131.29

Calibration for Rock Mass Models

After the intact rock behavior simulated by DEM is validated, reliable rock mass models then need to be built that can reflect the mechanical behavior of jointed rock masses with that obtained from laboratory experiments. Therefore, two sets of joint planes, i.e., 1 sub-vertical and 2 sub-horizontal (1V + 2H) jointed samples, are introduced (see Table 3 - 3) to match the patterns observed in the laboratory experiments of Alejano et al. (2017).

Likewise, there is a need to identify the corresponding micro properties for the smooth joint contact model. The SJ model has six essential parameters: joint normal stiffness (k_n^{sj}), shear stiffness (k_s^{sj}), joint tensile strength (σ_t^{sj}), joint cohesion (c^{sj}), joint friction (μ^{sj}), and dilation angle (ψ). Considering that the joint surfaces used in the laboratory experiments are planar and smooth, σ_t^{sj}, c^{sj} and ψ values are all set to 0 in the numerical model.

The strength and deformation modulus of a jointed rock depend on joint stiffness and frictional resistance. In the calibration process, k_n^{sj} is first determined using the inverse calibration method. This means that the joint normal stiffness k_n^{sj} is adjusted until the target value of the deformation modulus E_m measured in the laboratory experiment is reached. It is noted that the deformation modulus is calculated from the slope of stress–strain curves at 50 % of the peak stress. The ratio of k_n^{sj} / k_s^{sj} is then set to 2 as suggested by Vergara et al. (2016). Finally, μ^{sj} is adjusted to achieve the desired peak strength, which is consistent with the friction angle reported in the literature for similar granite samples (Huang et al. 2019).

Table 3 - 3. Numerical Configurations of Rock Blocks

Intact	1V + 2H	2V + 3H	3V + 5H	6V + 9H
	S_1 = 35 cm	S_1 = 20 cm	S_1 = 15 cm	S_1 = 10 cm
		S_2 = 20 cm	S_2 = 15 cm	S_2 = 10 cm

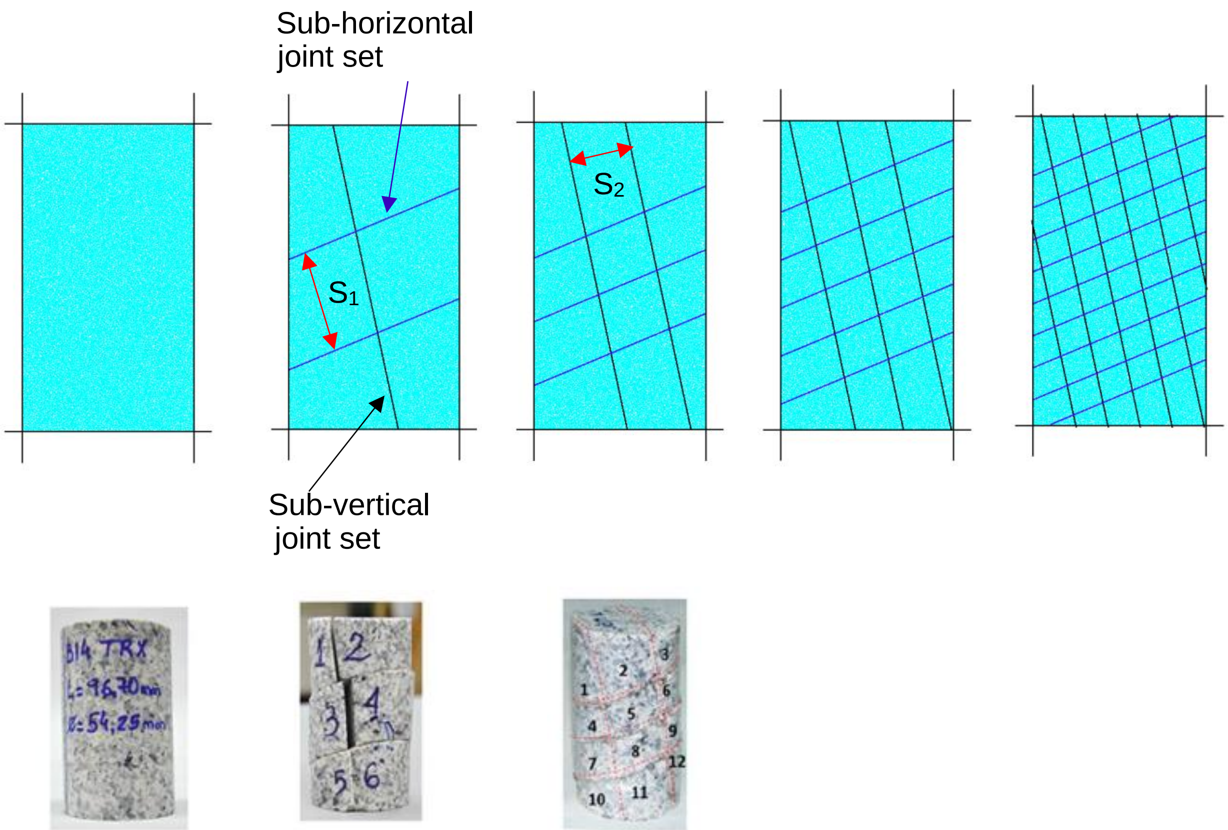

Note: Experimental figures are obtained from Alejano et al. 2017.

Figure 3 - 2b compares the numerical and experimental results showing that the macro response captured by the numerical model for the 1V + 2H jointed samples is in agreement with the experimental results. Quantitatively, the achieved macro-mechanical properties obtained numerically are reasonably close to the experimental results (see Table 3 - 2). Thus, the derived joint stiffness values and joint friction that reproduce deformation modulus and the strength of are the calibrated micro properties of the joints (listed in Table 3 - 1). However, compared to the calculated linear elastic deformations, the experimental stress–strain curves of the both intact and jointed samples at low stress levels (Fig. 3 - 2) show concave (hardening) and nonlinearity, which

mainly result from the closure of the pre-existing fissures or cracks in natural rock at the initial loading stage (Mas Ivars et al. 2011).

Since the main objective of this study is to investigate the influence of increased density of initial jointing on the macroscopic behaviour and the underlying micromechanical mechanism, it is not required to fully reproduce all the responses under different confining pressures. The performance of the numerical models subjected to confining pressure of 4 MPa is, therefore, evaluated and found to agree well with the experimental results.

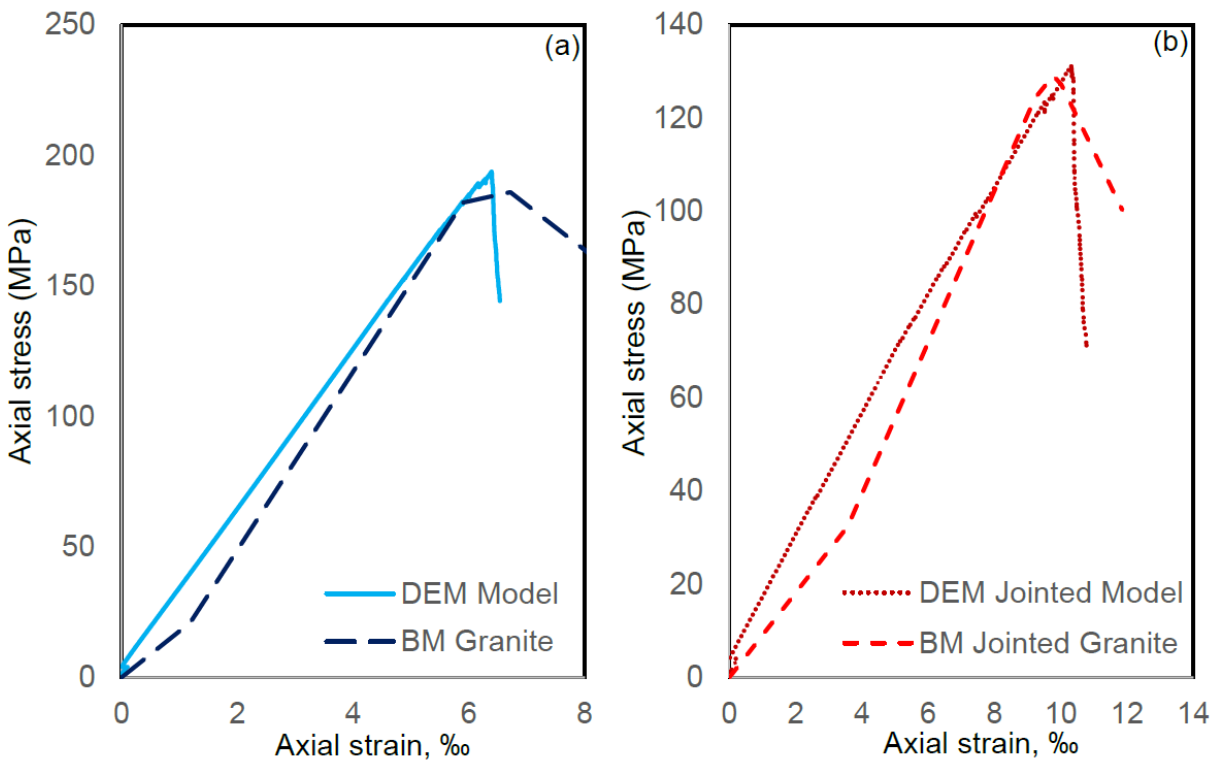

Figure 3 - 2. Stress–strain responses of (a) BS granite and DEM model; (b) BS jointed granite and DEM jointed model for validation micro-parameters.

Rock Mass Configuration for the Numerical Analysis

Once the discrete element models are validated, the mechanical behaviour of the jointed rock masses with various configurations of joint sets can be investigated. Besides, the aforementioned intact and 1V + 2H jointed samples, three models representing 2V + 3H, 3V + 5H and 6V + 9H jointed samples were developed. Additional data can then be generated to supplement laboratory tests, which compensates for the shortcomings of laboratory experiments. This numerical study has the merits of investigating the influence of the level of initial jointing on the macroscopic characteristics of the fracturing process of rock masses and the underlying mechanisms at the microscopic level. A detailed description of the jointed rock configuration is given in Table 3 - 3.

3.3. Numerical results and discussion

With the verified mechanical parameters, a discrete element numerical confined compression tests on both intact and jointed granite samples can be performed to investigate the deformability and failure mechanism thoroughly from micro–macro behaviour, including stress – strain relation, failure modes, kinematic activities, energy budgets, fabric evolutions, contact force distributions, and microstructure anisotropies.

3.3.1. Deformation and Failure Processes

Mechanical response

The stress–strain relationships as well as the number of micro-cracks generated for the intact and jointed rocks models in triaxial compression with 4.0 MPa confining pressures are presented in Fig. 3 - 3. The following observations can be made from this figure:

(1) Pre-existing discontinuities have significant effects on the stiffness, peak strength, and axial strain at peak. For example, significant decrease of stiffness and peak strength is found with the increase of initial joint frequency, and the corresponding information is presented in Table 3 - 4.

Table 3 - 4. Strength and deformability of intact and increasingly jointed samples

	Intact	1V+2H	2V+3H	3V+5H	6V +9H
Peak strength (MPa)	187.06	131.29	107.35	75.74	38.58
Deformation modulus (GPa)	31.74	14.08	10.91	7.69	5.32

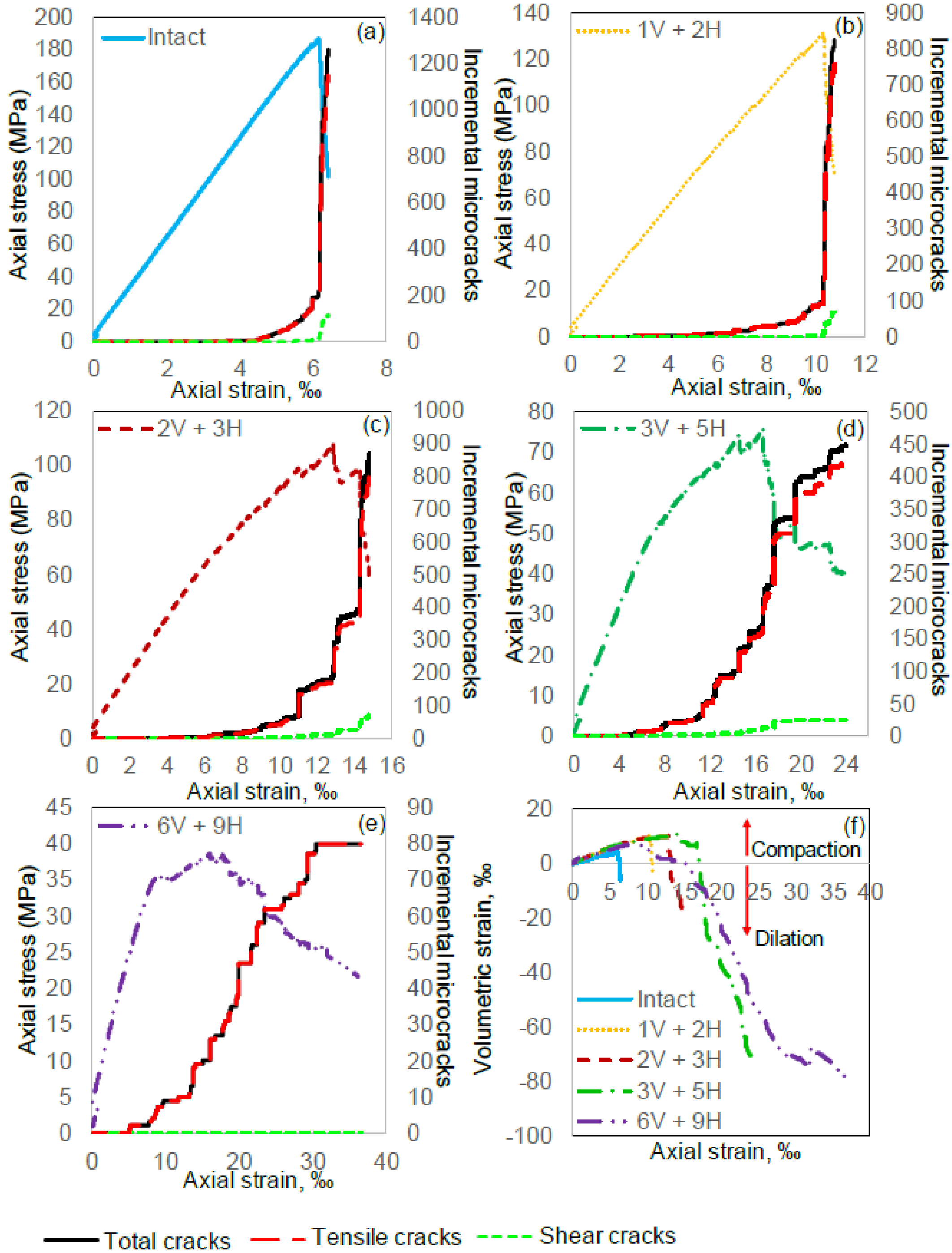

Figure 3 - 3. Stress–strain responses of (a) intact (b) 1V + 2H (c) 2V + 3H (d) 3V + 5H and (e) 6V + 9H rock samples; (f) Volumetric strain versus axial strain in numerical confined compression experiments.

(2) The onset of microcracking, also associated with material yielding, occurs at approximately 50–55% of the peak stress in agreement with the experimental observations of Alejano et al. (2017). In addition, with the increase in the joint density, strain hardening becomes more apparent as reflected by the deviation of the stress–strain curve with respect to its initial slope. This is because the increasing dominance of joint slip yielding mechanism in the increasingly jointed rock samples contributes to strain hardening, which is also in line with the conclusion made by Walton et al. (2018).

(3) The transition from brittle behaviour, at zero or low level of initial jointing, to more ductile behaviour, at high intensity of pre-existing discontinuity, can be clearly observed in the stress–strain responses of intact (Fig. 3 - 3a) and 6V + 9H samples (Fig. 3 - 3e), respectively. The increase in ductility with the increase in the degree of initial jointing is attributed to the highly jointed structure that largely suppresses the localization and coalescence of microcracks. This in turn inhibits the formation of a throughgoing macro-rupture plane associated with catastrophic failure. Consequently, the increase in initial joint frequency leads to reduced number of cracks with no apparent coalescence and more ductile response.

(4) With the increase in the degree of initial jointing, the evolution of cumulative micro-cracks transits from a surge with rapid increment of cracks into a step-wise manner characterized by an accumulation of cracks at a relatively slower rate. This is mainly due to the fact that the addition of further joints to the sample interrupts the localization and coalescence of freshly formed cracks, with a higher tendency for the rock mass to disaggregate along the joint planes.

(5) The number of shear cracks decreases significantly with increased density of initial joints, especially for the 6V + 9H samples, where no shear crack is generated during the entire deformation and failure process. This can be attributed to the fact that the cohesive rock unit is split into jointed blocks along the fully persistent joint sets. Microcracks are generated during the sliding of the jointed blocks at the emergent asperities along the pre-existing joints. Thus, the growth of fractures in the 6V + 9H rock samples occurs through the plucking of particles along the pre-existing joints as a result of the sliding of the jointed blocks, which is predominantly generated in tensile mode.

3.3.2. Failure mode and orientations of microscopic cracks

Each jointed block consists of intact portions of the model material interspaced with joints (Kulatilake et al. 2001). The effects of persistent rock discontinuities on the failure pattern of rock masses were reported in Kulatilake et al. (1997 & 2001), Singh et al. (2002), Wang and Huang (2009); Xu et al. (2013); Shang et al. (2018b). Three primary modes of rock mass failure are reported, namely failure through intact material, sliding on the joint plane, and mixed failure of the above two modes. Moreover, it is worth noting that microcracking has two modes, i.e., tensile and shear microcracks. A tensile microcrack forms when interparticle normal stress exceeds the tensile strength of the bond. Similarly, a shear microcrack results when local shear stress exceeds the shear strength of the bond in compression. To better investigate the influence of pre-existing discontinuities on the failure mechanisms of rock masses, detailed observations of various failure modes based on the damage behaviour, orientations of microscopic cracks and fragmentation characteristics are analyzed and discussed below.

Intact rock failure: the main mechanism of failure is the development of the macroshear plane within the intact rock samples, and the formation of axial splitting zone or tensile failure within the intact rock blocks for the jointed 1V + 2H rock sample (Fig. 3- 4a). The models exhibit high compressive strengths and brittle behaviour (Kulatilake et al. 1997). No macroscopic movements parallel or normal to the planes of the pre-existing discontinuities is observed. Failure occurs through the intact material exhibited by the sequence of elastic deformation, crack initiation, propagation, and crack coalescence. Consequently, large amount of fractures can nucleate and grow to completion, thus resulting in the disintegration of solids (i.e., the intact rock or jointed rock blocks) into smaller pieces. These pieces (i.e., fragments) are identified as sets of particles connected by the surviving bonded contacts as a consequence of the fragmentation process. Both tensile and shear cracks tend to nucleate in specific areas in the samples and form organized patterns, which are correlated to areas of high fragmentation concentration. The formation of well-organized cross-like shear band results from the coalescence of both tensile and shear cracks which clearly defines the contour of the sheared zone as shown in Fig. 3 - 4a & Fig. 3 - 6.

For intact rock, it can be observed that the orientation of microscopic tensile cracks is predominantly parallel to the direction of the maximum principal stress (Dinç and Scholtès, 2018). This is attributed to the dilation of the sample in the direction perpendicular to the loading

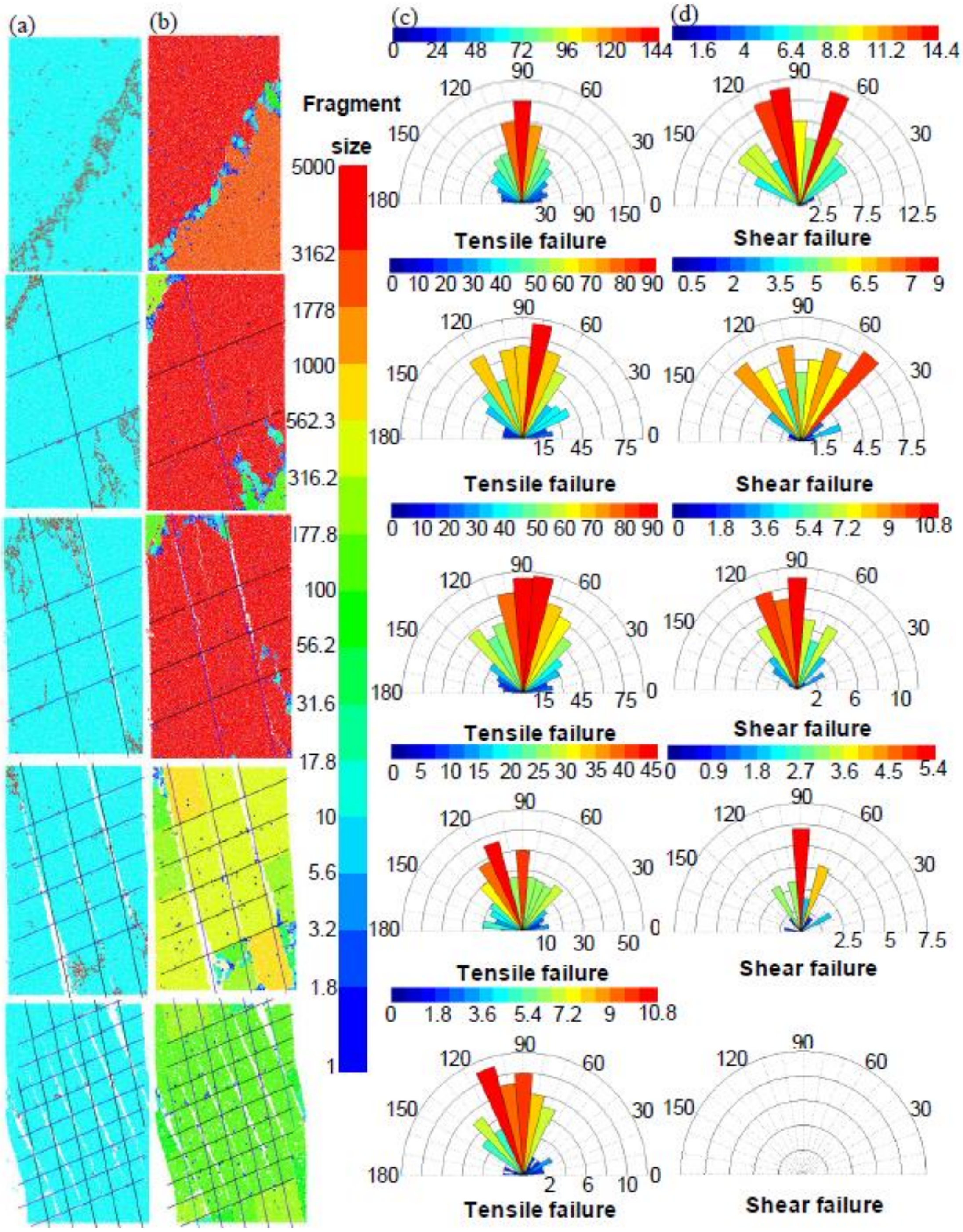

Figure 3 - 4. (a) Micro-crack distribution within the rock mass samples; (b) Fragment size distributions presented by the logarithmic hue scale; (c) Polar histogram for tensile failure; (d) Polar histogram for shear failure at the final damage stage.

(Poisson's effect). For the jointed 1V + 2H samples, the orientation of shear microcracks exhibits more isotropic. On the other hand, the concentration of tensile microcracks is found to deviate towards the direction of the sub-vertical joints with a mean dip of 77.9º.

Sliding along joint plane: for jointed 6V + 9H rock samples, the main mechanism of failure is sliding along the pre-existing discontinuities and thus the behavior of joints plays a dominant role on the global deformation, which are characterized by a dramatic decrease in the number of micro tensile cracks and the absence of micro shear cracks. This failure mode is associated with large deformations and subsequent dilations of the sample in the minor principal stress direction (see Fig. 3 - 4a). These samples exhibit significant ductile behaviour characterized by a relatively low peak strength at greater axial strain, and slower drop in post-peak strength. Only a small number of fragments are squeezed out due to the movement of the rock block (see Fig. 3 - 4b).

Mixed failure: the predominant failure mechanism for 2V + 3H and 3V + 5H rock samples is partly through intact rock failure and partly through pre-existing discontinuities. The orientation distribution of shear cracks transforms from distributed to predominantly vertical. The failure mode observed involves failure through the intact rock, which is also controlled by the interaction with pre-existing joints and the interlocking of the model blocks, inducing a gradual spreading of internal damage and relative movement of blocks along pre-existing joints. Thus, the rock mass can either disaggregate along the pre-existing discontinuities, or break along freshly formed faces resulting in fragments being generated at block corners. This phenomenon is consistent with the experimental observations in Alejano et al. (2017), and the numerical modelling of the failure mode of jointed rock blocks reported by Huang et al. (2019) and Zhou et al. (2019).

3.3.3. Particle-level kinematics and contact force information

The influence of rock discontinuities on the mechanism of rock failure can be captured through the distributions of particle-level kinematics, such as the translational and rotational granular temperatures, local strain, and void ratio, which are excellent indicators of damage evolution.

Granular temperature is proportional to the average value of the square of the grains' velocity fluctuations, with respect to their mean velocity. It can be used to quantify particle-level kinematical activities (Ma et al. 2018a&b):

$$v_x^i{}' = v_x^i - \overline{v_x^i} \qquad (11)$$

$$v_y^i\,' = v_y^i - \overline{v_y^i} \qquad (12)$$

$$\omega^i\,' = \omega^i - \overline{\omega^i} \qquad (13)$$

where translational velocity components v_x^i , v_y^i and angular velocity component ω^i of the selected i -th particle in the selected spherical region Ω_i can be divided into the mean velocity components $\overline{v_x^i}$, $\overline{v_y^i}$, and $\overline{\omega^i}$ and fluctuating parts $v_x^i\,'$, $v_y^i\,'$, and $\omega^i\,'$.

The mean velocity components, $\overline{v_x^i}$, $\overline{v_y^i}$, and $\overline{\omega^i}$ can be attained by averaging the velocities of particles surrounding the selected i -th particle in the chosen spherical region Ω_i (Ma et al. 2008a&b):

$$\overline{v_x^i} = \frac{1}{n}\sum_{j=1}^{n} v_x^j \qquad (14)$$

$$\overline{v_y^i} = \frac{1}{n}\sum_{j=1}^{n} v_y^j \qquad (15)$$

$$\overline{\omega^i} = \frac{1}{n}\sum_{j=1}^{n} \omega^j \qquad (16)$$

$$(x_j - x_i)^2 + (y_j - y_i)^2 \le r^2 \qquad (17)$$

where r is the radius of the spherical region Ω_i . In this study, the neighborhood size is set to $4d_{\max}$ (see Fig. 3 - 5a).

Hence, the translational T_V^i and rotational T_R^i granular temperatures representing the intensity of particle exchange (analogous to a thermodynamic temperature) are calculated from the velocity fluctuations as expressed below (Ma et al. 2008 a&b):

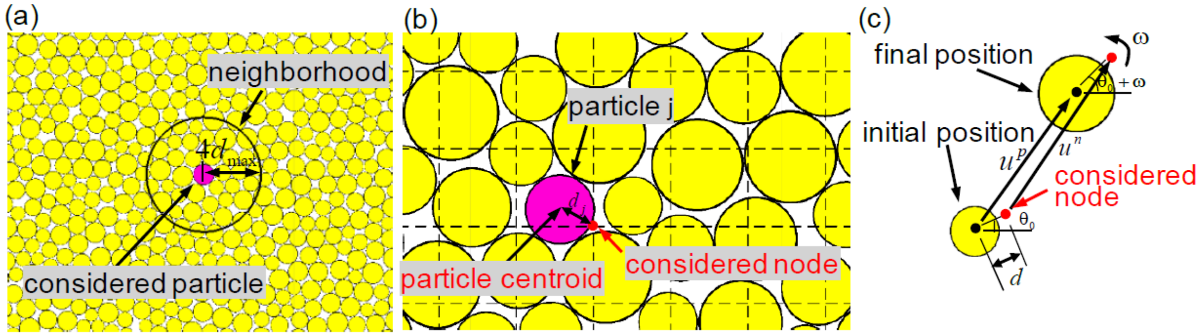

Figure 3 - 5. Schematic illustrations of (a) definition of the neighborhood of a particle; (b) association of grid node to particle, and (c) displacement of grid node and its associated particle.

$$T_V^i = \frac{1}{2}[(v_x^i\,')^2 + (v_y^i\,')^2] \tag{18}$$

$$T_R^i = \frac{I}{2m}(\omega^i\,')^2 \tag{19}$$

where I and m are moment of inertia tensor and mass of the particle.

Following Wang et al. (2007), and Ma et al. (2018a), a mesh-free strain calculation method is adopted in this study. The mesh-free method used in this study employs a grid type discretization over the reference configuration. A grid spacing of the median particle diameter (d_{50}) is suggested to capture the shear localisation at a satisfactory resolution. A rectangular grid is superimposed over the volume of particles prior to any deformation and serves as the continuum reference space (see Fig. 3 - 5b). Each grid point in the reference space is, then, assigned to an individual particle j such that (Wang et al. 2007):

$$\frac{d_j}{r_j} \le \frac{d_i}{r_i} \quad (i = 1,\ 2,\ \ldots,\ N_P;\ i \ne j) \tag{20}$$

where r_i is the radius of particle i , d_i is the distance between the centroid of particle i and the considered grid node, and N_P is the number of particles. If the distance ratio between particle centroid and its associated grid node to the particle radius is the smallest among all particles, then the association from this particle to the considered node is constructed (Wang et al. 2007).

The displacement of the grid point is calculated by (Wang et al. 2007):

$$u_x^g = u_x^p + d\left[\cos(\theta_0 + \omega) - \cos\theta_0\right] \tag{21}$$

$$u_y^g = u_y^p + d\left[\sin(\theta_0 + \omega) - \sin\theta_0\right] \tag{22}$$

where u_x^g, u_y^g and u_x^p, u_y^p are the x and y are displacement components of the grid point and particle centroid respectively; d is the distance between the grid point and the particle centroid; θ_0 is the initial phase angle of the grid point location relative to the particle centroid; and ω is the accumulated rotation of the particle (Fig. 3 - 5c).

On account of the particle rotation, this method is able to capture accurately the actual strains that the granular media is experiencing. Therefore, the Green – St Venant strain tensor E_{ij} can be obtained at any stage of the simulation (Wang et al. 2007):

$$E_{ij} = \frac{1}{2}(u_{i,j} + u_{j,i} + u_{k,i}u_{k,j}) \tag{23}$$

where $u_{i,j}$ is the displacement gradient tensor over the grid, which is based on the deformation measure related to the reference configuration.

It is found, in Fig. 3 - 6, that a strong degree of spatial association exists among the localization patterns of the kinematic quantities, shear strain, void ratio, contact force chains at the final damage stage (50% post-peak stress state), indicating their consistency in depicting the failure mechanism of the intact/pre-jointed rock models. Distinct localization bands can be observed in intact rock, where the localized shear strains and high void ratios in the granular assemblage are accompanied with high granular temperatures and strong force chain confined within a thin zone along the rupture surface, as shown in Fig. 3 - 6. Within this zone of primary shear fracture, the high granular temperature distributions (that indicate rapid particle exchange and higher rates of particle collisions) are mainly caused by the significant amount of bond breakage. The nucleation and coalescence of fractures result in a loss of interparticle bonds and a reduction in rock strength, imparting permanent changes in solid structure. Therefore, a growing number of particles are more susceptible to movement and change positions more intensely with nearest neighbors.

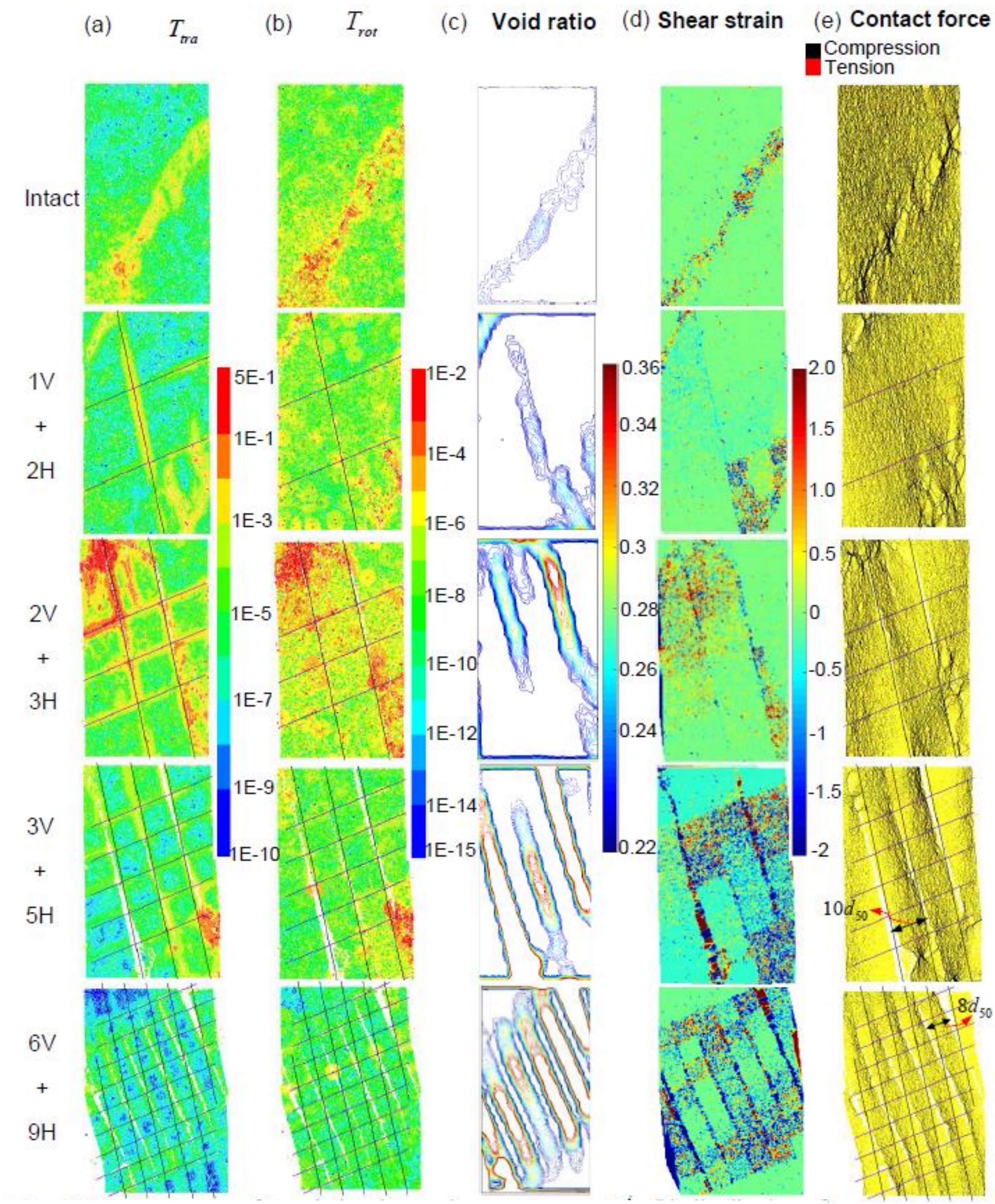

Figure 3 - 6. (a) distribution of translational granular temperature, T_V^i; (b) distribution of rotational granular temperature, T_R^i; (c) contour of void ratio; (d) contour of localized shear strains; (e) contact force chain at the final damage stage.

In contrast to intact rock samples, no visible bands of particles with high temperature are found in the 6V + 9H samples, which indicates that the localized shear bands are not formed in the bonded granular assembly (see Fig. 3 - 6). This is generally interpreted as a dominance of frictional sliding along the joint planes with a low percentage of interparticle bond breakages instead of localization of large amounts of fractures. Comparing to the intact rock failure mode, the difference is that the particles of the 6V + 9H samples remain largely bonded and move as rigid blocks while experiencing significant frictional movement. A few microcracks involved in the failure mode of sliding along pre-existing joints result from the breakage of particle conglomerates (or "coarse fragments") resisted by the frictional sliding process.

It is worth noting lack of distinct shear band is found in jointed samples. Instead, irregular, local zones of strain localization are observed in 1V + 2H, 2V + 3H, and 3V + 5H samples where intense fracturing activities are evidenced by the heterogeneous distribution of granular temperatures and localized distribution of contact force chains and void ratios. This phenomenon is expected as the breakage of bonds contribute to the nucleation and growth of fractures leading to the interparticle locking being reduced, thus fractured blocks are capable of moving and rotating freely manifesting the enhanced granular temperatures.

Compared to that of 1V + 2H samples, more intense granular agitations with frequent collisions depicted by the translational and rotational granular temperatures are observed for 2V + 3H and 3V + 5H rock samples where the mixed failure mode dominates the deformation and damage process. It suggests that additional degrees of freedom for interparticle motion is created not only by fracturing of the intact rock material but also the interaction with pre-existing discontinuities.

3.3.4. Spatial correlation and contact force heterogeneity

A more quantitative characterization of the influence of the initial joint density level on force chain structure can be obtained by computing the 2D spatial correlation function $G(r)$ of the magnitude of the normal contact forces acting on the particles. The $G(r)$ is defined in the same manner as in Løvoll et al. (1999):

$$G(r)=\frac{\sum_{i=1}^{N}\sum_{j>i}\delta(|r_{ij}-r|)\,f_i\,f_j}{\sum_{i=1}^{N}\sum_{j>i}\delta(|r_{ij}-r|)} \tag{24}$$

where N is the total number of contact points, f_i is the normalized normal contact force acting at contact i, r_{ij} is the distance between contacts i and j, and $\delta(0)=1$. A force pair is two normal forces f_i and f_j separated by r_{ij} which together contribute to the spatial correlation function. A nonzero value of $G(r)$ infers that, on average, two contacts separated by a distance r have forces that are correlated (Lois et al. 2007; Ma et al. 2018b)

The correlation demonstrates that two particles at distance r are connected through a cluster of simultaneously contacting particles, and the force from one particle is being transmitted through the network to the other particle (Lois et al. 2007). It thereby establishes a quantitative measurement of the average effect of force chains of length r in the assembly. Figure 3 - 7 illustrates the correlations of normal contact force for increasingly jointed rock samples at the final damage stage. Note that the radial distance has been normalized with respect to the mean particle diameter d_{50}.

For this 2D discrete element analysis, the minimum separation distance $r_{\min}\approx d_{50}/2$, which is consistent with the numerical observation of Silbert et al. (2002). Obviously, all samples have the strongest peak near $r\approx d_{50}$, and other prominent peaks are found at separation distances of $r\approx 2d_{50}, 3d_{50}$ and $4\,d_{50}$. These peaks are all located around integral multiples of the average grain size d_{50}. This corresponds to situations where contact forces are transmitted through the "force chain networks" that propagate from one grain to the next across grain-grain contacts.

Clearly, with the increase in initial joint frequency, the $G(r)$ has higher peaks before r reaches $5d_{50}$, representative of the higher interparticle locking. In addition, the local correlations between the positions of the contact points are stronger in highly jointed samples at the final damage stage indicating a more tightly connected distribution of contact points in the system as a result of the fewer amounts of microcracking being generated.

The amplitude of oscillation is found to decrease with the increase in radial distance. After extending to a distance greater than five times the mean particle diameters ($5d_{50}$), slight oscillations around unity are observed for intact, 1V + 2H, and 2V + 3H rock samples. However, for jointed 3V + 5H and 6V + 9H rock samples there is an obvious decline in $G(r)$, and this trend continues until r reaches $8d_{50}$ and $10d_{50}$, respectively, for these two samples. This is attributed to the slippage along the joint planes, creating space for each fracture opening with a separate distance being equivalent to $8d_{50}$ and $10d_{50}$, as shown in Fig. 3 - 6e.

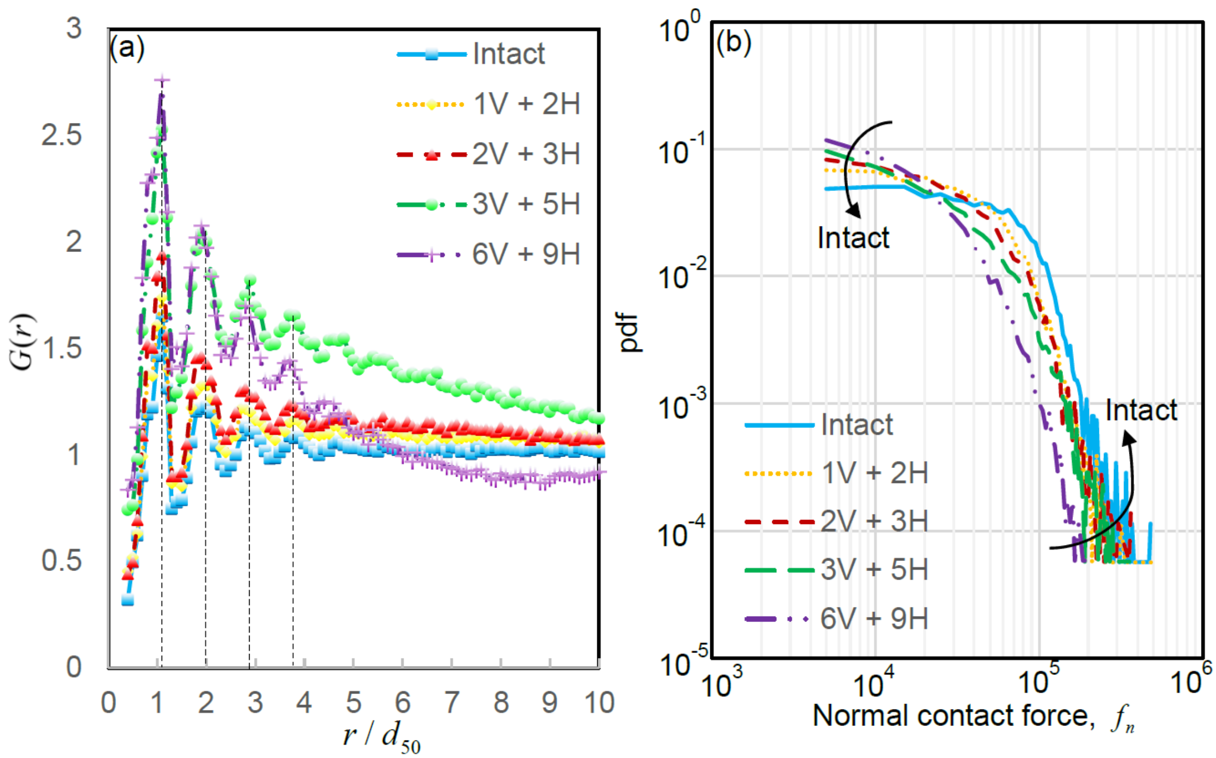

Figure 3 - 7. (a) Spatial force correlation function $G(r)$ for normal contact force plotted as a function of distance r normalized by mean particle diameter d_{50} for intact and jointed samples; (b) Probability distributions of normal contact forces f_n in log-log scales for intact and jointed samples.

The above demonstrates a continuous decreasing correlation pattern until fracture opening occurs, which constraints the transmission of contact forces through "force chain networks" formed by the topology of the contact network (Lois et al. 2007). It is noted that the $G(r)$ in 6V + 9H jointed samples finally decreases to a value smaller than that of the intact, 1V + 2H, and 2V + 3H rock samples, which differs from 3V + 5H rock sample that it is still larger than the other three cases. It mirrors the visual prominence of the force chain network in jointed 6V + 9H samples that has much larger fracture openings shown in Fig. 3 - 6e. In all cases, the results of this study demonstrate that contact forces are spatially correlated, but are much more affected by the level of initial jointing.

The influence of the level of initial jointing on the contact network can also be illustrated using the probability distribution function (PDF) of contact forces. Clearly, the results shown in Fig. 3 - 7b for the PDF of the normal contact forces at post-peak stress state demonstrate that the degree of initial jointing largely affects the contact force distribution. Note that the probability distribution of the tangential contact forces demonstrates a similar trend during compression, so there is no need to repeat it herein. Clearly, the PDF distribution for normal contact forces becomes narrower, and the corresponding inhomogeneity of the stress transmission becomes larger with increasingly jointed rock structure. This decreasing force homogeneity in the sense that with the increase in initial jointing, the granular media involves less strong force chains in number (see Fig. 3 - 6e) as well as the decrease in the magnitude of normal force.

The above can be further corroborated by examining the *Gini* coefficient for the normal force magnitudes. The *Gini* coefficient, often used to represent a nation's income inequality, describes the homogeneity of some quantity in a population. A *Gini* coefficient of 1 indicates complete inequality whereas a value of 0 indicates perfect equality and homogeneity. The definition is the same as that in Hurley et al. (2016), and calculated as follows:

$$G = \frac{1}{N_c}\left(N_c + 1 - 2\left(\frac{\sum_{i=1}^{N_c}(N_c + 1 - i) f_i^n}{\sum_{i=1}^{N_c} f_i^n}\right)\right) \tag{25}$$

The term N_c is denoted as the number of contacts. The increase in *Gini* coefficient indicates more evident inhomogeneity among the whole contact system. The normal contact force f_i^n is sorted in a non-decreasing order ($f_i^n \leq f_{i+1}^n$).

Table 3 - 5 indicates that the force heterogeneity intensifies as the initial joint frequency increases, which accords well with the observations from the PDF of the normal contact force.

Table 3 - 5. *Gini* coefficient

	Intact	1V+2H	2V+3H	3V+5H	6V +9H
Gini coefficient	0.5955	0.6549	0.7098	0.8032	0.8377

These two descriptions provide complementary points of view of the microstructure and demonstrate that the increasing heterogeneity of contact force distribution with the increase in the degree of initial joint frequency can be attributed to the increasing number of debonded particles along the joint plane.

3.3.5. Energy budget during deformation

Analyses of the energy budgets are of critical importance to establishing the linkage between micro- and macro-mechanical responses for a comprehensive understanding of the deformation process and failure mechanism of intact and pre-jointed rock. Relevant energy terms include boundary work dE_W, body work dE_b done by gravity force, elastic strain energy dE_s stored at particle contacts, bond energy dE_{pb} stored in parallel bonds, kinetic energy dE_k, frictional dissipation dE_f, damping dissipation dE_d, and the fracture energy E_{frac}, are calculated as the cumulative energy released by all bond breakage in the tensile and shear fracture modes. In this study, the body work dE_b is equal to zero as the gravity acceleration was set to zero.

The energy input due to the walls is represented by (Itasca Consulting Group 2014)

$$E_W^j = E_W^{j-1} + \sum_{i=1}^{N} F_W \Delta U_W \tag{26}$$

where E_W^{j} and E_W^{j-1} are the total accumulated work done by all walls on the assembly at the current and previous time steps; F_W is the resultant force acting on the wall; ΔU_W is the applied displacement occurring during the current time step.

According to the first law of thermodynamics, the energy components satisfy

$$dE_W = dE_s + dE_{pb} + dE_k + dE_f + dE_d + dE_{frac} \qquad (27)$$

where the last three terms define the plastic energy dissipation dE_p .

For 6V + 9H rock samples (see Fig. 3 - 8e), friction dissipation prevails over the strain energy build-up from the very beginning due to lower average coordination number; this situation further demonstrates sliding through the joint plane plays a dominant role in the rock deformation process. In contrast, for intact rocks (Fig. 3 - 8a), strain energies are predominantly accumulated due to the elastic compressions at the particle contacts before the occurrence of microcracking marking the onset of inelastic dissipation. The transition in energy evolution is expected as the solid microstructure being more disintegrated with lower contact intensity due to the increased jointing. The energy absorbed by the rock samples stored not only as elastic strain energy but accompanied by plastic energy dissipation due to a large amount of frictional movements occurring along the pre-existing discontinuities.

The major effect of microcracking activity, which itself only dissipates a small amount of the external work, is to promote the changes in solid microstructure by creating additional degrees of freedom for frictional sliding both through pre-existing discontinuities and frictional interparticle movements. The threshold of strain energy for initiating the bond breakage decreases with the increase in initial joint frequency, as evidenced by the downward shifts of the trend in Fig. 3 - 8. For intact (Fig. 3 - 8a) and 1V + 2H samples (Fig. 3 - 8b), stress drop occurs rapidly after the peak strength, and the stored energy is released quickly. Elastic and plastic energy do not dissipate gradually in this case. Elastic strain energy significantly reduced, while dissipated strain energy instantly increased to reach the total strain energy value.

The relative contribution of elastic energies to the energy budget declines with the increase in initial joint frequency, accounting for 41.9 % of the input energy for intact samples, 20.9 % for 1V + 2H samples, 14.8 % for 2V + 3H samples, 11.1 % for 3V + 5H samples, and 9.1% of the input

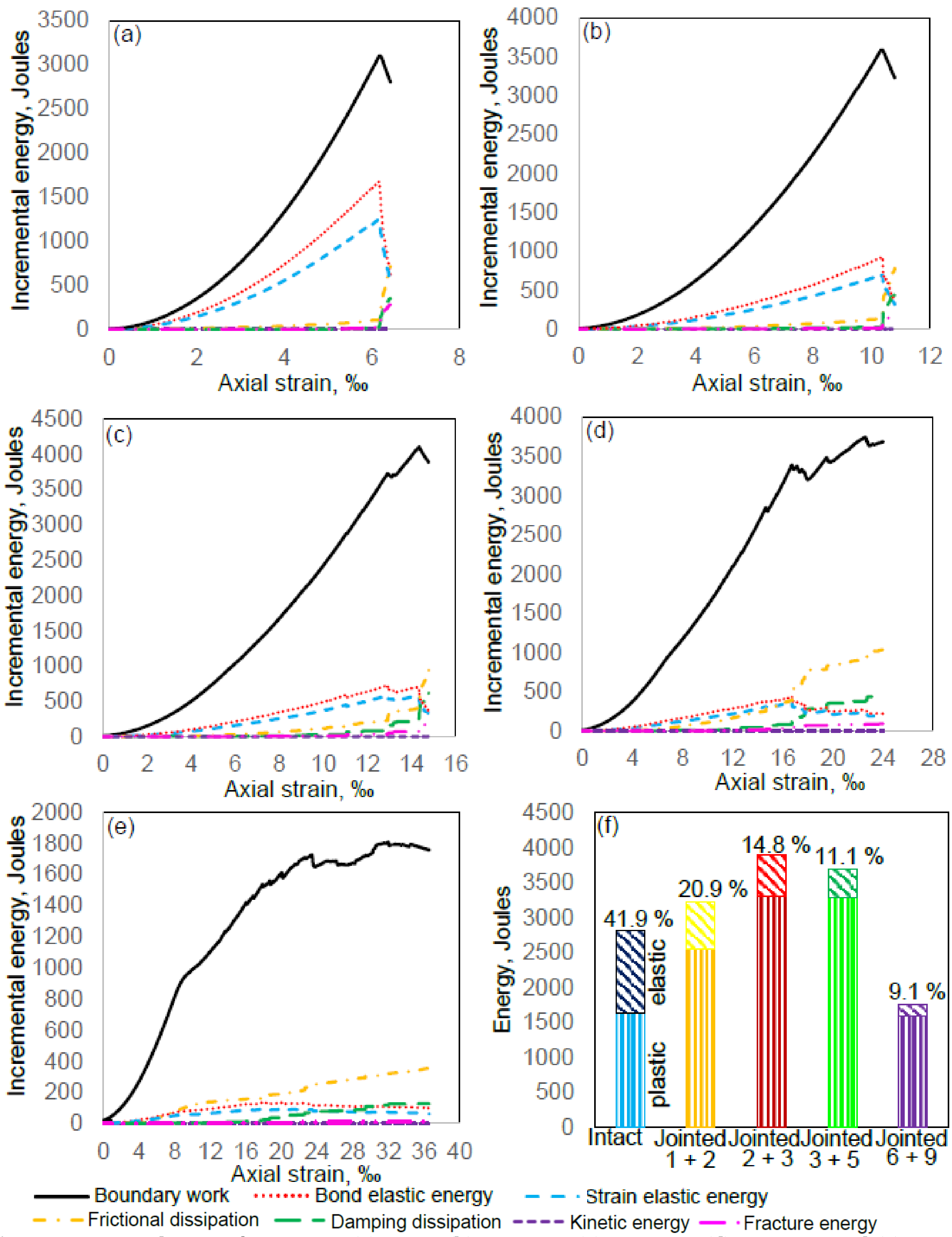

Figure 3 - 8. Evolution of energy in (a) intact (b) 1V + 2H (c) 2V + 3H (d) 3V + 5H and (e) 6V + 9H rock samples; (f) Energy partitioning into elastic energy and plastic energy during numerical confined compression experiment.

energy for 6V + 9H samples as illustrated in Fig. 3 - 8f. Simultaneously, fracture energy decreases from 279.9 J for the intact sample, 194.2 J at 1V + 2H samples, 190.3 J at 2V + 3H samples, 89.0 J at 3V + 5H samples to 10.9 J at 6V + 9H samples. The tensile and shear components of fracture energies in each case are summarized in Table 6. In addition, it is worth noting that although only 9.1%, 8.4 %, 8.3% and 5.3% of the total microcracks for intact, 1V + 2H, 2V + 3H, and 3V + 5H rock samples, respectively, occur in shear mode, they contribute to 23.3%, 20.8%, 22.1% and 17% of the fracture energy released for the corresponding rock samples.

It can be observed that fracture energy accounts for a small percentage of the input energy, similar to the energy budget estimations reported by Vora and Morgan (2019) for Berea Sandstone and Lac du Bonnet Granite. The decrease in fracture energy with the degree of initial joint frequency is due to the decrease in the number of microcracking activities. Thus, fracture energy is strongly influenced by the modes of microcracks, which is in turn controlled by the rock strength and level of joint intensity.

3.4. Micro-mechanism and Macro-response

3.4.1. Evolution of fabric and coordination number

The microstructure, or fabric, of a granular material can be interpreted by the orientation of the contact normal characterizing microscopic features. Satake (1978) quantified the fabric using a second order tensor. In tensorial notation, the second-order fabric tensor (Φ_{ij}) is given as:

$$\Phi_{ij} = \frac{1}{N_c} \sum_{N_c} n_i n_j \qquad (28)$$

where N_c is the total number of contacts, n is the unit normal vector of contact with $i,\ j = 1,\ 2$ for two dimensional (2D) analyses.

The contact normal is defined as vectors that are perpendicular to the plane defining the contact between two particles. The summation and averaging are taken over all N_c contacts in the contact network.

For 2D analyses, Eq. (28) gives a two-dimensional matrix:

$$\begin{pmatrix} \Phi_{xx} & \Phi_{xy} \\ \Phi_{yx} & \Phi_{yy} \end{pmatrix} = \frac{1}{N_c} \begin{pmatrix} \sum_{N_c} n_x n_x & \sum_{N_c} n_x n_y \\ \sum_{N_c} n_y n_x & \sum_{N_c} n_y n_y \end{pmatrix} \tag{29}$$

The eigenvalues of the fabric tensor give the principal fabrics Φ_1 and Φ_2, which can be used to describe the intensity of the anisotropy. The degree of anisotropy can be characterized by the deviatoric fabric expressed by (Shi and Guo 2018):

$$\Phi_1 - \Phi_2 = 2\sqrt{\left(\frac{\Phi_{xx} - \Phi_{yy}}{2}\right)^2 + \Phi_{xy}^2} \tag{30}$$

Four groups of contact normal are analyzed in this study: (i) considering all engaged contacts, (ii) contacts only transmitting compressive force, (iii) contacts only transmitting tensile contacts, (iv) bonded contacts. The corresponding evolutions of the deviatoric fabric of contact normal as a function of the axial strain are illustrated in Fig. 3 - 9.

Different patterns of evolutions can be noted for the fabric deviator of all contacts due to the presence of rock discontinuities (see Fig. 3 - 9a). For intact rock, deviatoric fabric rapidly increases to a peak value within a small axial strain whereas deviatoric fabric for 1V + 2H and 2V + 3H samples exhibit a similar upward trend but with significantly smaller peaks. In contrast, deviatoric fabrics for 3V + 5H and 6V + 9H samples act distinctly different where they fluctuate to peak and then evolve to be almost flat. This can be attributed to the fact that the frictional sliding of fractured blocks along the pre-existing discontinuities play an increasingly dominant role during the failure process.

Fig. 3 - 9b shows the evolution of deviatoric fabric for the contacts only transmitting compressive forces with axial strain in compression tests. It is evident that the increasing rate of deviatoric fabric, for the group where contacts only transmit compressive forces, starts to slow down as the initial joint intensity increases. In fact, the highly jointed rock structure effectively damps the contact intensity and microstructure evolution. After the peak, Fig. 3 - 9b also shows a sudden

decrease of the deviatoric fabric in intact, 1V + 2H, and 2V + 3H samples corresponding to degradation or collapse of the compressive contact network. Similar to all engaged contacts,

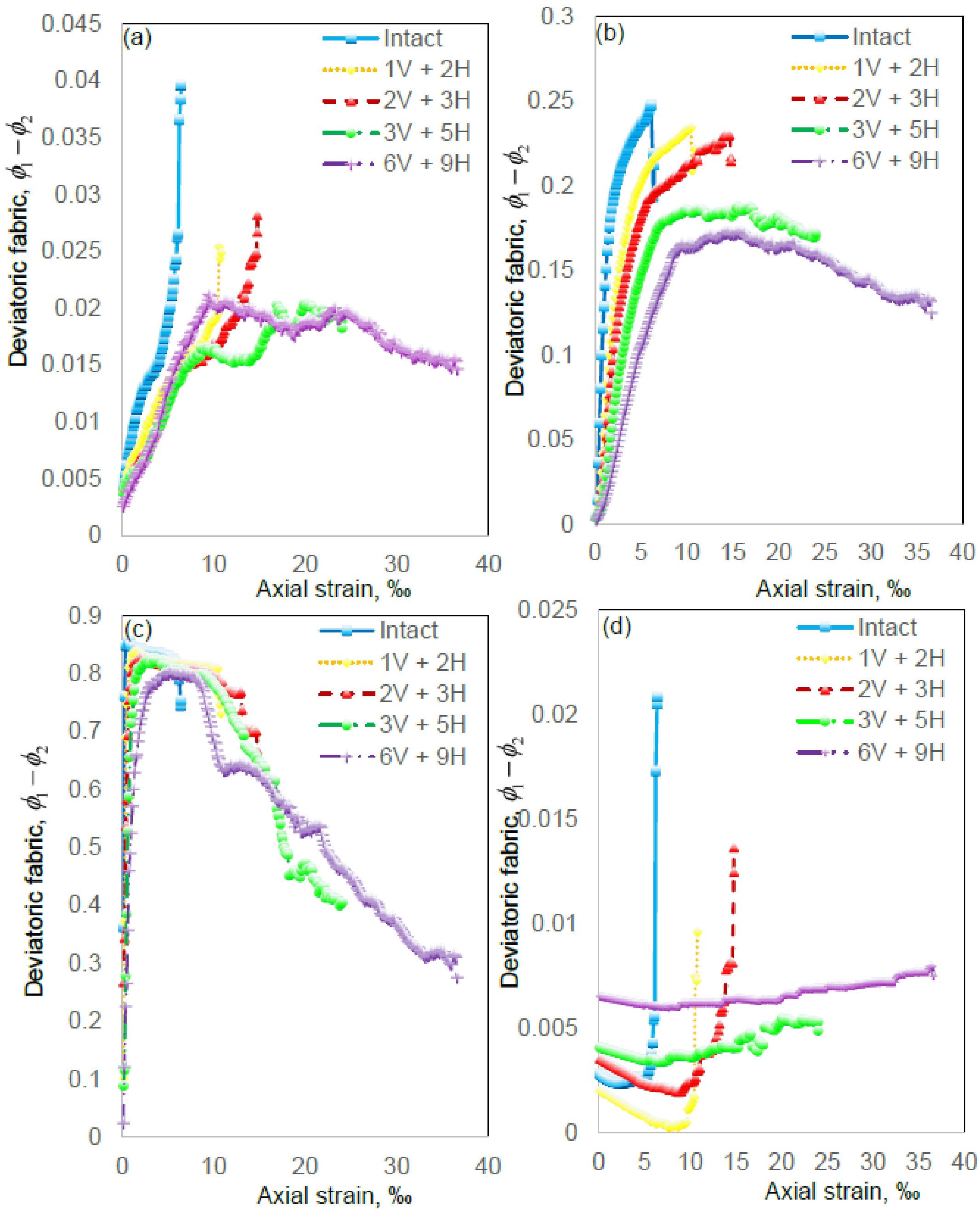

Figure 3 - 9. The deviatoric fabric in the intact and jointed rock samples: (a) considering all engaged contacts; (b) considering only contacts transmitting compressive forces; (c) considering only contacts transmitting tensile forces; (d) considering bonded contacts.

deviator fabrics of compressive contacts approach their peak values and then gradually decrease with the increase of axial strain to ultimate values in 3V + 5H and 6V + 9H samples.

The deviatoric fabric for contacts that transmits only tensile forces is initially highly anisotropic, and this anisotropy reduces during compressive loading (see Fig. 3 - 9c). It is worth noting that the deviatoric fabric of tensile contacts is generally much larger than that of the compressive contacts in all five cases, which is in agreement with previous numerical observations on high-porosity sandstones by Wu et al. (2018). The "tensile contacts" major principal fabrics is horizontal as a result of the Poisson effect (Cheung et al. 2013), leading to the breakage of more bonds in the horizontal direction and a reduction of the "tensile contacts" anisotropy. This, however, corresponds to an increase in "bonded contacts" anisotropy.

For bonded contacts, the deviatoric fabric experiences a short period of initial decrease as the model is being compacted (see Fig. 3 - 9d). The deviatoric fabric then begins to increase at a slow rate to a maximum value which is dependent on the initial joint frequency. Generally, when the amount of fracturing is large, a significant amount of particle rearrangement takes place resulting in large deviator fabric values.

In particular, the deviator fabric for bonded contacts in the intact rock sample increases rapidly to the largest value among all investigated joint configurations, due to the occurrence of the most intense microcracking activities associated with catastrophic failure of the internal structure. It correlates reasonably well with that of the brittle behaviour. Nevertheless, only a slight increase in deviatoric fabric for bonded contacts is observed for 6V + 9H sample. This is attributed to the fact that with the increased density of initial joints, the number of fractures significantly reduced. As a result, cohesion and interparticle restriction are largely maintained, which supresses particle motion during the compressive loading. Hence, particle orientation is less likely to be random, leading to a lower anisotropy in highly jointed samples.

The coordination number is calculated using the number of particles (N_p) and their contacts (N_c), as expressed below:

$$C_n = 2\frac{N_c}{N_p} \tag{31}$$

The evolution of the coordination number as a function of axial strain (ε_a) under different initial jointing conditions is presented in Fig. 3 - 10. It reveals that for the "all contacts" coordination number there is an upward trend before reaching the peak state, as a result of the increasing of overlapping between particles under elastic compression, and followed by a descending trend owing to the degradation of contacts and bonds. Moreover, figure 3 - 10a shows that for the case of "all contacts", coordination number increases at a slower rate to a maximum value as the degree of initial jointing increases. This difference can be attributed to the fact that the contact state of the intensely jointed rock sample is relatively loose and dispersive, which means that the formation of an effective force transmission structure and a connected interaction network is prevented.

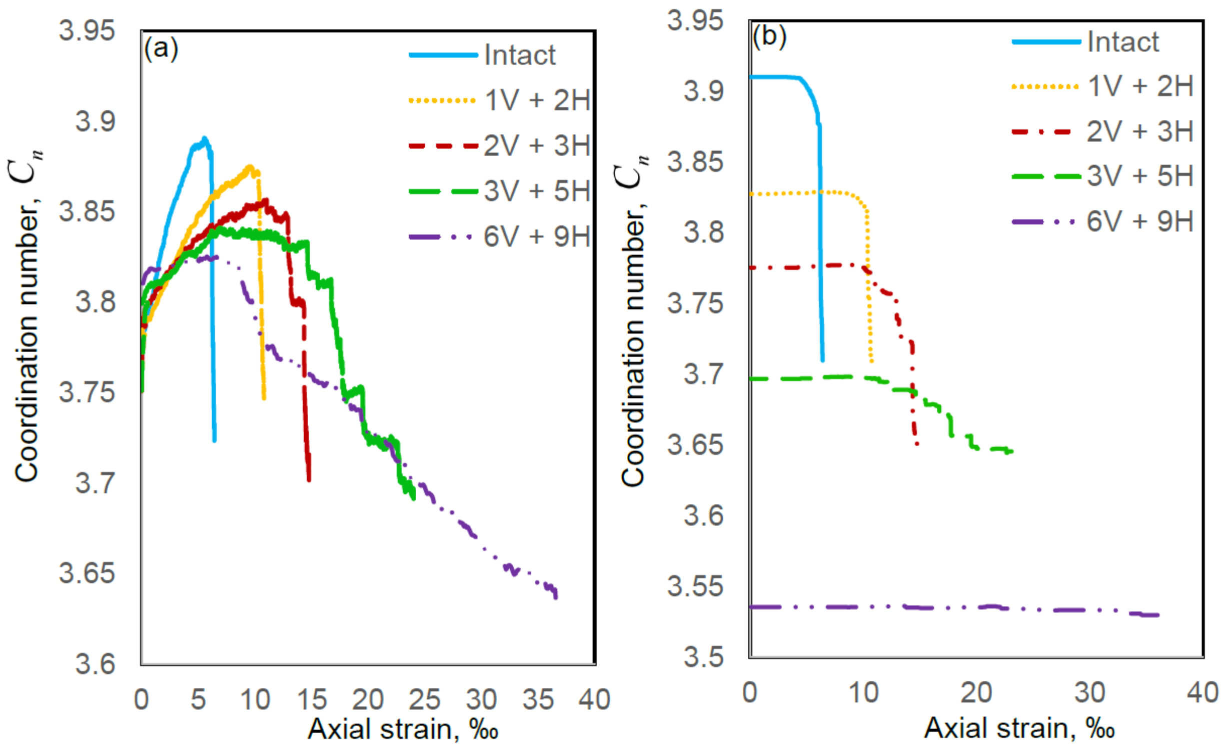

Figure 3 - 10. The coordination number in the intact/jointed rock samples: (a) considering all engaged contacts; (b) considering all bonded contacts.

For highly jointed rocks, contact force chains are more likely to reach the limiting value for sliding along the pre-existing joints, hence the decrease in the coordination number (or the loss of contact) is more gradual. The rate of increase or decrease in coordination number is closely related to the tendency of a particulate assemblage to dilate or contract as shown in Fig. 3 - 3f.

The coordination number of parallel bonds stays constant at the elastic deformation stage and then starts to decrease when ε_a reaches 4.48, 9.78, 10.59, 12.21 and 14.28 ‰ for intact and jointed 1V+2H, 2V+3H, 3V+5H, and 6V+9H samples respectively. This observation is in accordance with the fracturing behavior, where the increment of micro-cracks and increasing number of particles being debonded are observed, thereafter the coordination number of parallel bonds decreases significantly.

The late reduction in coordination number can further confirm the failure mode associated with brittle–ductile transition. This is due to the fact that with the increase in initial joint frequency, the frictional movements of particles on the joint planes is facilitated. It is noted that the increase of the degree of initial jointing prevents further increase of interlocking due to a growing number of particles being debonded, marked out by decreasing initial coordination number of parallel bonds (see Fig. 3 - 10b).

3.4.2. Microstructure Anisotropy

In quantifying anisotropy in a granular assembly, two anisotropy sources are distinguished: geometrical anisotropy and mechanical anisotropy (Ouadfel and Rothenburg 2001; Guo and Zhao 2013; Zhao et al. 2015).

Geometrical anisotropy is defined as the local orientation of a contact plane that gives rise to the global anisotropic phenomenon. Mechanical anisotropy is mainly caused by external forces and depends on the induced contact forces in relation to contact plane orientations (Zhao and Zhou 2017). For an assembly of circular particles, geometrical anisotropy can be expressed using the distribution of contact normal vectors.

The probability density function $E(\mathbf{n})$ of contact normal at a unit circle in 2D is introduced to identify the likelihood that a contact will have an orientation descried by the unit normal vector $\mathbf{n}$.

$$\int_{\Theta} E(\mathbf{n}) d\Theta = 1 \tag{32}$$

Therefore, the fabric tensor of contact normals can be represented as (Bathurst and Rothenburg 1990):

$$\Phi_{ij} = \int_{\Theta} E(\mathbf{n}) n_i n_j d\Theta = \frac{1}{N_c} \sum_{N_c} n_i n_j \tag{33}$$

The probability density function E(c) can be fitted using a Fourier series in tensorial form as

$$E(\Theta) = \frac{1}{2\pi} \left[1 + a_{ij}^c n_i n_j + a_{ijkl}^c n_i n_j n_k n_l \right] \tag{34}$$

where odd ordered tensors do not contribute to the series solution in terms of the symmetry of the directional data. With a second-order Fourier expansion of E(c), i.e., $E(\Theta) = \frac{1}{2\pi}\left[1 + a_{ij}^c n_i n_j\right]$, substituting into Eq. (33) and integrating, we get:

$$\Phi_{ij} = \frac{1}{2}\delta_{ij} + \frac{a_{ij}^c}{4} \tag{35}$$

where δ_{ij} is the Kronecker delta; the second-order tensor a_{ij}^c is deviatoric and symmetric, and characterises the fabric anisotropy. In a nutshell, a_{ij}^c can be represented with respect to the deviatoric fabric tensor Φ'_{ij} given by equation (35).

$$a_{ij}^c = 4\Phi'_{ij} \tag{36}$$

The mechanical anisotropy can be split into normal force anisotropy (caused by normal contact forces) and tangential force anisotropy (induced by tangential contact forces), which are respectively defined as follows (Guo and Zhao 2013; Shi and Guo 2018):

$$\chi_{ij}^n = \frac{1}{2\pi} \int_{\Theta} \bar{f}^n(\Theta) n_i n_j d\Theta = \frac{1}{N_c} \sum_{c \in N_c} \frac{f^n n_i n_j}{1 + a_{kl}^c n_k n_l} \tag{37}$$

$$\bar{f}^n(\Theta) = \bar{f}^0 [1 + a_{ij}^n n_i n_j] \tag{38}$$

and

$$\chi_{ij}^{t} = \frac{1}{2\pi}\int_{\Theta} \bar{f}^{t}(\Theta)t_i n_j d\Theta = \frac{1}{N_c}\sum_{c\in N_c} \frac{f^{t} t_i n_j}{1+a_{kl}^{c} n_k n_l} \tag{39}$$

$$\bar{f}_i^{t}(\Theta) = \bar{f}^{0}[a_{ik}^{t} n_k - (a_{kl}^{t} n_k n_l) n_i] \tag{40}$$

where

$$a_{ij}^{n} = 4\frac{\chi_{ij}'^{n}}{\bar{f}^{0}},\ a_{ij}^{t} = 4\frac{\chi_{ij}'^{t}}{\bar{f}^{0}} \tag{41}$$

Similar to the previous cases, $\bar{f}^{0} = \chi_{ii}^{n}$ is the average normal force calculated over different Θ and may differ from the average normal force $\bar{f}$ over all contacts.

Collectively, the three anisotropic tensors, a_{ij}^{c}, a_{ij}^{n} and a_{ij}^{t}, are defined to characterize the anisotropic behavior. Because all three tensors are deviatoric in nature, the deviatoric invariants are then used to quantify the degree of anisotropy, given as (Guo and Zhao 2013):

$$a_{*} = sign(S_r)\sqrt{\frac{1}{2} a_{ij}^{*} a_{ij}^{*}} \tag{42}$$

where the sub/super-script $*$ stands for c, n or t, corresponding to one of the three cases of anisotropy mentioned above, respectively.

S_r is defined in Eq. (42), and more details can be found in Guo and Zhao (2013).

$$S_r = \frac{a_{ij}^{*}\sigma_{ij}'}{\sqrt{a_{kl}^{*} a_{kl}^{*}}\sqrt{\sigma_{mn}'\sigma_{mn}'}} \tag{43}$$

The evolution of anisotropy coefficients of intact and pre-jointed rock samples during confined compressive strength tests is shown in Figure 3 - 11. Although the deviatoric fabric for all engaged contacts is found to be equal to $\frac{a_c}{2}$ (Azéma et al. 2013; Ma et al. 2015), the evolution of contact normal anisotropy (a_c) has the same trend as that of deviatoric fabric (Fig. 3 - 9a). Hence, there is no need to further discuss the evolution of contact normal anisotropy herein.

The increasing initial joint frequency appears to restrain the growth rate of all anisotropy coefficients. However, the variation of the anisotropy coefficient (a_n) for intact, 1V + 2H, and 2V + 3H rock samples follows similar manners during rock deformation, the anisotropy coefficients increase with axial strain up to the peak value of around 1.26, 1.23, and 1.22 and then it drops instantaneously to 1.09, 1.13, and 1.14, respectively. Similar to geometric anisotropy (a_c), the variations of the anisotropy coefficient (a_n) for 3V + 5H and 6V + 9H samples experience a slower progression where the anisotropy coefficients increase to peaks as the loading proceeds and then relaxes to a residual values up to fluctuations of rather small amplitude. In fact, the rise and fall observed in the value a_n during the loading process correspond respectively to the generation and collapse of microstructures. For instance, the significant drop of a_n in the intact sample implies that the reduction in a_n coincides with the reduction observed in the rock strength as well as the high level of fracturing. As already explained, this dropping point are in response to the onset of coalescence of pre-existing microcracks and freshly formed fractures into a throughgoing rupture.

As initial joint frequency intensifies, an abrupt fall after peak in 3V + 5H and 6V + 9H rock samples cannot be observed, instead the variation of a_n fully mobilized at larger axial strain and the following reduction becomes less significant compared to other samples. This decreasing trend for a_n indicates that the sliding through pre-existing joints in the rock deformation process plays an increasingly governing role by activating large frictional movement of unbroken blocks as well as the high degree of dilation until the intact material failure mode are entirely replaced. Compared with the other mechanical anisotropy a_n, the tangential force anisotropy a_t during the loading course is obviously smaller.

It is worth noting although this rapid rise of mechanical anisotropy can be observed for all cases, the growth rate is still significantly reduced with the degree of initial jointing, because the assembly is kinematically locked initially and deforms elastically, however the highly jointed rock structure effectively damps the granular dynamics and contact intensity as stated by Zhao et al. (2018). In general terms, this rapid rise of the anisotropies of contact tangential force a_t corresponds to the development of frictional resistance as a result of the relative translational movement of particles. The variation of anisotropy coefficient a_t is analogous to what happens with the normal contact

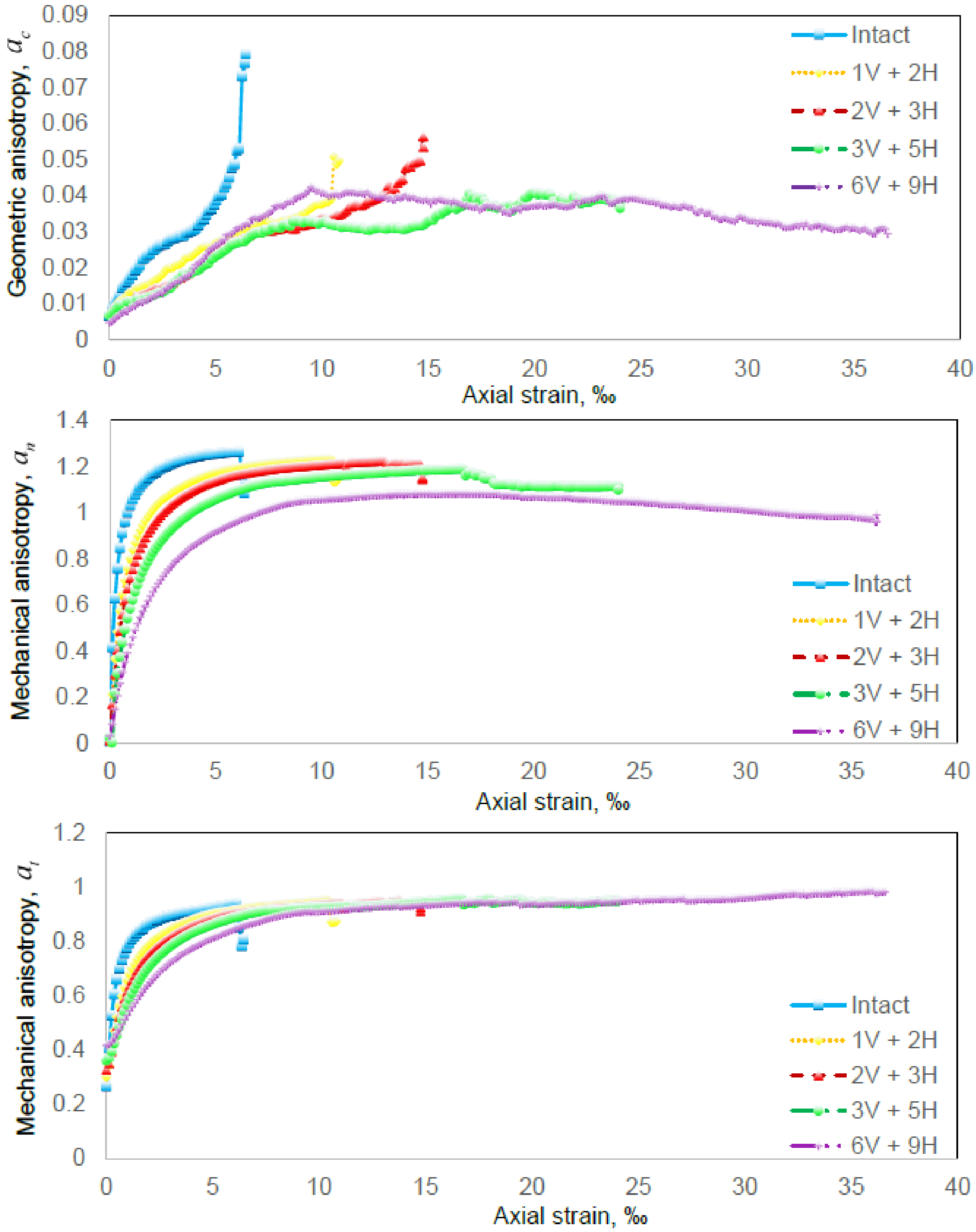

Figure 3 - 11. (a) – (c) Evolution of geometrical anisotropy a_c, mechanical anisotropy a_n, and mechanical anisotropy a_t as a function of cumulative axial strain in intact and jointed rock samples.

force a_n for intact, 1V + 2V, and 2V + 3H rock samples, which it reaches a peak value at a finite axial strain and then it accompanies an abrupt drop indicting that the large rise of bond breakage as well as the reduction of contact density leads to particles gaining rotational freedom, as a result, tangential forces are slowly released.

In contrast to a_n for the 3V + 5H and 6V + 9H rock samples, variation of a_t acts in a different manner where it continuously increases with axial strain up to the end of the test without any onset of decreasing. This may be attributed to the fact that the rotational mobility of the particles is strongly reduced as a result of tightly connected structure due to much lower fracturing intensity so that the largely bonded particles tend to slide rather than rolling with a strong increase of friction mobilization. Indeed, it further confirms that as the governing failure mechanism is progressively transited from mix failure mode to sliding through pre-existing discontinuities with the increasing degree of initial jointing, the level of friction mobilization, which reflects the dependence of the mechanical stability of the material on friction forces, also increases. Nevertheless, this a_t increase is not large enough to additively compensate for the decrease of a_c and a_n, so that the shear strength continues to exhibit a softening trend.

3.4.3. Anisotropic distribution

Given the preceding picture of the anisotropy evolutions under different joint configurations for confined compression tests, further examination of the polar distributions of the geometric and mechanical anisotropies in terms of micro-structural mechanism can provide a better description of the complex macroscopic behavior including the topology of arrangement of particles as well as the internal force transmissions. Therefore, the polar distributions of anisotropies of fabric, contact normal and shear forces at three distinct (initial, peak and 50 % post peak) states for the intact, 2V + 3 H, and 6V + 9H samples are selected to reflect microstructural changes during the rock deformation, of which failure mechanisms are governed by intact rock failure, mixed failure, and sliding through pre-existing joints, respectively. In addition, the numerically measured data is presented together with the approximations to the distributions using second-order tensorial relationships (33), (38), and (40). This second-order tensorial relationships has been widely applied to quantity the spatial orientations of micro-mechanical descriptors, such as contact normals (Kanatani 1984; Sun and Zheng 2019), and contact forces (Ouadfel and Rothenburg 2001). Figures 3 - 12 – 3 - 14 show that the approximations appear to visually well-represent the numerically measured data and the initial anisotropy condition totally evolves due to the induced anisotropy within intact and pre-jointed samples. More precisely, compared to the polar distributions of mechanical anisotropies, the polar histograms of contact normals seem to have approximately a circular form during the loading process as a result of the value of contact normal anisotropy is far below than 1, as suggested by Hosseininia (2011 & 2013) that the circle deforms as a peanut when the value of a_c increases and closes to 1 indicating a high degree of anisotropy. Nevertheless, polar histograms for the intact samples during the deformation process are observed to be more elongated along the loading axis due to interparticle contacts being disintegrated reflected by the relatively marked rise of anisotropy.

The polar histogram of contact normal force for the selected three samples at the initial state seems to have approximately a circular form, which reveals that the magnitude of average contact normal force is almost the same in all directions (see Fig. 3 - 12). This is expected since all samples were initially compacted under isotropic condition. The histograms, however, are elongated, at the peak stress state (see Fig. 3 - 13), along the loading axis and slimed along the horizontal direction for the intact rock samples. In addition, the long axis of histograms for jointed samples is increasingly deviated anticlockwise from the loading axis with the higher level of initial jointing. This evolution in the normal force anisotropy distribution suggests the development of new contacts as well as the increase in the magnitude of normal forces along the loading axis in relation to those in the horizontal direction are largely affected by the increased initial joint frequency. After the entire loading course, the anisotropies of contact normal forces decrease rapidly accompanied by the significant rotation of its orientations, particularly for 6V + 9H samples (see Fig. 3 - 14). The reduction in contact normal force anisotropy, is related to reorganization of microstructure when the dilation is intense. Dilation is initiated by movement of highly compressed conglomerates of particles that move as rigid blocks and disrupt the assembly, therefore, the 6V + 9H samples characterized by the highest dilatant activity shows the lowest degree of contact normal force anisotropy as well as the continuous decreasing trend.

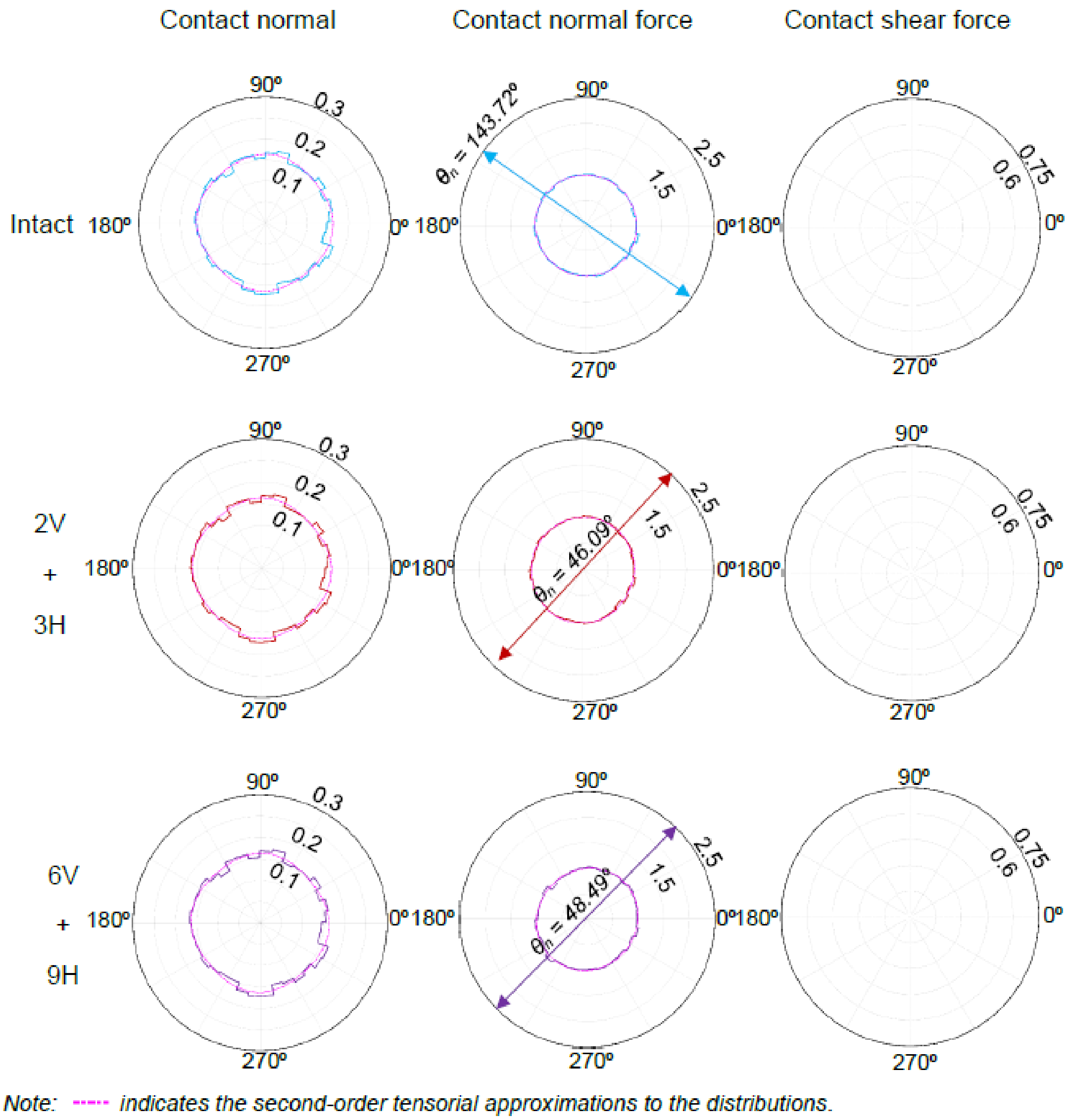

Figure 3 - 12. Distribution of anisotropies of contact normal, normalized average contact normal force ($\bar{f}^{n}(\Theta)/\bar{f}^{0}$) and normalized average contact shear force ($\bar{f}_{i}^{t}(\Theta)/\bar{f}^{0}$) of the intact and two jointed rock samples at initial stress state.

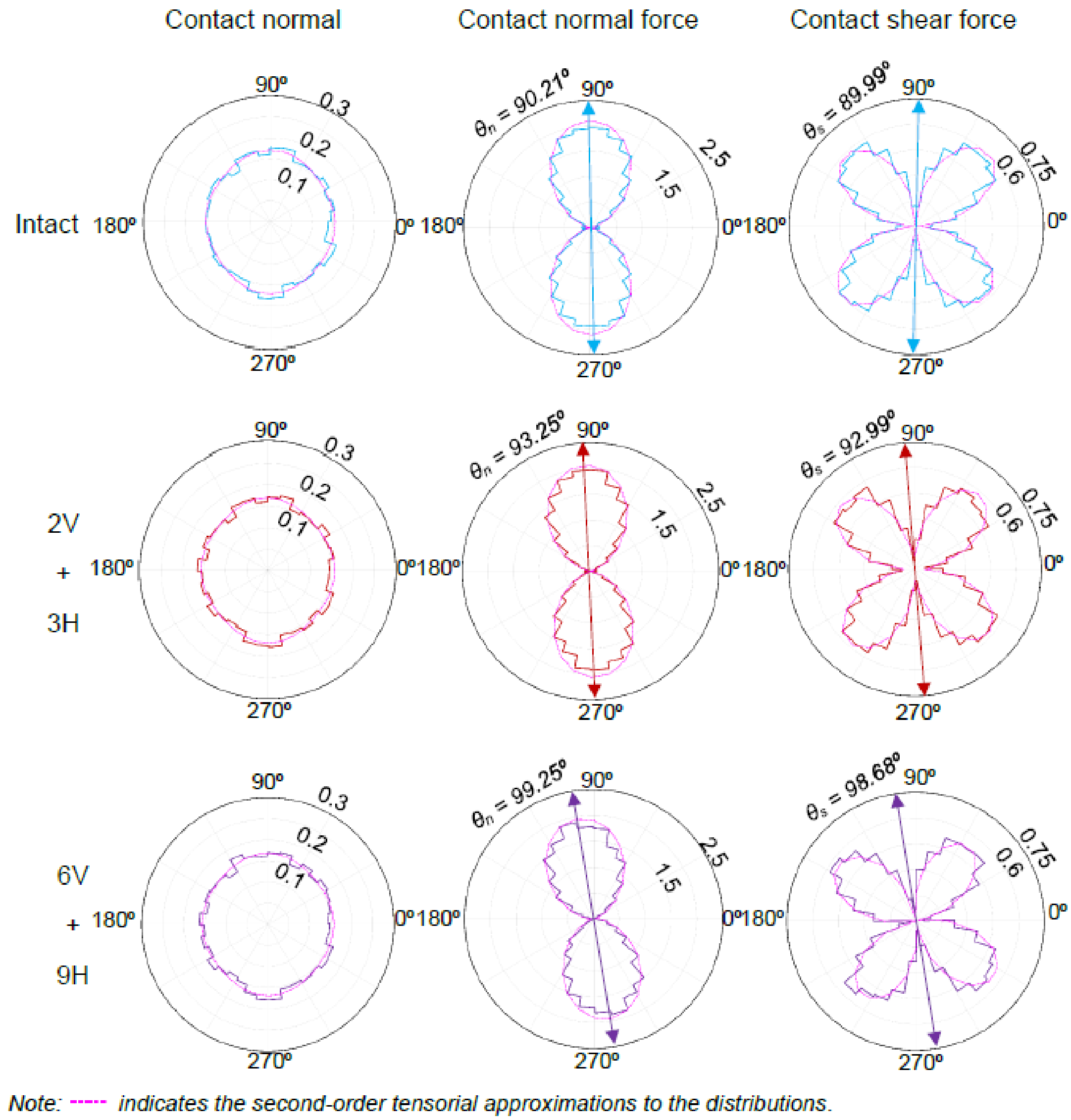

Figure 3 - 13. Distribution of anisotropies of contact normal, normalized average contact normal force ($\bar{f}^n(\Theta)/\bar{f}^0$) and normalized average contact shear force ($\bar{f}_i^t(\Theta)/\bar{f}^0$) of the intact and two jointed rock samples at peak stress state.

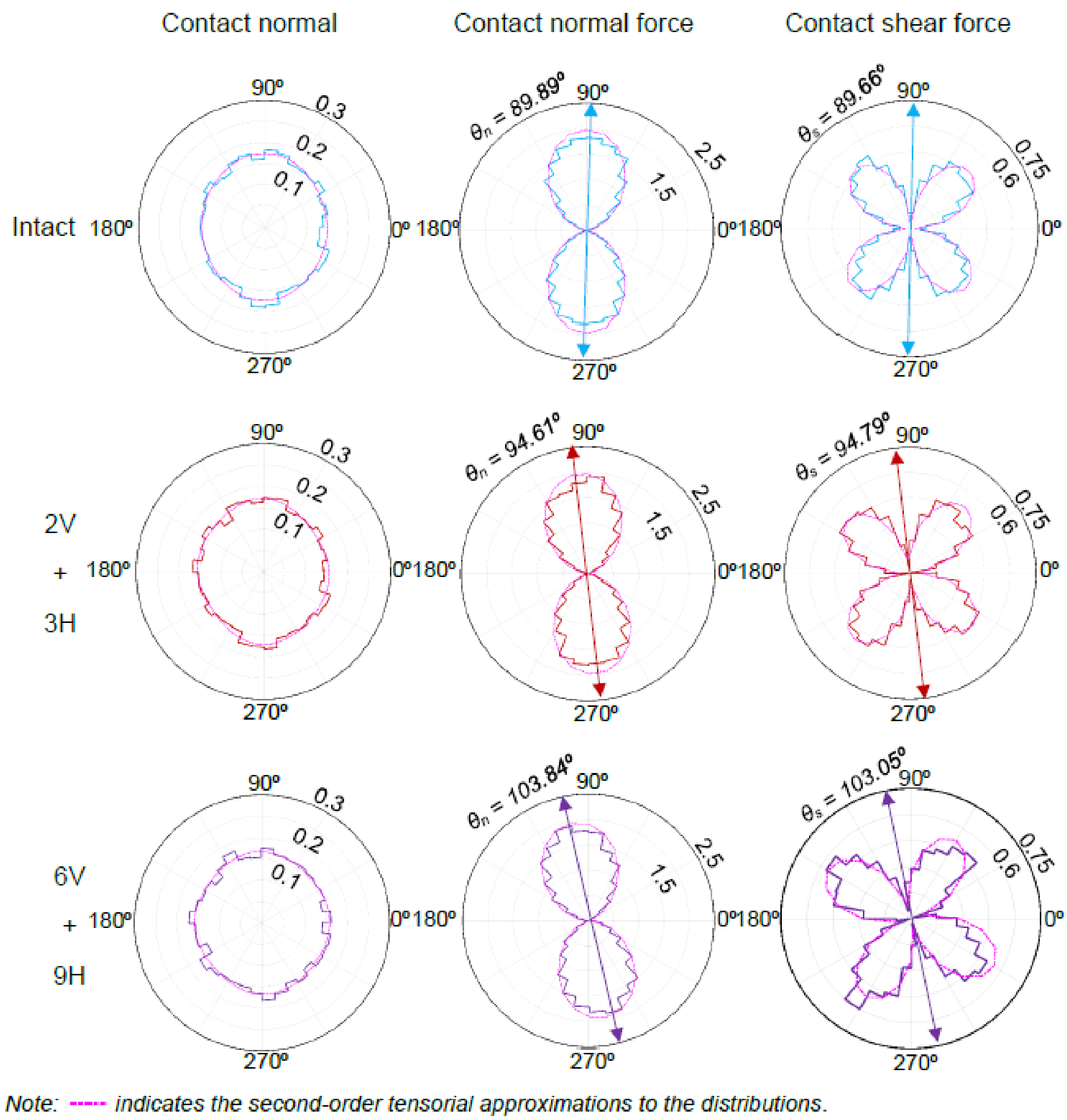

Figure 3 - 14. Distribution of anisotropies of contact normal, normalized average contact normal force ($\bar{f}^{n}(\Theta)/\bar{f}^{0}$) and normalized average contact shear force ($\bar{f}_{i}^{t}(\Theta)/\bar{f}^{0}$) of the intact and two jointed rock samples at 50% post-peak stress state.

The initial contact tangential force inside all the samples is close to zero, because the initial loading relates to an isotropic compaction and no shear deformation occurs. As a consequence, no shear stress is mobilized among particles. For the peak stress state, however, it is observed that the polar histograms of tangential forces are paraded by four leaps instead of having a peanut-like form such as happened for contact normal force distribution. The reason explained by Hosseininia (2011) is that the direction of the contact tangential force is perpendicular to the contact normal force and thus, the distribution of tangential contact force differs.

Analogous to what happens with the contact normal force, the principal direction of tangential force anisotropy (θ_t) rapidly orients along loading axis ($\theta_t = 90°$) for the intact rock samples, while it is inclined around 3 and 9 degrees anticlockwise with respect to the loading axis for 3V + 5H and 6V + 9H rock samples at peak stress state, subsequently it is rotated counter-clockwise by approximately 5º and 13º with respect to the loading axis when it reaches the 50% post-peak stress state. This can be attributed to the fact that the orientations of joint sets within the assemblies strongly influences the direction of maximum mobilized shear stress. In addition, by comparing the variation of θ_t with that of θ_n at the peak and post-peak stress states, it is observed that the principal directions of contact force and fabric anisotropies are essentially coincident. The explanation for this observation is that distribution of contacts is defined by contacts that actively transmit force then the coincidence of contact force and fabric tensors is assured (Bathurst and Rothenburg, 1990).

3.4.4. Marcoscale Response & Microscopic Origin

Based on a detailed 2D DEM analysis, better understanding of how the rock mass responds to the increase in the intensity of initial joints has been achieved. From the macroscopic point of view, the level of such weakness planes influences the mechanical characteristics of the rock mass through: (i) a reduction in stiffness and peak stress, (ii) brittle–ductile transition, (iii) less accentuated post-peak stress drops, (iv) decrease in microcracking intensity (Fig. 3 - 3), (v) shift in failure modes, and (vi) variations of orientation distributions of micro tensile and shear cracks (Fig. 3 - 4).

The above effects on the mechanical behaviour is also manifested in the energy budget spent during rock deformation. The addition of further jointing to the sample weakens the rock brittleness nature and leads to the less intense fracturing in the microstructure, which, from the viewpoint of energy, makes the energy storage capacity lower while the energy dissipation capacity of the rock becomes higher. This prohibits strain energy accumulation and facilitates friction dissipation (Fig. 3 - 8).

The fracturing activity, which itself only dissipates a negligible amount of input energy (Table 3 - 6 & Fig. 3 - 8), imparts permanent changes to the solid microstructure that can be delineated by the enhanced deviator fabric (Fig. 3 - 9d) and the reduced coordination number below the initial state (Fig. 3 - 10b). It is worth noting that the change in both the deviator fabric and coordination number for bonded contacts has been significantly affected by the increase in initial joint intensity. This observation is due to the fact that the decrease in the amount of fracturing leads to more particles remain bonded. Consequently, particles may survive in the fabric rearrangement process as a result of the slow release of inter-particle constraints and the change in both deviator fabric and coordination number is significantly reduced.

Table 3 - 6. Tensile and shear fracture energy

	Intact	1V+2H	2V+3H	3V+5H	6V +9H
Tensile fracture energy (J)	214.7	153.9	148.2	73.9	10.9
Shear fracture energy (J)	65.2	40.3	42.1	15.1	0

Further insights have been gained by examining the development of particle kinematics, shear strain, void ratio, and force chain distributions in intact and pre-jointed samples, which are not easily visualized in experiments or continuum models. It has been found that in an intact sample, the macroscopic rupture surface exhibits a high concentration of shear strains, and a large amount of translational and rotational granular temperatures (Fig. 3 - 6). With increasing initial joint frequency, many isolated zones of strain localization are observed, yet they fail to form a connected zone. Therefore no catastrophic failure associated with macrofailure planes traversing the entire sample is formed. In particular, neither apparent localized patterns of shear strain nor granular temperatures can be found in 6V + 9H samples. This is due to the sliding that develops on pre-existing discontinuity being the dominant failure mechanism as a result of large plastic deformation (Fig. 3 - 3) occurring without crack nucleation.

From a micromechanical standpoint, the strengths of intact and pre-jointed samples depend on its ability to develop anisotropies. The trend found for the mechanical anisotropies (see Fig. 3 - 11) is generally synchronized with that for the macroscopic stress observed in Fig. 3 - 3, which was also reported in several laboratory and numerical studies (Rothenbur and Bathurst 1989; Bathurst and Rothenburg 1990; Guo and Zhao 2013).

With the increase in initial joint frequency, the rock sample behaves in a more brittle-ductile fashion with less prominent post-peak stress (see Fig. 3 - 3) and progressive transition to sliding failure mode along the joint planes (Fig. 3 - 4&6). This evolution of macroscopic deformation can be traced back to the micromechanical origins where a softening trend of the contact normal force anisotropy is compensated by a gradual increase of the tangential force anisotropy instead of significant falloffs of the both mechanical anisotropies. This further confirms the addition of further jointing to the sample leads to an increasing dominance of the sliding failure mode on the rock deformation, thus a strong activation of tangential forces is ensured to balance the increasing mobilization of friction forces (Bathurst and Rothenburg 1990; Azéma et al. 2013).

3.5. Discussion

3.5.1. Limitation and Future Outlook

Discrete element modeling of grain-scale heterogeneity, i.e., particle size distribution or non-spherical distinct element, plays an important role in controlling its emergent macroscopic response under compression. However, no matter which particle size distribution or grain shape is used, it is necessary to re-calibrate the values of the micro-mechanical parameters used in the analysis to match the measured macro-mechanical behaviour. This means that when the arrangement of the spherical particles changes, some self-adjustment of the micro-mechanical parameters takes place to produce the expected macro-mechanical behavior (Hatzor and Palchik 1997; Fan et al, 2015). Therefore, the main trends related to the addition of joints on the strength and deformability of the rock samples remain essentially the same even though some slight changes on the exact values are possible.

Substantial insights have already been gained from discrete element numerical modelling of acoustic emissions (AEs) in progressive mechanisms of rock failure (Hazzard and Young 2000; Zhang and Zhang 2017; Zhang et al. 2019; Song et al. 2019). In particular, acoustic emissions result from sources of internal damage due to sudden local dislocations in the form of tensile or shear microcracks can foster a deeper understanding of the onset and propagation of microcracking and provide significant additional information to complement micromechanical study to analyze fracture growth mechanisms and their correlation with increasing level of initial jointing.

3.6. Conclusion

The deformability and failure behavior (progressive fracture growth, material damage, failure) of intact rock and rock samples containing two sets of persistent joints with increased initial joint frequency has been investigated through confined compression tests by discrete element numerical simulation. The smooth-joint contact model and the linear parallel bond model were selected in the numerical model for the pre-existing joints and the rock matrix, respectively. The entire deformation and failure process are visually represented and the failure mode in reasonable accordance with experimental results is obtained. The results show that the failure mechanism is much affected by the degree of initial jointing. The following preliminary conclusions can be drawn from the numerical tests:

(1) As the density of the initial jointing increases, the rock deformation behaves in a more brittle-ductile fashion with corresponding patterns of visible strain hardening, reduced stress drops and fracturing activities, and dispersed microcracking distribution. This is generally synchronized with transition of failure mode to joint slip yielding mechanism leading to the absence of nucleation and coalescence of fractures as a consequence of the movement of conglomerates of particles along the joint plane.

(2) The relative contributions of the elastic energies to the energy budget and to the fracture energy are found to decline with the increase in initial joint intensity. This is compatible with the fact the frictional energy dissipation gradually prevails over the elastic strain energies build-up as a result of the sliding along the joint plane.

(3) With the increase in initial joint intensity, rock samples are prevented from developing larger fabric and force anisotropies, which further result in a smaller macroscopic peak strength.

(4) Consistent with the macroscopic deformation behaviour, i.e., stress-strain curve, the variations of geometric and mechanical anisotropies provide micromechanical evidence that a transition from brittle to ductile behavior occurs with increasing initial joint frequency.

Preface to Chapter 4

The discrete element approach developed in the previous chapter has demonstrated its efficiency in investigating the fracturing behaviour of rock mass. In these analyses, the rock matrix were modeled using bonded grains and the smooth joint contact model was utilized to simulate the mechanical response of joint set. The model was used to study the role of initial joint frequency on the damage and failure processes and provide a micromechanical description of the mechanisms involved. In this chapter, to examine the capability of the DE simulation in rock fracturing behaviour in the context of large-scale geodynamic process, the joint set is now reproduced with bond removal method. The detailed behaviour of the rock fracture growth mechanism during the landsliding process is investigated. The suitability of the proposed numerical technique to solve this class of problems is therefore demonstrated.

Chapter 4

Insights into the Transport and Fragmentation Characteristics of Earthquake-Induced Rock Avalanche: A Numerical Study

Abstract

The earthquake-induced rock avalanche in the Tangjia Valley was the most notable geological disaster triggered by Lushan earthquake in 2013. In order to investigate the transport kinematics and depositional mechanism of this catastrophic landslide, a 2D discrete element model is developed and calibrated using field data. The model is then used to analyze the seismic response and mass transport process of a natural slope. The slope response to earthquake is numerically studied focusing on crack initiation, propagation, and coalescence within the rock mass. The mass movement and accumulation process are interpreted in terms of evolution of stress and solid fraction, kinematic behaviour and energy conversion. During the mass transport process, the slope is fragmented progressively due to intense shearing, allowing a basal layer of gradually fining solid particles to be generated with simultaneous occurrence of violent collisions, increase in particle kinematic activities, and the reduction of solid concentration. To further study this deformation process, fragment size distributions and fractal dimensions are described by Weibull distribution and power-law function, respectively. This statistical analysis reveals that dynamic disintegration continuously operates with the increasing runout distance. It is also found that the distribution of the fragment shapes becomes stable as the avalanche loses its momentum and deposition starts in the runout area. The proposed framework for the analysis of rock avalanches can be used to understand the physics of similar geological hazards.

Keywords: Earthquake-induced landslide; Rock avalanche; Fragmentation; Fragment shape; Discrete element analysis.

∗ A version of this chapter has been published in ***International Journal of Geomechanics ASCE***, 20(9), 1-23.

4.1. Introduction

Large earthquakes in mountainous regions commonly result in catastrophic and widespread landsliding, which is a significant hazard during and in the immediate aftermath of ground shaking (Keefer, 1994). These events have been reported worldwide in the past few decades (Tian et al. 2019). For example, co-seismic landslides that developed during the 2005 Kashmir earthquake (Ms = 7.6) caused about 30% of the total fatalities (Havenith and Boureau 2010). In the 2008 Wenchuan earthquake (Ms = 8.0), a quarter of the total deaths and over one third of the total damage cost were caused by earthquake-triggered landslides (Yin et al. 2009). Less than five years later, a strong shock happened once again along the Longmen Shan fault zone located about 80 km southwest of the epicenter of the 2008 event and induced as many as 15,645 co-seismic landslides (Xu et al. 2015 a&b). In recent years, there has been an increasing interest in the study of earthquake-triggered landslides; however, much uncertainty still exists regarding the transport mechanism and fragmentation process.

Rock avalanches are among the most destructive landslide that are commonly triggered by strong earthquakes. In the literature, many hypotheses have been proposed to explain the rock transport kinematics and dynamics, including air or vapour lubrication (Kent 1966; Shreve 1968; Habib 1975); mechanical fluidization (Bagnold 1954; Davies 1982); momentum transfer (Eisbacher 1979; Davies et al. 1999); acoustic fluidization (Melosh 1986); energetic disintegration (Davies and McSaveney 1999); and basal rock melting (Erismann and Abele 2001; De Blasio and Elverhøi 2008). Although some of the invoked mechanisms may be important for some specific events, none has so far gained universal acceptance for elucidating the rock avalanche mobility. In natural conditions, the deposited material in long runout rock avalanches has been observed in diverse geological conditions to be composed of highly fragmented parent material (Locat et al. 2006; Crosta et al. 2007; Perinotto et al. 2015; Wang et al. 2015; Zhang et al. 2019). Thus, dynamic rock fragmentation within the flow has been invoked as a possible mechanism for effective lubrication in rock avalanches (Davies et al. 1999; Davies and McSaveney 2009; McSaveney and Davies 2009). The related research has been performed by means of field observations of real rock avalanche deposits (Locat et al. 2006; Crosta et al. 2007; Dunning 2007; Zhang and Yin 2013) and laboratory experiments (Giacomini et al. 2009; Imre et al. 2010; Bowman et al. 2012; Haug et al. 2016). Crosta et al. (2007) described the spatial distributions of the fractal dimension values measured at both the source and deposit areas, which delineate the fragmentation process and the corresponding energy consumption. Imre et al. (2010) performed a series of centrifuge tests and stated that the interparticle collisions play a dominant role in the fragmentation of a rock avalanche.

Extensive effort has been exerted to reproduce the runout behavior of landslides numerically (Campbell 1990; Calvetti et al. 2000; Campbell 2006; Antolini et al. 2016; Gong and Tang 2017; Shen et al. 2017; Shen et al. 2018; Gao and Meguid 2018 a&b), particularly as the complex nature and rapid process of landslide may not be comprehensively analyzed using field investigations or experiments. Such efforts involve the application of discrete or continuum methods. Continuum method is inherently capable of simulating the dynamic movements of actual landslides. However, continuum-based numerical models often fail to reproduce the progressive failure of rock slopes, especially the dynamic release and the accompanying complex internal distortion, dilation, and fracture (Stead et al. 2006). Unlike continuum models, the discrete element method (DEM), does not limit the extent of element separation, and the mass movement process from fracture to separation can be fully simulated. More importantly, from the mesoscopic view, the internal disruption of rock avalanches is very high signifying the nearly complete disaggregation into individual soil grains or small rock fragments. Therefore, the distinct element method (DEM) is considered an effective tool for modelling rock avalanches, in which the avalanching process is extremely rapid and exceedingly complex involving sliding or flow. By employing DEM simulations, Campbell (1989) demonstrated that particles in the base exhibit high fluctuations with increase of granular temperature and thus increasing apparent friction reduction of landslides. Campbell et al. (1995) observed that the stratification is well preserved in their original order within the debris and suggested that the material at the top of the debris may have been very gently handled which accounts for the large, angular, and obviously unagitated fragments found on the surface of the actual landslide deposit.

A large body of literature on DEM aspects of modelling earthquake-induced landslides focused on the kinematic behavior and deformation evolution of the actual landslides triggered by seismic activities only throughout simple recording of the displacements and velocities (e.g. Tang et al. 2009; Zhou et al. 2013; Yuan et al. 2014). However, less attention has been paid to studying the dynamic fragmentation process and transport mechanism of earthquake-induced landslides with complex geological and geomorphological settings (Meunier et al. 2007; Zhao and Crosta 2018).

Therefore, the Tangjia Valley rock avalanche, as one of the few identified large-scale landslides resulting from the seismic event of Lushan earthquake, was selected as a natural laboratory to investigate the characteristics of earthquake-induced rock avalanche, including joint distribution, crack evolution, energy transition, dynamic fragmentation, and deposition pattern. In this study, a suitable set of micro parameters was calibrated using uniaxial compression strength (UCS), and the developed numerical model was validated based on the recorded information at the site. The sedimentary fabric within the rock deposit and the fragment statistics presented in this study provide new insight into the deposition mechanism of a bonded granular system associated with a large-scale rock avalanche.

4.2. The Tangjia Valley Rock Avalanche

The Tangjia Valley rock avalanche (30º 10′ 43′′ N, 102º 45′ 40′′ E) occurred in the Damiao village, Laochang Township, Tianquan county, Sichuan province, China, is the largest rock avalanche triggered by the Lushan earthquake.

4.2.1. Geological and Geomorphologic Setting

The 2013 Lushan earthquake occurred on the easternmost margin of the Tibetan plateau. A series of predominantly north–northeast striking thrust faults were observed at the base of the Longmen Shan Mountains, at the northwestern edge of the Sichuan Basin (Tang et al. 2015). The fault belt consists of three thrust faults: the Maoxian-Wenchuan fault (back-range fault), the Yingxiu-Beichuan fault (central fault) and the Guanxian-Jiangyou fault (front-range fault). The 2008 Wenchuan earthquake occurred on the central part of the Longmen Shan fault belt, whereas the 2013 Lushan earthquake occurred on the southwestern segment. The epicenter of the Lushan event was near the Shangshi-Dachuan fault (see Fig. 4 - 1a). The Tangjia Valley rock avalanche is located in the footwall of the fault branch (see Fig. 4 - 1b). The violent ground shaking triggered by the seismic fault results in the largest Lushan earthquake-triggered landslide. In the rock avalanche area (Fig. 4 - 1b), lithology of the footwall (southeast plate) is composed of late Triassic light gray thick sandstone, quartzitic sandstone, mudstone of Xujiajointe Group (T_3x), the Quaternary deposits (Q_4^{del}) with a thickness of 3-5 meters.

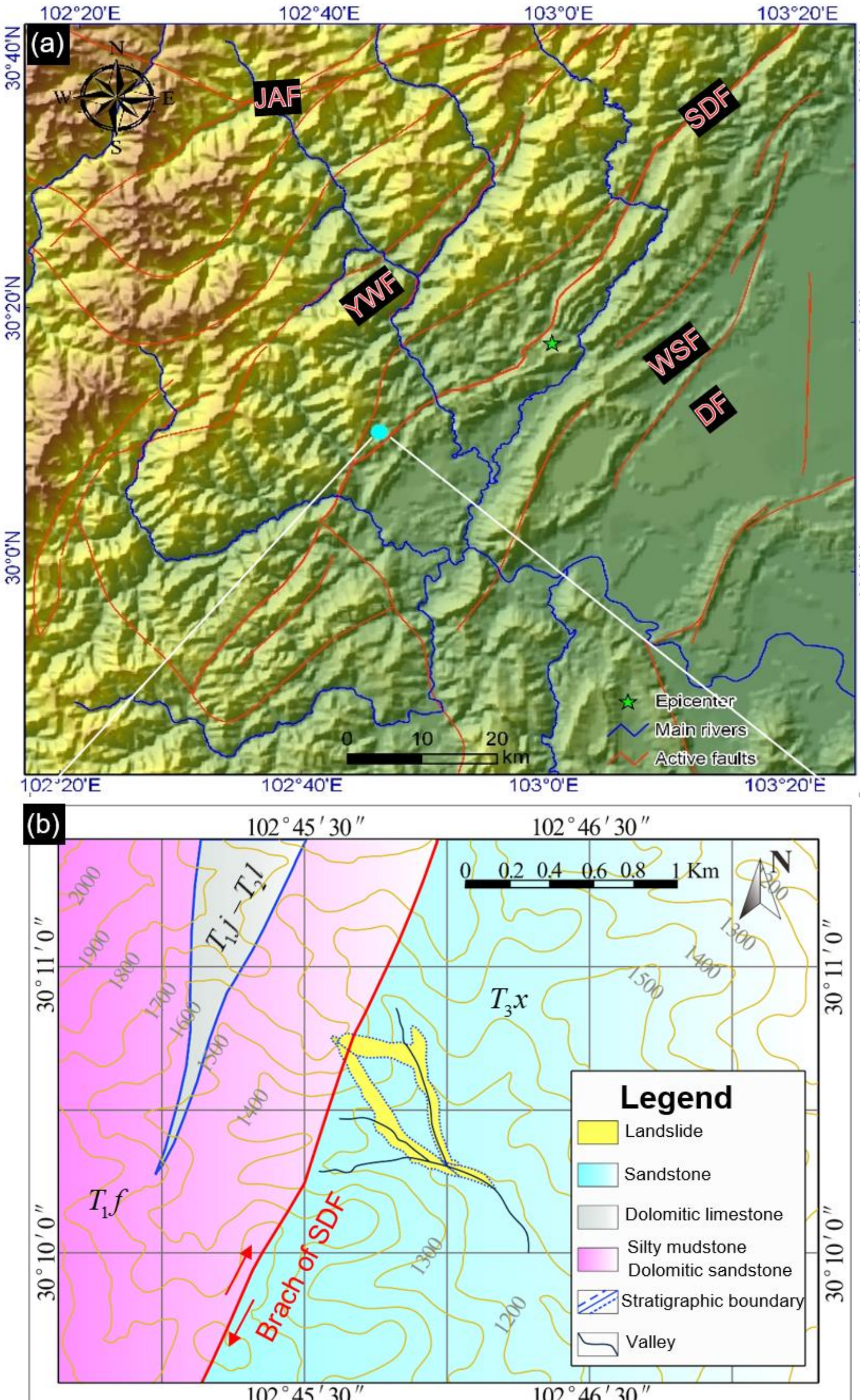

Figure 4 - 1. (a) The tectonic setting of the 2013 Lushan earthquake (SDF: Shuangshi-Dachuan fault; WSF: western Shangli fault; DF: Dayi fault; YWF: Yanjing-Wulong fault; JAF: Jintang Arc fault; (b) A geological map of landslide area. (Adapted from Xu et al. 2015a.)

The hanging wall (northwest plate) is composed of early Triassic purple silty mudstone and dolomitic sandstone in moderate-thin layers ($T_1 f$) and thick, gray dolomitic limestone of Jialingjiang Group ($T_1 j$), which is overlapped by the Leikoupo Group ($T_2 l$) of the middle Triassic age.

From a geomorphologic point of view (Fig. 4 - 2), rock avalanche source area lies on a narrow mountain ridge with an average width of 10 m, which is characterized by two steep lateral flanks with slope gradients of 60° - 63°, and deeply incised valleys (i.e., Chunjianwo and Gangoutou Valleys) in the frontal region.

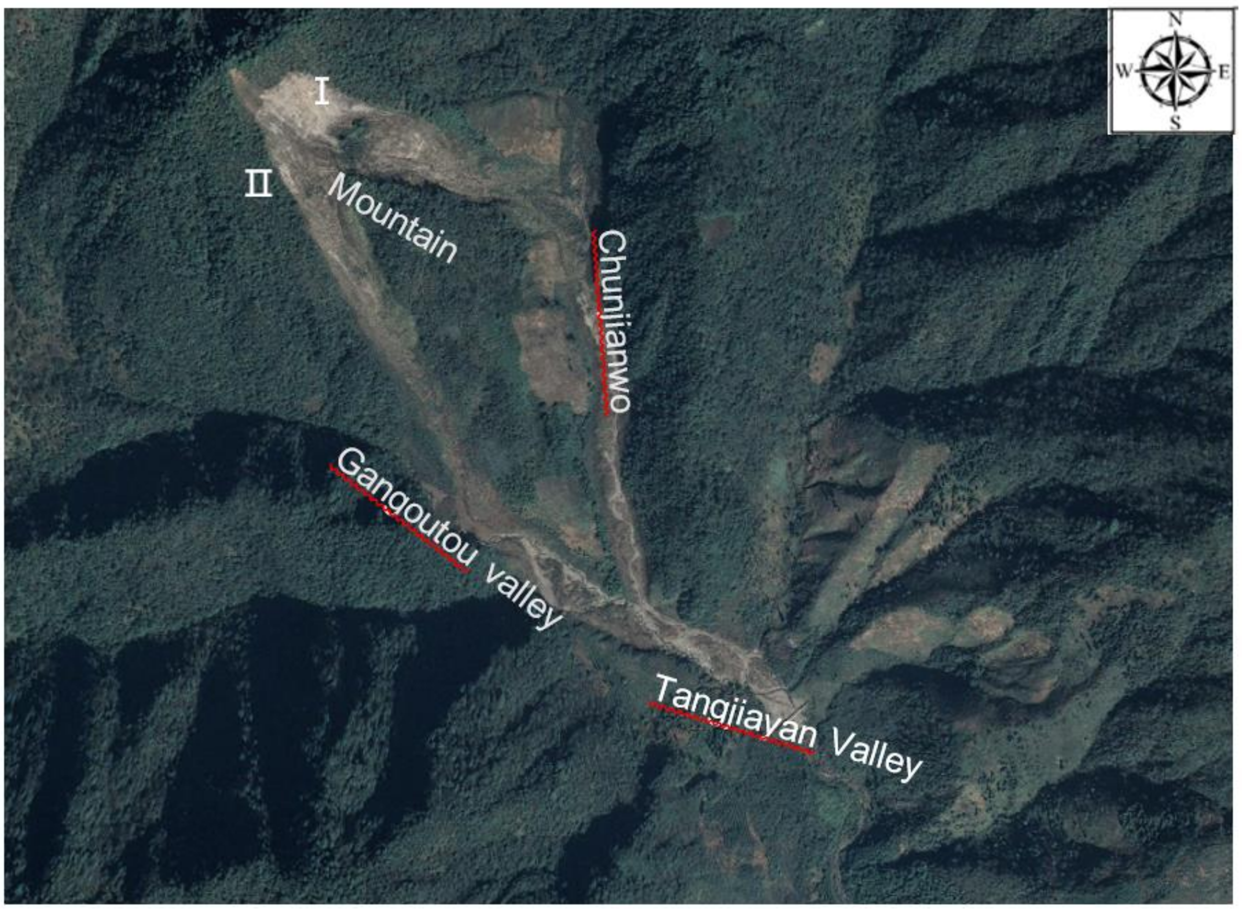

Figure 4 - 2. Overview of local geomorphologic conditions of the Tangjia Valley rock avalanche. (Image: Google Earth, CNES/Airbus, 2019)

4.2.2. Failure mechanism and dynamic process

The landslide can be divided into the following four areas: the source area, transport area, deposition area, and converging area (see Fig. 4 - 3), and the corresponding possible failure process is as follows (Hu et al. 2013; Li et al. 2017):

(1) The intense seismic shakings loosened and weakened the slope materials, facilitating further degradation of highly weathered rock mass strength. As a result, the rock slopes shattered and collapsed at a high speed, afterward the rock material travelled towards the direction of 130º over a short time period from the source area. At an elevation of 1,500 m a.s.l., due to the presence of the mountain ridge (see Fig. 4 - 4a), the displaced slope mass was split into two streams (see Fig. 4 - 3a), i.e., the left stream (rock avalanche I) towards the direction of 104º and the right stream (rock avalanche II) towards the direction of 156º. Thus, the source area can be divided into two subzones: S-Ia and S-Ib, which represent the source area for the left stream (Fig. 4 - 3b & Fig. 4 - 4b) and right stream (Fig. 4 - 3c & Fig. 4 - 4c), respectively. The complete geometric and geologic information of the source area is summarized in Table 4 - 1.

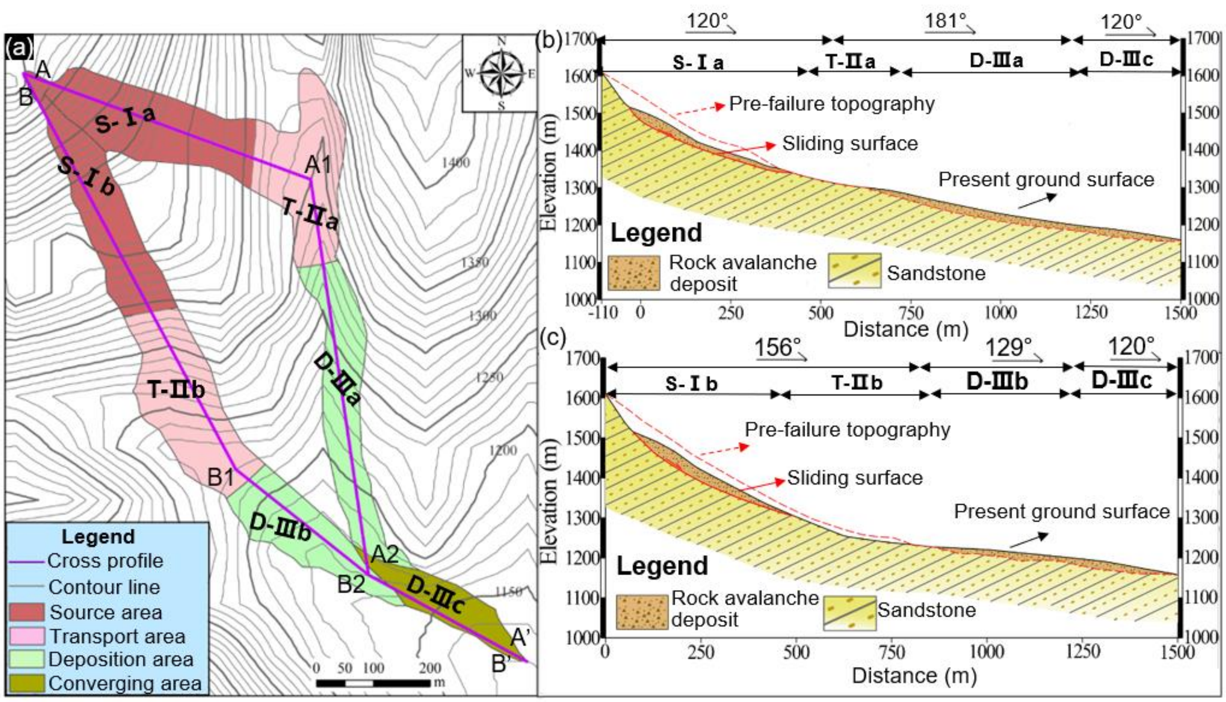

Figure 4 - 3. (a) Detailed topography of the Tangjia Valley rock avalanche along the main movement direction; (b) geological section map of the left stream of the avalanche along line A-A'; (c) geological section map of the right stream of the avalanche along line B-B'.

(2) The slope mass ran down rapidly in the transport areas T-IIa and T-IIb for the left and right stream, respectively. Subsequently, the translating slope mass was transformed into debris flows as it collided onto the opposite mountains of the left bank of Chunjianwo Valley and the right bank of Gangoutou Valley for the left and right streams, respectively. After the rock mass disintegrated, a small portion of the material within the left stream climbed up against the opposite valley bank to a maximum height of 35 m at location A1 (see Fig. 4 - 3a), whereas most of the fragmented rock continued traveling rapidly along the steep terrain. In addition, the sliding mass of the right stream super-elevated on the right bank of the Gangoutou Valley with a height of 15 m at location B1 (see Fig. 4 - 3a), which forced the fragmented rock flow to move with a 33° deflection and then continued to travel downward in a rapid motion along the valley.

Table 4 - 1. Field information of source area

Geometric and geologic conditions	Zone S-Ia	Zone S-Ib
Length (m)	160 - 170	230 - 240
Width (m)	110	75
Average slope (°)	53	50
The head scarp in elevation (m)	1,605	1,600
The toe of rupture surface in elevation (m)	1,340	1,340
Height difference (m)	265	260

(3) Due to the longitudinal gradients of the valleys being relatively small with 17.5‰ (≈ 10°) for Chuanjiawo valley and 144‰ (≈ 8°) for Gangoutou valley, respectively. The left stream debris accumulated in the subzone D-IIIa, which was located along the Chunjianwo Valley at elevations ranging from 1,170 m to 1,270 m a.s.l (Fig. 4 - 3a & Fig. 4 - 4d). The right stream debris accumulated in the subzone D-IIIb, which was located along the Gangoutou Valley at elevations ranging from 1,170 m to 1,215 m a.s.l.

(4) After running out a distance of around 763 m and 409 m for left and right stream, respectively, the displaced material converged in the area D-IIIc (see Fig. 4 - 3a & Fig. 4 - 4e) at an elevations ranging from 1,144 m to 1,170 m a.s.l. Finally, with the decrease of mass movement velocity, the landslide came to a stop at the Tangjiayan Valley after traveling about 223 m.

Figure 4 - 4. Characteristics of the Tangjia Valley rock avalanche: (a) the mountain ridge controls the landslide initiation; (b) The upper part of the Chunjianwo valley towards the source area; (c) The upper part of the Gangoutou valley towards the source area; (d) Deposits in the Chunjianwo Valley; (e) The two streams converge into the Tangjia Valley.

4.3. Discrete Element Modeling

4.3.1. Numerical Model

In this distinct element (DE) analysis, the rock mass is simulated as an assembly of particles cemented together using the parallel bond model (Itasca Consulting Group 2014). The parallel bond models, characterized by tensile and shear strength and normal and tangential stiffness have been widely used to study cracking and fragmentation of rock material (Potyondy and Cundall 2004).

The maximum tensile and shear stresses acting on the parallel-bond periphery are calculated from the beam theory to determine whether an interparticle bond breaks, as

$$\bar{\sigma} = \frac{\bar{F}_n}{\bar{A}} + \frac{\left\| \bar{M}_b \right\| \bar{R}}{\bar{I}} \tag{1}$$

$$\bar{\tau} = \frac{\left\| \bar{\mathbf{F}}_{\mathbf{s}} \right\|}{\bar{A}} + \begin{cases} \dfrac{\left| \bar{M}_t \right| \bar{R}}{\bar{J}}, & 3\text{D} \\ 0, & 2\text{D} \end{cases} \tag{2}$$

where $\bar{F}_n$, $\bar{\mathbf{F}}_{\mathbf{s}}$ are normal and shear parallel-bond force, $\bar{M}_t$, $\bar{\mathbf{M}}_{\mathbf{b}}$ denote twisting and bending parallel-bond moments; $\bar{R}$, $\bar{A}$, $\bar{I}$ and $\bar{J}$ are the bond radius the cross-sectional area, moment of inertia of the parallel bond cross-section and the polar moment of inertia of the parallel bond cross section, respectively.

Fig. 4 - 5 shows the numerical model of the rock avalanche, built using PFC^{2D} 5.0 based on the profile map depicted in Figs. 4 - 3b & c. The sliding surface is modeled using wall elements and the sliding body is constructed using 12,000 and 12,056 ball elements with the same particle size distribution for the left and right streams of the avalanche, respectively (Fig. 4 - 5a & 4 - 5b). On the basis of in situ observation in the landslide area (Hu et al. 2013), the adopted minimum disk diameter is 1.0 m and the size ratio $r_{\max} / r_{\min}$ of the rigid particles is taken as 1.66 to prevent a reorganization of the particles within a closed-packed lattice, which otherwise would dramatically alter the behavior of the particle assembly (Potyondy and Cundall 2004; Imre et al. 2010). To gain insights into the kinematics and dynamics of the left stream of the avalanche, four particles are monitored, as shown in Fig. 4 - 5a.

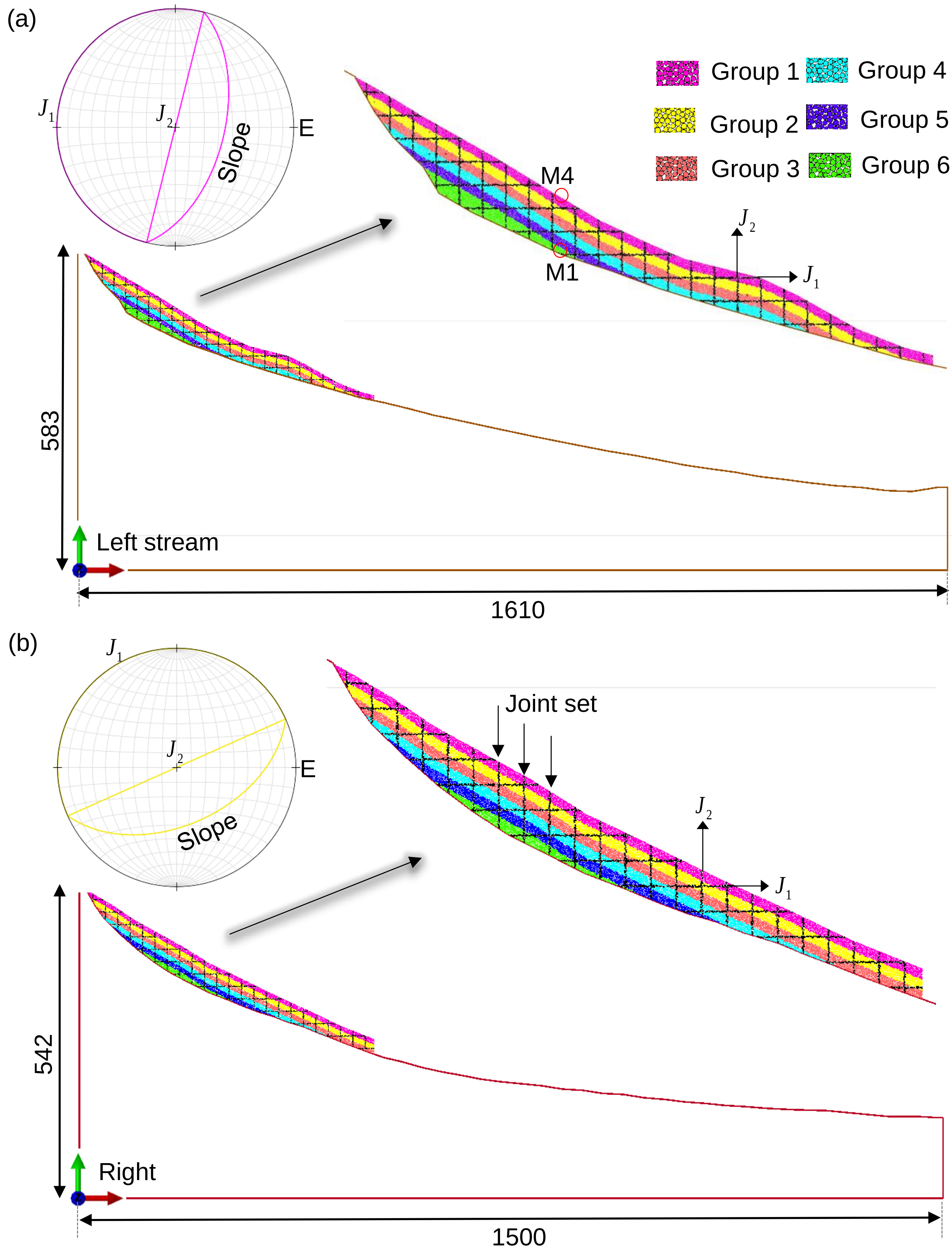

Figure 4 - 5. Two-dimensional discrete element model of the rock avalanche: (a) Left stream; (b) Right stream.

In addition, to better visualize the emplacement process of the landslide, six layers are identified using different colors (see Fig. 4 - 5). It is worth noting that only the left stream of the avalanche is analyzed thoroughly in this study to illustrate the mechanism of the earthquake-induced landslides. The right stream of the rock avalanche is presented, however, for the purpose of comparison and validation.

4.3.2. Physical and Mechanical Parameters

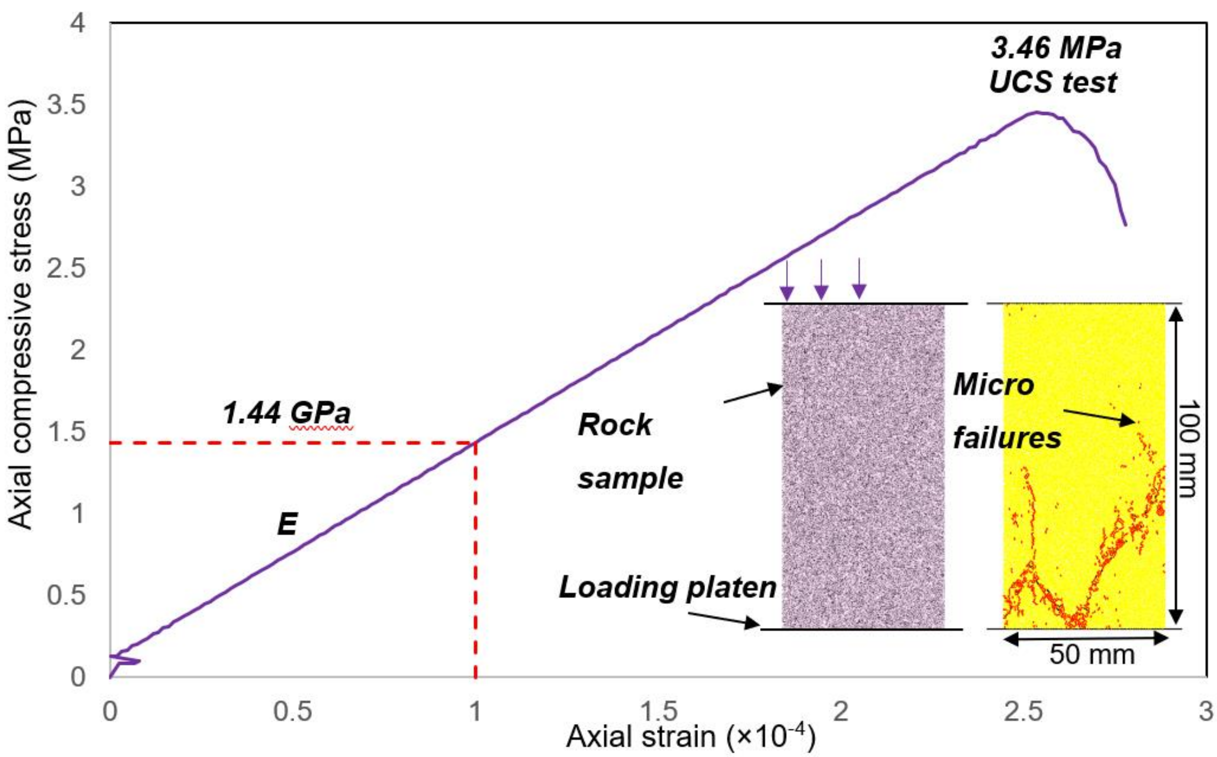

Figure 4 - 6. Modeling the unconfined compression test.

To enable the use of PFC models as a reliable simulation tool, it is necessary to establish reasonable relationship between the numerical parameters and the mechanical characteristics of the problems (Potyondy and Cundall 2004). However, there is no straightforward relationship between macroscopic and microscopic parameters (Calvetti et al. 2000; Tang et al. 2009; Garcia and Bray 2018; Gao and Meguid 2018c). In this study, the micro-parameters needed for the PFC model (Table 4 - 2) are derived from uniaxial compression (Fig. 4 - 6). The unconfined compressive strength of the rock mass (UCS_m) and Poisson ratio (v) are fitted with that of Tangjia Valley rock mass. The UCS_m of the Tangjia Valley rock mass (mainly sandstone) is estimated to be 3.45 MPa, by an empirical relationship $UCS_m = \sqrt{S}UCS_r$ (Hoek and Brown 1997; Hoek et al. 2000), where UCS_r, the unconfined compressive strength of intact sandstone, is 108.9 MPa, according to Chang and Zhang (2007); S is an empirical parameter related to discontinuities in the rock mass that is estimated to be 0.001 according to Hoek et al. (2000).

Table 4 - 2. Micromechanical parameters used for the DE model

Parameter	Assigned value
Particle density	2600
Friction coefficient (ball-ball)	0.4
Friction coefficient (ball-wall)	0.15
Effective contact modulus (GPa)	5
Normal-to-shear stiffness ratio (*kn / ks)*	2.5
Bond effective modulus (GPa)	6
Bond normal-to-shear Stiffness ratio ($\overline{kn}/\overline{ks}$)	2.5
Parallel bond tensile strength (MPa)	3.44
Parallel bond cohesion (MPa)	3.44
Parallel bond friction angle (Degree)	30
Parallel radius multiplier (-)	1.0

4.3.3. Earthquake Loading and Boundary Conditions

After the primary stress field is generated due to gravity, seismic motion is applied at the wall boundary by integrating the corrected accelerations recorded at the Baoxing seismic station during the Lushan earthquake. Seismic shaking duration of 45 s is adopted in this study. Fig. 4 - 7 shows the combined acceleration records used in the analysis. Velocity time histories (Figs. 4 - 7b, d and f) are obtained by integrating the acceleration records (Figs. 4 - 7a, c and e), respectively. The horizontal earthquake waves represent the projection in the main sliding directions (N104°E) and (N156°E) for the left and right streams of the avalanches using the acceleration records in E–W and N–S directions as computed by equations (3) and (4), respectively. The input vertical earthquake velocity (Fig. 4 - 7f) is integrated from the acceleration records in U–D direction, as shown in Fig. 4 - 7e.

$$a_H^{Left} = a_{E-W} \cdot \sin 104° + a_{N-S} \cdot \cos 104° \qquad (3)$$

$$a_H^{Right} = a_{E-W} \cdot \sin 156° + a_{N-S} \cdot \cos 156° \qquad (4)$$

where a_H^{Left} and a_H^{Right} are the horizontal accelerations of the left and right streams, respectively; a_{E-W} and a_{N-S} are the acceleration records in the east-west and north-south directions, respectively. The angles $104°$ and $156°$ represent the main sliding directions for the left and right streams of the avalanches, respectively.

4.3.4. Joint Characteristics

In addition to the discontinuities that are normally considered in estimating rock mass strength, larger discontinuities, such as bedding surfaces and joints, cannot be disregarded when constructing a numerical model (Barla et al. 2012; Zou et al. 2017). In particular, the Tangjia Valley rock slope is heavily jointed according to field investigations. Many of the rock blocks found in the rock avalanche are broken along pre-existing discontinuities, such as bedding surfaces and joint sets. However, it is not practical to reconstruct the exact system of joint sets due to the complicated nature of the discontinuities and unfavourable site conditions at the source area. Therefore, debonding particles along the orthogonal planes (J_1 and J_2) with an average spacing of 20 m are incorporated in the 2D DE model (see Fig. 4 - 5) to approximately simulate the natural joint systems at the site. Additionally, it is worth noting that all joints are assumed to be fully persistent along the orthogonal pattern, so that they can slice the rock block completely.

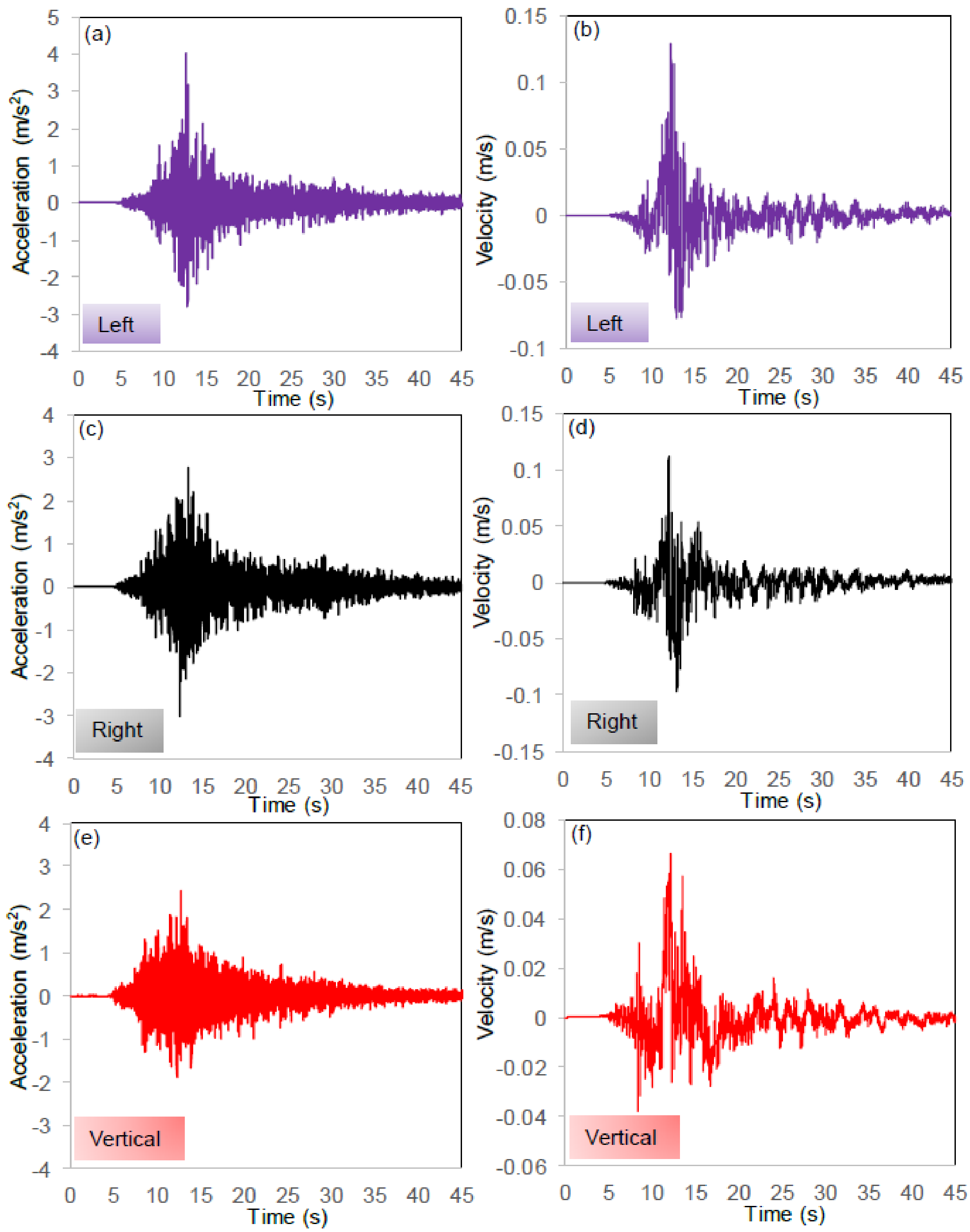

Figure 4 - 7. Seismic time history curves: (a) Horizontal acceleration for the left stream; (b) Horizontal velocity for the left stream; (c) Horizontal acceleration for the right stream; (d) Horizontal velocity for the right stream; (e) Vertical acceleration; (f) Vertical velocity.

4.3.5. Damping

Previous studies reported by Calvetti et al. (2000), Zhou et al. (2016), Lai et al. (2017), Gao and Meguid (2018 a & b), and Zhang and Evans (2019) illustrated that dynamic simulations are sensitive to the presence of damping. Moreover, in a system of particles, energy is mainly dissipated through frictional sliding and viscous damping at particle-particle or particle-wall contacts (Zou et al. 2017). Viscous damping, proportional to the relative velocities of the particles in contact, is employed to replicate the energy dissipated by particle asperities being sheared off and the plastic deformations of the contacting particles. In this study, the viscous normal v_n and shear v_s damping constants of granular particles within the rock mass (particle-particle contacts) are selected to be $v_n = v_s = 0.02$, which are similar to those adopted by Zhao et al. (2017). As stated by McNamara (2013), the high viscous damping at the base could effectively mimic the absorbing boundary condition for the seismic wave transmission and reflection at the slope base, therefore, the normal and shear damping coefficients of the particles along the failure plane (particle-wall contacts) are selected to be 0.21 and 0.02, respectively, as suggested by Feng et al. (2017).

4.4. Simulation Results

4.4.1. Kinematics of the Rock Avalanche

Fig. 4 - 8a shows that the rock avalanche experiences a complex sequence of accelerations and decelerations as the earthquake wave propagates. The average velocity reaches 10 m/s after approximately 15s, and attains a peak value of 15 m/s at t = 30 s. At that time, most of the avalanche material disintegrates and departs from the cliff, as shown in Figs. 4 - 9a & b. Afterward, the rock avalanche gradually decelerates to 10 m/s at t = 45 s, and the subsequent landslide deposition leads to continuous decrease of velocity until it finally become 0 at t = 75 s. The comparison between the rock avalanche at t = 45 s (Fig. 4 - 9c) and the final deposit in Fig. 4 - 9d illustrates that the rock avalanche completes most of its long runout motion during earthquake excitement, which accords well with the field observations (Hu et al. 2013). Therefore, the movement process can be divided into three phases: (i) early acceleration (t < 10 s) with low seismic shaking intensity; (ii) high-speed long-runout with intense seismic shakings (10 s < t < 45 s); (iii) final, low-speed

deposition under gravity only (t > 45 s). The maximum velocities of the rock mass are then used to reveal the agitation in the rock avalanche. The maximum velocities can be found such that $V_{max} = \max(v_i)$, where v_i is the velocity of a granular particle at a certain time, and i ranges from 1 to n; n is the number of the particles in the distinct element model. It is shown that the maximum velocity of the granular system is between 40 – 45 m/s, which is approximately three times higher than the average velocity of the avalanche mass. The average velocity of the rock avalanche gradually declines after t = 30 s, while the maximum velocity of the flowing mass remains high up to t = 60 s. This observation indicates that despite the fact that the partial deposition with a decrease in seismic shaking intensity results in a drop in the average velocity, some of the far-traveled particles continue to travel at high-speed under gravity accompanied by the ongoing disintegration and fragmentation processes. The analyses of both the average and the maximum velocity of the granular system can be used as a complementary way to quantify the intensity of the rock mass movement in the perspective of time and location.

Fig. 4 - 8b shows that particles originating at a given vertical section of the avalanche body have similar velocity trends, indicating that they follow similar acceleration and deceleration patterns; however, the velocities decrease gradually from the top to the bottom of the slide. During the first 10 s, the velocities of the monitored particles are almost the same, which indicates that the avalanche mass is moving as one unit. The velocities then increase at a distinct rate, with maximum velocities appearing at 20–40 s. Subsequently, the speeds gradually decrease, with the avalanche gradually starting to deposit after the end of the seismic loading at time of 45 s. Though rock blocks from the upper layers of the avalanche experience more runout distance and higher velocities than those that originated in the lower layer, the trajectories of the monitoring points show that their relative vertical positions are maintained during the landslide propagation and deposition (see Fig. 4 - 8c), indicating strata are well preserved in their original order within the debris. This can be verified by the granular dynamic evolution, shown in Fig. 4 - 9(a-d), in which the colored layers are preserved in their original order. This phenomenon of stratigraphy preservation has also been reported in some well-documented numerical and field investigations (Campbell et al. 1995; Chang and Taboada 1999; Zhao and Crosta 2018).

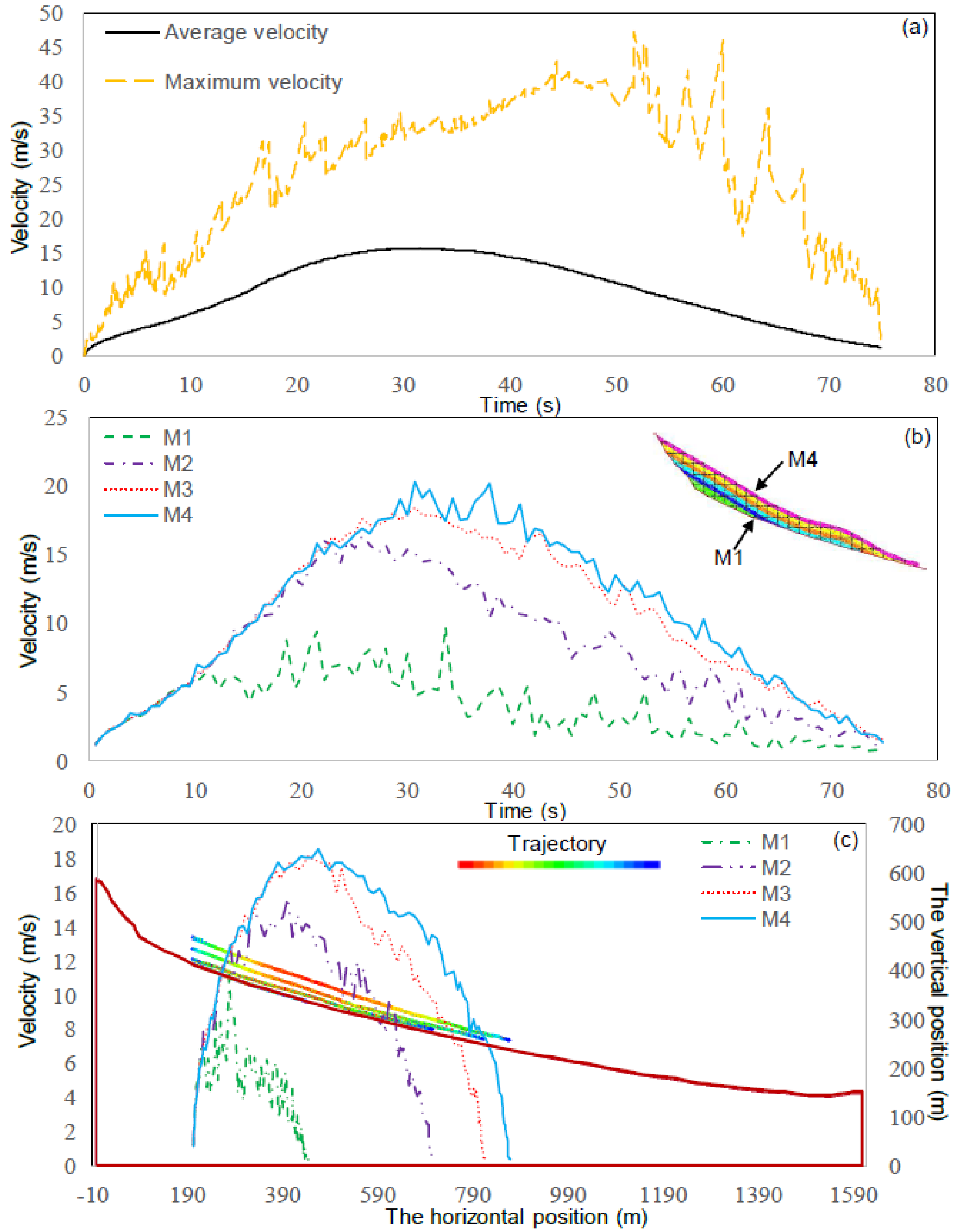

Figure 4 - 8. (a) Maximum and average velocities of the mass during motion; (b) Velocities of the monitoring points along a vertical section with the time; (c) Velocity trajectories of the monitoring particles along a vertical section.

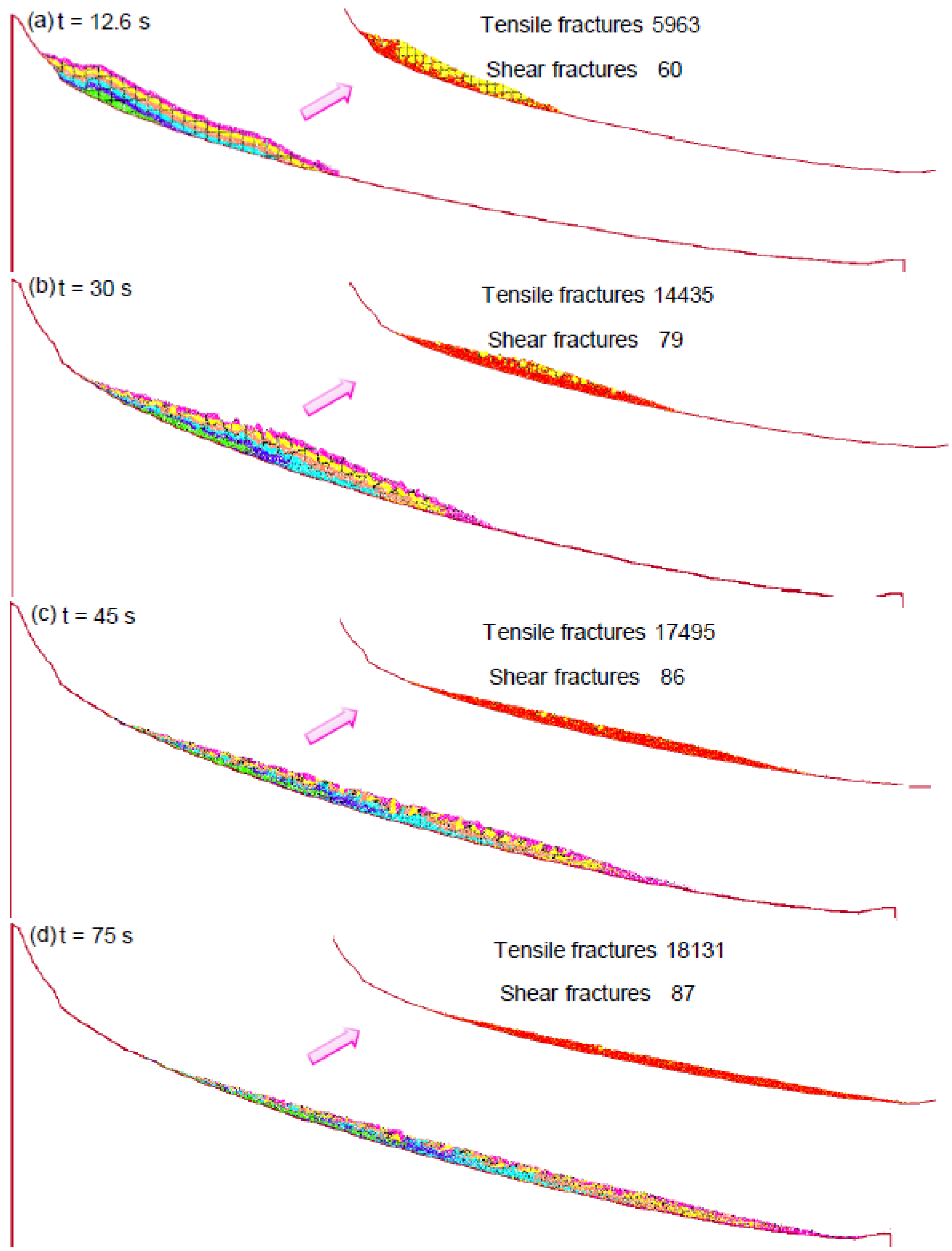

Figure 4 - 9. Evolution of the landslide process at different time stamps.

The evolving motion of the rock avalanche is presented in Fig. 4 - 9(a-d). At the early stage (Fig. 4 - 9a), the seismic velocities in the two directions reaches their peak values. Meanwhile, failure starts at several closely spaced points and multiple cracks grow simultaneously relaxing the tensile stresses within the tail region of the avalanche due to the downward pulling forces exerted by the lower avalanche mass. Between 12.6 s to 30 s, the intense shakings result in high shear stresses at the base. Consequently, cracks develop and grow to coalescence from both the front and tail regions towards the middle of the moving rocks (Fig. 4 - 9b). This facilitates fragmentation and pulverization of the solid rocks within the middle region. The entire avalanche body, then, accelerates and runs down the valley (Fig. 4 - 9c). Finally, the rock avalanche decelerates and settles gradually (Fig. 4 - 9d). The displaced material travels a horizontal runout distance of about 1,560 m with a descent of approximately 447 m. This corresponds to a Fahrböschung of 16°, which is slightly smaller than the 16.7°reported by Li et al. (2017).

4.4.2. Stress evolution and Solid Concentration

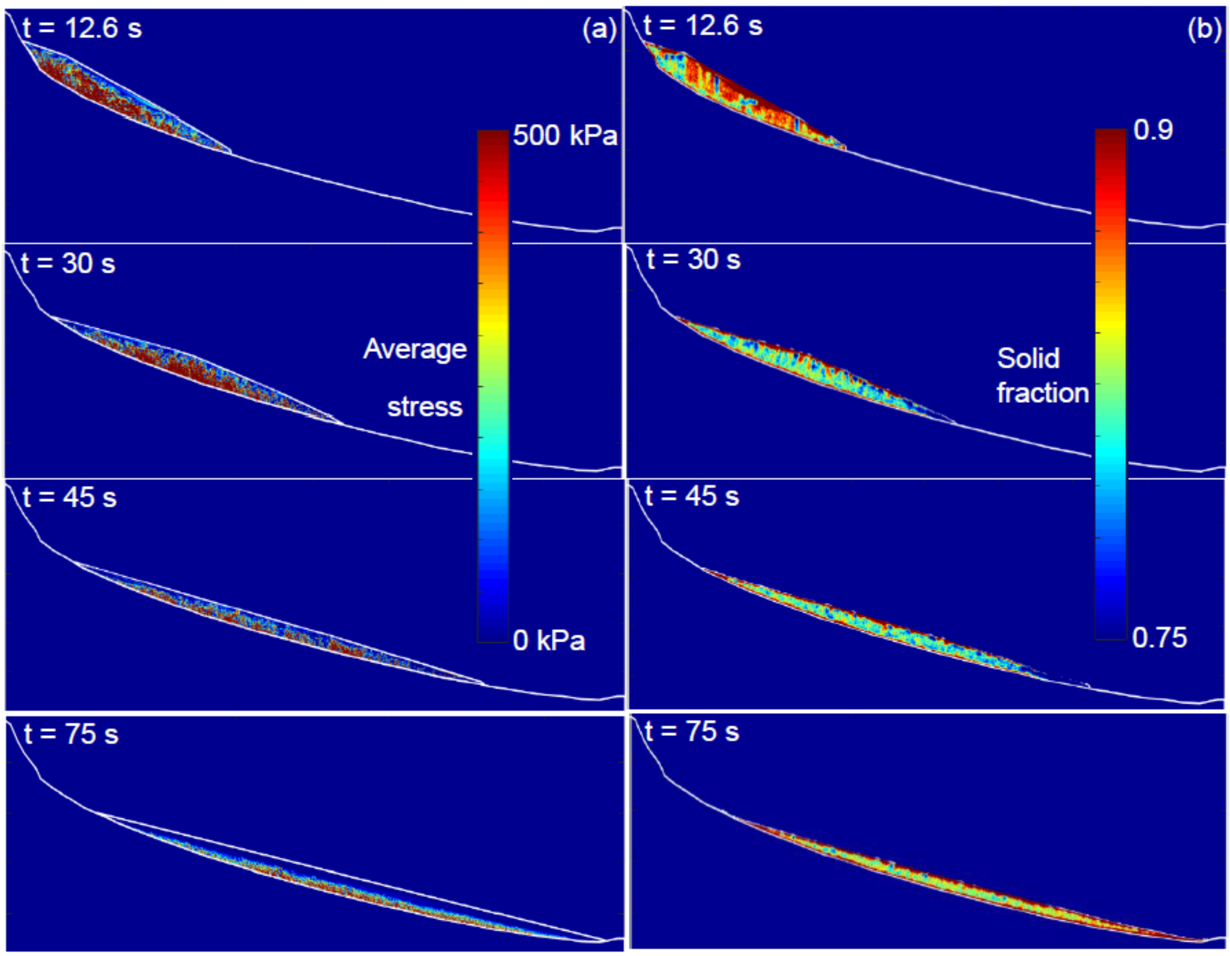

Figure 4 - 10. Evolution of the interpolated (a) average stress and (b) solid concentration fields within the avalanche at different time stamps.

In order to gain further insights into the dynamic process of rock mass movement, the stress and the solid fraction fields inside the avalanche are computed using the spatial interpolation techniques, which has been applied by Mollon et al. (2012) to analyze the collective behavior of granular flows in a planar slope. The average stress evolution, as demonstrated in Fig. 4 - 10a correlates well with the progression of the fracturing. The stress concentration begins at the basal region of the granular mass. The increase of these stresses may facilitate the fracture and block fragmentation of the slope mass. The cracks are initiated at the joint tips, propagated and cut through the rock bridges. The coalescence of cracks in the basal region (see Fig. 4 - 9b) results in higher stresses (see Fig. 4 - 10a), promoting the development of fragmented fine-grained basal shearing layers during avalanche emplacement. As the cracks propagate to the surface, cluster and coalesce in the main body with the avalanche transiting into the deposition phase, the major part of the avalanche body has been severely disintegrated as shown in Fig. 4 - 9b&c and only some coarse-grained blocks are embedded in a fine-grained matrix. In addition, it is worth noting the low stresses at the top of the slope help to preserve the angular surface or fractured coarse blocks, often found in large avalanche deposits.

As stated by Mollon et al. (2012), the solid fraction can provide a good qualitative assessment of the kinematics and dynamics inside the flow. First, a representative volume is defined for the particles in the area that needs to be investigated. This representative volume is defined by the non-convex envelope of neighboring particles, n_v. The solid fraction is then defined in terms of the total representative volume V_{tot} within the non-convex envelop, and the volume V_m of granular material inside the V_{tot}. To account for the fact that increase of the number of particles inside the representative volume can reduce the inaccuracy, the n_v is chosen to be 50 in this study. The solid fraction is then calculated using:

$$s = \frac{V_m}{V_{tot}} \qquad (5)$$

The solid fraction pattern in the sliding mass (Fig. 4 - 10b) is spatially synchronized with the fracturing initiation, propagation, and coalescence (Fig. 4 - 9), and the areas of low solid fraction accord well with the ones experiencing substantial amount of disintegration. In addition, the distribution of solid fraction in the avalanche can be a dynamic indicator for the fragmented flow, i.e., first, the rock blocks are tightly connected by the bonds, forming a high solid concentration. Then, as the ground shaking intensity increases, bond breakages accumulate gradually to form a connected fragmented granular layer beneath the translating slope mass (see Fig. 4 - 9). This may lead to the more pronounced low solid fraction as the avalanche develops, promoting the subsequent landslide propagation (see Fig. 4 - 10b). Concurrently, the front head of the granular body is also observed to possess the lowest solid concentration, which infers that an increasing number of solid particles within this region become dilute and easily jump away from the main body as shown in Fig. 4 - 10b (at time t = 30 s and t = 45 s). Finally, as the fragmented flow accumulates and deposits (t = 75 s), the granular body transits to possess a high solid fraction. This can be explained by the fact that the distribution of the solid fraction in the avalanche corresponds well with the dilation and compaction. The dilation is found to start at the base of the avalanche, and propagates through the entire mass as the avalanche develops. After cracking, fracturing and deforming under the action of gravity and seismic forces, the bonded granular system is disintegrated into be clast and fine-grained matrix. This process results in continuous rearrangement and re-compaction as the avalanche loses momentum and particles are progressively deposited in the run-out area.

4.4.3. Energy Regime and Rock Damage

Evaluation of the energy regime of the rock avalanche is helpful for the understanding of the mechanism of rock fragmentation, and kinetic characteristics of rock fragments. Following Utili et al. (2015), Zhao et al. (2017), the potential energy of the rock mass, E_p, is defined with respect to a reference point, in this analysis, the reference point is the origin as shown in Fig. 4 - 5.

$$E_P = \sum_{i=1}^{N} m_i g h_i \tag{6}$$

where N is the total number of particles in the sliding body, m_i and h_i being the mass and height of each particle in the body. It is worthwhile to note, the E_P is also the total energy of the granular system in the sliding body, E_0, before downward movement.

The energy input due to earthquake waves acting on the boundaries is represented by

$$E_w^j = E_w^{j-1} + \sum_{i=1}^{N} F_w \Delta U_w \tag{7}$$

where E_w^j and E_w^{j-1} are the total accumulated work done by all walls on the assembly at the current and previous time steps; F_w is resultant force acting on the wall; ΔU_w is the applied displacement occurring during the current time step.

From the law of conservation of energy, the energy balance equation is typically as follows

$$E_0 + E_w(t) = E_p(t) + E_{strain}(t) + \bar{E}_{bstrain}(t) + E_k(t) + E_f(t) + E_\mu(t) + E_\beta(t) \qquad (8)$$

As shown in Fig. 4 - 11, before the earthquake wave propagates, the system has only potential energy and no energy is dissipated. As the flow develops, different types of energies (potential energy, kinetic energy, elastic energy, and dissipated energy) inside the granular mass evolve. When the avalanche develops with the combined effect of gravity and seismic forces, the potential energy decreases and the kinetic energy increases due to particle movements. The sum of the kinetic and potential energies during the avalanche is not equal to the total energy E_0 owing to energy dissipation. Causes of energy dissipation are related to base friction, granular mass contact friction and inelastic collisions. Detailed calculations of elastic strain (E_{strain}) and bond strain energies ($\bar{E}_{bstrain}$), kinetic energy (E_k), cumulative energy dissipated by friction (E_μ) and viscous damping (E_β) can be found in the documentation of Itasca Consulting Group (2014).

At the initial acceleration stage, the energy dissipation rate is found to be low. Afterward, in the high-speed runout phase, dynamic collisions among the fragments are intensified, which results in a sharp increase in the rate of energy dissipation before the fragmented flow transits to the low-speed deposition phase characterized by the gradual decreasing rate in energy dissipation. Ultimately, all the total energy E_0 is dissipated by friction (56.1 %) and by collisions (43.9 %). It is worth noting although energy dissipation by breaking bonds is less significant in deposition stage, particle breakage still plays a major role in the dissipation process as it creates additional degrees of freedom for the inter-particle motion, which in turns facilitates friction dissipation. Similar conclusions have been reached by Bolton et al. (2008) and Ma et al. (2016) for breakable granular materials. Low fragmentation energy input in disintegrating the rock mass has been documented by Locat et al. (2006), Crosta et al. (2007), and Zhao et al. (2017).

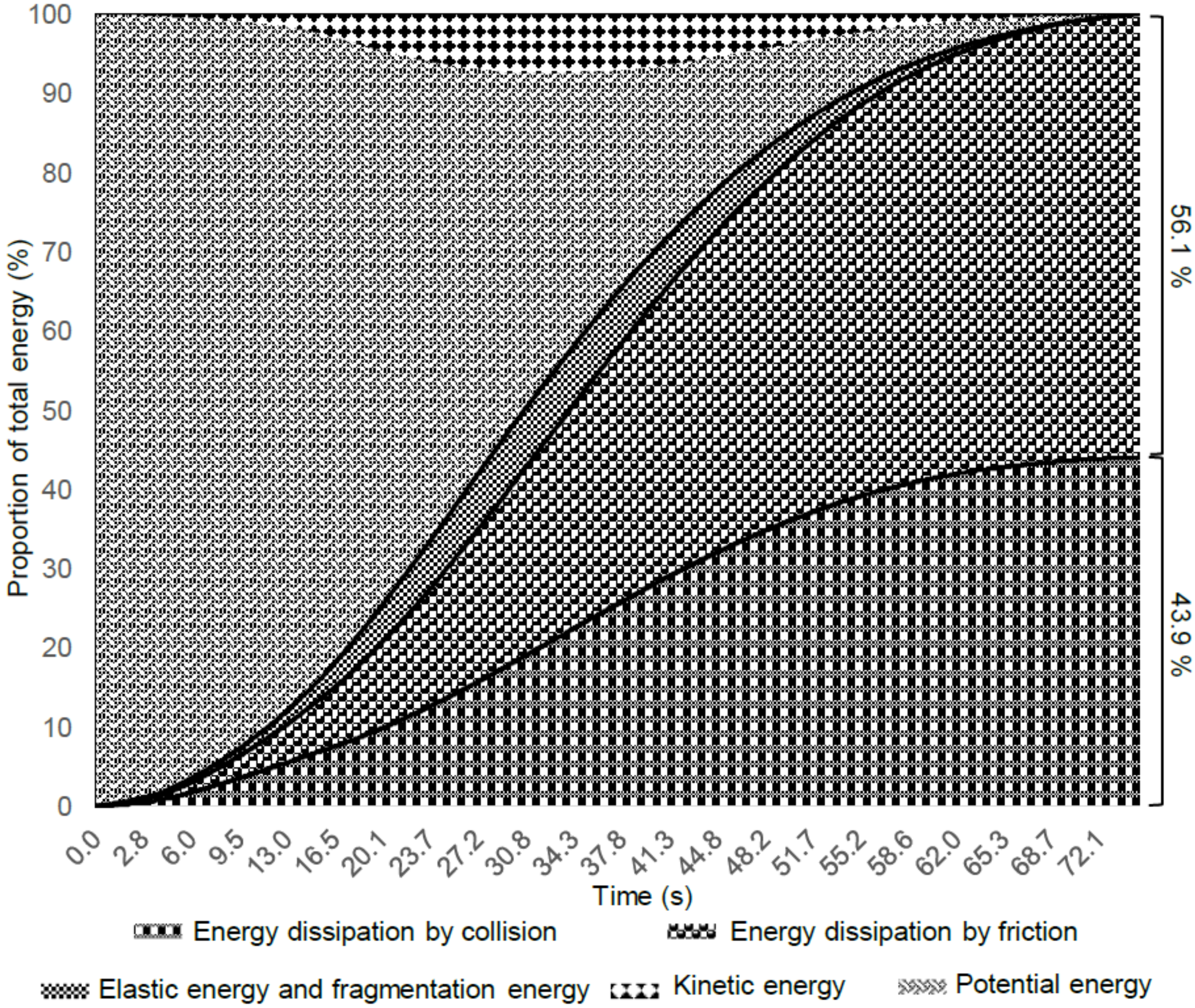

Figure 4 - 11. Energy transfers resulting from the analysis of the rock avalanche.

In the analyses, the damage ratio (D) (Thornton et al. 1996) has been used to quantify rock fragmentation intensity, which is defined as the ratio of the number of broken bonds under the combined effect of gravity and seismic forces to the total number of bonds at initial static state. According to Fig. 4 - 12a, it can be seen that the damage ratio increases rapidly characterized by the rapid cumulation of energy released by all bond breakages as the avalanche enters the phase of high-speed runout phase. The subsequent sliding and collision of fragments in the low-speed deposition phase leads to an additional 3% of bond breakage. From the point of view of fragmentation energy, for the entire landsliding process, micro-tension failure occurs at a higher rate in comparison to micro-shear failure and plays a dominant role in the initiation of slope instability. Results show that the dissipated energy by fragmentation follows a linearly increasing trend similar to that of the damage ratio (Fig. 4 - 12b).

The degree of fragmentation shown in F_D, provides a measure for the damage that the material has experienced (Haug et al. 2016).

$$F_D = \frac{M}{m_{\max}} \tag{9}$$

where M is the mass of the sample, and $m_{\max}$ is the mass of the largest fragment.

A value of F_D = 1 reflects a completely intact sample, while an increasingly value reflects an increasingly fragmented avalanche mass. In this study, F_D started from a value higher than 1, because the existence of joint sets that influence the integrity of the avalanche body. Fig. 4 - 12c shows how the degree of fragmentation (F_D) is related to damage ratio (D) for the rock avalanche. According to the plots, it is apparent that the degree of fragmentation (F_D) is rarely found to undergo a significant increase in rate until the damage ratio (D) reaches 0.2. Then it starts an immediate increase before the damage ratio (D) increases to 0.7, following a sharp increase to peak value when the damage ratio (D) reaches 0.74. It indicates the development of rock damage induces a large amount of fractures within the rock avalanche. Consequently, fractures can nucleate and grow to completion quickly, leading to relatively small fragments, and the corresponding degree of fragmentation (F_D) rises immediately to a high value. As presented in Fig. 4 - 12d, it is interesting to note that the evolution of fragment number follows a similar trend to that of the landslide overall velocity (see Fig. 4 - 8a). This phenomenon is expected as the landslide initiation and propagation promote the disintegration of the jointed rock mass within the slope with an obvious increase of medium and large fragments. Subsequently, continuous rapid dynamic avalanching motion in response to the increased seismic intensity may work to disaggregate the entire avalanche, which leads to the coarse fragments being completely broken to fine-grained particles, inducing a continuous decrease in fragment number. In addition, these fine-grained particles play an important role in the absorption of a large portion of the kinetic energy of incoming fragments. Thus, the presence of shattered and disaggregated clasts with relatively larger size can be preserved from the collision and freefall motions during the landslide propagation and deposition as shown in Figs. 4 - 15c & d.

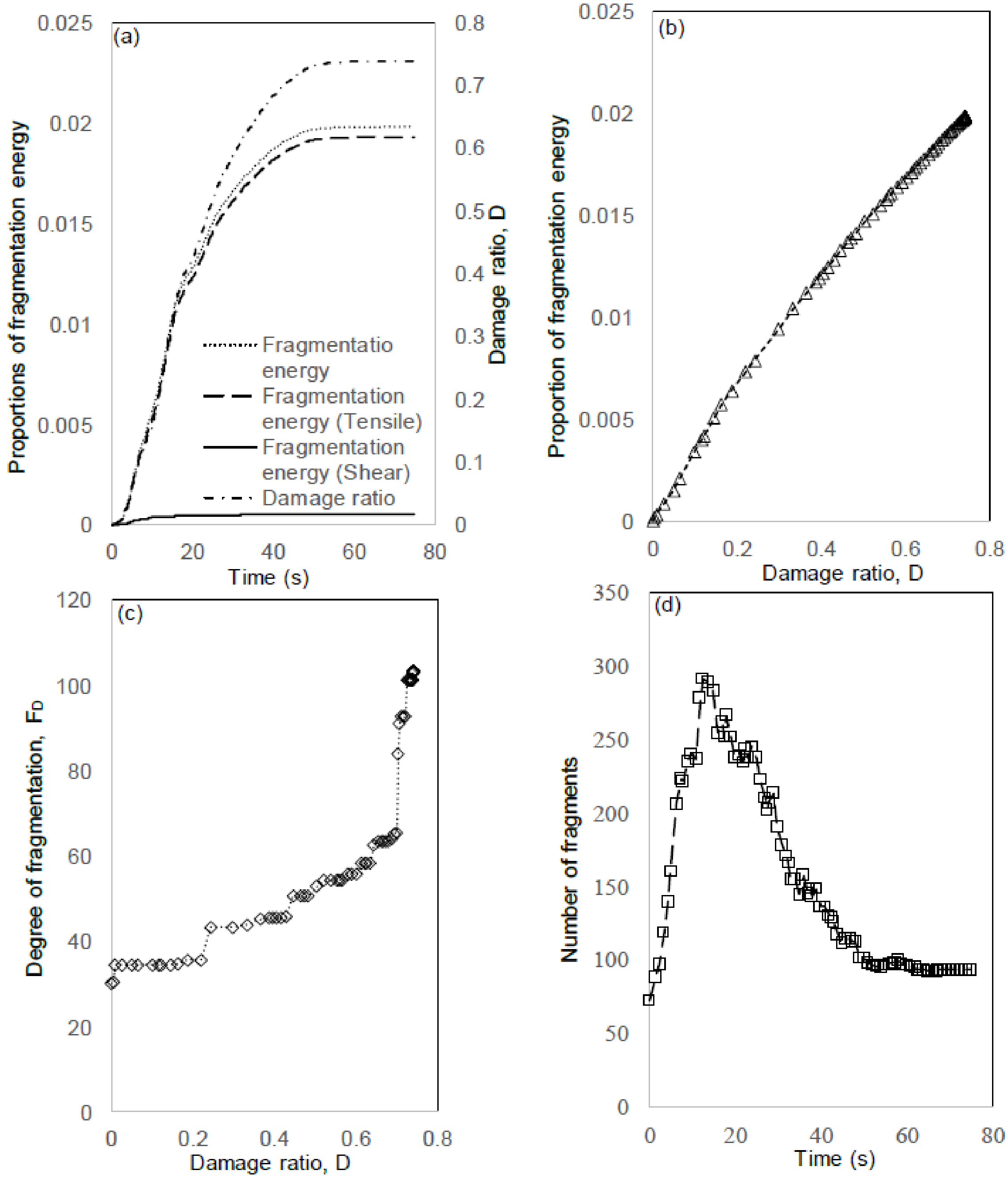

Figure 4 - 12. (a) Changes in fragmentation energy with the time; (b) Fragmentation energy versus damage ratio; (c) Degree of fragmentation versus damage ratio; (d) Number of fragments evolution.

4.4.4. Lubrication Mechanism and Friction Reduction

As stated by Campbell (1989) and Cleary and Campbell (1993), for the completely fragmented granular system, particles at the base are intensely agitated with frequent collisions and could act as a lubricating layer to reduce the overall effective friction of the fragmenting grain flow. The intensity of particle agitation can be quantified by the vibrational and rotational granular temperatures (Campbell 2006) and defined as:

$$v_x^i(t)' = v_x^i(t) - \overline{v_x^i(t)} \quad (10)$$

$$v_y^i(t)' = v_y^i(t) - \overline{v_y^i(t)} \quad (11)$$

$$\omega^i(t)' = \omega^i(t) - \overline{\omega^i(t)} \quad (12)$$

where translational velocity components $v_x^i(t)$, $v_y^i(t)$ and angular velocity component $\omega^i(t)$ of the selected i-th particle in the selected spherical region Ω_i can be divided into the mean velocity components $\overline{v_x^i(t)}$, $\overline{v_y^i(t)}$, and $\overline{\omega^i(t)}$ and fluctuating parts $v_x^i(t)'$, $v_y^i(t)'$, and $\omega^i(t)'$.

The mean velocity components $\overline{v_x^i(t)}$, $\overline{v_y^i(t)}$, and $\overline{\omega^i(t)}$ can be attained by averaging the velocities of particles surrounding the selected i-th particle in the selected spherical region Ω_i:

$$\overline{v_x^i(t)} = \frac{1}{n}\sum_{j=1}^{n} v_x^j(t) \quad (13)$$

$$\overline{v_y^i(t)} = \frac{1}{n}\sum_{j=1}^{n} v_y^j(t) \quad (14)$$

$$\overline{\omega^i(t)} = \frac{1}{n}\sum_{j=1}^{n} \omega^j(t) \quad (15)$$

$$(x_j - x_i)^2 + (y_j - y_i)^2 \le r^2 \quad (16)$$

where r is the radius of the selected spherical region Ω_i. In this study, the neighborhood size $2r$ is set to $5\,d_{50}$ according to the Zhou et al. (2016).

Hence, the vibrational $T_V^i(t)$ and rotational $T_R^i(t)$ granular temperatures representing the intensity of particle exchange analogous to a thermodynamic temperature are calculated from the velocity fluctuations are expressed below:

$$T_V^i(t) = \frac{1}{2}[(v_x^i(t)')^2 + (v_y^i(t)')^2] \tag{17}$$

$$T_R^i(t) = (\omega^i(t)')^2 \tag{18}$$

The distributions of $T_V^i(t)$ and $T_R^i(t)$ are presented in Fig. 4 - 13 and Fig. 4 - 14, respectively and demonstrate that a layer of agitated particles does exist at the slope base during the emplacement of rock avalanche, which can effectively reduce the landslide friction with increased mobility. It indicates that during landslide propagation, extensive fluctuations of vibrational and rotational granular temperatures are activated in the basal layer where the intense shearing promotes particle rearrangement characterized by vigorous particle agitations (see t = 30 s in Figs. 4 - 13 & 14). This observation agrees well with numerical results of Zhao and Crosta (2018), who calculated the evolution of granular temperature of an estimated 25 m thickness of granular basal layer and demonstrated that the generated particle vibrations are responsible for the apparent reduction of friction in long runout landslides, though they did not show how the granular temperatures exactly distributed within the slope mass. It is worth noting that the lack of obvious enhancement of granular temperatures and fluctuations around the coarse fragments reflects that continuous fragmentation produces a thick layer of dispersed grains near the bottom which can to some extent lubricate the landsliding motion but also significantly consumes a large portion of energy of the incoming large rock fragments. This indicates that the large boulders at the surface were passively carried by the finer material below during movement.

The above observations match some of the well-documented field data of long-runout landslides reported in Dufresne et al. (2010) and Zhang et al. (2019). In addition, a low solid density area can be observed at the basal shearing layer (see Fig. 4 - 10b), which further demonstrates that because of frequent intensive collisions, the overburden acting on the shearing layer can be counteracted.

Therefore, the enhanced granular temperatures allow for the occurrence of dilation in the basal facies characterized by the sparse solid fraction and the increased mobility, which is consistent with the observations that the entire granular flow is levitated above the vibrating base by a layer of highly energetic particles (Lim 2010; Zhou and Sun 2013). After the cessation of seismic shakings, the landslide propagates to the low-speed deposition phase, therefore the entire granular body exhibits a gradually attenuating fluctuation intensity (see t = 75 s in Figs. 4 - 13 & 14). This phenomenon accords well with the statement that the granular temperature can dissipate or vanish rapidly due to interparticle collisions when external energy stops (Campbell 1990).

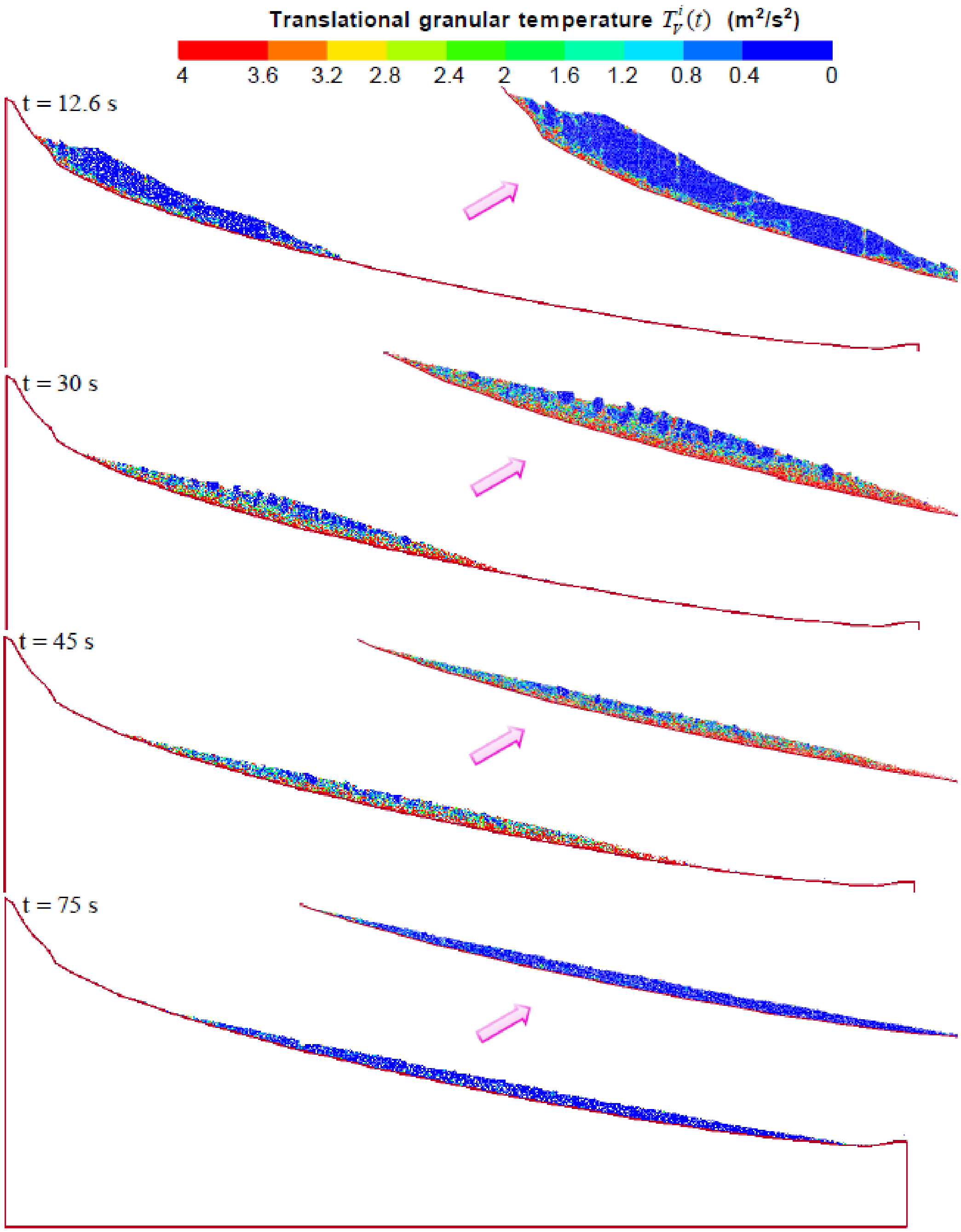

Figure 4 - 13. The distribution of translational granular temperatures $T_V^i(t)$ at different time stamps.

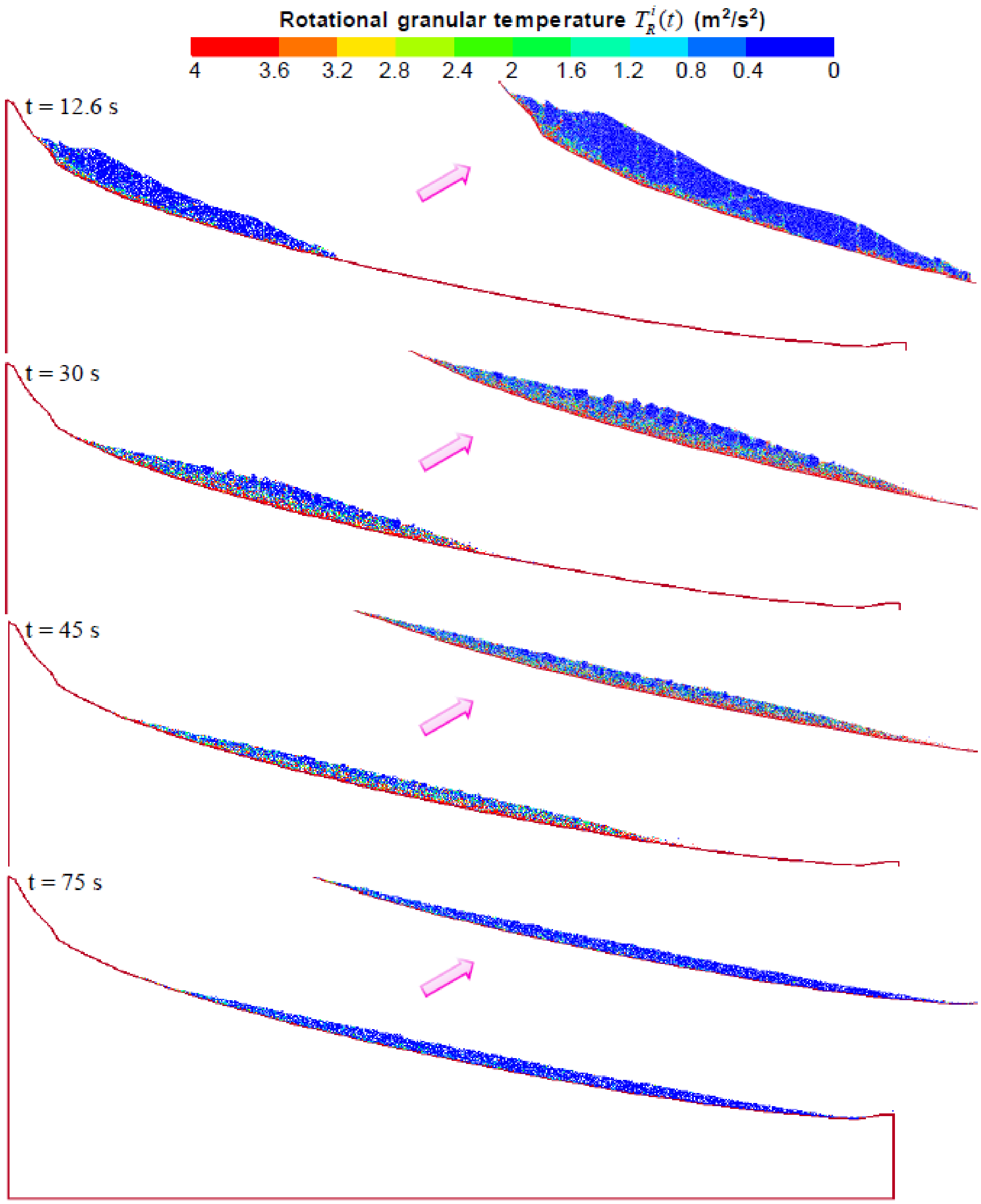

Figure 4 - 14. The distribution of rotational granular temperatures $T_R^i(t)$ within the avalanche at different time stamps.

4.4.5. Fragmentation and Fragment Distribution

Numerical simulations of the fragmentation process during the rock avalanche are shown in Fig. 4 - 15 (the hue scale in the figure is logarithmic). As the ground shaking accelerates, bond breakages accumulate gradually such that the fracture network separates the sliding body into a large number of fragments of comparable sizes (see Fig. 4 - 15 at t = 12.6 s). Then, as the intense seismic shakings proceed, the subsequent landslide propagation and deposition cause more damages to the slope mass leading to intensive cracking, especially near the front and rear regions, reflected by the continuous enlargement of fine-grained materials, shown in Fig 4 - 15b and Fig. 4 - 15c. The final low-speed deposition phase (see Fig. 4 - 15d) shows that the major part of the slope mass has been intensely disaggregated and large boulder content is more abundant in the middle areas, while the fine grains are predominant in distal locations. The distribution pattern of large rock blocks in the final deposits agree well with the field observations (Hu et al. 2013) that the middle region contains many larger boulders and blocks. In addition, it is worth noting that the difference of fragmentation between Fig. 4 - 15c and Fig 4 - 15d is not significant; this can be explained by the fact that accumulation of fine-grained particles reduces the collision rate between the coarser fragments and partially inhibits the disintegration of the debris in the avalanche (Perinotto et al. 2015).

To obtain the fragment size distribution, the characteristic fragment size is defined as

$$d = \sqrt{V_f / V_0} \tag{19}$$

where V_f is the volume of a fragment (calculated as the total volume of particles in the fragment), and V_0 is the volume of the rock mass within the source area at initial static state.

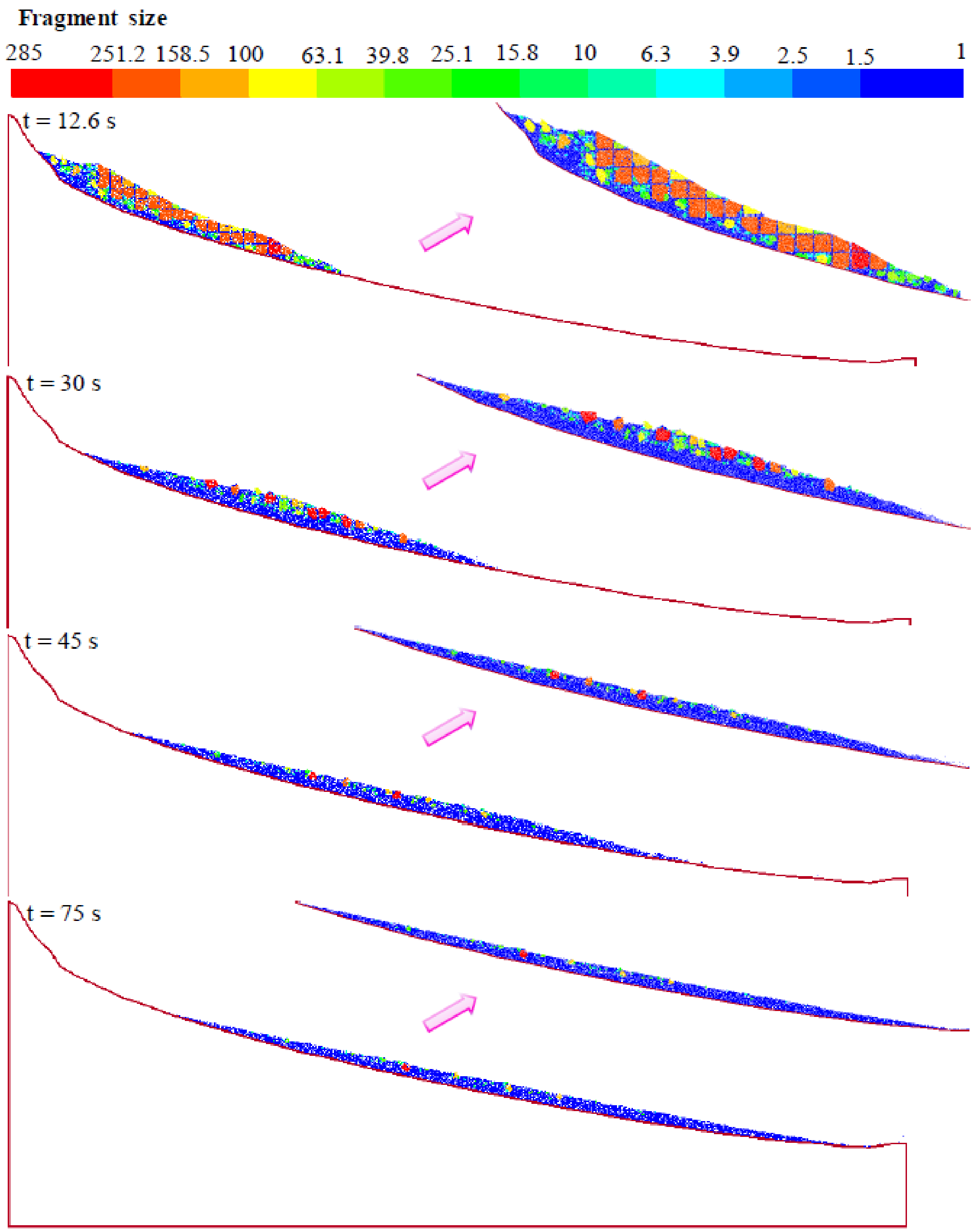

Figure 4 - 15. Changes in fragment size at different time stamps.

The cumulative distribution of fragmented rock mass can be fitted using a two parameter Weibull equation. This distribution, which is equivalent to the Rosin-Rammler distribution (Rosin and Rammler 1933), has been successfully used in characterizing the fragment size of spherical solid grains (Ma et al. 2018) and rock grains (McSaveney 2002; Ma et al. 2017; Shen et al. 2017). The two-parameter Weibull distribution can be expressed as

$$P = 1 - \exp\left[-(\frac{d}{d_c})^{\nu} \right] \tag{20}$$

where d_c and ν are fitting parameters. ν indicates the width of the distribution, and larger values of ν correspond to narrower distributions.

Fig. 4 - 16a shows the volume-based cumulative fragment size distributions and the corresponding fitting curves of fragmented rock mass at progressive earthquake loading times. It can be seen that the two-parameter Weibull equation provides a good description of the simulated fragment size distribution. As noted earlier, d_c can be used as an index to quantify the content of fines in the fragmenting system (Ma et al. 2017). Therefore, a low d_c value is expected if the fragmenting system consists of a high level of fines. The parameter ν is a measure of the spread of the fragment size distribution, where the distribution is narrower for a larger value of ν. For fragment size distributions weighted by fragment mass (Fig. 4 - 16a), the parameter d_c decreases with landslide propagation (see Fig. 4 - 9). It reflects that fragment size reduction obviously takes place in the course of downslope movement. It is consistent with observations that the fragmented debris in the landslide deposits is consecutively reduced in grain size along the transport path, which has been reported in some well-documented numerical and field studies (Langlois et al. 2015; Perinotto et al. 2016; Zhang et al. 2016 & 2019). The parameter ν generally increases indicating a narrower fragment size distribution is generated, except at the time of 30 s then decreases from 1.809 to 1.5, resulting in a wider span of fragment regime (Fig. 4 - 16a). This exception occurs mainly due to the transition (Fig. 4 - 16a) from the phase of early acceleration (t < 10 s) to the phase of low-speed deposition (t > 45 s). This can be explained by the fact that early stages of emplacement contribute the most to the rock mass break-up. Relatively minor fragmentation occurs in the weak solid structures resulting in particle size distribution that spans a narrower range around the relatively large particles. Subsequently, the ground shaking intensity increases, leading

to the propagation of cracks along the joint sets and the separation of fragments. When the low-speed deposition phase is reached, the majority of the slope mass is fragmented into fine-grained particles which causes the size distribution to be dominated by relatively small grain sizes. It is found that, at all examined time stamps, the middle part of the fragment size distribution is almost linear within the range of 0.015 to 0.05. Also, the distributions fluctuate at 12.6 s indicating the presence of large unbroken pieces, which can be corroborated by the sedimentary fabric within the deposit as shown in Fig. 4 - 15 at t = 12.6 s.

The fragments produced by weathering, abrasion, impact and geological loading often satisfy a fractal condition over a wide range of scales (Turcotte 1986). Therefore, it is necessary to examine the fractal characteristics during the entire transport phase of the avalanche (see Fig. 4 - 16b).

A fractal character can be described by the power-law relationship between the number and size, as follows

$$N = Cd^{-D} \tag{21}$$

where N is the number of fragments with a characteristic linear dimension larger than d , D is a proportional constant and D is the fractal dimension. Then, the absolute value of D (the slope of the best-fit line on a log-log scale) is equivalent to the fractal dimension of the particle size distribution (Turcotte 1986). The higher the value of D , the more graded the particle size distribution and the larger the number of fine particles (Crosta et al. 2007).

Fig. 4 - 16b illustrates that with landslide propagation and deposition, more and more fines are produced, reflected by an increase in the value of fractal dimension, D . The larger the value of the fractal dimension, the wider the range of particle size. In addition, the fractal dimension, D of a particle size distribution increases sharply (up to 30s) then slows down significantly with increased duration of movement, which infers that the fragmentation energy during the rapid runout movement is quite high (see Fig. 4 - 12a) before reaching the low-speed deposition phase. This is in agreement with previous field and experimental observations (Crosta et al. 2007), which concluded that fractal dimension initially increases sharply before slowing down with the range of duration for rock avalanches. It is worth noting that power law prevails in the range of small to intermediate size regimes of all the distributions, and a more complete fitting is observed when the landslide has not experienced an intense fragmentation process, as illustrated in Fig. 4 - 16b.

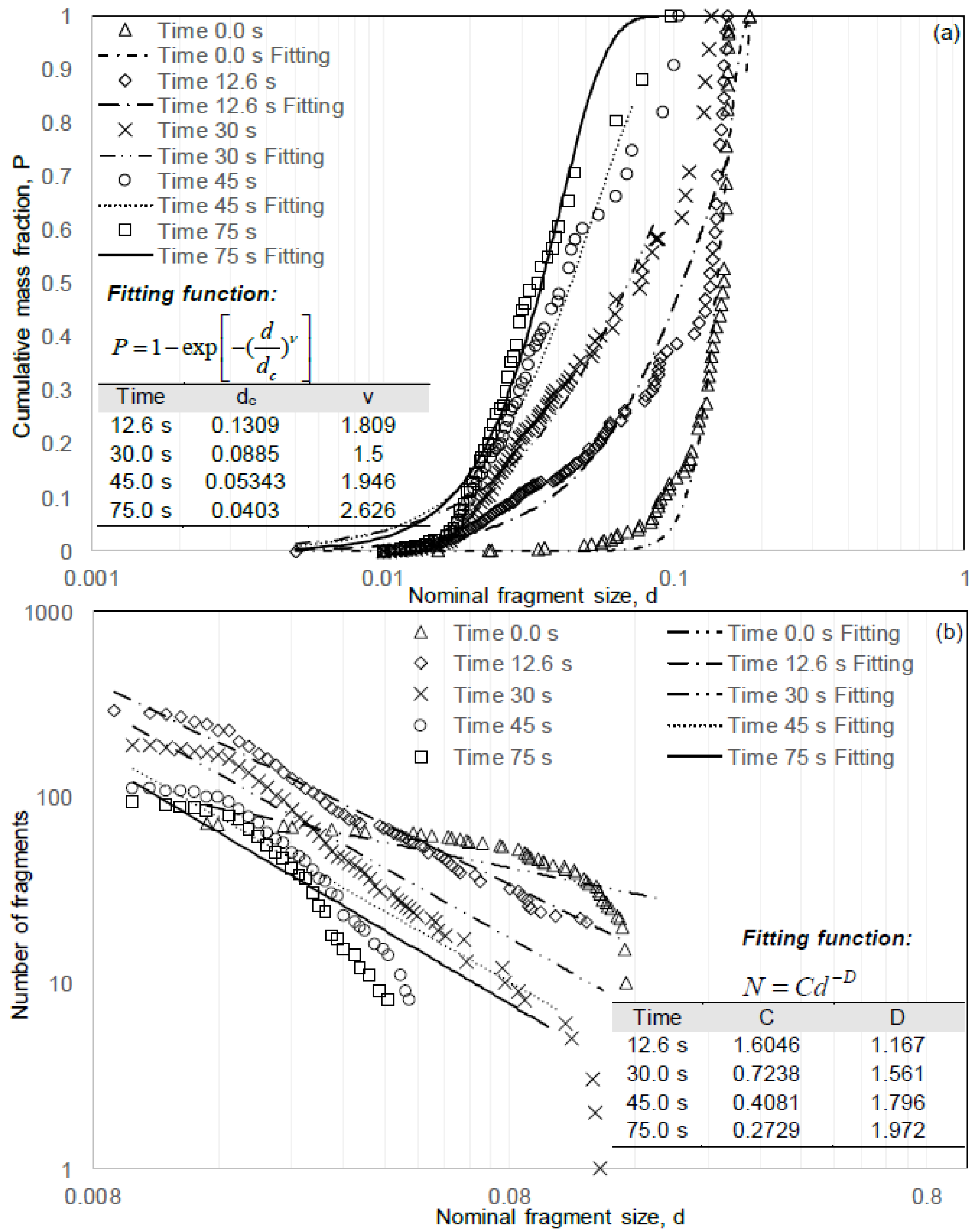

Figure 4 - 16. (a) Relationship between cumulative mass fractions and fragment sizes for increasing loading time; (b) Fractal distributions of fragment sizes for increasing loading time.

It is apparent that fractal characteristics significantly change with respect to rock avalanche dynamics. During the emplacement process, fractal dimension changes and particle assemblages will either be destroyed or preserved, as illustrated in Fig. 4 - 4c and confirmed by the numerical results in Fig. 4 - 15. This is also consistent with the field observations reported by Pollet and

Schneider (2004), Crosta et al. (2007), Pedrazzini et al. (2013), Perinotto et al. (2015), Wang et al. (2018). At the investigated time stamps, the intermediate fractal dimension is almost linear within nominal size that range from 0.009 to 0.03, which is justified well with the observations of the fragment size distributions weighted by fragment mass. This linearity indicates that the distribution of the fragment sizes has a fractal structure.

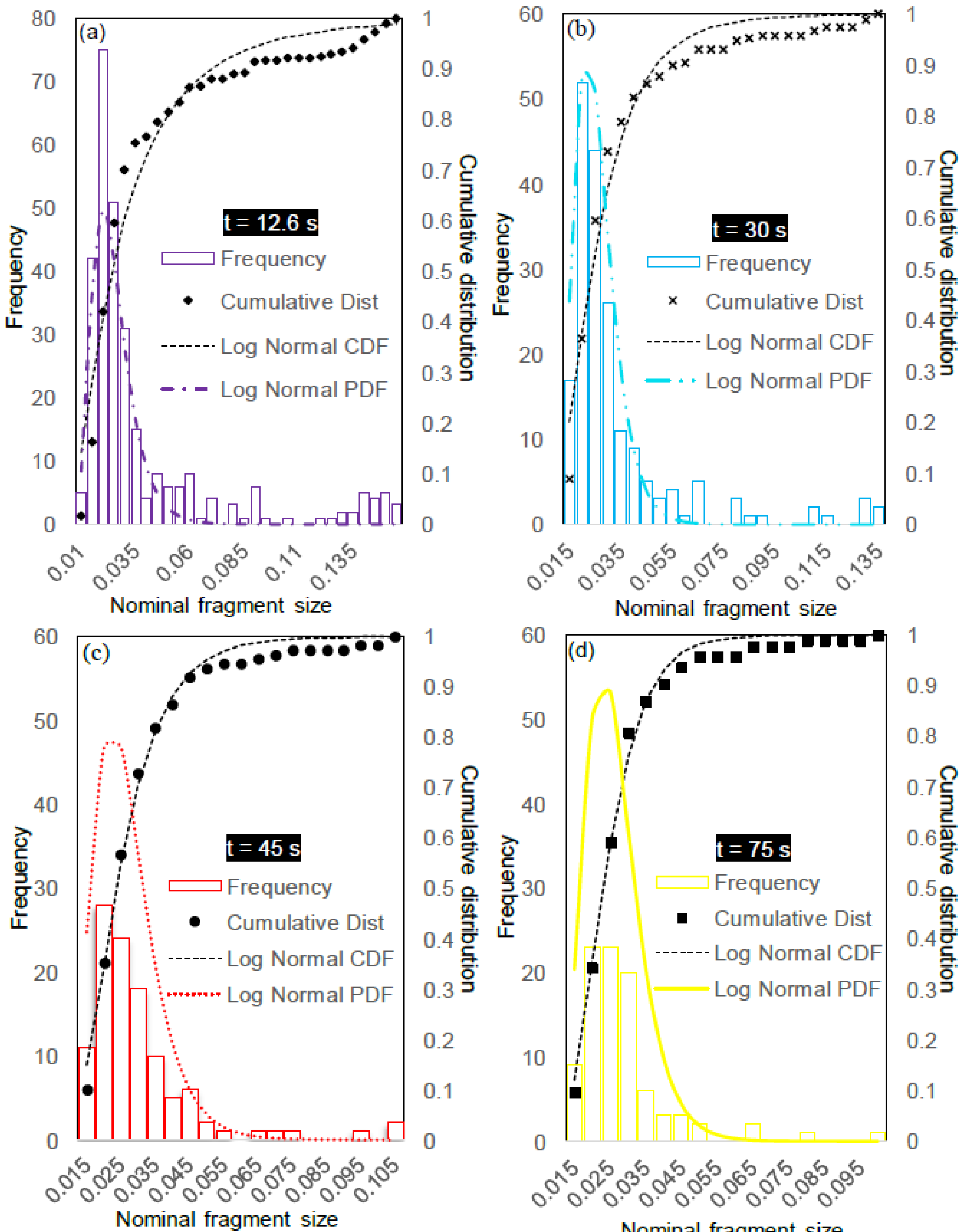

Figure 4 - 17. Fragment size frequency distributions with corresponding log-normal approximations for the four investigated timestamps.

A statistical analysis is conducted to investigate the characteristics of fragment populations. It is apparent from Fig. 4 - 17 that the distribution of nominal fragment sizes in each examined timestamps is asymmetric, being skewed toward the smaller sizes. Such a distribution lends itself to approximation of a log-normal distribution (Fityus et al. 2013). The cumulative distribution and probability density functions of the log-normal distribution are expressed by equations (22) and (23), respectively:

$$F_X(x) = \frac{1}{2} + \frac{1}{2} erf\left[\frac{\ln(x) - \mu}{\sqrt{2}\sigma}\right] \tag{22}$$

$$f_X(x) = \frac{1}{\sigma\sqrt{2\pi}x} e^{-(\ln x - \mu)^2/2\sigma^2} \tag{23}$$

where erf is the complementary error function, σ (the standard deviation) is the shape parameter which affects the general shape of the distribution, and μ (the mean) is the location parameter that controls the location on the x-axis.

As presented in Fig. 4 - 17, it is evident that most of the fragments distribute within a nominal fragment size range ($0.01 \leq d \leq 0.035$) being dominant at all examined time stamps although the differences are significant. The histograms of earlier time stamps (i.e., at time of 12.6 s and 30 s) show the largest quantity of fragments distributes around the nominal fragment size ($0.015 < d \leq 0.02$), comparing to other size ranges being far less frequent. As the avalanche transits into low-speed deposition phase, the already fractured rock mass becomes further deteriorated into a number of smaller fragments, and the peak shown in the histograms between 0.015 and 0.2 gradually disappear and the difference in the size ranges becomes less obvious with more evenly distributed size ranges in $0.02 \leq d \leq 0.03$. In addition, too coarse fragments do not exist for low-speed deposition phase (t = 75 s), inferring a severe fragmentation of the rock mass during the avalanche transport induces a substantial reduction of clast size.

In advance of more detailed investigation on the mechanisms associated with the transport of a coseismic rock avalanche, a statistical analysis is carried out to examine the shape characteristics of the fragment populations by checking the fragment shape isotropy (see Fig. 4 - 18). The shape isotropy can be calculated using the square root of the ratio of the larger I_1 and smaller I_2

eigenvalues of the tensor of inertia of the 2D fragment shape (Timár et al. 2010). The tensor of inertia can be calculated as follows

$$I_{ij}^{fragment} = \sum_{d=1}^{N_d} (I_{ij}^{d} \delta_{ij} + m^d x_i^d x_j^d) \tag{24}$$

where each fragment contains N_d base disks of mass m^d and inertial tensor $\mathbf{I}^d$ relative to the disk local Cartesian axis, and δ_{ij} is Kronecker delta. The vector $\mathbf{x}^d$ is given by $x_j^d - x_j^{fragment}$, where $\mathbf{x}^d$ and $\mathbf{x}^{fragment}$ are vectors describing the constituent disk and fragment centroids, respectively.

The coefficient of variations ($C_v = \dfrac{\text{Standard deviation}}{mean}$) of $\sqrt{I_1 / I_2}$ for the fragment shapes display significant variability in conjunction with emplacement and deformation of the rock avalanche in response to the ground motion. They are found to be significantly larger (1.05) at the initial time stamp (t = 12.6 s) and decrease from 0.99 to 0.92 during the rock movement. Finally, the mean and standard deviation of $\sqrt{I_1 / I_2}$ are found to be 1.3 and 0.17, respectively, with a coefficient of variation of 0.13 when the avalanche comes to a final stop (see Fig. 4 - 18). A $C_v < 1$ is known as a relatively low variation, indicating a high level of fragment shape isotropy.

Significant deviation from the mean value of $\sqrt{I_1 / I_2}$ is observed at earlier timestamps, in particular at time of t = 12.6 s and t = 30 s. This is expected, as the ground shaking intensity increases, bond breakages continue gradually and cut through the slope mass to form coarse blocks. These freshly broken rock blocks have not yet undergone textural changes such as friction abrasion, continuous comminution and grinding, which promotes the particles are more mature characterized by higher rounding and smoothness (Perinotto et al. 2015). The subsequent landslide propagation and deposition are found to cause more damages to the slope mass, as reflected by the gradual enlargement of damage zones and the increase in shape isotropy. This also resulted in an increase in the proportion of fine-grained matrix to coarse-grained blocks with distance. Although the fragment shape isotropy is relatively high at the final deposition stage, deviation from the mean value is observed around the large grain sizes; this suggests that both texturally immature (coarse blocks) and mature (fine particles) deposits form the landslide deposit. The similar behavior was also observed in other large-scale rock avalanches (e.g. Crosta et al. 2004 & 2007). The reduction in variance of the distribution of shape isotropy parameter ($\sqrt{I_1 / I_2}$) for the fragmented blocks can be interpreted as a signature of the dynamic disintegration that occurs continuously during the transport process and the presence of significant subsequent abrasion of newly fragmented blocks (stable distribution of $\sqrt{I_1 / I_2}$ values).

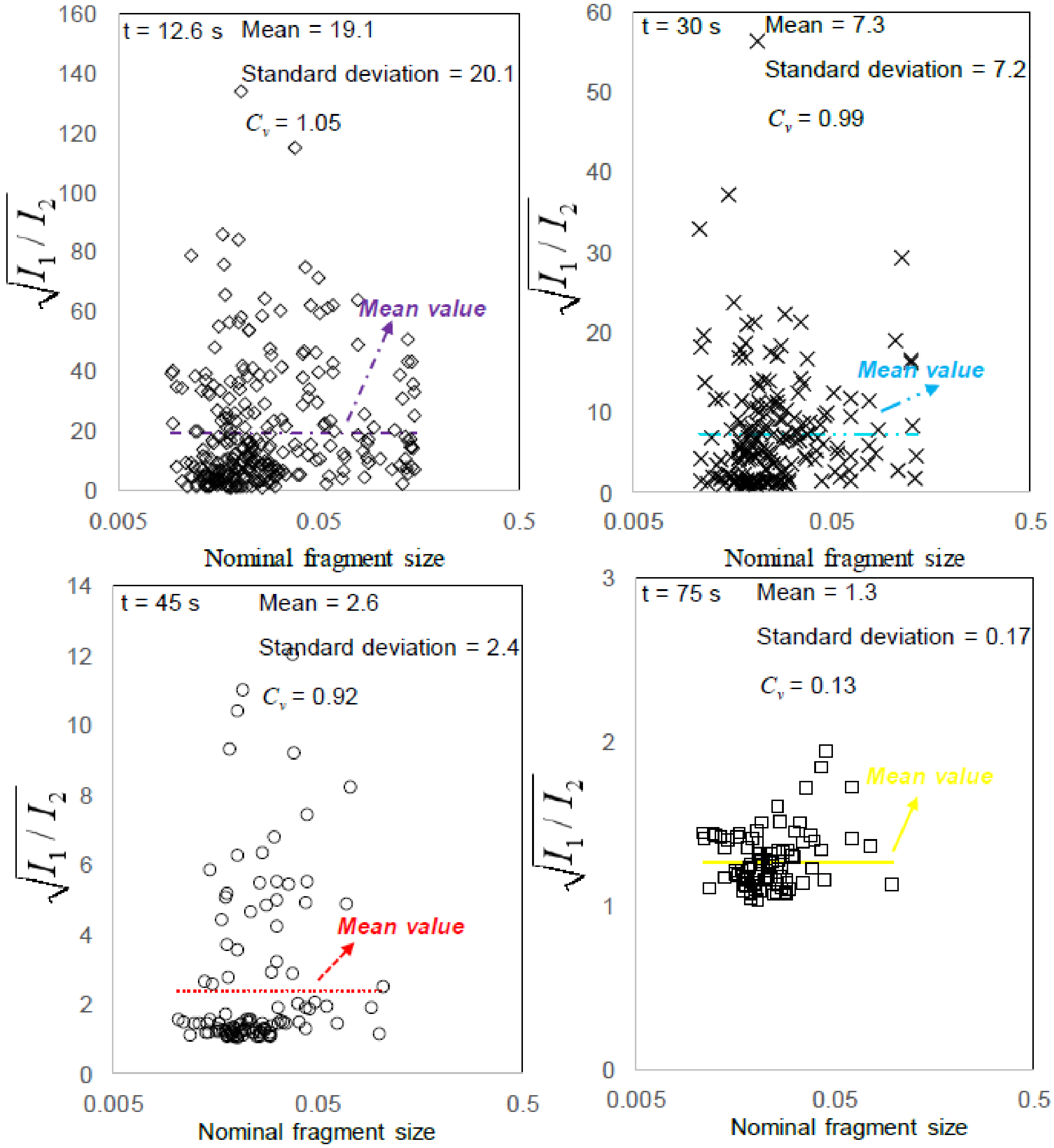

Figure 4 - 18. Distributions of the square root of the ratio of the larger and smaller eigenvalues of the tensor inertia of the fragment shape for checking shape isotropy at different loading times.

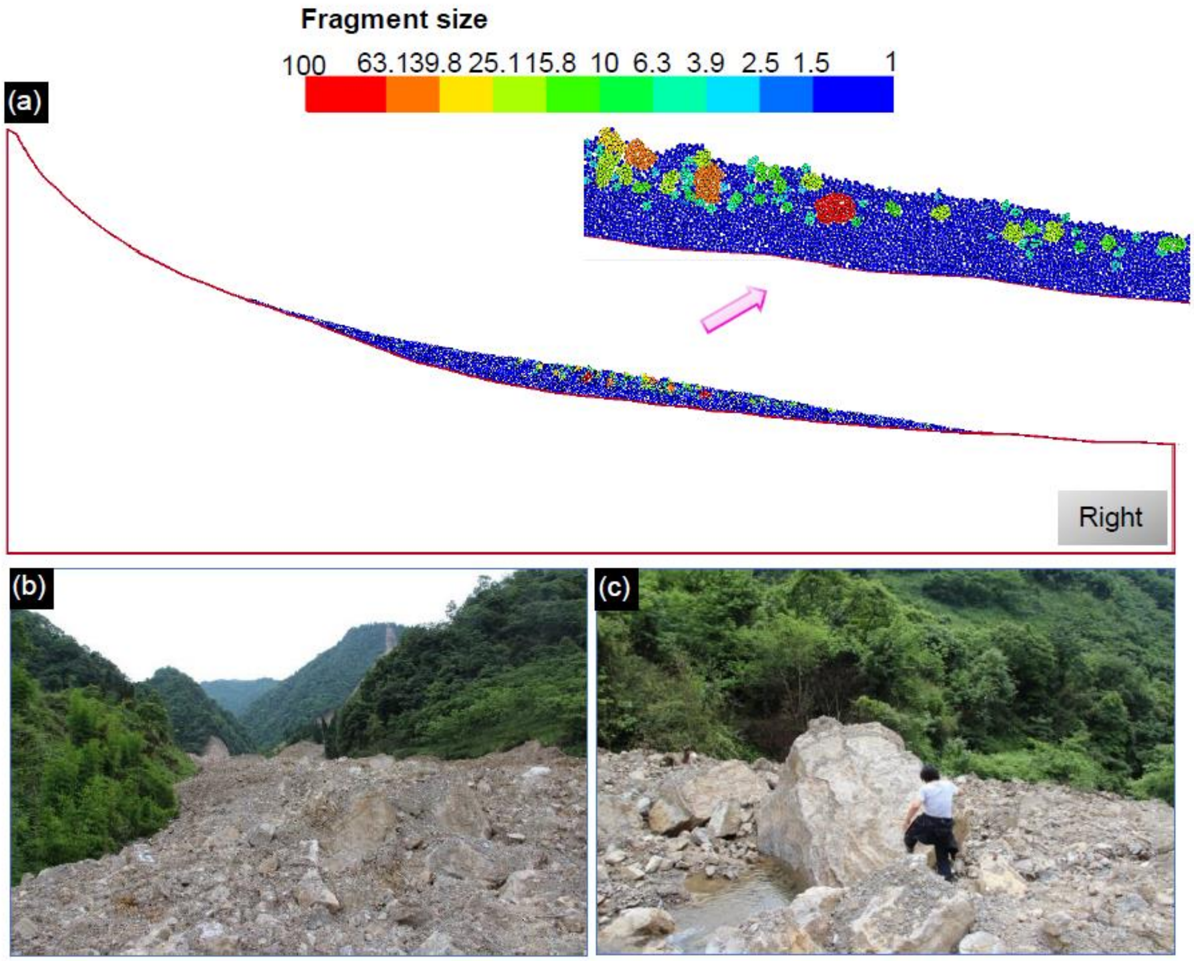

Figure 4 - 19. Aspects of the fragmented deposits for the right stream of Tangjiayan avalanche: (a) Discrete element numerical observation; (b) Field investigation; (c) Large rock blocks observed only in deposits of the right stream.

As shown in Fig. 4 - 19a, the sizes of fractured coarse blocks within deposition of the right stream of rock avalanche remain much larger than that of the left stream deposition. This is in good agreement with the sedimentary fabric found at the site. Compared to the deposits of the left stream (see Fig. 4 - 4c), the field investigations demonstrate that deposition of the right stream of Tangjia Valley rock avalanche consists of a larger quantity of coarse boulders and blocks, as shown in Fig. 4 - 19b, and even huge blocks up to 3 m in size (see Fig. 4 - 19c) can be observed in the deposit of right stream whereas they are not found in the deposit of left stream. Furthermore, the maximum diameter of the deposited boulder within the accumulation zone in the right stream is found to be 3 m, whereas the maximum diameter found in the left stream of the rock avalanche is found to be about 2 m. This can be explained by the fact that the left stream detaches and move down a steep slope, which facilitates a higher-speed movement and fosters more rock fragmentation and finer deposits.

4.5. Conclusion

In this study, DEM analyses that incorporates spatial interpolation technique and statistical analyses is performed. The results provided new insights on the characteristics of dynamic rock fragmentation and the mechanisms governing the transport kinematics of a co-seismic landslide, including trajectory motion, fracture propagation, the evolution of stresses, and the solid concentration. Compared to previous analyses, the novelty is in portraying evolution of granular temperature and solid fraction to identify and interpret the dilative behavior associated with particle dynamic fragmentation. In addition, the original application of fragment shape isotropy for highlighting the deposition of the rock avalanche demonstrates that the fragmentation process continues throughout the entire runout. Additionally, the observed features from field investigations are used to verify the validity of the numerical model. The major findings of this study are summarized as follows:

(1) In the initiation of the landslide, earthquake load plays a pivotal role in fracturing and fragmentation of the rock mass leading to slope destabilization. This is reflected in the internal rock damage that occurs and propagates gradually along the basal failure plane.

(2) During the coseismic landslide propagation and deposition, the interpolated stress fields within the avalanche reveals a stress concentration in the basal layer of the slope mass, where rock fragmentation and deformation are likely to occur, inducing a dilution of solid concentration. The evolution of solid concentration within the slope mass is found to accord well with the dilation and compaction of the dynamically fragmented flow process. The granular body has relatively pronounced solid concentrations as it starts with a tightly bonded contact network before dilation occurs. This is attributed to stretching and thinning of the avalanche body with the slope mass transforming into a fully developed fragmented flow, inducing reduction in bulk density of the avalanche body, in particular, the basal area and free surface, where the kinetic energy is greatly enhanced promoting high speed and long runout of the rock avalanche. Finally, a compaction

follows as the avalanche loses momentum and gradually accumulates in the deposition area. Lack of stress at the top of the granular body with the relatively high solid concentration, contribute to the development of fractured large boulders found in large avalanche deposits.

(3) During the high-speed motion of the sliding mass after detaching from the source area, an intensely sheared, dilute, and agitated layer spontaneously appears at the base of the slope mass promoting the occurrence of particle dynamic fragmentation in basal layer. This can further dilate and disperse the basal facies material allowing the solid concentration to decrease and flow mobility to increase.

(4) Characteristics of fragmentation during rock avalanches is systematically analyzed in terms of the statistics of the fragment size and fractal dimensions. The two-parameter Weibull equation provides an adequate description of the simulated fragment size distributions. The variations d_c and ν indicate that the occurrence of rock disintegration during landslide initiation and propagation is characterized by an obvious increase of various sizes of fragments, causing the fragment size distribution spans a wider range first, then as the slope damage zone propagates gradually from the failure plane to the internal slope mass. Consequently, the entire avalanche body experiences severe fragmentation, which promotes a large proportion of fragments that has been broken into fine-grained particles, inducing an increasingly narrower fragment size distribution.

(5) The generated fragment shapes tend to be well isotropic during the avalanche deposition process. The coefficient of variations of the inertia tensor of $\sqrt{I_1 / I_2}$ changes significantly to lower values. This reflects the textural maturation by fragmentation with considerable shearing and continued friction abrasion during the transport process.

Preface to Chapter 5

The results presented in the previous chapter demonstrate the efficiency of the discrete element method in investigating rock fracturing behaviour with particular emphasis on dynamic fragmentation during landslide propagation. In this chapter, to continually demonstrate the applicability of the DE simulation, the more realistic slope dynamic response to seismic loading is now investigated with application of absorbing boundary condition. Therefore, the fact that the seismic traveling wave is not synchronized along the failure plane due to different elevations can be captured. Comparisons are then made regarding the boundary conditions of the rock basement that avoid the adverse effects of seismic wave reflection back into the model. The capability of the proposed DE approach to advance insights into the role of dynamic disintegration in the rockslide is verified.

Chapter 5

Dynamic disintegration processes accompanying transport of an earthquake-induced landslide

Abstract

Aiming to understand the dynamic disintegration and transport behaviour of an earthquake-induced landslide, a dynamic discrete element method has been employed to analyze the Wangjiayan landslide triggered by the 2008 Ms 8.0 Wenchuan earthquake. Absorbing boundary condition is used for the seismic wave transmission and reflection at the slope base. The numerical results show that under seismic loading, internal rock damage initiates, propagates, and coalesces progressively along the weak solid structure and subsequently leads to fragmentation and pulverization of the slope mass. This can be quantitatively interpreted with the continuously rapid increase of the damage ratio and sudden decline of growth ratio of the number of fragments after the peak seismic shaking. During emplacement evolution, fragmented deformation patterns within the translating joint-defined granular assemblies are affected by the locally high dilatancy with a simultaneous occurrence of highly energetic collisions related to the action of shearing, and this can be quantified by the enhancement of particle kinematic activities (high vibrational and rotational granular temperatures) and intense fluctuations of location-dependent global dispersive stress. In this process, slope destabilized and transports downward in a rapid pulsing motion as friction bonds are locally and continually overcome by the seismic- and gravity-induced shear forces. The joint-determined fragment network before movement initiation and the final fragmented depositions after the rapidly-sheared transport have been systematically investigated by fragment statistics (fragment size distribution, fragment mass distribution, and fractal dimension) and morphometric characters (fragment shape isotropy) to offer new insights into the disintegration characteristics of the earthquake-induced catastrophic mass movements.

Keywords: Earthquake-induced landslide; Discrete element method; Absorbing boundary condition; Granular temperature; Fragment statistics.

∗ A version of this chapter has been accepted for revision in ***Landslides*** *Journal*.

5.1. Introduction

Earthquake-induced landslides are among the natural hazards that can pose serious threats to communities and infrastructures. This is particularly true when the rock slopes are close to the main earthquake fault and on the hanging-wall side (Huang and Li 2009). Many catastrophic landslides of this type have recently occurred worldwide, including over ten thousand landslides in the North Canterbury and Marlborough regions of New Zealand triggered by the 2016 Mw7.8 Kaikōura Earthquake that concentrated in a 3600 km^2 area around the rupture zone (Massey et al. 2018); landslides in Nepal caused by the 2015 Mw 7.8 Gorkha earthquake that leads to thousands of deaths and billions of dollars in economic losses (Roback et al. 2017) and thousands of others that were triggered by the 2008 Mw 7.9 Wenchuan earthquake (Chigira et al. 2010; Dai et al. 2011; Gorum et al. 2011; Zhang and Yin 2013; Tang et al. 2015; Zhan et al. 2017). There has been an increasing interest in the study of earthquake-triggered landslides during recent years; however, much uncertainty still exists about the relationship between earthquake (seismic) characteristics and co-seismic slope deformation and catastrophic instability (Ghahramani and Evans 2018).

For many years, significant effort has been made by researchers to investigate the failure of slopes and the subsequent dynamic runout (Wu et al. 2009; Wu and Chen 2011; Cagnoli and Manga 2004; Cagnoli and Piersanti 2017; Zhao and Crosta 2018). The rockslides or rock avalanches are always associated with rock fragmentation together with high spreading velocities, long runouts, and energy release, however, the process of fragmentation is rarely directly observed as it occurs in nature due to the destructive capacity and unpredictability of rockslides (Haug et al. 2016; Wang et al. 2018; Davies 2020). To understand the complex interplay between the disintegration process and the transport mechanism, the related research has been extensively performed by means of field investigations in real rockslide or rock avalanche deposits, experimental studies of a fragmentable, brittle, solid rock analogue material sliding over a simple slope geometry, and numerical simulations. Based on field investigations of deposits of landslides, Crosta et al. (2007) measured the representative rock block size distribution at the source and deposit area of the 1987 Val Pola rock avalanche and quantified their relationships with the fragmentation process and the corresponding energy consumption, indicating that more than a single comminution process acted during rock avalanche emplacement. Through a detailed mechanical analysis of the microscopic surface texture on quartz grains sampled from the basal facies of two earthquake-triggered landslides, Wang et al. (2015) proposed that both the overburden pressure and the self-excited vibration energized by an undulating slip surface may play dominant roles in the occurrence of particle dynamic fragmentation in the basal facies. Perinotto et al. (2015) combined field studies, grain size, exoscopic, and new morphometric measurements using fractal dimension and circularity indicators based on various particle sizes and bring new insights on dynamic disintegration processes which contribute to the extreme mobility of landslides. Experimental studies using a series of analogue models under different testing conditions show that fragmentation can increase the travel length of the front of landslide deposits (Bowman et al. 2012; Haug et al. 2016) and produce fine materials that may act as a lubrication (De Blasio and Elverhøi 2008; Wang et al. 2017; Zhao and Crosta 2018) or dispersive stresses from exploding fragments may effectively reduce the normal stress at the base (Davies and McSaveney 2009). This process involves energy losses (Haug et al. 2016) and an increase in volumetric fraction of fine-grained material (Langlois et al. 2015) affecting both the fragment trajectory and dynamic runouts (De Blasio and Crosta 2014). Field investigations and physical models are, therefore, to infer dynamic disintegration and transport characteristics a posteriori from the deposits (Pollet and Schneider 2004; Locat et al. 2006; Crosta et al. 2007; Pedrazzini et al. 2013; Ruiz-Carulla et al. 2015, 2017; Zhang and McSaveney 2017; Dufresne and Dunning 2017; Dufresne et al. 2019; Dufresne and Geertsema 2020). However, due to the lack of recordings on the transport processes and opportunities to observe the interiors of landslides (Zhang et al. 2019), moreover, these methods suffer from a large number of assumptions and simplifications (Dammeier et al. 2011; Haug et al. 2016), the propagation mechanisms and dynamic fragmentations of such events are still not completely understood and a lively discussion continues on.

Numerical modelling of rockslides or rock avalanche, including continuum or discontinuum approaches, has been widely used (Thompson et al. 2009; Yin et al. 2015; Gao and Meguid 2018a&b; Borykov et al. 2019).Continuum methods, such as the smoothed particle hydrodynamics (SPH) model, the depth-averaged numerical (DAN) model, and the finite element model (FEM), are able to simulate either the initiation or propagation of slope failures (Eberhardt et al. 2004; Hungr and McDougall 2009; Yerro et al. 2016). Continuum-based numerical models often fail to reproduce the progressive failure of rock slopes, especially the dynamics of kinematic release accompanying complex internal distortion, dilation, and fracture (Stead et al. 2006). Unlike the continuum-based models, the discrete element method (DEM), does not limit the scale of separation and displacement behaviors of elements, and can simulate the rock failure process from microcracking to macrofailure without any complex constitutive models. Therefore, the discrete-element method (DEM) is an effective tool that is used in modeling the rock fragmentation and mass movement process of landslides. Langlois et al. (2016) employed a two-dimensional discrete element model to study the failure, collapse, and flow of brittle granular column over a horizontal surface for understanding dynamic rock fragmentation in a landslide. They suggest that the runout distance is higher when the deposit is highly fragmented, which confirms previous hypotheses proposed by Davies et al. (1999). Because of severe rock fragmentation occurring along the preexisting discontinuities or along the freshly formed fracture surfaces as controlled by the initial joint sets during the landslide emplacement, it is important to mention the role of rock discontinuity at ruling fracture nucleation and fragmentation during initiation, propagation and deposition of landslides. Zhao et al. (2018) performed three-dimensional DEM analysis of a multiple arrangement of jointed rock blocks sliding over a simple slope geometry. They reported that runout distance decreases with the increase of initial fragmentation intensity.

Notwithstanding these advancements, less attention has been paid to studying the dynamic disintegration process and transport mechanism of earthquake-induced landslides with complex geological and geomorphological settings (Meunier et al. 2007; Zhao and Crosta 2018; Wei et al. 2019). In recent years, some of the reported studies related to modeling earthquake-induced landslides (e.g. Tang et al. 2009; Lo et al. 2011; Yuan et al. 2014, 2015; Zhou et al. 2015; Scaringi et al. 2018) focused on the kinematic behavior and deformation mechanics of the system only throughout simple recording of the displacements and velocities, however, little details were provided unraveling the response of jointed rock materials during landslide emplacement subjected to intense seismic shaking from insights into transport mechanism and dynamic disintegration.

A case study of a landslide that took place in China in 2008 is investigated and used for the validation of the developed discrete element numerical model. A detailed description of the geological setting in the area and the mechanical properties of the rock material is first presented. A series of numerical simulations is then performed to examine the effect of using absorbing boundary conditions on the response of the model. The deformation evolution, disintegration process and fragmentated deposition of the landslide under earthquake loading is then investigated focusing on the fracturing propagation, particle agitation, dispersive stress fluctuation, fractal behavior and shape characteristics of the fragment populations.

5.2. Geological and Geomorphologic setting

On 12 May 2008, a Mw 7.9 earthquake hit southwestern China and caused more than 15,000 geohazards (Yin et al., 2009). One of the most catastrophic landslides, Wangjiayan landslide, occurred in the urban area of Beichuan County, Sichuan Province and resulted in approximately 1600 fatalities and ruined in dozens of buildings including a kindergarten, the county hospital, and Qushan elementary school. The landslide involved displaced material from the source area of 1.6 million m^3. Wangjiayan landslide traveled about 700 m with a vertical drop of 320 m, and deposited in an area of 0.2 km^2 (Fig. 5 - 1). The Wangjiayan landslide occurred in the south of old Beichuan County town (104°26'56.4" E, 31°49'33.6" N), where it was destroyed by the 2008 earthquake, and now is reserved as earthquake geological relics along with the Wenchuan earthquake memorial museum for education about earthquake-induced geohazards. Therefore, research into geologic disasters from post-earthquake rapid and long-runout landslide in these areas will be very important for post-disaster reconstruction completion and tourists' safety.

5.2.1. Landforms and Topography

The old Beichuan County, which belongs to the southeastern margin of erosional tectonic middle mountains and hill landforms within a valley characterized by steep slopes ranging from 30° to 50°, most of which are over 40° with sparse vegetation, as presented in Fig. 5 - 1. The town was constructed in the first terrace of right bank of the tributary of upstream of Fu River and in a relatively lower location. The north, the south, and the west sides of the town are surrounded by mountains, while the east side faces the river. The deep erosion from the Fu River and the strong seismic motions due to Wenchuan earthquake resulted in drastic changes in the landforms in this area. Wangjiayan rock slope was located in the west part of the old Beichuan County in the region between the Mishi and Shenjia Valleys, as shown in Fig. 5 - 1a. The middle to lower slope was at the elevation of 660.0 – 980.0 m, with a slope angle of 50 °.

Figure 5 - 1. (a) Airborne remote sensing image of Wangjiayan landslide; (b) Overview of the Wangjiayan landslide**.**

5.2.2. Geological and Structural Settings

The geological structure in the Wangjiayan landslide area is mainly controlled by the nearby Yingxiu-Beichuan rupture belt that extends through the leading edge (the toe) of the steeply dipping (60°-70°) slope. It is approximately 130 km to the northeast of Wenchuan Earthquake epicenter and approximately 400 m from Yinxiu-Beichuan fault (Yin et al. 2015; Li et al. 2016), as shown in Fig. 5 - 2a. Specifically, the landslide area is on the hanging wall of the fault, in which the fault is regarded as the boundary between the front and the back of Longmenshan fold belt. Moreover, the complex structure of the slope is characterized by three main families of joints (J_1, J_2, and J_3), as shown in Fig. 5 - 2b. Two sets (J_1 and J_2) are sub-vertical, cut the slope transversely and are responsible of the presence of prominent spurs; one set (J_3) has inclination almost parallel to the slope and define its main geometrical features.

From a lithological point of view, the exposed rocks in the Wangjiayan landslide area mainly include the Qingping Group (∈1c) thin layers of sandstone, grey sandy shale, siltstone and sandy slate of the Upper Cambrian due to the influence of the fault. Its surface was covered by a quaternary eluvium-deluvial unconsolidated formation of thickness < 3 m, and the soil consisted mostly of clay interbedded with fragmented rocks.

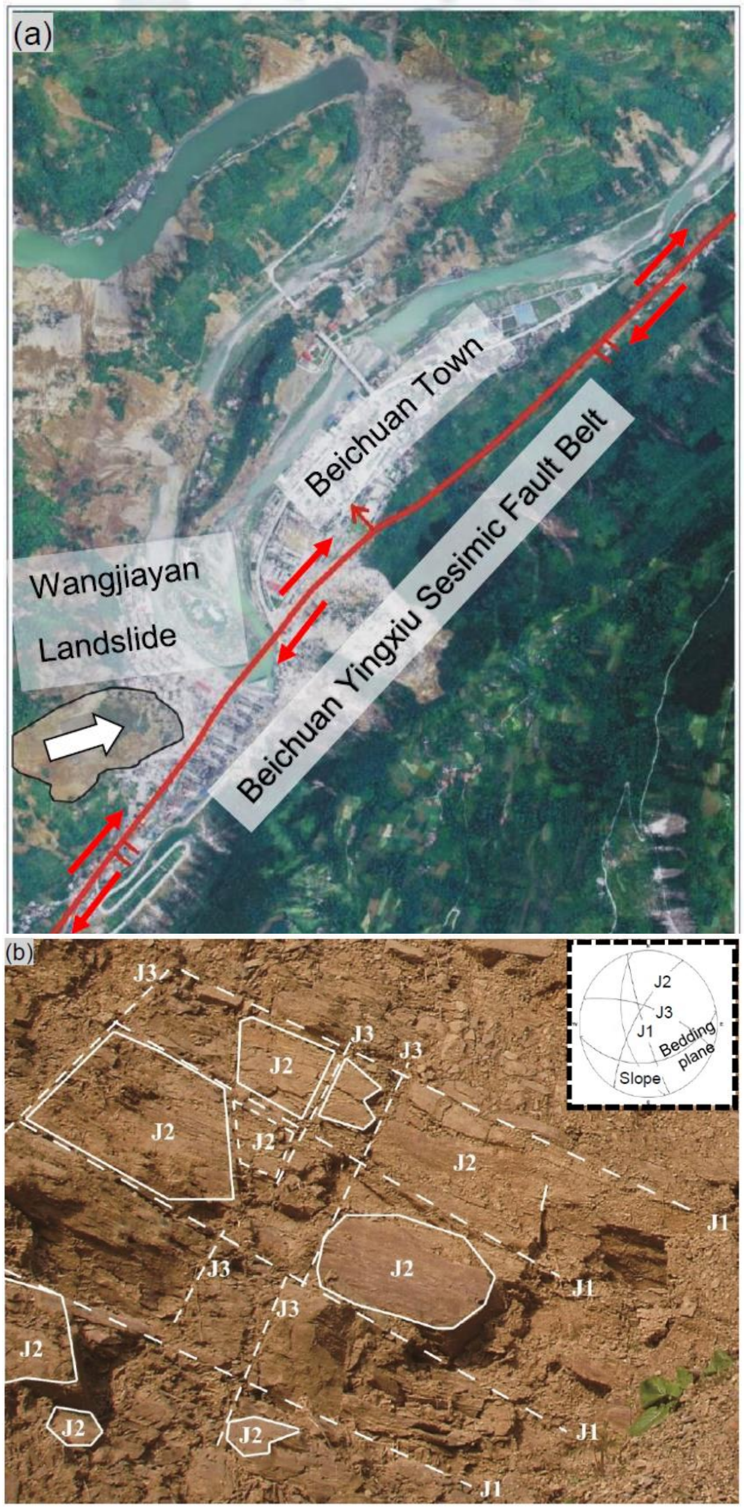

Figure 5 - 2. Geological and structural Settings of the Wangjianyan landslide area. (a) The fault belt location; (b) Details of the geological structural features.

5.3. Wangjiayan landslide

On the basis of a detailed field investigation, a downslope route and longitudinal profile of the Wangjiayan landslide are presented in Fig. 5 - 3, respectively. The landslide initiated as a rock slide in the sandstone rock mass with a strike 80° NE and a dip angle of 35°.After detaching from its source area, the sliding mass collapsed downwards directly to the valley floor along the direction of 76°. The displaced materials ran out a horizontal distance of about 350 m with a descent of 320 m. It is noted that the previously damaged buildings by the strong earthquake shocks at the outer margin of the deposition area had been destroyed to ruins by the air blast (Fig. 5 - 4a). The existence of impact marks commonly found in the deposited boulders (Fig. 5 - 4b) further reveals that extremely fast-moving displaced mass exert a powerful downthrusting force.

The source area contains steep terrain with a slope ranging from 45° to 55°, even up to 60° at some part, which favors rapid movement of the landslide (see Fig. 5 - 3a). The rear elevation of the Wangjiyan landslide ranged from 800 m a.s.l to 980 m a.s.l., forming the main scarp with a height up to 180 m (see Fig. 5 - 3a and Fig. 5 - 4c). The toe of the surface of the rupture elevation was around 660 m, giving a height difference of 320 m (see Fig. 5 - 3b). The source area was an irregular wedge on the profile, and the detached mass mainly consisted of Cambrian sandy slate and shale with a thickness of 0 - 40 m and an average of 14 m. The longitudinal extent was 250 - 400 m, with an average of 350 m. The source area presented an irregular quadrilateral shape on the plan with a lateral width of 290 - 370 m and an average width 330 m. On the whole, the topography displays higher in the west and lower in the east with gentle lower section and steep upper section. From Fig. 5 - 4d, it can be seen obviously that the exposed bedding plane was strongly scraped with some evident scratches. This reflects the rapid movement of the landslide characterized by its high kinetic and impact energy. A summary of the physical properties of the rock mass according to previous studies in Wangjiayan area (Cui et al. 2011) is provided in Table 5 - 1.

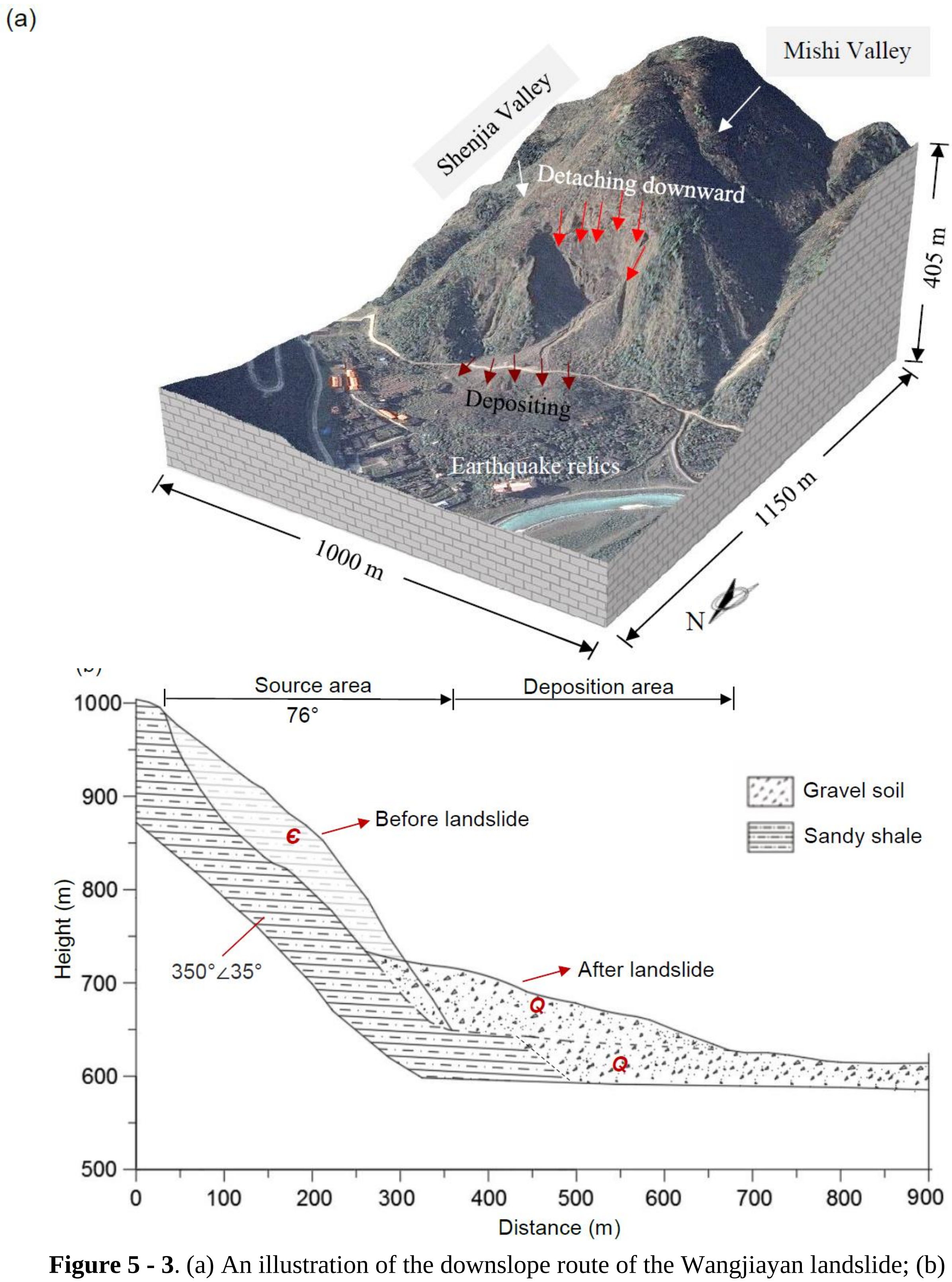

Figure 5 - 3. (a) An illustration of the downslope route of the Wangjiayan landslide; (b) Longitudinal profile of the Wannjiayan landslide.

Deposition area is located at elevations ranging from 650 to 700 m extending from the lower section of the slope to the old town of Beichuan County. The deposition area has a longitudinal length of 273 m, a lateral with of 343 m, an area of 52,422 m^2, an average thickness of about 20 m, maximum thickness of 27 m and a volume of 1.4 Mm^3. The slope angle of the upper section of the deposits is around 35°, and gradually decreases along the runout path. The overall slope angle of the deposition area is relatively flat, with an average of about 12°. From a macroscopic view, the displaced mass exhibited obvious radial spreading and flattening and finally deposited in a fan shape.

During the rapid transporting and depositing processes, the accumulated mass exhibited micro-geomorphic features characterized by the five hummocks due to the composition of the slope material and the difference in the speed of movement. These hummocks distributed around the front margin of the deposit area with diameters of 210 - 250 m and slope angles ranging from 10° to 20°, which were located at elevations ranging from 651 to 689 m a.s.l. with a height difference of 38 m. Per site investigation, the deposited mass is composed mostly of grey, and grayish yellow rubble blocks containing gravel, boulders, and sandy soil, of which the parent rock was loose-dense thin layer of sandy shale, siltstone, and sandstone. About 60% - 90% of the rock debris was rubbles and gravels of highly weathered rocks ranging from 10 cm to 20 cm in sizes and several large boulders (up to ~1m in diameter) can also be observed, as shown in Fig. 5 - 4e. The measured thickness of the deposit was between 10 m and 30 m, with an average of 18 m. The local deposit front has not been completely disintegrated, and the original structure of rock mass was still well-preserved, as presented in Fig. 5 - 4f.

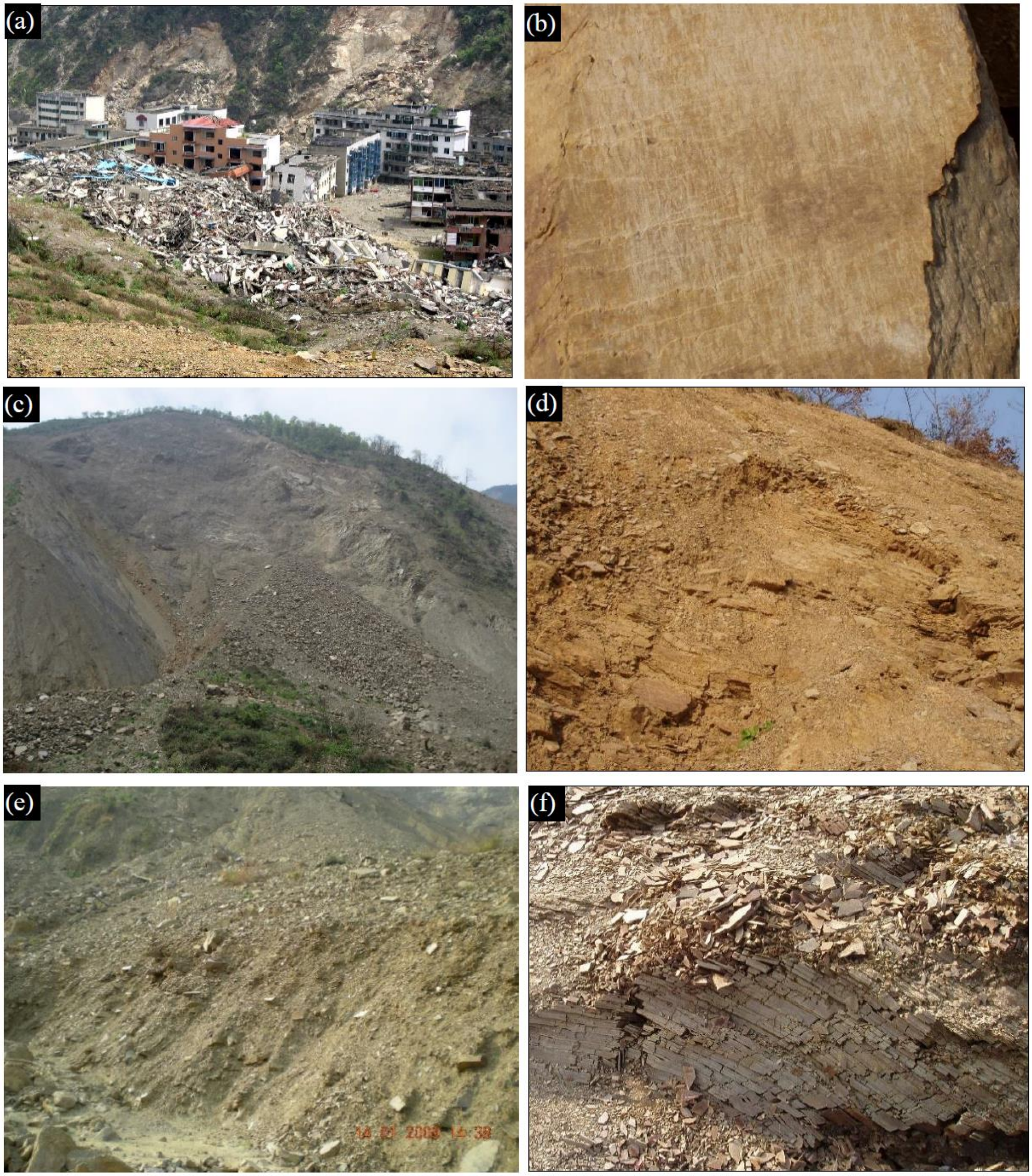

Figure 5 - 4. Characteristics of the Wangjiayan landslide: (a) The earthquake damaged buildings ruined into pieces by the turbulence generated by the rapid-moving rock mass; (b) The impact marks commonly existed in the deposited rock blocks; (c) The scarp of the rupture surface; (d) The scratches left on the bedrock; (e) Features of hummocky deposits; (f) A view of accumulation body still retaining original rock structures.

5.4. The Discrete Element Model

Discrete element method (DEM) has proven to be efficient in modeling intact rock taking into account of the fracture initiation and propagation, the rock brittleness, the texture effect and the macroscopic non-linear failure envelopes. Model details and validation procedure are discussed below.

5.4.1. DEM bonded particle model

The particle flow code (PFC^{2D}) was used in this study to model the Wangjiayan landslide with dimension of 905 m in length and 535 m in height. The rock mass modeled using this method does not require a user-defined constitutive model. Alternatively, built-in parallel bond models are applied with suitable contact parameters. The parallel bond models have been widely used to study cracking and fragmentation of rock material. This type of particle bond acts as a conceptual cementitious material characterized by tensile and shear strength and normal and tangential stiffness (Potyondy and Cundall 2004). When the contact force exceeds either tensile or shear strength, the parallel bond breaks and a micro-crack forms between the particles. More specifically, if the tensile strength limit is exceeded ($\bar{\sigma} > \bar{\sigma}_c$), the bond breaks in tension. On the other hand, if the bond is not broken in tension, then the shear strength limit is enforced. The shear strength $\bar{\tau}_c = -\sigma \tan\bar{\phi} + \bar{c}$, where $\sigma = \frac{\bar{F}_n}{\bar{A}}$ is the average normal stress acting on the parallel bond cross section. If the shear strength limit is exceeded ($\bar{\tau} > \bar{\tau}_c$), then the bond breaks in shear. More details can be found herein:

The maximum tensile and shear stresses acting on the parallel-bond periphery are calculated from the beam theory as

$$\bar{\sigma} = \frac{\bar{F}_n}{\bar{A}} + \frac{\left\|\bar{\mathbf{M}}_{\mathbf{b}}\right\|\bar{R}}{\bar{I}} \tag{1}$$

$$\bar{\tau} = \frac{\left\|\bar{\mathbf{F}}_{\mathbf{s}}\right\|}{\bar{A}} + \begin{cases} \frac{\left|\bar{M}_t\right|\bar{R}}{\bar{J}}, & \text{3D} \\ 0, & \text{2D} \end{cases} \tag{2}$$

where $\bar{F}_n$, $\bar{\mathbf{F}}_\mathbf{s}$ are normal and shear parallel-bond force, $\bar{M}_t$, $\bar{\mathbf{M}}_\mathbf{b}$ denote twisting and bending parallel-bond moments; $\bar{R}$, $\bar{A}$, $\bar{I}$ and $\bar{J}$ are the bond radius the cross-sectional area, moment of inertia of the parallel bond cross-section and the polar moment of inertia of the parallel bond cross section, respectively.

Finding the microparameters (radii, stiffness and strength) of the particles and the parallel-bonded contacts to properly represent the rock material requires model calibration using standard tests to establish reliable relationships between the micro- and macro responses (Gao and Meguid 2018c). This approach has been successfully used by several researchers. For example, Tang et al. (2009) utilized biaxial tests to determine the micro-properties of the rock material needed for the analysis of a landslide triggered during the Chi-Chi earthquake; Wang et al. (2003) used compression and Brazilian tests to calibrate a parallel bonded model for the stability analysis of heavily jointed rock slopes.

Table 5 - 1. Physical and mechanical properties of the rock mass

Rock mass of Wangjiayan landslide					
Density (kg/m^3)	Young's Modulus (GPa)	Internal friction Angle (°)	Compressive strength (MPa)	Brazilian tensile strength (MPa)	Poisson's ratio
2600	10.5	35	15.5	3.2	0.25

To determine the mechanical properties of the modeled rock material used in this study, a series of uniaxial compression tests was performed. A sample measuring 100 mm in height and 50 mm in width is built using 12694 discrete element disks as illustrated in Fig. 5 - 5a. The unconfined compressive strength, and Young's modulus are found to be 15.1 MPa, and 10.2 GPa, respectively. Besides the compressive behavior of the rock sample, it is necessary to consider its tensile properties because of its relative lower strength, and therefore, Brazilian test was modeled, and the results presented in Fig. 5 - 5b. The corresponding micro-properties required for the PBM model are summarized in Table 5 - 2, which are quite consistent with the measured rock properties given in Table 5 - 1.

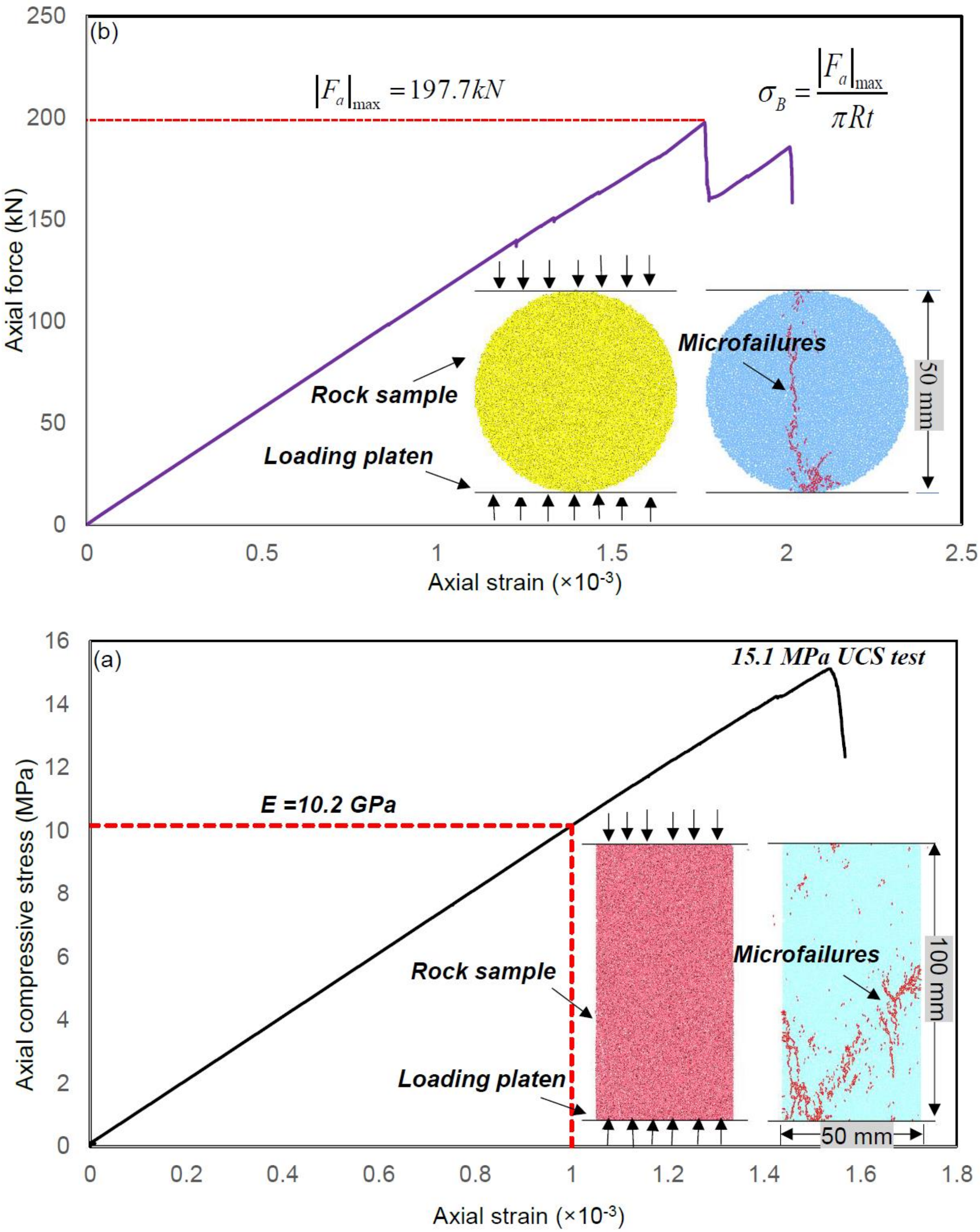

Figure 5 - 5. Micro-parameters calibration: (a) Modeling the unconfined compression test; (b) Modelling the Brazilian test.

Table 5 - 2. Numerical parameters used in the discrete element analysis

Item	Micromechanical properties
	Rock mass
Ball-ball contact effective modulus	10.0 GPa
Ball stiffness ratio (k_n/k_s)	2.0
Ball friction angle	30°
Parallel bond effective modulus	10.0 GPa
Parallel bond stiffness ratio (k_n/k_s)	2.0
Parallel bond tensile strength	11.0 MPa
Parallel bond shear strength	22.0 MPa

5.4.2. Boundary conditions

Compared to previous studies (e.g., Tang et al. 2009; Yuan et al. 2014&2015; Zhao and Crosta 2018; Zhang et al. 2019), the novelty in this landslide numerical analysis is the application of absorbing boundaries for avoiding the adverse effects of seismic wave reflection back into the model. The absorbing boundaries are created by adding dashpots in both the normal and shear directions along the base. Similar approach was successfully used by Zhang et al. (2014) and Gischig et al. (2015). This process is expressed in equations (3) through (8) below:

$$\sigma_n = -\rho V_p v_n \qquad (3)$$

$$\sigma_s = -\rho V_s v_s \qquad (4)$$

where σ_n and σ_s are the time-dependent normal and shear stresses at the base boundary, V_p and V_s are the P and S wave velocities, respectively, v_n and v_s are the instantaneous normal and shear velocities of the boundary particles.

Replacing stresses, σ, using forces, F, such that $F = \sigma \times 2R$ in two dimensions. Equations (3) and (4) can be expressed in terms of boundary forces, F_n and F_s, and velocities, v_n and v_s:

$$F_n = -2R\rho V_p v_n \tag{5}$$

$$F_s = -2R\rho V_s v_s \tag{6}$$

where R is particle radius and ρ is the material density.

The following two equations are used to specify a given earthquake velocity in the vertical and horizontal directions.

$$F_n = 2R\rho V_p (2v_n^{equ} - v_n) \tag{7}$$

$$F_s = 2R\rho V_s (2v_s^{equ} - v_s) \tag{8}$$

where, v_n^{equ} and v_s^{equ} are the applied velocity decomposed in the vertical and horizontal directions.

It is worth noting that the factor of two for injected velocity (v_n^{equ}, v_s^{equ}) accounts for the equal partition of energy at the boundary.

According to the wave propagation theory, V_p and V_s can be determined using the following equations:

$$V_p = \sqrt{\frac{E(1-\nu)}{\rho(1+\nu)(1-2\nu)}} = \sqrt{\frac{3K+4G}{3\rho}} \tag{9}$$

$$V_s = \sqrt{\frac{E}{2\rho(1+\nu)}} = \sqrt{\frac{G}{\rho}} \tag{10}$$

where E, K, G, ν and ρ are the Young's modulus, Bulk modulus, shear modulus, Poisson's ratio, and density.

The effect of boundary conditions on the response to wave propagation is examined by analysing a rock column that consists of a string of parallel-bonded particles with numerical parameters shown in Table 5 - 2. Three different boundary conditions are assigned to the top of the column, namely, absorbing (viscous) boundary, free boundary, and fixed boundary as illustrated in Fig. 5 - 6. The rock column is 60 m in length, 1 m in diameter and each particle has a radius of 0.5 m. Kuhlemeyer and Lysmer (1973) recommended at least eight to ten elements per wavelength of input motion for reliable dynamic computation. Similar approach was used by Gu and Zhao (2009) and Zhang et al. (2014) who proposed the use of element size that ranges from 1/15 to 1/20 of the shortest wavelength. In this study, particles measuring 1/15 if the shortest wavelength are chosen. Ricker wavelets (expressed in equation 11) with amplitude of 0.1 m/s and a time period of 3.0 s is injected from the bottom of the model and the response to different boundary conditions is calculated.

$$v_R(t) = A(1-2\pi^2 f^2 (t-1)^2)e^{-\pi^2 f^{2(t-1)^2}} \tag{11}$$

where A is the amplitude and f is central frequency of the signal.

To compare the column response to the investigated boundary conditions, five measurement points along the column, namely, A, B, C, D and E, are used and the results are summarized in Fig. 5 - 7. The calculated velocity time history for the case of absorbing boundary are shown in Fig. 5 - 7a. The velocity at point E, located at the top of the model, is found to be twice that of the input values of the Ricker wavelet which is consistent with the expected theoretical response at the boundary in this case. The absence of further oscillation at about 2.0 s indicates that the absorbing boundary has efficiently absorbed the induced energy. The slight oscillation seen after 2.0 s is related to the discrete nature of the medium (Itasca consulting group, 2014). For the case of free boundary at point E, the velocity time history (Fig. 5 - 7b) reveals significant oscillation after 2.0 s which indicates the presence of wave reflection in this case. When fixed boundary was introduced (see Fig. 5 - 7c), the velocity at point E became zero with significant oscillation elsewhere after elapsed time of 2.0 s. It confirms that using fixed boundary results in wave reflection back into the model as no energy is absorbed at the boundary.

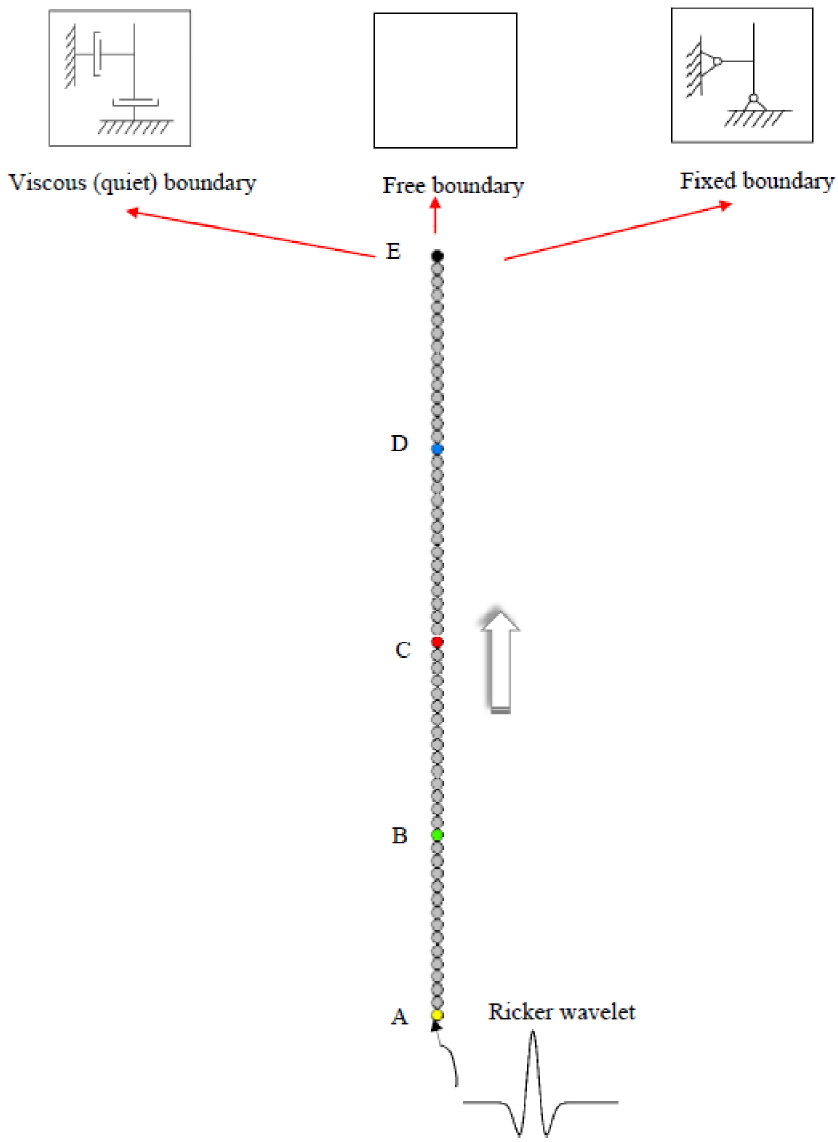

Figure 5 - 6. Calculation model for a rock column using Ricker wavelet to demonstrate the different boundaries reacting.

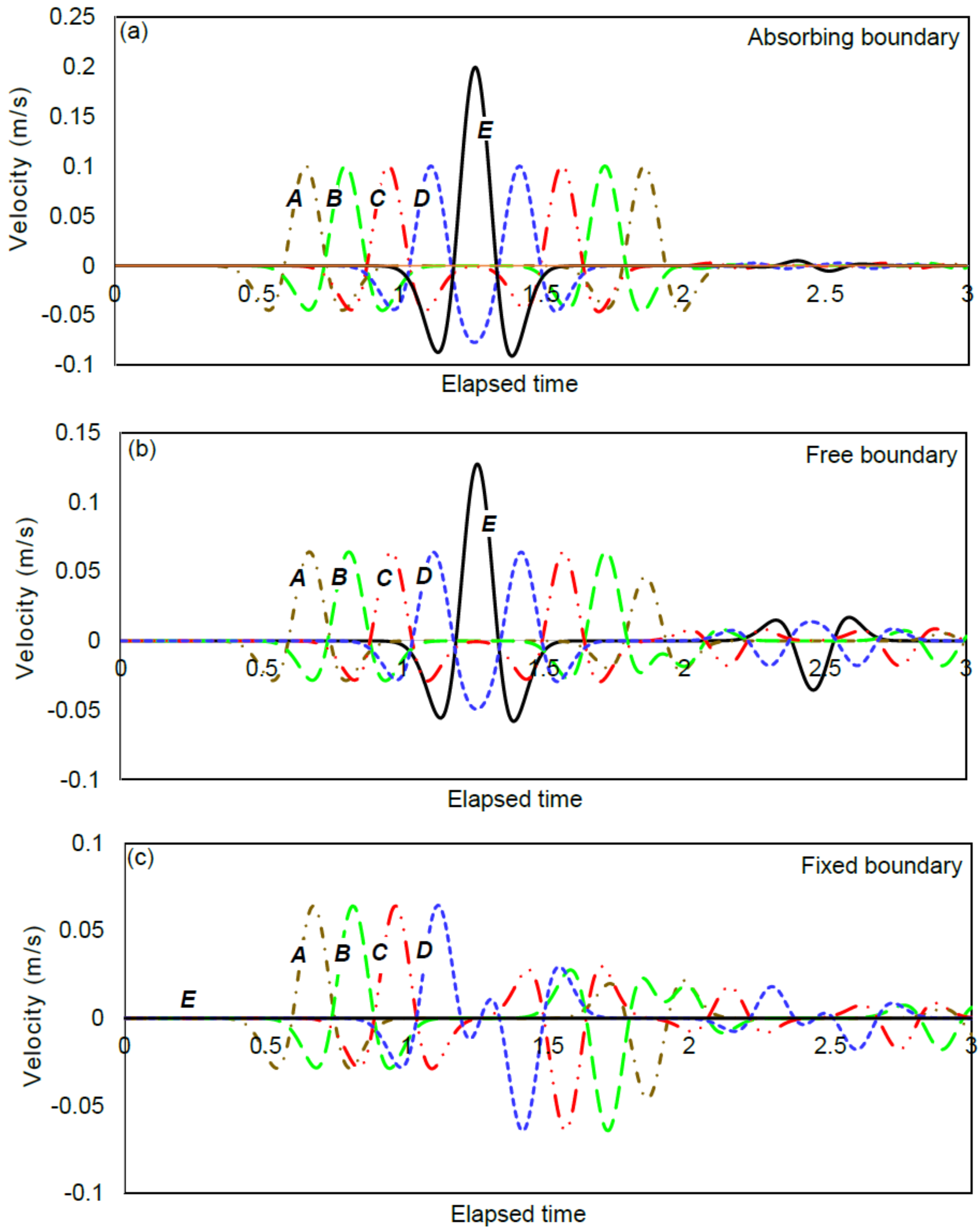

Figure 5 - 7. Ricker wavelet time history calculated at five points along the rock column using DEM. (a) absorbing boundary; (b) free boundary; (c) fixed boundary.

5.4.3. Damping

To study the collisional characteristics of the landslide, viscous damping must be applied with supplementary employment of local damping to reproduce a realistic response. When viscous damping is active, normal and shear dashpots are added at each contact and act in parallel with the parallel bond model. Damping force is then calculated by the relative velocity at each contact, and acts to oppose motion. The normal and shear viscous damping ratios are selected to be 0.21 and 0.02, respectively, as suggested by Feng et al. (2017).

The local damping, which adds a drag force to the accelerating particles to dissipate energy, is a simple but feasible approach to simulate the air friction (Jiang et al. 2015). The local damping coefficient is determined by comparing the numerical and theoretical results obtained for free falling tests:

$$v = \sqrt{2g \cdot h} \qquad (12)$$

where v is the rock block velocity, h is the drop height.

It can be seen from Fig. 5 - 8 that the local damping constant is set to 0.02, in which the DE simulated result is in agreement with the theoretical calculation.

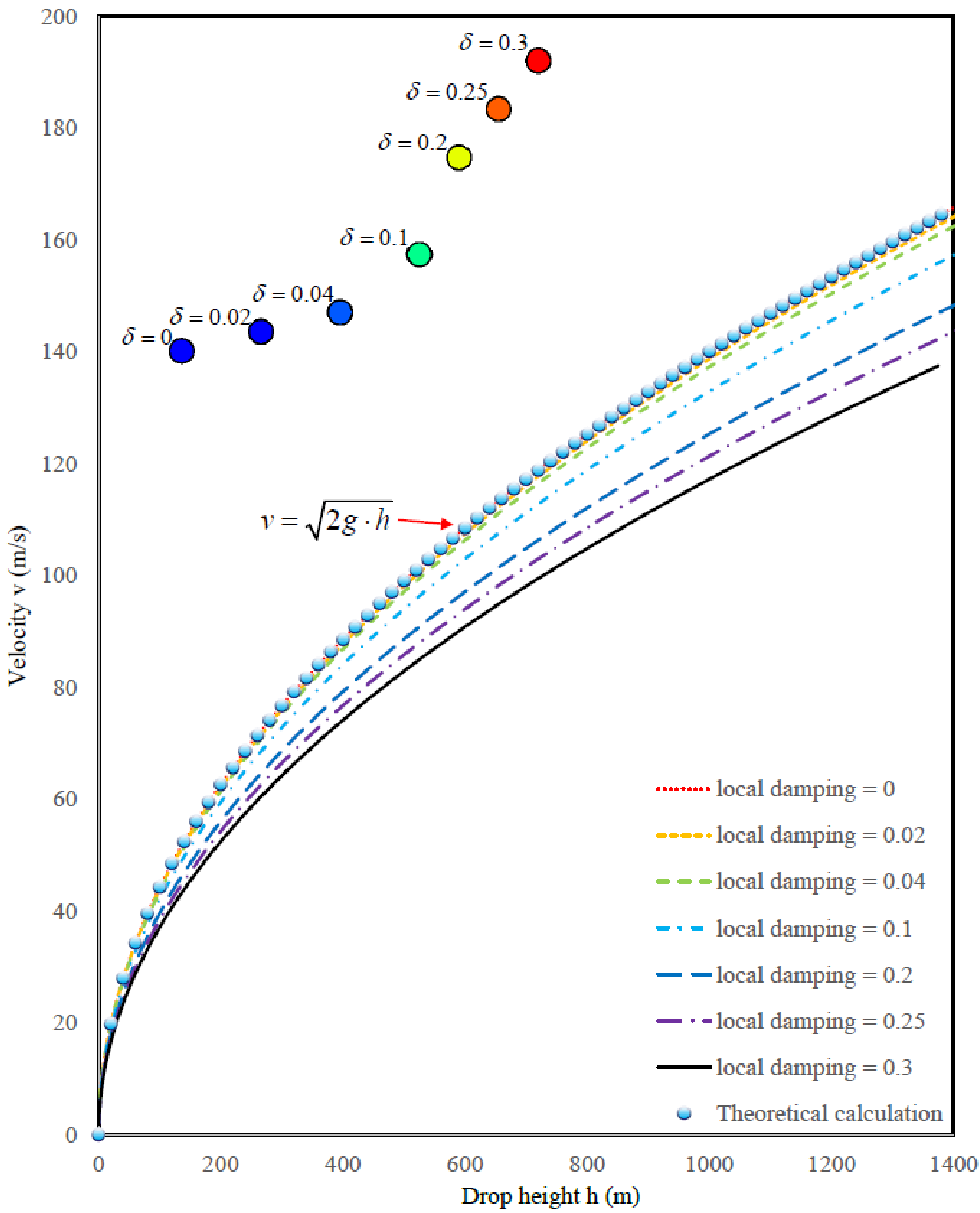

Figure 5 - 8. Relationships between velocity and drop height with different local damping coefficients obtained from DEM free falling tests and theoretical calculation.

5.4.4. Model setup

The DEM model has been developed to replicate the site conditions at the location of the investigated landslide. The steps taken to create the model are summarized as follows:

(a) The first step consists in generating an assembly of particles within the slope area to represent the rock material. As the modeled area in this case is relatively large, efforts are made to keep the computational cost at a reasonable level by using ranges of particle sizes that are relatively small near the zone of the sliding mass and larger particles elsewhere in the model. Thus, the sizes of the 2D discrete elements (disks) are chosen such that the minimum diameter is 1.0 m in the source area and increases to 2.5 m within the rest of the model (the bedrock) as shown in Fig. 5 - 9a. In addition, the size ratio $r_{\max} / r_{\min}$ of the rigid particles numbers 1.6 to prevent a reorganization of the particles within a closed-packed lattice, which otherwise would dramatically alter the behavior of the particle assembly (Potyondy and Cundall 2004; Imre et al. 2010). A total of 30286 elements are used in the model including 11069 and 19217 elements for the source area and the bedrock, respectively. Linear contact model is first assigned to all distinct elements and the model is cycled to equilibrium to ensure that a steady state condition is achieved.

(b) After the system reaches equilibrium, the generated assemblies of particles in both the bedrock and the source area were assigned linear parallel-bonded contacts to simulate the rock material. The microparameters for particles in the source area are adopted from the aforementioned calibration. It is worth noting that the interparticle bonds in the bedrock need to be large enough to effectively represent the rock bridges between adjacent particles, contributing enough cohesion to the intact sandy slate and shale. To better visualize the emplacement process of the landslide, four layers are painted using different colors, as shown in Fig. 5 - 9a.

(c) During the third step, joint sets are implanted into the numerical model. On account of complexity of actual rock mass structure, it is difficult to accurately reflect and model field conditions. In fact, the persistence, pattern and orientation of joint sets in real natural rock slopes vary spatially and small discontinuities are also contributing to the degradation of rock mass strength. However, modeling the representative joint sets is helpful for understanding the performance of the DE analysis on the failure, runout and fragmentation behavior of landslides. Therefore, in this study three main joint sets are introduced in the 2D simulation model, including the joint sets J_1 (dip 68°, dip direction 120°), J_2 (dip 65°, dip direction 200°), and J_3 (dip 82°, dip direction 72°), subparallel to topography. J_1 and J_2 as lateral release surfaces of the instabilities have important effects on dissecting the rock mass into multi-shaped blocks. J_3 plays a fundamental role in contributing to initiation and development of shear planes. Because of the absence of infilling material in all discontinuities, the joints in a given zone are here defined by debonding particles along the joint plane with a 1.2 m thickness (≈ the mean particle diameter). Here all joint sets are created to be fully persistent and a certain amount of debonded particles will be dispersed in the joint gaps, therefore, the rock mass is altered with pre-existing joint sets, and presented in the form of fragment network as shown in Fig. 5 - 9b. Following the introduction of the joint sets, the model is cycled again to equilibrium under gravity to ensure steady-state condition is reached.

(d) The final step of the modeling process consists in applying the seismic-induced ground velocities along the base of the model at the horizontal and vertical directions. According to the landslide profile direction of N76°E, the resultant seismic shaking in the horizontal direction starting from the EW (see Fig. 5 - 10a) and NS (see Fig. 5 - 10b) seismic components can be calculated as shown in Fig. 5 - 10c, and the vertical acceleration is set as the UD component of seismic motion (see Fig. 5 - 10e). By integrations, baseline corrections, and band-pass filtering, the horizontal and vertical ground velocities is obtained as shown in Fig. 5 - 10d&f. Previous studies using DEM for analyzing earthquake-induced landslides have simplified the process that the slope shaking is synchronized along the failure plane in spite of different elevations (Tang et al. 2009; Wu et al. 2009; Wu and Chen 2011). In fact, considering that the seismic shaking wave reaches the predefined failure plane being non-synchronous due to the different elevations. Therefore, in this study the seismic wave is set to travel from the bedrock upwards into the slope mass, which makes numerical model can replicate the natural systems more accurately. In addition, the traveling velocities of P and S waves in this region is calculated using equations (9) and (10) as 2,243 m/s (V_p) and 1222 m/s (V_s)， which is in consistent with previously stated facts that relatively low P wave velocities near the ground surface were found in the area of the Longmenshan fault range consisting of mainly Quaternary deposits (Wu et al., 2009).

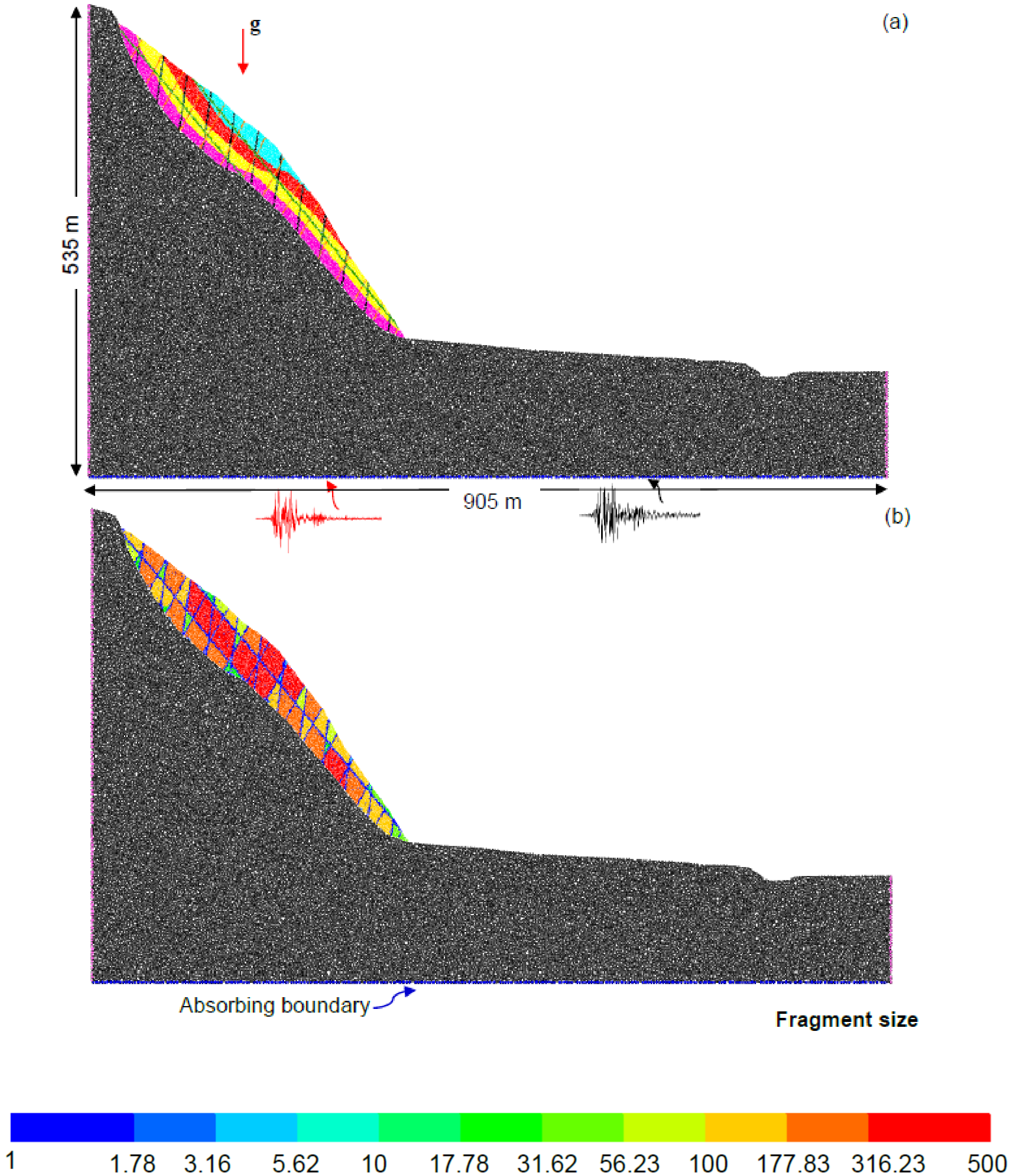

Figure 5 - 9. (a) Two-dimensional discrete element model of the landslide; (b) The corresponding fragment network due to the presence of the rock discontinuities.

Note: The logarithmic hue scale indicates the size of each fragment. Large fragments are represented by green to red colours whereas fine particles are given blue colour.

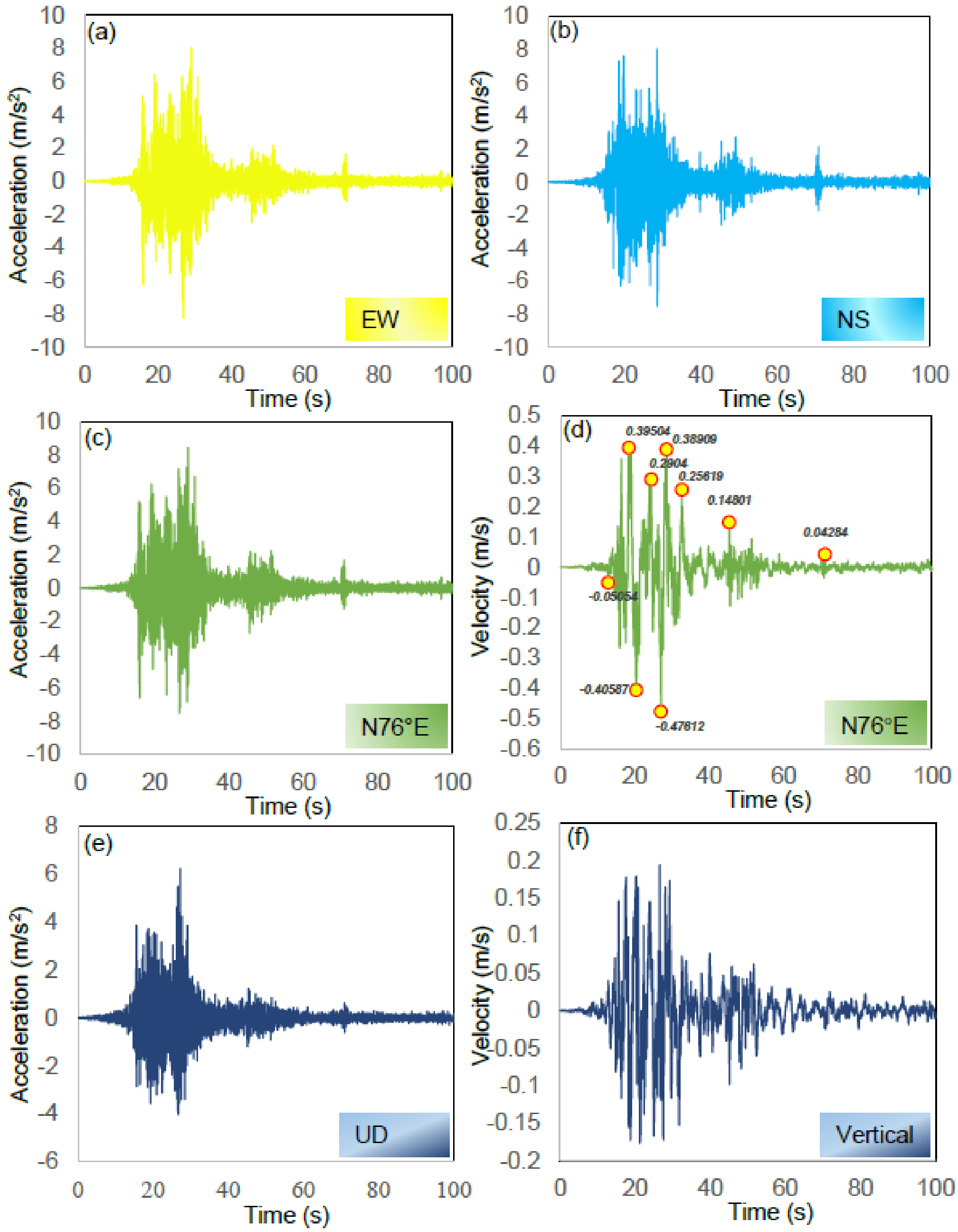

Figure 5 - 10. Seismic time history curves: (a) EW acceleration; (b) NS acceleration; (c) Horizontal acceleration; (d) Horizontal velocity; (e) Vertical acceleration; (f) Vertical velocity.

5.5. Results and Discussion

5.5.1. Deformation evolution

A visual presentation of the dynamic deformation process of the earthquake-induced Wangjiayan landslide is provided by selecting 9 distinct timestamps, as shown in Fig. 5 - 11. According to the figure, the slope failure occurs at about 7.1 s when tensile cracks initiate from the joint tip and propagate along the joint to the upper front region of the slope, corresponding to the location where the tensile stresses were concentrated. The failure initiated with disintegration of the slope material through the breakage of interparticle bonds, leading to loss of internal cohesion. In the meantime, the ground seismic shaking accelerations in two directions both begin to have relatively obvious fluctuations (see Fig. 5 - 10). After the failure initiation, block sliding occurs when the coalescence has formed among the fractures in the rock bridges, the joints, and the tensile cracks that propagated to the slope surface. From 12 to 28 s, there is an abrupt change of ground motion, such that the cracks widened laterally and propagated vertically to the detachment surface, facilitating the subsequent downslope acceleration of landslide. As a result, the rock mass instantly begins to collapse into progressively smaller and more numerous joint-determined fragments as it travels down rapidly along the failure plane. Thus, rotation and collision are remarkable in the failure process, and some more rapid superficial movement and subsequent successive destabilizations at the sliding front are observed during the earthquake excitement (see Fig. 5 - 11c – 5 - 11e). After about 28.5 s (see Fig. 5 - 11d), the clustered fractures in the rear region of the lower portion of the slope, which corresponds to the topographic convexity, begins to propagate upward along the joint set and grow to completion rapidly, leading to the separation of rock mass and the production of many fragments with relatively small sizes. The detached slope mass experiences intense interactions with the bedrock as the landslide collides onto the valley and continue to travel across the flat terrain at a high speed (see Fig. 5 - 11d&e). The subsequent landslide propagation causes more damages to the slope mass, especially within the sliding front and topography change regions (transiting from topographic convexity to topographic concavity) as reflected by the gradual enlargement of damage zones. As the enlarged damage zone coalesce to completion from the failure plane to the internal slope mass (see Fig. 5 - 11f&g), this enables the complete development of dynamic disintegration and dilatancy (controlled by pre-existing sub-vertical discontinuity sets J_1 and J_2) transforming the rock mass into a granular material promoting the full separation and whole movement along the sliding surface. As presented in Fig. 5 - 11i, the collective motion works to stretch and thin the detached slope mass and represents a graduate decrease in inclination angle of the final deposit from proximal to distal sections. The inclination angle within the rear part of the deposition measured in the numerical simulation is 33º， which is slightly smaller than that obtained from field investigation. In addition, the final runout distance (L_f in Fig. 5 - 11i) is 337.2 m, which is unsubstantially longer than the observed one, i.e., 320 m.

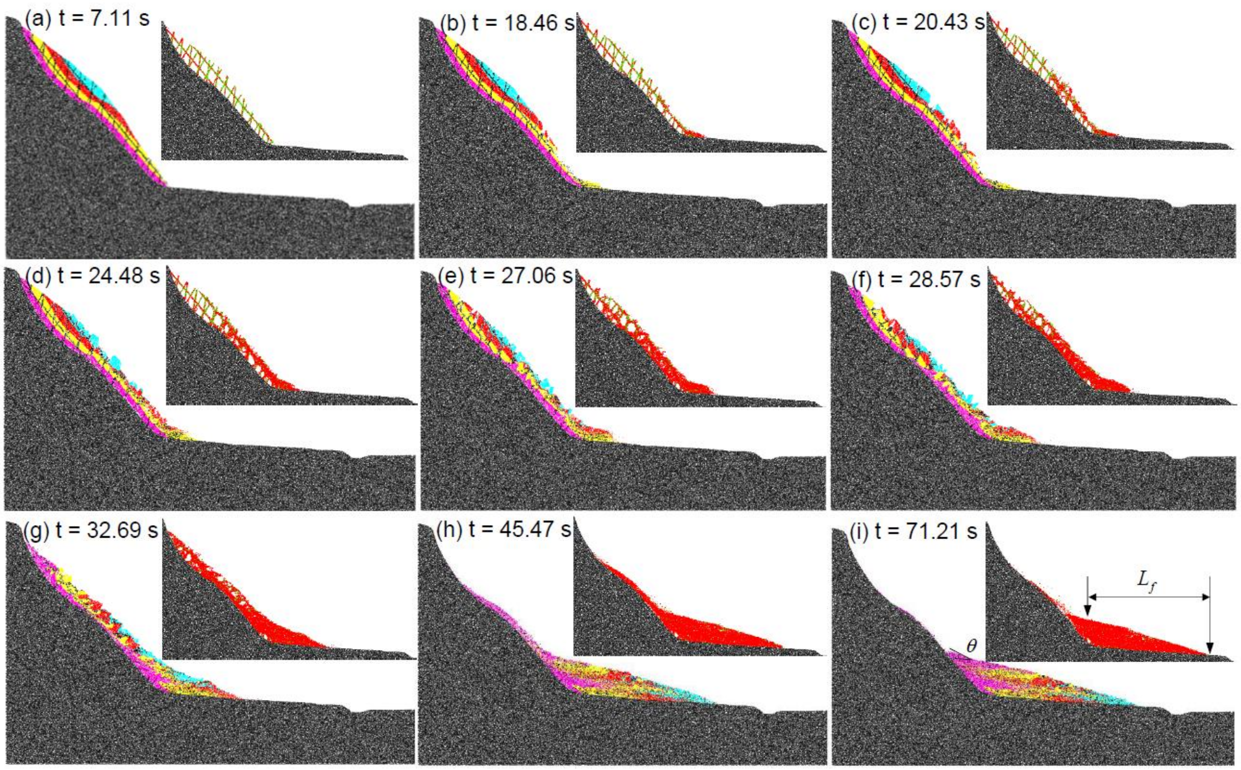

Figure 5 - 11. The emplacement evolution of the Wangjiayan landslide at the selected timestamps: (a) 7.11 s; (b) 18.46s; (c) 20.43 s; (d) 24.48 s; (e) 27.06 s; (f) 28.57 s; (g) 32.69 s; (h) 45.47 s; (i) 71.21 s.

Note: The inset plot shows the details of crack distribution developed at the selected timestamp

5.5.2. Disintegration process

The landslide starts out as a jointed rock mass that can disintegrate during transport. Disintegration process can be divided into two types (Pollet and Schneider, 2004; Haug, 2015). (i) A primary (static), where the rock mass separates by breaking the rock bridges connecting fragments of competent rock (Eberhardt et al. 2004), and (ii) dynamic fragmentation where these particles are continuously reduced in size by grinding and comminution (Pollet and Schneider 2004; Imre et al. 2010; Haug 2015; Perinotto et al. 2015). This sequence of disintegration process can also be observed in this analysis, as shown in Fig. 5 - 12. It is worth mentioning that the same 9 timestamps used for deformation evolution of Fig. 5 - 11 is still applied here. Each joint-determined block in the source area is attributed a color that depends on its volume, expressed as the number of unit particles it contains (the hue scale in the figure is logarithmic). Before being released, the slope mass remains almost static and only elastic deformation occurs with very few bond breakages (see Fig. 5 - 12a&b). Then, as the ground shaking intensity increases, bond breakages nucleate at the slope toe and cause instability from loosening rock blocks along the discontinuity (e.g., Fig. 5 - 12c at t = 20.43 s). Then, failure propagated upward to an upper region of the slope with further material disintegration and the rock block is then progressively fragmented, producing lots of small fragments in the frontal region (see Fig. 5 - 12d&e). Concurrently, as the intensive seismic shakings proceed, the rock fracturing development progresses rapidly up to the slope crest, thus joint-bound rock material overlying the failure plane becomes detached, moves downward, runs out for some distance, and subsequently deposits downslope (See Fig. 5 - 12f – 5 - 12h). It is worth noting the final disintegrated landslide deposit material contained large intact blocks preserving original structures, along with highly-fragmented rock with prevalence of finely crushed matrix material within the center of deposit (See Fig. 5 - 12i), which matches well with the actual deposit. In addition, it implies a dynamic disintegration created by intensive shearing and dilatancy along the failure planes (Pedrazzini et al. 2013; Wang et al. 2018) accompanied by progressive grain size reduction during the entire transport phase of the landslide. The dynamics of disintegration can be quantified by recording the internal rock damage ratio (D) over time and computing at each timestamp the number of fine fragments. The fine fragments are those that have been reduced to a unit disk particle and cannot be further split (Langlois et al. 2015). The rock damage ratio D is defined as the percentage of broken bonds occurring during the landslide over the total number of bonds at the initial static state. As stated by Zhao et al. (2018), the evolution of D can effectively characterize the progressive damage of a rock mass. In the analyses, the ground shaking velocities in the vertical and the sliding directions are also plotted in Fig. 5 - 13a to illustrate the seismic-induced slope damage (Zhao and Crosta 2018). It can be observed in Fig. 5 - 13a that no damage occurs before 7.11 s (t_0) because of the very small intensity of seismic shaking. Between t_0 to t_1 (16.8 s), the ground shaking intensity increases abruptly, particularly in the sliding direction. Thus, the percentage of slope damage in the layer *II* increases very rapidly with time, indicating that the fracturing initiated along the rock discontinuities with disintegration of the slope material through the breakage of interparticle bonds. This can be explained by that with the arrival of intense seismic shakings and the presence of the network of existing discontinuities, the slope mass is more susceptible to lose cohesions due to debonded grains being relatively unconstrained. As the intense earthquake ground motions continuously vibrates, joint-bounded intact rock strength was degraded as damage ratio accumulated fairly linearly until it reaches a relatively large value at t_2 (49.7 s). The subsequent sliding and impacting of fragmented rock blocks onto the valley floor during the landslide deposition can lead to further increase of D. During this process, layer *I* suffers the highest damage among the four layers due to the intense shearing with the bedrock. Layer *IV* also exhibits relatively high damage at the deposition stage, mainly because of its low strength and high compression loading near the ground surface. Middle layers *II* and *III*, in particular, layer *III* shows the smallest final rock damages, being constrained by the upper and lower layers. The final stable peak values of D, D - *I*, D - *II*, D - *III* and D - *IV* are 70.0%, 75.0%, 66.5%, 68.9 % and 69.5%, respectively.

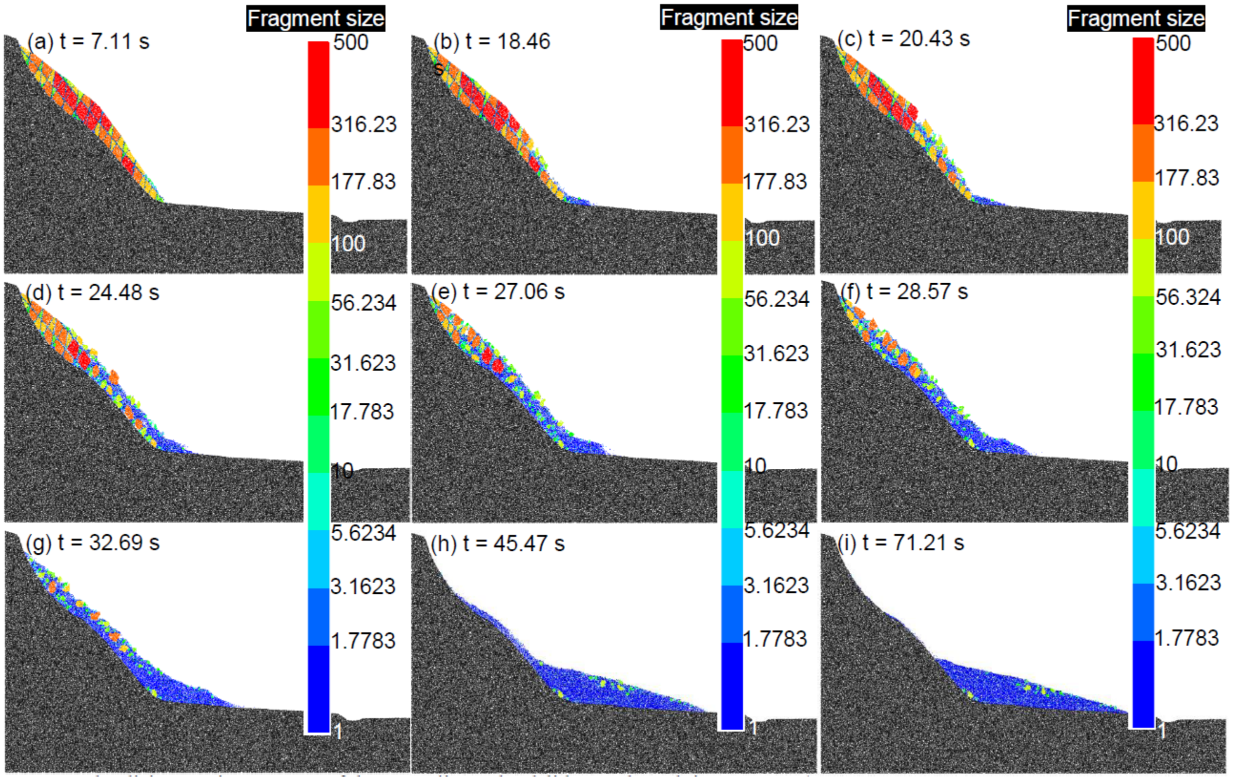

Figure 5 - 12. The disintegration process of the Wangjiayan landslide at selected timestamps: (a) 7.11 s; (b) 18.46s; (c) 20.43 s; (d) 24.48 s; (e) 27.06 s; (f) 28.57 s; (g) 32.69 s; (h) 45.47 s; (i) 71.21 s.

Note: The logarithmic hue scale indicates the size of each fragment. Large fragments are represented by green to red colours whereas fine particles are given blue colour.

As stated by Langlois et al. (2015), the volume fraction of fine particles can provide a good quantitative assessment of the fragmentation dynamics in a landslide. The evolution of the volumetric fraction of the fine fragments is found to follow the same trend as the damage ratio (see Fig. 5 - 13b). Before slope failure at time t_0 (7.11 s), at relatively small ground shaking velocities, the volume fraction of fine fragments remains constant around 0.02 as a result of the debonded particles dispersing along the joint planes. As the ground shaking accelerates, an increase in finer fraction is found to reach around 0.07 at time t_1 (16.8 s), suggesting that the disintegration of the material starts immediately after the collapse. Then, as the intense seismic shakings last for a period to t_2 (49.7 s), the volume fraction of fine fragments increases at a much more quickening rate characterized by the rapid growth of cracks and obvious reduction of clast size. It should be noted that the runout is only 50% of its final value but 75% of the final number of fine fragments have already been produced at time around 32 s (see Fig. 5 - 12i). Thus, disintegration obviously takes place in the course of downslope ride. It is concordant with observations that the fragmented debris in the landslide deposits is consecutively reduced in grain size along the transport path, which has been reported in some well-documented numerical and field examples (Perinotto et al. 2016; Zhang et al. 2016 & 2019). Moreover, the growth rate of fragment number is then used to as an indicator to quantifying rock fragmentation intensity during the emplacement evolution of seismic-induced landslide. According to Figure 5 - 13b, the general variation of growth ratio of fragment number indicates that during landslide (i.e., initiation, propagation and deposition), the number of fragments has been reduced. After t_1 (16.8 s), as the seismic shakings remain at high intensity, propagating cracks could extend and coalesce with neighbouring joints resulting in the development of a connected fragmented granular material along the failure plane, as reflected by the rapid growth rate of fragment number up to maximum at 27.5 s. This corresponds well with the horizontal seismic velocity reaching its maximum magnitude. Subsequently, multiple fractures grow continuously at many, closely spaced points, and persist accumulating as long as external input energy is available until the landslide loses momentum and deposits in the runout area. However, during the same period from t_1 to t_2 (49.7 s), the number of fragments declines rapidly. This phenomenon is expected as the fragmentation of the joint-bound rock mass produced a large amount of dispersed grains under the sustained intense seismic shakings, which leads to freshly broken fragments material progressively pulverized into fine-grained material. As a consequence, a decrease in the number of fragments can be observed. In addition, the prevalence of the fine-grained matrix can absorb a large portion of kinetic energy of the incoming rock fragments, which in turn preserves some relatively large boulder clusters.

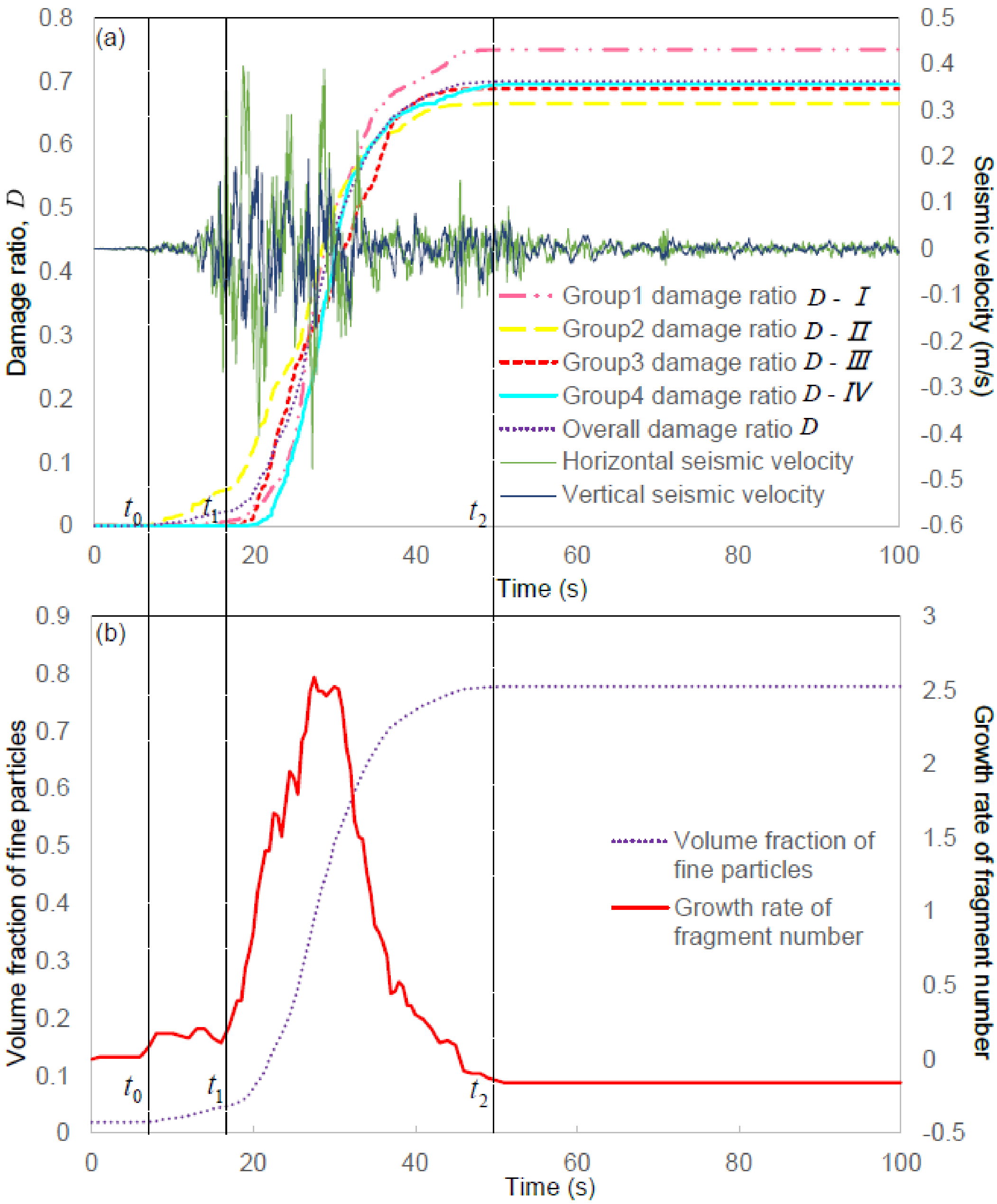

Figure 5 - 13. (a) Evolution of rock damage in each slope layer and ground seismic shaking; (b) Evolution of volumetric fraction of fine fragments and growth rate of fragment number.

5.5.3. Granular temperature and dispersive stress

During the high-speed motion of the sliding mass after detaching from the source area, particles along the discontinuities exhibit high fluctuations due to the transformation of particle translational energy to vibrational energy. This induced a high collisional frequency between particles producing a strong impact pressure that easily exceeds the ultimate particle strength and induces a dynamic fragmentation with brittle features. Granular temperature in this context is proportional to the average value of the square of the grains' velocity fluctuations, with respect to their mean velocity. In this approach, and is used here as a mean to measure the velocity fluctuations of a particle (Zhou et al. 2016):

$$v_x^i(t)' = v_x^i(t) - \overline{v_x^i(t)} \tag{13}$$

$$v_y^i(t)' = v_y^i(t) - \overline{v_y^i(t)} \tag{14}$$

$$\omega^i(t)' = \omega^i(t) - \overline{\omega^i(t)} \tag{15}$$

where translational velocity components $v_x^i(t)$, $v_y^i(t)$ and angular velocity component $\omega^i(t)$ of the selected i -th particle in the granular ensemble can be divided into the mean velocity components $\overline{v_x^i(t)}$, $\overline{v_y^i(t)}$, and $\overline{\omega^i(t)}$ and fluctuating parts $v_x^i(t)'$, $v_y^i(t)'$, and $\omega^i(t)'$.

The mean velocity components $\overline{v_x^i(t)}$, $\overline{v_y^i(t)}$, and $\overline{\omega^i(t)}$ can be attained by averaging the velocities of particles surrounding the selected i -th particle in the assembly of discrete solid mass:

$$\overline{v_x^i(t)} = \frac{1}{n}\sum_{j=1}^{n} v_x^j(t) \tag{16}$$

$$\overline{v_y^i(t)} = \frac{1}{n}\sum_{j=1}^{n} v_y^j(t) \tag{17}$$

$$\overline{\omega^i(t)} = \frac{1}{n}\sum_{j=1}^{n} \omega^j(t) \tag{18}$$

Hence, the vibrational $T_V^i(t)$ and rotational $T_R^i(t)$ granular temperatures representing the intensity of particle exchange analogous to a thermodynamic temperature are calculated from the velocity fluctuations are expressed as follows:

$$T_V^i(t) = \frac{1}{2}[(v_x^i(t)')^2 + (v_y^i(t)')^2] \qquad (19)$$

$$T_R^i(t) = (\omega^i(t)')^2 \qquad (20)$$

Moreover, by averaging $T_V^i(t)$ and $T_R^i(t)$ of all the particles composing the slope mass, the parameter $T_V(t)$ and $T_R(t)$ exhibiting the fluctuation intensity (degree of agitation) for the entire landslide is introduced:

$$T_V(t) = \frac{1}{N}\sum_{i=1}^{N} T_V^i(t) = \frac{1}{2N}\sum_{i=1}^{N}(v_x^i(t)')^2 + (v_y^i(t)')^2 \qquad (21)$$

$$T_R(t) = \frac{1}{N}\sum_{i=1}^{N} T_R^i(t) = \frac{1}{N}\sum_{i=1}^{N}(\omega^i(t)')^2 \qquad (22)$$

Figure 5 - 14 illustrates the evolution of granular temperature for the entire granular system. It can be seen that after slope failure (t_0), both vibrational and rotational granular temperatures increase immediately with time. There is a slight increase of both temperatures between 7 and 16 s due to landslide acceleration. $T_V(t)$ and $T_R(t)$ reach the peak values of 63.1 and 12.0 m^2/s^2, respectively, at around 35.02 s. Then, they both decrease gradually to nil when the bulk landslide mass gradually ceases motion after 70 s. According to the overall evolution of the granular temperatures for the entire granular system, five distinct timestamps are selected to show the distribution of $T_V^i(t)$ and $T_R^i(t)$ inside the granular body as presented in Fig. 5 - 15. At timestamp t = 15.74 s, the vibrational and rotation granular temperatures develop synchronously along the rock discontinuities because of their relatively weaker rock structure and fewer restriction. As the seismic shakings proceed, there is an abrupt change of ground motion (see the seismic acceleration vectors and the horizontal and vertical velocity components in Fig. 5 - 10), such that more intense fracturing propagates and coalesce along the rock discontinuities accompanied with substantial release of fluctuation (e.g.,

Fig. 5 - 15c at 24. 5s). With development of more intense seismic shaking, cracks develop and grow to completion quickly along the basal failure plane, where it is composed of particles that, moving and colliding at high velocity, activate extensive fluctuations of vibrational and rotational granular temperatures (see Fig. 5 - 15e&f). This observation indicates that during landslide propagation high granular temperature is generated in the basal layer where the intense sharing promotes the particle rearrangement characterized by vigorous particle agitation. This higher granular temperature implies more rapid particle exchange and higher rates of particle collisions. However, the coarse fragments on the free surface are passively carried by neighboring fine-grained particles and are barely collision dominant, with the enhancement of granular temperature and fluctuation rarely observed. With the subsequent sliding and impacting of detached slope mass onto the valley floor during the landslide deposition, the granular temperatures possess relatively large values near the front and rear regions and quickly dissipates towards the interior of the accumulated deposit. This phenomenon is explained by the fact that particles in the rear region that are still falling down the slope transfer their momentum by pushing the deposit forward, and therefore frontal slope mass becomes even more collision dominant with collisions on the free surface enhanced under little constraint. After the intense seismic shaking period, the particles in the accumulated deposit therefore exhibit a gradually attenuating fluctuation intensity. This phenomenon accords well with the statement that the granular temperature can be dissipated or vanished rapidly due to interparticle collisions when external energy stops (Campbell 1990).

As stated by Wang et al. (2012), particle fragmentation caused by frequent intensive collisions will occur as the increase of granular temperature accumulated in particles, at the same time, this process can result in the generation of dispersive stresses, which can further dilate and disperse the detached slope material (Davies et al. 1999), facilitating the occurrence of fragmentation and leading to a farther movement of the avalanche. Hence, the deviator stress q' introduced by Imre (2010) is calculated to quantify the dispersed state and analyze the influence of fragmentation on the emplacement of landslides, which is shown below:

$$q' = \frac{1}{\sqrt{2}}\left[\left(\sigma'_{1,f} - \sigma'_{2,f}\right)^2\right]^{1/2} \tag{23}$$

The input average normal and shear stress tensor $\bar{\sigma}_{ij}^{(P)}$ of a particle (p) is calculated as

$$\bar{\sigma}_{ij}^{(P)} = \frac{1}{V^{(P)}} \sum_{N_c} \left| x_i^{(c)} - x_i^{(p)} \right| \cdot n_i^{(c,p)} \cdot F_j^{(c)} t_f \qquad (24)$$

where V is the volume of the particle, N_c is the number of particle/particle or particle/ground contacts acting on (p), $x_i^{(p)}$ and $x_i^{(c)}$ are the locations of the particle centroid and its contacts, $n_i^{(c,p)}$ is the unit normal vector directed from a particle centroid to its contact location and $F_j^{(c)}$ is the force acting at a contact. The magnitudes and the directions of the principal stresses $\sigma_{1,f}^{'}$ and $\sigma_{2,f}^{'}$ of particles undergoing fragmentation are calculated from (24) as the eigenvalues and eigenvectors of the stress tensor $\bar{\sigma}_{ij}^{(P)}$.

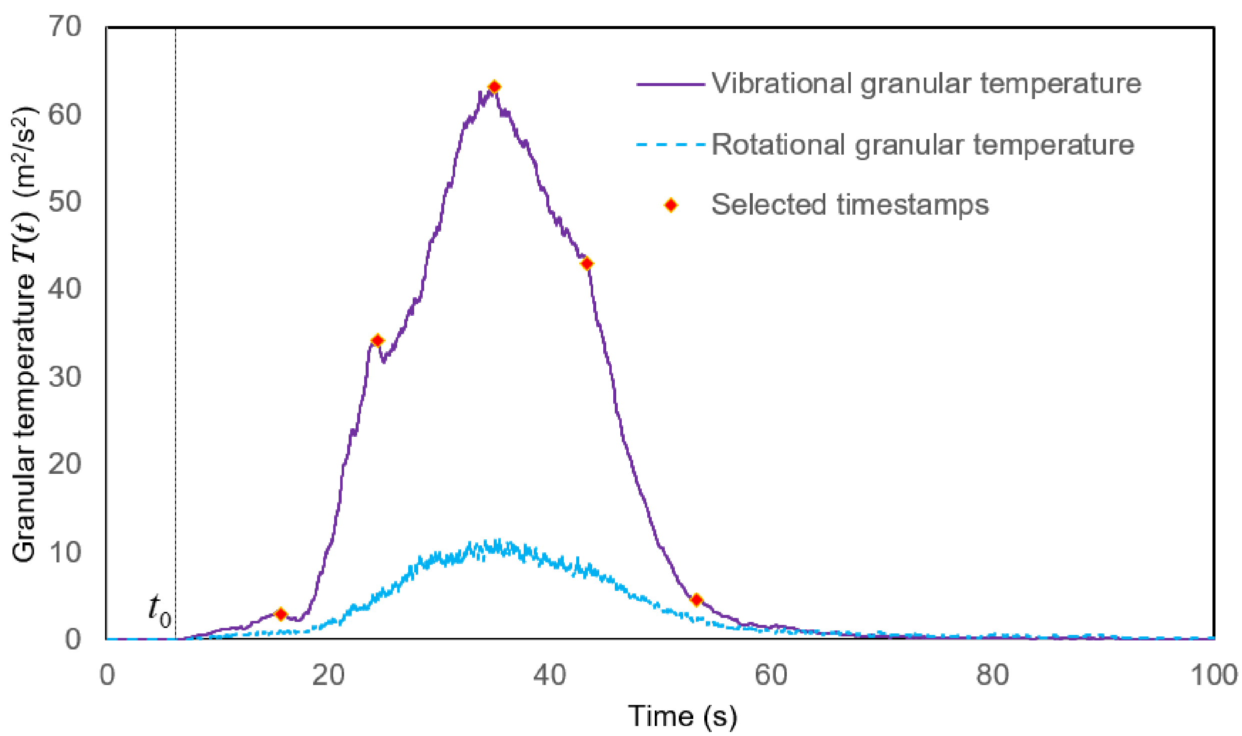

Figure 5 - 14. Evolution of the vibrational (T_V) and rotational (T_R) granular temperatures within the translating slope mass.

Fig. 5 - 16a illustrates the variation of q' over time during the landslide simulation. According to the figure, it can be seen that from 0 to 4.6 s, q' fluctuates slightly around a constant value of 1.7 MPa due to seismic shaking. Then, it fluctuates abruptly from 1.7 to 0.9 MPa during a short period

of time near t_0 = 7.11 s before the slope failure. As the ground shaking accelerates, the rock bridges break intermittently and the cracks grow steadily within the detached slope mass, resulting in a significant increase of dispersive stress with increased fluctuation intensity. The value of q' reaches high value of 10.95 MPa at 16.5 s as the slope mass descends from its in situ position and experiences temporary relief when frictional bonds along the pre-existing discontinuities are progressively overcome. As the ground continuously vibrates, the deviator stress q' reaches its maximum of 16.8 MPa at 22.7 s and experiences wild fluctuations in the subsequent landslide propagation, immediately following rock mass break-up with relatively minor fragmentation as the sliding body evolves from block sliding with a finite increment of landslide motion to more dynamic fragmented flows. A rock mass subject to such stress fluctuations will be more readily fractured and therefore latter development of the stress variation with increased fluctuation intensity may promote the development of fragmented or fine-grained basal shearing layer. Furthermore, it results in an increasing proportion matrix to blocks with displacement in response to progressive dynamic disintegration of an increasing number of finer grains. As illustrated in Fig. 5 - 16c&d, at time of t = 16.5 s and t = 22.7 s, when the deviator stress q' reach the 11.0 MPa, and 16.8 MPa (highest), respectively, the relative velocities between the particles are so high that stresses sufficient to yield fragmentation occur. Particles coloured in blue indicate a practically stress free, dispersed zone of the assembly where all particles are fracturing, collapsing and dilating as it does so into a loose granular mass (see Fig. 5 - 16d). With the presence of particle dilation and enhancement of particle fluctuation during the intense shaking period, the intensity of particle collisions will be strengthened by increasing a relative velocity and induce the occurrence of intense dynamic fragmentation. This phenomenon illustrates clearly that during the extremely rapid motion of the sliding mass, a strongly sheared and agitated layer spontaneously appears representing a highly dynamic collisional granular regime. Correspondingly, a dispersive pressure is generated with the occurrence of a locally high dilation and supports a relatively sparse packing of grains moving as a whole, which is well in accordance with dynamic fragmentation hypotheses (Davies 1982; Taberlet et al. 2007; David et al. 1999; Wang et al. 2015). In the highly dispersed state, indicated by the blue colouring of the particles (see Fig. 5 - 16e), the generation of a dispersive stress due to fragmentation also can further dilate and disperse the particle assembly, further facilitating the occurrence of dynamic disintegration. After t_1 = 71.2 s, q' remains relatively small (≈ 0.32 MPa) and then slightly dropped to 0.28 MPa at t = 100 s (See Fig. 5 - 16f & g), because the slope mass has arrived at a low-speed deposition state and readjust to accommodate much of the deformation taking place in the sliding body during emplacement, and allowing itself organizing into a steady flow across the horizontal runout valley.

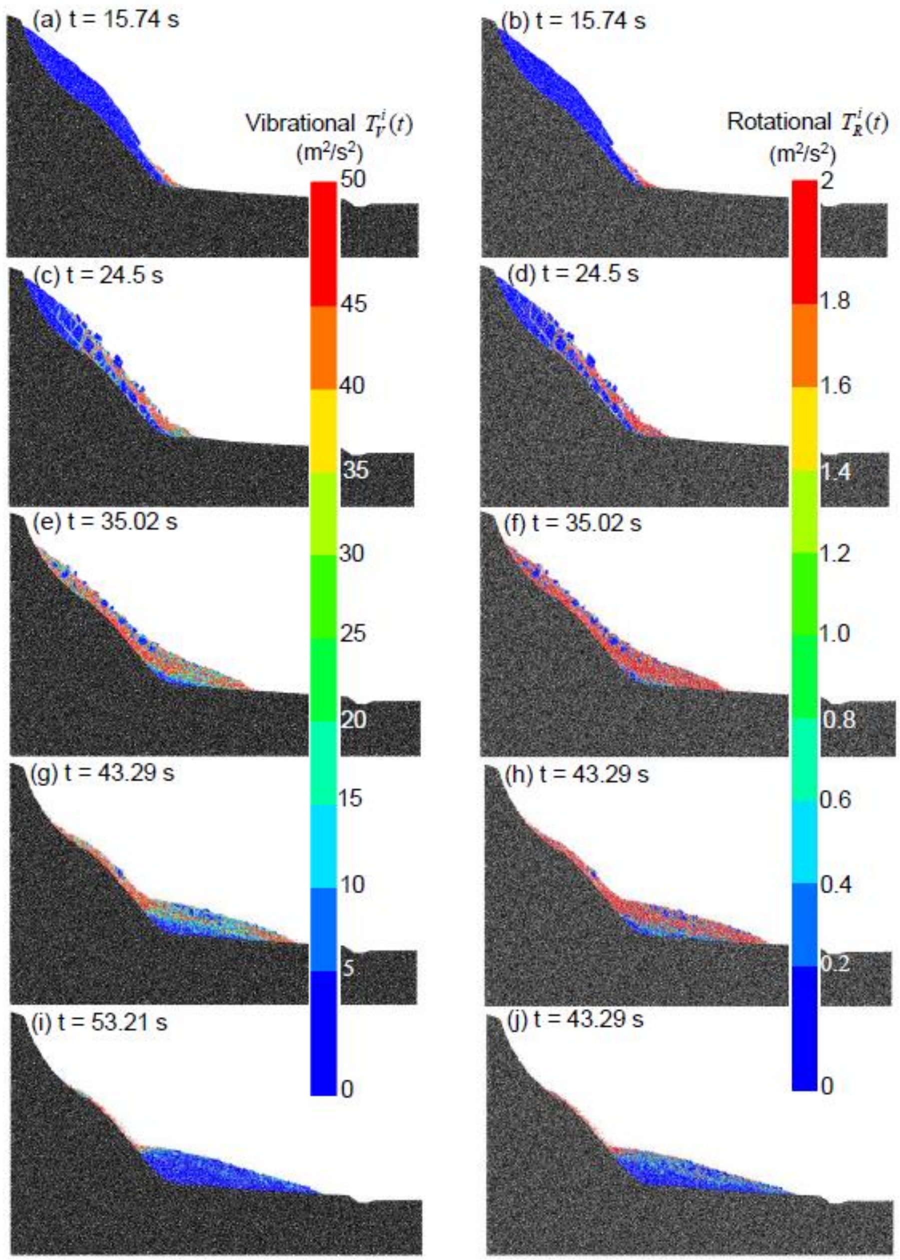

Figure 5 - 15. The distribution of granular temperatures within the Wangjiayan landslide at the selected timestamps: (a), (b) 15.74 s; (c), (d) 24.5s; (e), (f) 35.02 s; (g), (h) 43.29 s; (i), (j) 53.21 s.

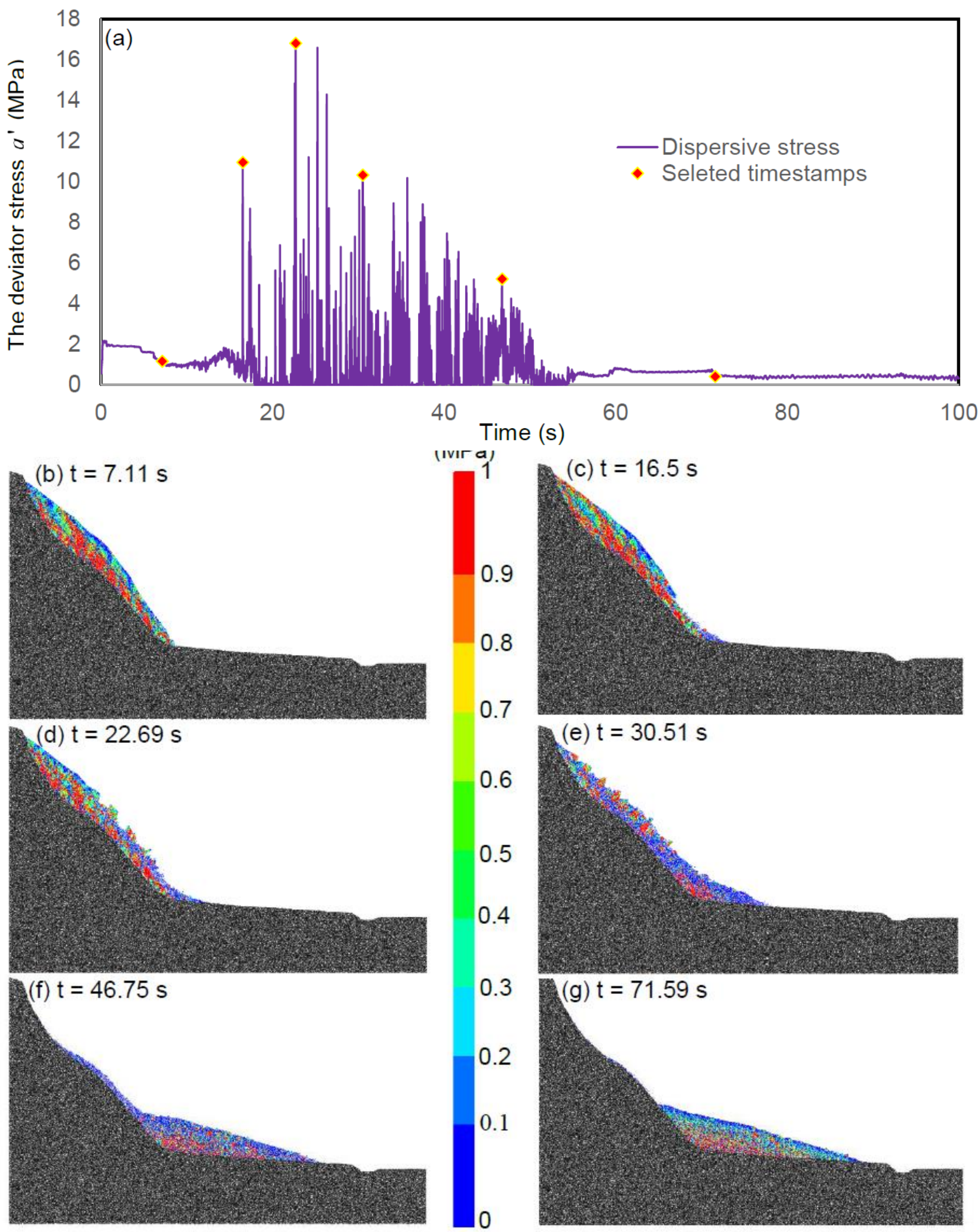

Figure 5 - 16. (a) Variations of the deviator stress of the Wangjiayan landslide; the distribution of the deviator stress within the landslide at the selected timestamps: (b) 7.11 s; (c) 16.5s; (d) 22.69 s; (e) 30.51 s; (f) 46.75 s; (g) 71.59 s.

5.5.4. Morphology and structure of fragmented deposits

Rapid earthquake loadings cause cross-cutting fractures to be nucleated in different, closely spaced parts of the slope material nearly simultaneously, subsequently growing and merging leads to instantaneous fragmentation and pulverization of the solid. Eventually, with the declination of decreased seismic intensities, the fragmented slope comes to a final stop. This catastrophic process appears chaotic and unpredictable. However, out of the randomness, the mass distribution of fragments $p(m)$ as the most important characteristic quantity of the fragmenting system is found to exhibit a power law behavior:

$$p(m) \sim m^{-\tau} \tag{25}$$

where $p(m)dm$ is the number of fragments in the mass and ranges between m and $m + dm$. The value of the exponent τ is mainly determined by the dimensionality of the fragmenting system (Åstrom et al. 2004; Ma et al. 2017&2018) and by the brittle and ductile characteristics of the mechanical response of the material (Timár et al. 2010).

To obtain the fragment mass distribution, the characteristic fragment size is defined as:

$$d = \sqrt{V_f / V_0} \tag{26}$$

where V_f is the volume of a fragment (calculated as the total volume of particles in the fragment), and V_0 is the volume of the sample.

In addition to the fragment mass distribution defined in Eq. (25), a fractal distribution is given by the relationship between the fragment number and size:

$$N(d > d_i) = Cd_i^{-D} \tag{27}$$

where $N(d > d_i)$ is the number of fragments with size greater than a certain size d_i, C is the number of elements at a unit length scale, and D is the fractal dimension.

However, it is very difficult to accurately estimate the total number of fragments. Moreover, the N value calculations are typically unavailable from the conventional size distribution (Xu et al. 2013). Hou et al. (2015) estimated the fractal dimension using the Gates–Gaudin–Schuhmann distribution based on the following expression:

$$M(d < d_i)/M_T = (d_i / d_{\max})^n \tag{28}$$

where $M(d < d_i)$ is the cumulative mass of particles smaller than d_i; M_T is the total mass of all of the fragments; $d_{\max}$ is the size of the largest fragment.

A natural logarithm transformation is applied for both sides of Eq. (28), and the fractal dimension can be calculated as:

$$\ln[M(d < d_i)/M_T] = n * \ln(d_i / d_{\max}) \tag{29}$$

where n represents the slope of the fitting line in the coordinate system of $\ln[M(d < d_i)/M_T]$~ $\ln(d_i / d_{\max})$.

Based on simple mathematical derivations, Turcotte (1986) found that the power law distribution defined in Eq. (25) is equivalent to the fractal distribution defined in Eq. (27), and their exponents have a relationship $D = 3(\tau - 1)$. The Gates–Gaudin–Schuhmann distribution is also equivalent to the fractal distribution with $D = 3 - n$.

The fragment mass distributions of the initial static and final deposition states are presented in Fig. 5 - 17a. It can be observed that magnitude of exponent value $\tau = 1 + D/3$ of the power law approximation for fragment mass distributions increases significantly from 1.09 at initial static state to 1.6 at final deposition state. The higher the value of D, the more graded the particle size distribution and the larger the number of fine particles will be (Crosta et al. 2007). Therefore, the obtained fractal dimension $D = 3(\tau - 1)$ increases sharply from 0.27 to 1.8, indicating the severe grain crushing and comminution occurring within the translating joint-bound rock mass. Moreover, as shown in Fig. 5 - 17b, the slope of the fitting straight line $n = 3 - D$ decreases after the cessation of earthquake ground motions. As a result, fractal dimension D increases with comminution time and with the increased production of fines, revealing that larger fragments are segmented along the well spatially distributed pre-existing rock discontinuities owing to the propagation of seismic waves, and fully developed fractures and fine debris are produced after the 100 s duration of seismic shaking, thus leading to higher values of D. The measured D of 0.25 and 1.73 at initial static and final deposition states are close to the fractal dimension value of 0.27 and 1.8 by calculating the exponent of power law approximation for fragment mass distribution.

It reflects that the calculated fractal dimension can be validated as a convincing descriptor in fragmentation characteristics for its physical soundness and mathematical rigor. Though the obtained fractal dimension from DE simulation are slightly lower than measured fractal dimension of real landslides deposits (Crosta et al. 2007). This is attributed to the nature of distinct element that does not allow the dispersed disk grains to be further disaggregated. However, it still can qualitatively demonstrate that the sliding rock mass consecutively experienced an obvious reduction in grain size along the transport path.

The sedimentary fabric and depositional features can be tracked via cumulative fragment size distribution to acquire a deep knowledge of the dynamic disintegration process within the landslide emplacement in response to the seismic shakings. Fig. 5 - 17c illustrates the fragment size distribution obtained for jointed rock blocks before (hollowed symbols) and after (solid symbols) seismic loading. Close examination of fragment size distribution reveals that at the initial static state before the arrival of seismic waves, the jointed rock mass consists of a large number of coarse fragments of varied sizes ($d > 0.07$, $P > 94\%$). At the end of the seismic motion, a large quantity of fine-sized fragments is generated, leading the fragment size distribution to shift leftward to the fine size range ($d \leq 0.07$, $P > 90\%$). The initial and final fragment size distributions can be fitted well by a Weibull's distribution function. This distribution, which is equivalent to the Rosin–Rammler distribution, has successfully provided a good description of the simulated fragment size distribution (Shen et al. 2017; Ma et al. 2017&2018). The two-parameter Weibull distribution can be expressed as

$$P = 1 - \exp\left[-(\frac{d}{d_c})^{\nu} \right] \tag{30}$$

where d_c and ν are fitting parameters. d_c is an index to quantify the level of fines in the fragmenting system. A low d_c value is expected if the fragmenting system consists of a high level of fines. The parameter ν is a measure of the spread of the fragment size distribution, where the distribution is narrower for a larger value of ν.

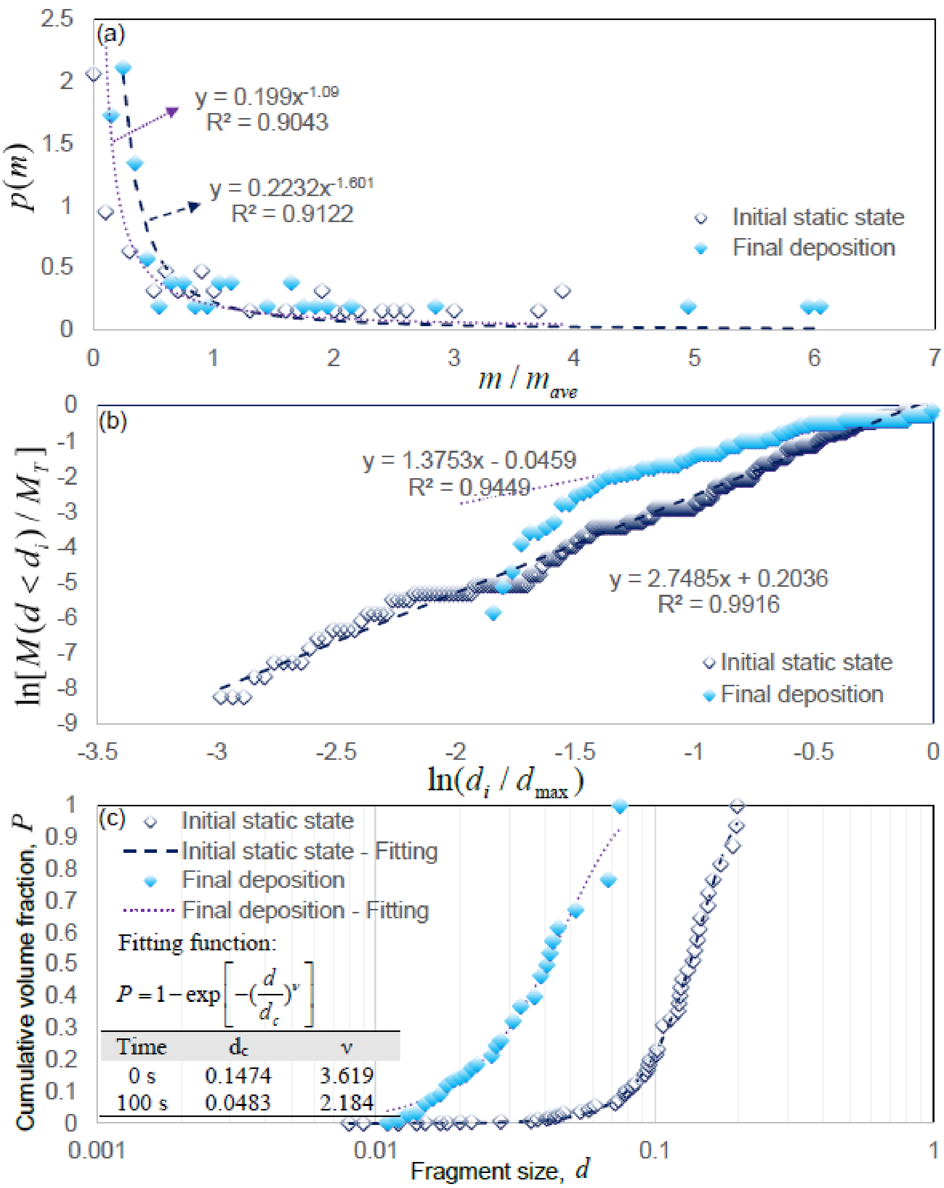

Figure 5 - 17. (a) Mass distribution of fragments using the power law distribution; (b) Mass distribution of fragments using the Gates–Gaudin–Schuhmann distribution; (c) Volume-based size distributions of fragments.

Note: Numerical results are represented by the scattered data points and fitted distributions are represented by lines.

Significant decreases in parameters d_c (from 0.15 to 0.05) and ν (from 3.6 to 2.2) can be observed (see Fig. 5 - 17c) from initial static state to the final deposition after the end of earthquake motions. It reflects that a severe rock fragmentation intensity within the translating slope mass occurs under the strong earthquake ground motion, a large number of fine particles is produced, characterized by a more graded and wider particle size distribution.

Further insights into the disintegrated slope mass at the final deposition can be acquired by exploring the features of the fragment-size statistics, therefore, a statistical analysis is performed to examine the characteristics of fragment populations of the landslide deposit. It can be observed in Fig. 5 - 18a that the distribution of nominal fragment sizes for the landslide deposit is asymmetric, being skewed towards the smaller sizes. Such a distribution lends itself to approximation of a log-normal distribution (Fityus et al. 2013). The cumulative distribution and probability density functions of the log-normal distribution are expressed by equations (31) and (32), respectively:

$$F_X(x) = \frac{1}{2} + \frac{1}{2} erf\left[\frac{\ln(x) - \mu}{\sqrt{2}\sigma}\right] \tag{31}$$

$$f_X(x) = \frac{1}{\sigma\sqrt{2\pi}x} e^{-(\ln x - \mu)^2/2\sigma^2} \tag{32}$$

where erf is the complementary error function, σ (the standard deviation of $\ln(x)$) is the shape parameter which affects the general shape of the distribution, and μ (the mean of $\ln(x)$) is the location parameter that controls the location on the x-axis.

As demonstrated in Fig. 5 - 18a the nominal fragment size follows a lognormal distribution. Most of deposited fragments sizes distribute within a nominal fragment size range ($0.01 < d \leq 0.015$) being dominant around 33% in total, inferring a dynamic disintegration of the slope mass occurs continuously during the landslide transport. In addition, the lognormal Quantile-Quantile (Q-Q) analysis is applied to evaluate how well the distribution of fragment sizes matches a lognormal distribution and to better interpret fragment size statistics (see inset plot in Fig. 5 - 18a). It can be observed from (Q-Q plot) that the distributions are fluctuating at coarse fragment size range, indicating the presence of large unbroken blocks.

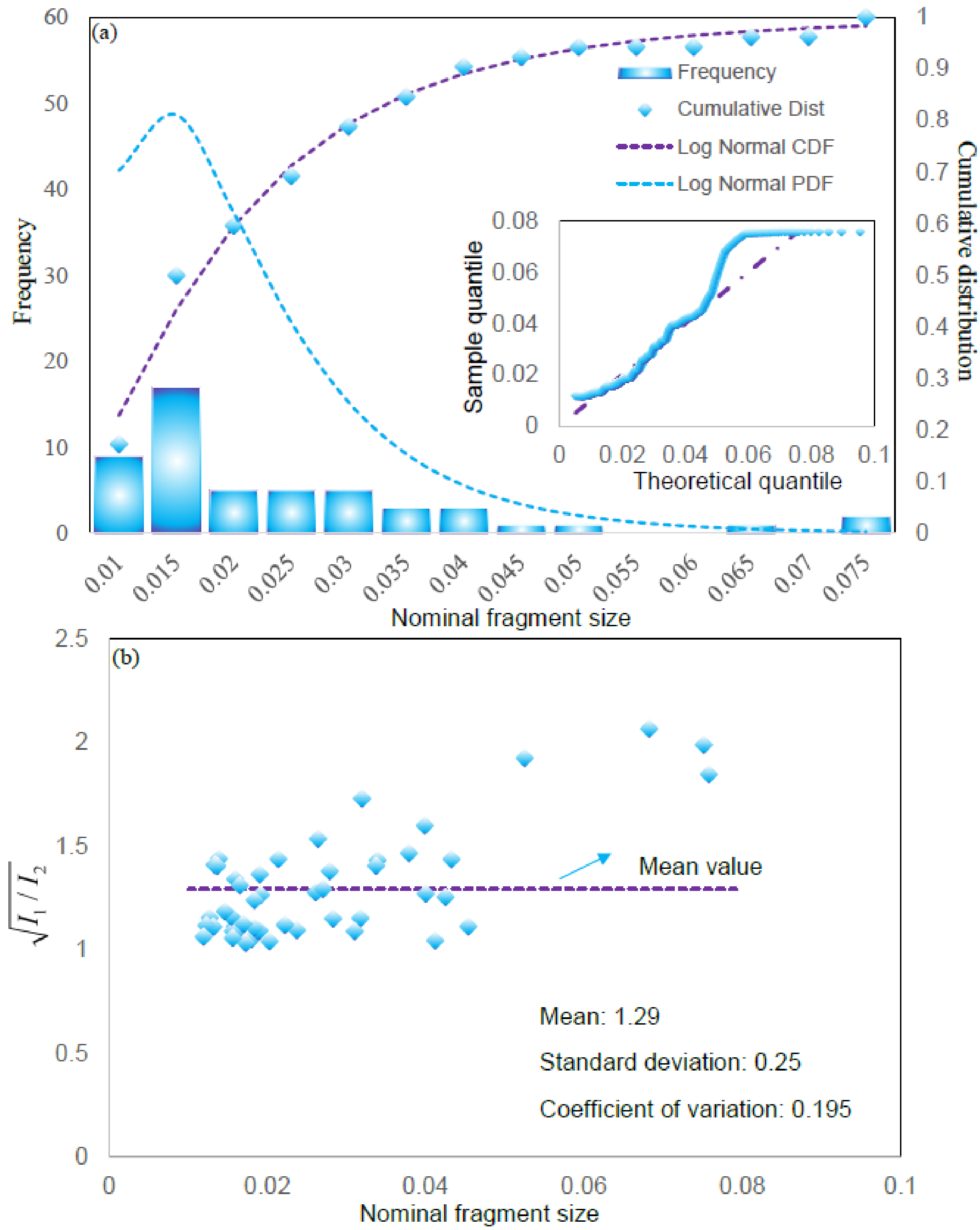

Figure 5 - 18. (a) Fragment size frequency distributions of the deposit with corresponding log-normal approximations. (b) Distributions of the square root of the ratio of the larger and smaller eigenvalues of the tensor inertia of the fragment shape for checking shape isotropy of the deposit.

In advance of more detailed investigation on the mechanisms operating during the transport of an earthquake-induced landslide, a statistical analysis is put forward to examine the shape characteristics of fragment populations by checking the fragment shape isotropy. The shape isotropy can be calculated using the square root of the ratio of the larger I_1 and smaller I_2 eigenvalues of the tensor inertia of the 2D fragment shape (Timár et al. 2010). The tensor inertia can be calculated as follows

$$I_{ij}^{fragment} = \sum_{d=1}^{N_d} (I_{ij}^{d} \delta_{ij} + m^d x_i^d x_j^d) \tag{33}$$

where the fragment contains N_d base disks, each with mass m^d, and inertial tensor $\mathbf{I}^d$ relative to the disk local Cartesian axis, and δ_{ij} is the Kronecker delta. The vector $\mathbf{x}^d$ is given by $x_j^d - x_j^{fragment}$, where $\mathbf{x}^d$ and $\mathbf{x}^{fragment}$ are the vectors describing the constituent disk and fragment centroids respectively.

The mean and standard deviation of $\sqrt{I_1 / I_2}$ is found to be 1.29 and 0.25, respectively, with a coefficient of variation (C_v) of 0.195 for the landslide deposit (see Fig. 5 - 18b). A $C_v < 1$ is known as a relatively low variation, indicating a high level of fragment shape isotropy. It is interesting to note that although the fragment shape isotropy of the deposition is relatively high, an obvious deviation from the mean value of $\sqrt{I_1 / I_2}$ is found in the larger fragment size. This is expected because coarse blocks have not undergone any further textual maturation, such as friction abrasion, continuous comminution and grinding, which promotes the fact that particles are more mature with higher rounding and smoothness (Perinotto et al. 2015). Similar behavior was also observed in other reported large-scale landslides (e.g. Crosta et al. 2004; Zhang et al. 2011).

5.5.5. Fragmentation Degree and Landslide Runout

As discussed in the previous sections, a set of rock properties has been employed in a preliminary numerical investigation of the Wangjiayan landslide. The obtained numerical results reveal the dynamic disintegration and emplacement mechanism of landslide during its propagation and deposition. To generalize this research, a systematic parametric study on the influence of rock strength on slope damage, dynamic runout, and fragmented deposition has also been performed. In testing the effect of rock strength, the same pattern of rock discontinuities is kept, while the bonding strength of particles is varied from 11 to 36 MPa with an increasing step of 5 MPa.

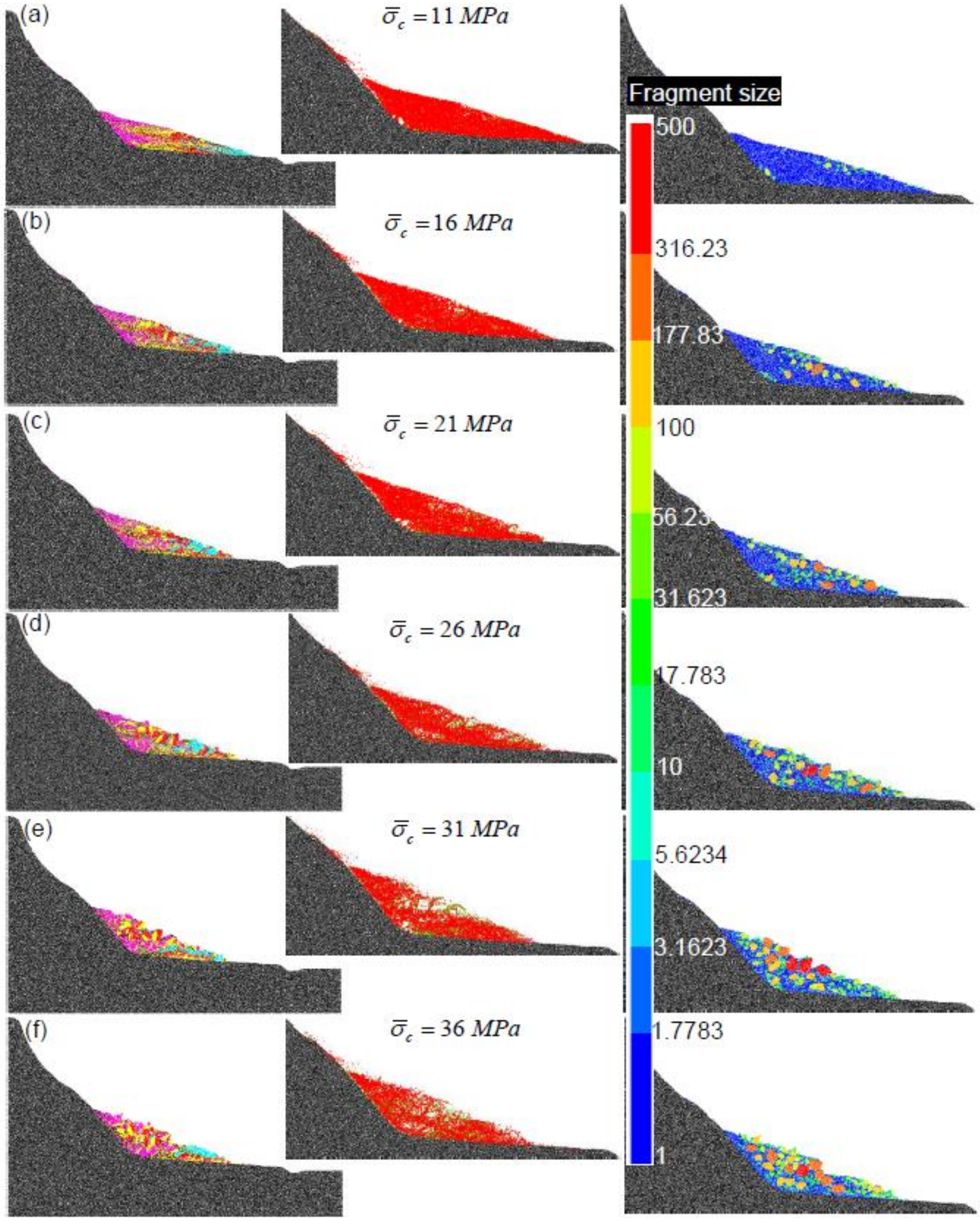

Figure 5 - 19. Numerical investigation of final landslide deposit for tests with various particle bonding strengths: (a) 11 MPa; (b) 16 MPa; (c) 21 MPa; (d) 26 MPa; (e) 31 MPa; (f) 36 MPa.

The left column denotes distribution of slope mass, the medium column presents distribution of slope internal damage, and the right column depicts distribution of fragment size in the final landslide deposits, respectively.

Figure 5 - 19 compares the distribution of final slope damage and the sedimentary fabric within the deposit for tests on rock slopes with various strengths. It can be seen that when the rock strength increases, the surface of the deposit becomes less smooth with larger irregularities. It is worth noting that regardless of the rock strength, the internal structure of the deposit experience significant disturbance with the emergence of rock material from the inner layers can be observed at the surface. Consistent with previous observations, the final deposits consist of rafted large blocks laying on matrix of fine-grained material (Wang et al. 2018). Although large blocks are found at the surface of the deposit, their distribution remains very heterogeneous and the size of outcropping blocks can vary significantly. For tensile strengths $\bar{\sigma}_c$ = 11 MPa and 36 MPa, the largest fragment sizes are 0.076 and 0.153, respectively. This is in good agreement with the observations made at the surface of natural events (Evans et al. 2006).

In order to precisely identify the effect of bonding strength ($\bar{\sigma}_c$) on the dynamic runouts of the earthquake-induced landslide, the degree of fragmentation F_D is used to provide a measure for the damage that the material has experienced (Haug et al. 2016), which is calculated as $F_D = \frac{M_{\max}}{m_{\max}}$ with $M_{\max}$ and $m_{\max}$ being the mass of the largest fragment at initial static state and final deposition, respectively.

The degree of fragmentation (F_D) observed in the numerical simulations for varying bonding strength ($\bar{\sigma}_c$) is plotted in Fig. 5 - 20a. It is found that F_D drops drastically as $\bar{\sigma}_c$ increases to 31 MPa and then slightly increases as $\bar{\sigma}_c$ reaches 36 MPa. However, the overall slope damage ratio decreases exponentially with the increase in particle bonding strength. The numerical results are also analyzed with respect to the mobility of the rock mass in Fig. 5 - 20b, where the travel distance of the center of the sliding mass (L) and travel length of the front of the deposits (L_f) is plotted with respect to the degree of fragmentation (F_D). The distance L can be obtained using equation 34 and L_f is defined as the horizontal distance of the slope mass's initial front position and the front of the final deposits.

$$L = \sum_{i=1}^{N} m_i l_i / M \tag{34}$$

where M being the sum of the mass of all particles and l_i is the spreading distance of particle i.

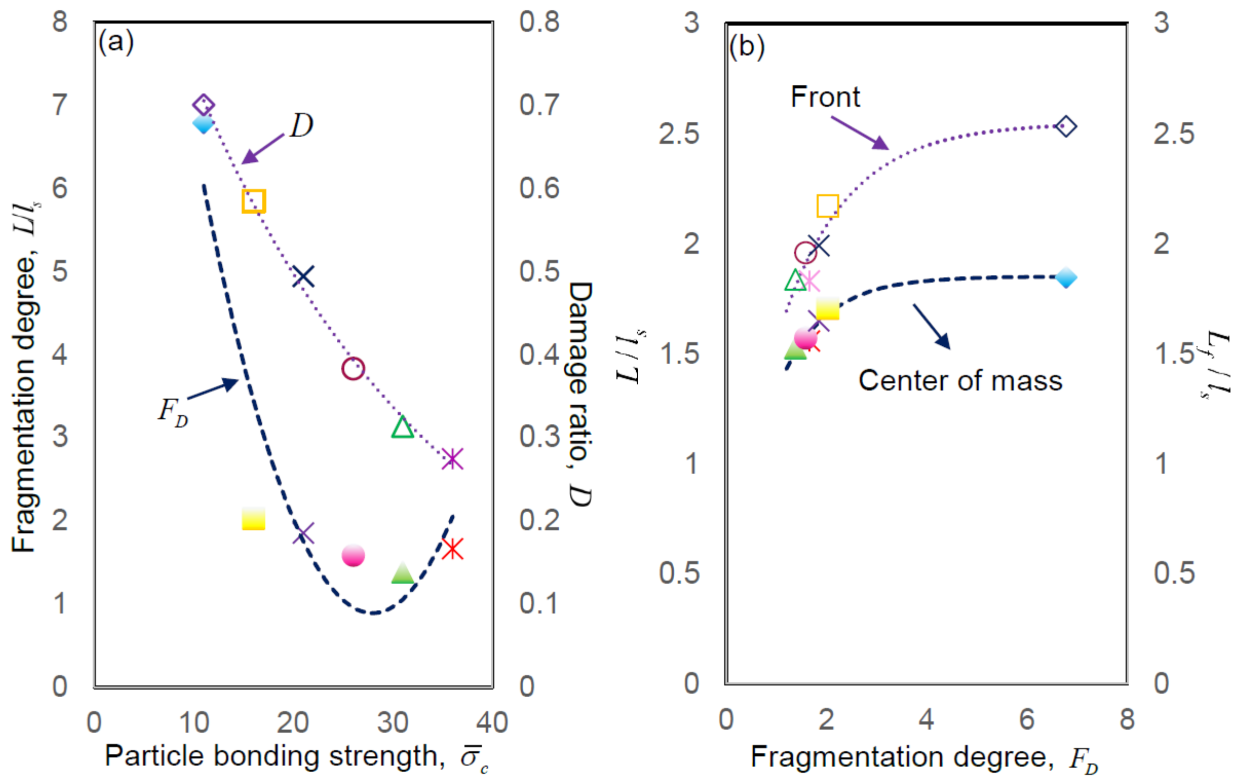

Figure 5 - 20. (a) Variations of degree of fragmentation and damage ratio with the particle bonding strength; (b) The travel distance of the center of slope mass and the displacement of the front of the deposits with the degree of fragmentation.

As the degree of fragmentation is dimensionless, the travel distance can be set as dimensionless relative to its own size, which is defined using the square root of the area of the rock material. It can be seen in Fig. 5 - 20b that the distance traveled by the front of the landslide shows an increase with the increase in the degrees of fragmentation. The front is also observed to be strongly affected by the degree of fragmentation below $F_D \approx 5$. For degree of fragmentation above this value, displacement of the front of the deposits seems to reach saturation. This finding can well match the scaled analogue physical models in Bowman et al. (2011) with respect to the dynamic disintegration of intact and jointed rock blocks and the well-documented field observations in Legros (2002). It is worth noting that the travel distance of center mass follows a similar trend but with a milder increasing rate and an earlier saturation state for F_D. This can be explained by the sliding front that experiences intense interactions with the bedrock during the landslide propagation and deposition, allowing it to attain a higher energy as the main driver for fragmenting the rock mass and promoting long runout. According to Fig. 5 - 20, the numerical results (i.e., F_D, L_f, and L) can be well fitted by exponential functions of the form:

$$Y = C_1(1 - e^{-C_2(F_D - 1)}) \tag{35}$$

Where Y is the dependent variable (L_f, and L); C_1 and C_2 are fitting constants; and F_D is the degree of fragmentation.

5.6. Conclusions

To understand the role of rock fragmentation and transport mechanism in earthquake-induced landslide at the macroscopic and microscopic levels, the processes of rock slope failure, runout, and deposition were investigated using 2D plane strain DEM. The following conclusions are drawn based on the results of the performed analyses:

(a) The landslide is initiated and the subsequent complex dynamic response of jointed rock mass, such as fracture initiation and propagation, develops as the seismic shaking intensifies. The rock damage ratio continuously increases resulting in the formation of a widespread internal slope fragmentation. In this process, the granular temperatures, which present the agitation and collision of the particles inside the slope mass, initiate immediately along the weak solid structures, and further propagate to the basal surface due to the intense shearing. Simultaneously, the deviator stress, which indicates the development of dilatancy of the granular material, experiences wild fluctuations that can facilitate rock disaggregation and further dilate and disperse the translating slope mass. The enhancement of granular temperatures contemporaneous with the appearance of dilatancy contributes to the cause of extremely rapid fragmented flow.

(b) Characteristics of fragmentated deposition is systematically analyzed in terms of the statistics of the fragment mass, fragment size, and fractal dimension. The two-parameter Weibull analysis provides an adequate description of the simulated fragment size distributions. The significant decrease of d_c and ν demonstrated that the slope mass experiences severe fragmentation, which causes the fragmented system to have higher level of fines with a wider span. The fractal dimension value is close to the exponent τ of the analytical predication of the fragment mass distribution. The fractal dimension evolution further attests that the slope mass experiences obvious consecutive fragmentation during its emplacement. The distribution of fragment shape isotropy of the modeled deposit agrees well with that observed in the nature system, i.e., both texturally immature (coarse blocks) and mature (fine debris) deposits concurrently exist within the landslide.

(c) When particle strength increases, the fragmentation degree first drops significantly and then increases following a parabolic relationship, however, the damage ratio decreases exponentially. The increased travel length of the front and the center mass of the deposits is found to increase with the fragmentation degree. This indicates that the greater the degree of fragmentation, the greater the runout. When the material is stronger, the deposit is rough and the proportion of clast to matrix progressively increases. On the contrary, a granular deposit is found to be smooth for low particle strength ($\bar{\sigma}_c$ =11 MPa) with a few large intact blocks laying on top of a thick layer of fine-grained particles.

Chapter 6

Conclusions and Recommendations

6.1. Conclusions

In this thesis, the discrete element method is used to analyze the micromechanical aspects of rock destabilization processes focusing on the mechanisms leading to failure. The adopted numerical technique allows a rock sample or a rock mass to be represented as a set of disk-shaped particles in two-dimensions, allowing particles to interact at their points of contact. Thus, a crack can be represented as the surface where bonds no longer exist between particles, and its propagation can be represented by the points at which bonds are broken. Numerical results are compared with experimental measurements and field data to validate the proposed DE simulations. The efficiency of the discrete element method in analyzing this class of rock fracturing problems was demonstrated.

The developed discrete element method has been implemented and used to evaluate fracture growth mechanism by analyzing the nature and distribution of microcracks and their correlations with anisotropy evolution at the microscopic scale. Initially, laboratory-scale models (simulations of biaxial and triaxial laboratory experiments) are used to manifest the role of propagation and coalescence of fracture in rock destabilization problems. The dynamic response of a large scale rock slope is then investigated under seismic loading and fracture growth and fragmentation behaviour are examined. Specific conclusions are summarized below:

1) In chapter 3, the results showed that the failure mechanism in rock samples is much affected by the degree of initial jointing. The detailed analysis of contact fabric and force anisotropies allowed us to highlight the microscopic mechanisms that lead to the dependence of deformability and rock strength with respect to initial joint intensity. The increase in initial jointing results in the evolution of contact normal or tangential force anisotropy. From a macro mechanical standpoint, the difference in trends of fabric and force anisotropies relates to transition of the failure mechanism from brittle failure to ductile bulk plastic flow. The increase in rock failure strength with initial joint frequency is attributed to a net increase in the fabric and force anisotropies. At higher initial joint

density a decrease of the normal contact force anisotropy is compensated by an increase of shear contact force anisotropy, leading to saturation of rock failure strength.

2) In chapter 4, the discrete element model is then used to analyze the seismic response and mass transport process of a natural slope. The slope response to earthquake is studied focusing on crack initiation, propagation, and coalescence within the rock mass. The mass movement and accumulation process are interpreted in terms of evolution of stresses and solid fractions, kinematic behaviour and energy conversion. During the mass transport process, the slope is fragmented progressively due to intense shearing, allowing a basal layer of gradually fining solid particles to be generated with simultaneous occurrence of violent collisions, increase in particle kinematic activities, and the reduction of solid concentration. The entire avalanche body was found to experience severe fragmentation, which promotes a large proportion of fragments that has been broken into fine-grained particles. It is also found that the distribution of the fragment shapes becomes stable as the avalanche loses its momentum and deposition starts in the runout area.
3) In chapter 5, The DEM analysis aimed at understanding the role of rock fragmentation and transport mechanism in earthquake-induced landslide at the macroscopic and microscopic levels. The rock damage ratio continuously increases resulting in the formation of a widespread internal slope fragmentation. In this process, the granular temperatures, which present the agitation and collision of particles inside the slope mass, initiate immediately along the weak solid structures, and further propagate to the basal surface due to intense shearing. Simultaneously, the deviator stress, which indicates the development of dilatancy of the granular material, experiences fluctuations that can facilitate rock disaggregation and further dilate and disperse the translating slope mass. The distribution of fragment shape isotropy of the modeled deposit agrees well with that observed in the investigated natural system. The increased travel length of the front and the center mass of the deposits is found to increase with the fragmentation degree. This indicates that the greater the degree of fragmentation, the greater the runout.

6.2. Recommendations for Future Work

The obtained scientific insights into the propagation mechanisms and depositional morphology of landslides can be extended to define the potential impact areas and the mitigation structures needed for the protection and remediation of unstable rock slope sites.. In addition, various rock engineering problems can be studied following the methodology developed in this thesis including:

- Studying the three-dimensional rock failure process under various confining pressures.
- Considering more natural scenarios including more realistic distributed discrete fracture network, and possible infilling of natural fracture.
- Understanding rock fragmentation process during the emplacement of landslide with focus on the terrain effect.
- Simulating the different stabilization techniques used to enhance the stability of rock slopes.
- Establishing a numerical framework that takes fluid flow effect into account for the analysis of rock mass and assessing its role on the failure of rock slopes.

References

Alejano LR, Arzúa J, Bozorgzadeh N, Harrison JP (2017) Triaxial strength and deformability of intact and increasingly jointed granite samples. Int J Rock Mech Min Sci 95:87–103

Antolini F, Barla M, Gigli G, Giorgetti A, Intrieri E, and Casagli N (2016) Combined finite discrete numerical modeling of runout of the Torgiovannetto di Assisi rockslide in central Italy. Int J Geomech 16(6):04016019

Asadi M, Rasouli V, Barla G (2012) A bonded particle model simulation of shear strength and asperity degradation for rough rock fractures. Rock Mech Rock Eng 45:649–675

Asadi MS, Rasouli V, Barla G (2013) A laboratory shear cell used for simulation of shear strength and asperity degradation of rough rock fractures. Rock Mech Rock Eng 46:683–699

Azéma E, Radjai F, Dubois F (2013) Packings of irregular polyhedral particles: strength, structure, and effects of angularity. Phys Rev E 87(6):062203

Åstrom JA, Ouchterlony F, Linna RP, Timonen J (2004) Universal dynamic fragmentation in D dimensions. Phys Rev Lett 92(245506–1)

Bagnold RA (1954) Experiments on gravity-free dispersion of large solid sphere in a Newtonian fluid under shear. Proc R Soc 225(1160):49–63.

Bahaaddini M, Hagan PC, Mitra R, Hebblewhite BK (2015) Parametric study of smooth joint parameters on the shear behaviour of rock joints. Rock Mech Rock Eng 48(3):923-940

Bahaaddini M, Hagan PC, Mitra R, Hebblewhite BK (2016) Numerical study of the mechanical behaviour of non-persistent jointed rock masses. Int J Geomech 16:04015035

Bahaaddini M, Sharrock G, Hebblewhite BK (2013a) Numerical direct shear tests to model the shear behaviour of rock joints. Comput Geotech 51:101–115

Bahaaddini M, Sharrock G, Hebblewhite BK (2013b) Numerical investigation of the effect of joint geometrical parameters on the mechanical properties of a non-persistent jointed rock mass under uniaxial compression. Comput Geotech 49:206–225

Barla M, Piovano G, and Grasselli G (2011) Rock slide simulation with the combined finite discrete element method. Int J Geomech 711–721

Bathurst RJ, Rothenburg L (1990) Observations on stress-force-fabric relationships in idealized granular materials. Mech Mater 9(1):65–80

Bolton MD, Nakata Y, Cheng YP (2008) Micro-and micromechanical behaviour of DEM crushable materials. Géotechnique 58(6):471–480

Bowman ET, Take WA, Rait KL, and Hann C (2012) Physical models of rock avalanche spreading behaviour with dynamic fragmentation. Can Geotech J (4):460–476

Borykov T, Mège D, Mangeney A, Richard P, Gurgurewicz J, Lucas A (2019) Empirical investigation of friction weakening of terrestrial and Martian landslides using discrete element models. Landslides 16:1121–1140

Brideau MA, Yang M, Stead D (2009) The role of tectonic damage and brittle rock fracture in the development of large rock slope failures. Geomorphology 103:30-49

Brown ET, Trollope DH (1970) Strength of a model of jointed rock. ASCE J Soil Mech Found Div Proc 1970:685–704

Cagnoli B, Manga M (2004) Granular mass flows and Coulomb's friction in shear cell experiments: implications for geophysical flows. J Geophys Res Solid Earth 109: F04005

Cagnoli B, Piersanti A (2017) Combined effects of grain size, flow volume and channel width on geophysical flow mobility: three-dimensional discrete element modeling of dry and dense flows of angular rock fragments. Solid Earth 8:177–188

Calvetti F, Crosta G, Tatarella M (2000) Numerical simulation of dry granular flows: from the reproduction of small-scale experiments to the prediction of rock avalanches. Riv Ital Geotech 34(2):21–38

Campbell CS (1989) Self-lubrication for long run-out landslides. J Geol 97:653-665

Campbell CS (1990) Rapid granular flows. Annu Rev Fluid Mech 22(1):57–90

Campbell CS, Cleary PW, Hopkins M (1995) Large-scale landslide simulations: Global deformation, velocities and basal friction. J Geophys Res 100(B5):8267–8283

Campbell CS (2006) Granular material flows: an overview. Powder Technol 162:208–229

Chang KJ and Taboada A (2009) Discrete element simulation of the Jiufengershan rock-and-soil avalanche triggered by the 1999 Chi-Chi earthquake, Taiwan. J Geophys Res Earth Surf 114: F03003

Chang SB and Zhang SM (2007) Hand book of engineering geology [M]. 4th edition. Beijing: China architecture & Building press,169–170

Chen X, Zhang SF, Cheng C (2018) Numerical study on effect of joint strength mobilization on behavior of rock masses with large nonpersistent joints under uniaxial compression. ASCE Int J Geomech 18(11):04018140(1)–04018140(21)

Cheung LYG, O'Sullivan C, Coop MR (2013) Discrete element method simulations of analogue reservoir sandstones. Int J Rock Mech Min Sci 63:93–103

Chigira M, Wu X, Inokuchi T, Wang G (2010) Landslides induced by the 2008 Wenchuan earthquake, Sichuan, China. Geomorphology 118(3–4):225–238

Chiu CC, Wang TT, Weng MC, Huang TH (2013) Modeling the anisotropic behavior of jointed rock mass using a modified smooth-joint model. Int J Rock Mech Min Sci 62:14-22

Cho N, Martin CD, Sego DC (2007) A clumped particle model for rock. Int J Rock Mech Min Sci 44(7):997-1010

Crosta GB, Chen H, Lee CF (2004) Replay of the 1987 Val Pola Landslide, Italian Alps. Geomorphology 60:127– 146

Crosta GB, Frattini P, Fusi N (2007) Fragmentation in the Val Pola rock avalanche, Italian Alps. J Geophys Res 112: F01006

Cui FP, Xu Q, Tan RJ, Yin YP (2011) Numerical simulation of collapsing and sliding response of slope triggered by seismic dynamic action. J TongJi Univ (Nat Sci) 39(3):446 – 450 (in Chinese)

Cundall PA (1980) UDEC—a generalized distinct element program for modelling jointed rock. Rept PCAR-1–80, Peter Cundall Association Report, European Research Office, U.S. Army. Contract DAJA37-79-C-0548

Cundall PA (1971) A computer model for simulating progressive, large-scale movements in blocky rock systems. Proc. Symp. Znt. Sot. Rock Mech., Nancy 2, NO. 8

Cundall PA (2000) Numerical experiments on rough joints in shear using a bonded particle model. In: Aspects of tectonic faulting. Springer, Berlin, 1–9

Cundall PA (2001) A discontinuous future for numerical modelling in geomechanics? Proc. ICE Geotech Eng 149(1):41–47

Cundall PA, and Strack ODL (1979) A discrete numerical model for granular assemblies. Géotechnique 29(1):47–65

Dai FC, Xu C, Yao X, Xu L, Tu XB, Gong QM (2011) Spatial distribution of landslides triggered by the 2008 Ms 8.0 Wenchuan earthquake, China. J Asian Earth Sci 40(4):883–895

Dammeier F, Moore JR, Haslinger F, Loew S (2011) Characterization of alpine rockslides using statistical analysis of seismic signals. J Geophys Res 116(F4): F04024

Davies TRH (1982) Spreading of rock avalanche debris by mechanical fluidization. Rock Mech 15(1):9–24

Davies TH, McSaveney MJ (2009) The role of dynamic rock fragmentation in reducing frictional resistance to large landslides, Eng Geol 109:67-79

Davies TRH, Reznichenko NV, McSaveney, MJ (2020) Energy budget for a rock avalanche: fate of fracture-surface energy. Landslides 17:3–13

Davies TRH, McSaveney MJ (2009) The role of rock fragmentation in the motion of large landslides. Eng Geol 109(1-2):67–79

Davies TRH, McSaveney MJ, Hodgson KA (1999) A fragmentation spreading model for long-runout rock avalanches. Can Geotech J 36(6):1096–1110

De Blasio FV, Elverhøi A (2008) A model for frictional melt production beneath large rock avalanches. J Geophys Res 113: F02014

De Blasio FV, Crosta G (2014) Simple physical model for the fragmentation of rock avalanches, Acta Mech 225(1):243–252

De Blasio FV, Crosta GB (2015) Fragmentation and boosting of rock falls and rock avalanches. Geophys Res Lett 42(20):8463–8470

De Blasio FV, Elverhøi A (2008) A model for frictional melt production beneath large rock avalanches. J Geophys Res 113: F02014

Dinç O, Scholtès L (2018) Discrete analysis of damage and shear banding in argillaceous rocks. Rock Mech Rock Eng 51:1521-1538

Duan K, Kwok CY, Tham LG (2015) Micromechanical analysis of the failure process of brittle rock. Int J Numer Anal Meth Geomech 39(6):618–634

Duan K, Kwok CY, Ma X (2017) DEM simulations of sandstone under true triaxial compressive tests. Acta Geotech 12:495–510

Dufresne A, Dunning SA (2017) Process dependence of grain size distributions in rock avalanche deposits. Landslides 14:1555–1563

Dufresne A, Geertsema M (2020) Rock slide–debris avalanches: flow transformation and hummock formation, examples from British Columbia. Landslides 17:15–32

Dufresne A, Wolken GJ, Hibert C, Bessette-Kirton EK, Coe JA, Geertsema M, Ekström G (2019) The 2016 Lamplugh rock avalanche Alaska: deposit structures and emplacement dynamics. Landslides 16:2301–2319

Dufresne A, Davies TR, McSaveney MJ (2010) Influence of runout-path material on emplacement of the Round Top rock avalanche, New Zealand. Earth Surf Processes Landforms 35:190–201.

Dunning SA, Mitchell WA, Rosser NJ, Petley DN (2007) The Hattian Bala rock avalanche and associated landslides triggered by the Kashmir earthquake of 8 October 2005. Eng Geol 93:130-144

Dunning SA (2006) The grain-size distribution of rock avalanche deposits in valley-confined settings, Ital J Eng Geol Environ 1:117–121

Eberhardt E, Stead D, Coggan J (2004) Numerical analysis of initiation and progressive failure in natural rock slopes the 1991 Randa rockslide. Int J Rock Mech Min Sci 41(1):69–87

Eisbacher G (1979) Cliff collapse and rock avalanches (sturzstroms) in the Mackenzie Mountains, northwestern Canada. Can Geotech J 16:309–334

Erismann TH, Abele G (2001) Dynamics of rockslides and rockfalls. Springer, Berlin.

Eshiet KII, Sheng Y (2016) The role of rock joint frictional strength in the containment of fracture propagation. Acta Geotech 12:897–920

Evans S, Mugnozza GS, Strom A, Hermanns R, Ischuk A, Vinnichenko S (2006) Landslides from massive rock slope failure and associated phenomena, in Landslides From Massive Rock Slope Failure, 03–52, Springer, Netherlands.

Fan X, Kulatilakec PHSW, Chen X (2015) Mechanical behavior of rock-like jointed blocks with multi-non-persistent joints under uniaxial loading: a particle mechanics approach. Eng Geol 190:17–32

Feng P, Dai F, Liu Y, Xu NW, Du HB (2019) Coupled effects of static-dynamic strain rates on the mechanical and fracturing behaviors of rock-like specimens containing two unparallel fissures, Engineering Fracture Mechanics 207:237–253

Feng ZY, Lo CM, Lin QF (2017) The characteristics of the seismic signals induced by landslides using a coupling of discrete element and finite difference methods. Landslides 14(2):661–674

Fityus S, Giacomini A, Buzzi O (2013) The significance of geology for the morphology of potentially unstable rocks. Eng Geol 162:43-52

Fu JW, Liu SL, Zhu WS, Zhou H, Sun ZC (2018) Experiments on failure process of new rock-like specimens with two internal cracks under biaxial loading and the 3-D simulation. Acta Geotech 13(4):853–867

Gao G and Meguid MA (2018a). Modeling the impact of a falling rock cluster on rigid structures. ASCE Int J Geomech 18(2):1-15

Gao G and Meguid MA (2018b) On the role of sphericity of falling rock clusters- Insights from experimental and numerical investigations. Landslides 15(2):219-232

Gao G and Meguid MA (2018c) Effect of particle shape on the response of geogrid-reinforced systems: Insights from 3D discrete element analysis. Geotext Geomembr 46(6):685-698

Garcia FE, and Bray JD (2018) Distinct element simulations of earthquake fault rupture through materials of varying density. Soils Found 58(4):986–1000

Garcia FE, and Bray JD (2018) Distinct element simulations of shear rupture in dilatant granular media. Int J Geomech18(9):04018111

Giacomini A, Buzzi O, Renard B, Giani GP (2009) Experimental studies on fragmentation of rock falls on impact with rock surfaces. Int J Rock Mech Min Sci 46(4):708–715

Ghazvinian A, Sarfarazi V, Schubert W, Blumel M (2012) A study of the failure mechanism of planar non-persistent open joints using PFC2d. Rock Mech Rock Eng 45:677–693

Ghahramani N, Evans SG (2018) The 1985 earthquake-triggered North Nahanni rockslide, Northwest Territories, Canada: the co-seismic movement of a sedimentary rock mass conditioned by residual strength. Eng Geol 247:1-11

Gischig V, Eberhardt E, Moore JR, Hungr O (2015) On the seismic response of deep-seated rock slope instabilities-insights from numerical modelling. Eng Geol 193:1–18

Glynn EF, Veneziano D, Einstein HH (1978) The probabilistic model for shearing resistance of jointed rock. In: Proceedings of the 19th US symposium on rock mechanics, Stateline, Nevada, 66–76

Gong B, and Tang CA (2017) Slope-slide simulation with discontinuous deformation and displacement analysis. Int J Geomech 17(5): E4016017

Gorum T, Fan X, van Westen CJ, Huang RQ, Xu Q, Tang C, Wang G (2011) Distribution pattern of earthquake-induced landslides triggered by the 12 May 2008 Wenchuan earthquake. Geomorphology 133(3):152–167

Guo N and Zhao JD (2013) The signature of shear-induced anisotropy in granular media. Comput Geotech 47:1–15

Gu J, Zhao ZY (2009) Considerations of the discontinuous deformation analysis on wave propagation problems. Int J Numer Anal Meth Geomech 33(12):1449–1465

Habib P (1975) Production of gaseous pore pressure during rock slides. Rock Mech 7(4):193-197

Hatzor YH, Palchik V (1997) The influence of grain size and porosity on crack initiation stress and critical flaw length in dolomites Int J Rock Mech Min Sci, 34:805-816

Haug ØT, Rosenau M, Leever K, Oncken O (2016) On the energy budgets of fragmenting rockfalls and rockslides: insights from experiments. J Geophys Res Earth Surface 121:1310–1327

Huang RQ, Li WL (2009) Analysis of the geo-hazards triggered by the 12 May 2008 Wenchuan earthquake, China. Bull Eng Geol Environ 68(3):363–371

Havenith HB, Bourdeau C (2010) Earthquake-induced landslide hazards in mountain regions: a review of case histories from central Asia. An inaugural lecture to the society. Geol Belg 13(3): 137-152

Hazzard JF, Young RP (2000) Simulating acoustic emissions in bonded-particle models of rock. Int J Rock Mech Min Sci, 37(5):867-872

Hazzard JF, Young RP (2002) Moment tensors and micromechanical models. Tectonophysics, 356 (1–3):181-197

Hazzard JF, Young RP (2004) Young Dynamic modelling of induced seismicity. International Journal of Rock Mechanics and Mining Sciences, 41(8):1365-1376

Hoek E, Brown ET (1997) Practical estimates of rock mass strength. Int J Rock Mech Min Sci 34(8):1165–1186

Hoek E, Kaiser PK, Bawden WF (2000) Support of Underground Excavations in Hard Rock. CRC Press

Hosseininia E. Seyedi (2012) Investigating the micromechanical evolutions within inherently anisotropic granular materials using discrete element method. Granul Matter 14:483-50

Hosseininia E. Seyedi (2103) Stress–force–fabric relationship for planar granular materials. Géotechnique 63:830-841

Hou TX, Xu Q, Zhou JW (2015) Size distribution, morphology and fractal characteristics of brittle rock fragmentations by the impact loading effect. Acta Mech 226(11):3623-3637

Huang D, Cen D, Ma G, Huang R (2015) Step-path failure of rock slopes with intermittent joints. Landslides 12:911–926

Huang F, Shen J, Cai M, Xu CS (2019) An Empirical UCS Model for Anisotropic Blocky Rock Masses. Rock Mech Rock Eng 52:3119

Hungr O, McDougall S (2009) Two numerical models for landslide dynamic analysis. Comput Geosci 35:978-992

Hurley RC, Hall SA, Andrade JE, Wright J (2016) Quantifying interparticle forces and heterogeneity in 3D granular materials. Phys Rev Lett

Imre B, Laue J, Springman S (2010) Fractal fragmentation of rocks within sturzstroms: Insight derived from physical experiments within the ETH geotechnical drum centrifuge. Granul Matter 12(3):267–285

Itasca Consulting Group (2014) Particle flow code in three dimensions (PFC2D 5.0), Minneapolis.

Jiang MJ (2012) A. Murakami Distinct element method analyses of idealized bonded-granulate cut slope Granul. Matter 14:393-410

Jiang MJ, Jiang T, Crosta GB, Shi Z, Chen H, Zhang N (2015) Modeling failure of jointed rock slope with two main joint sets using a novel DEM bond contact model. Eng Geol 193:79–96

Kanatani K (1984) Distribution of directional data and fabric tensors. Int J Eng Sci 22:149-164

Keefer DK (1994) The importance of earthquake-induced landslides to long term slope erosion and slope-failure hazards in seismically active regions. Geology 10:265–284

Kermani E, Qiu T, and Li T (2015) Simulation of collapse of granular columns using the discrete element method. Int J Geomech 15(6):04015004

Kent PE (1966) The transport mechanism in catastrophic rock falls. J Geol 74(1):79–83

Koyama T and Jing L (2007) Effects of model scale and particle size on micro-mechanical properties and failure processes of rocks—A particle mechanics approach. Eng Anal Boundary Elem 31(5):458–472

Kobayashi Y (1994). Effect on basal guided waves on landslides. Pure Appl Geophys 142(2):329–346

Kuhlemeyer RL, Lysmer J (1973) Finite element method accuracy for wave propagation problems. J Soil Mech Foundations Div ASCE 99:421-427

Kulatilake PHSW, He W, Um J, Wang H (1997) A physical model study of jointed rock mass strength under uniaxial compressive loading. Int J Rock Mech Min Sci 34(3):165.e1-165.e15

Kulatilake PHSW, Liang J, Gao H (2001) Experimental and numerical simulations of jointed rock block strength under uniaxial loading. J Eng Mech 127(12):1240-1247

Kulatilake PHSW, Malama B, Wang J (2001) Physical and particle flow modeling of jointed rock block behavior under uniaxial loading Int J Rock Mech Min Sci 38:641-657

Langlois VJ, Quiquerez A, Allemand P (2015) Collapse of a two-dimensional brittle granular column: Implications for understanding dynamic rock fragmentation in a landslide. J Geophys Res Earth Surf 120(1866–1880): JF003330

Legros F (2002) The mobility of long-runout landslides. Eng Geol 63(3-4):301–331

Lee H, Jeon S (2011) An experimental and numerical study of fracture coalescence in pre-cracked specimens under uniaxial compression. Int J Solids Struct 48(6):979-999

Levy S, Molinari JF, Vicari I, Davison A (2010) Dynamic fragmentation of a ring: predictable fragment mass distributions. Phys Rev E 82(6):066105

Li B, Xing A, Xu Ch (2017) Simulation of a long-runout rock avalanche triggered by the Lushan earthquake in the Tangjia Valley, Tianquan, Sichuan, China. Eng Geol 218:107–116

Lim EWC (2010) Granular Leidenfrost effect in vibrated beds with bumpy surfaces. The European Physical Journal E: Soft Matter 32(4):365–375

Li X, Konietzky H, Li XB, Wang Y (2019) Failure pattern of brittle rock governed by initial microcrack characteristics. Acta Geotech 14:1437–1457

Li X, Wu Y, He S, Su L (2016) Application of the material point method to simulate the post-failure runout processes of the Wangjiayan landslide. Eng Geol 212:1–9

Liu J, Wautier A, Bonelli S, Nicot F, Darve F (2020) Macroscopic softening in granular materials from a mesoscale perspective. Int J Solids Struct 193-194:222-238

Lois G, Lemaître A, Carlson J (2007) Spatial force correlations in granular shear flow. I. Numerical evidence. Phys Rev E 76 (2): 021302

Locat P, Couture R, Leroueil S, Locat J, Jaboyedoff M (2006) Fragmentation energy in rock avalanches. Can Geotech J 43(8):830–851

Lo CM, Lin ML, Tang CL, Hu JC (2011) A kinematic model of the Hsiaolin landslide calibrated to the morphology of the landslide deposit. Eng Geol 123:22–39

Løvoll G, Måløy KJ, Flekkøy EG (1999) Force measurements on static granular materials. Phys Rev E 60(5):5872

Ma G, Regueiro RA, Zhou W, Liu J (2018a) Spatiotemporal analysis of strain localization in dense granular materials. Acta Geotech 14(4):973–990

Ma G, Regueiro RA, Zhou W, Wang Q, Liu J (2018b) Role of particle crushing on particle kinematics and shear banding in granular materials. Acta Geotech 13(3):601–618

Ma G, Zhou W, Ng TT, Cheng YG, Chang XL (2015) Microscopic modeling of the creep behavior of rockfills with a delayed particle breakage model. Acta Geotech 10(4):481–496

Ma G, Zhou W, Chang XL, Chen MX (2016). A hybrid approach for modeling of breakable granular materials using combined finite-discrete element method. Granul Matt 18:7

Ma G, Zhou W, Regueiro RA, Wang Q, Chang XL (2017) Modeling the fragmentation of rock grains using computed tomography and combined FDEM. Powder Technol 308:388-397

Ma G, Zhou W, Zhang Y, Wang Q, Chang X (2018) Fractal behavior and shape characteristics of fragments produced by the impact of quasi-brittle spheres. Powder Technol 325:498-509

Ma G, Zhang YD, Zhou W, Ngc TT, Qiao W, Xing C (2018). The effect of different fracture mechanisms on impact fragmentation of brittle heterogeneous solid. International Journal of Impact Engineering, 113:132-143

Manouchehrian A, Marji MF (2012) Numerical analysis of confinement effect on crack propagation mechanism from a flaw in a pre-cracked rock under compression. Acta Mech Sinica 28(5):1389-1397

Manouchehrian A, Sharifzadeh M, Marji MF, Gholamnejad J (2014) A bonded particle model for analysis of the flaw orientation effect on crack propagation mechanism in brittle materials under compression. Arch Civ Mech Eng 14(1):40-52

Mas Ivars D, Pierce ME, Darcel C, Reyes-Montes J, Potyondy DO, Young RP, Cundall PA (2011) The synthetic rock mass approach for jointed rock mass modelling. Int J Rock Mech Min Sci 48(2):219–244

Massey C, Townsend D, Rathje E, Allstadt KE et al (2018) Landslides triggered by the 14 November 2016 Mw 7.8 Kaikōura Earthquake, New Zealand. Bull Seismol Soc Am 108:1630-1648

McNamara S (2013) Absorbing boundary conditions for granular acoustics. Paper Presented at the III International Conference on Particle Based Methods—Fundamentals and Application, PARTICLES 2013, Stuttgart, Germany.

McSaveney MJ (2002) Recent rockfalls and rock avalanches in Mount Cook National Park, New Zealand, in Catastrophic Landslides: Effects, Occurrence, and Mechanisms: Reviews in Engineering Geology. edited by S. G. Evans, and J. V. DeGraff, Geol. Soc Am Rev Eng Geol XV 35–70

McSaveney MJ, Davies T (2009) Surface energy is not one of the energy losses in rock comminution. Eng Geol 109:109–113

Melosh HJ (1986) The physics of very large landslides. Acta Mech 64(1–2):89–99

Meunier P, Hovius N, Haines AJ (2007) Regional patterns of earthquake-triggered landslides and their relation to ground motion. Geophys Res Lett 34: L20408

Mollon G, Richefeu V, Villard P, Daudon D (2012) Numerical simulation of rock avalanches: influence of a local dissipative contact model on the collective behavior of granular flows. J Geophys Res Solid Earth 117: F02036

Nichol SL, Hungr O, and Evans SG (2002) Large-scale brittle and ductile toppling of rock slopes. Can Geotech J 39:773–788

Ouadfel H, Rothenburg L (2001) 'Stress–force–fabric' relationship for assemblies of ellipsoids. Mech Mater 33:201–221

Pariseau W, Puri S, Schmelter S (2008) A new model for effects of impersistent joint set on rock slope stability. Int J Rock Mech Min Sci 45:122–131

Park B, Min KB (2015) Bonded-particle discrete element modeling of mechanical behavior of transversely isotropic rock. Int J Rock Mech Min Sci 76:243–255

Park JW, Song JJ (2009) Numerical simulation of a direct shear test on a rock joint using a bonded-particle model. Int J Rock Mech Min Sci 46:1315–1328

Park JW, Song JJ (2013) Numerical method for the determination of contact areas of a rock joint under normal and shear loads. Int J Rock Mech Min Sci 58:8–22

Pedrazzini A, Jaboyedoff M, Loye A, Derron MH (2013) From deep seated slope deformation to rock avalanche: Destabilization and transportation models of the Sierre landslide (Switzerland). Tectonophysics 605:149–168

Perinotto H, Schneider JL, Bachèlery P, Bourdonnec FXL, Famin V, and Michon L (2015) The extreme mobility of debris avalanches: A new model of transport mechanism. J Geophys Res Solid Earth 120:8110–8119

Pierce M, Cundall P, Potyondy D, Mas Ivars D (2007) A synthetic rock mass model for jointed rock. Paper presented at the rock mechanics: meeting society's challenges and demands, 1st Canada-U.S. Rock Mechanics Symposium, Vancouver

Pollet N, Schneider JL (2004) Dynamic disintegration processes accompanying transport of the Holocene Flims sturzstrom (Swiss Alps). Earth Planet Sc Lett 221(1–4):433–448

Potyondy DO, Cundall PA (2004) A bonded-particle model for rock. Int. J. Rock Mech. Mining Sci. 41(8):1329–1364

Potyondy DO, Cundall PA, Lee C (1996) Modeling of rock using bonded assemblies of circular particles M. Aubertin (Ed.), Proceedings of the 2nd North American Rock Mechanics Symposium – NARMS'96, A.A. Balkema, Brookfield, USA, 1934-1944

Prudencio M, Van Sint Jan M (2007) Strength and failure modes of rock mass models with non-persistent joints. Int J Rock Mech Min Sci 44(6):890–902

Quiñones J, Arzúa J, Alejano LR, García-Bastante F, Mas Ivars D, Walton G (2017) Analysis of size effects on the geomechanical parameters of intact granite samples under unconfined conditions. Acta Geotech 12:1229–1242

Rasouli V, Harrison JP (2010) Assessment of rock fracture surface roughness using Riemannian statistics of linear profiles. Int J Rock Mech Min Sci 47:940–948

Roback K, Clark MK, West AJ Zekkos D, Li G, Gallen SF, Chamlagain D, Godt JW (2017) The size distribution and mobility of landslides caused by the 2015 Mw7.8 Gorkha earthquake, Nepal. Geomorphology 301:121–138

Rothenburg L, Bathurst RJ (1989) Analytical study of induced anisotropy in idealized granular materials. Géotechnique 39:601-614

Rosin P, and Rammler E (1933) Laws governing the fineness of powdered coal. J Inst Fuel 7:89–105

Ruiz-Carulla R, Corominas J, Mavrouli O (2015) A methodology to obtain the block size distribution of fragmental rockfall deposits. Landslides 12(4):815–825

Ruiz-Carulla R, Corominas J, Mavrouli, O (2017) A fractal fragmentation model for rockfalls. Landslides 14:875–889

Satake M (1978) Constitution of mechanics of granular materials through graph representation. In: Proceedings of the 26th Japanese national congress of theoretical and applied mechanics 257–66

Scaringi G, Fan X, Xu Q. Liu C, Ouyang CJ, Domènech G, Yang F, Dai LX (2018) Some considerations on the use of numerical methods to simulate past landslides and possible new failures: the case of the recent Xinmo landslide (Sichuan, China). Landslides 15:1359–1375

Scholtès L, Donzé FV (2012) Modelling progressive failure in fractured rock masses using a 3D discrete element method. Int J Rock Mech Min Sci 52:18–30

Schöpfer MPJ, Abe S, Childs C, Walsh JJ (2009) The impact of porosity and crack density on the elasticity, strength and friction of cohesive granular materials: insights from DEM modeling. Int J Rock Mech Min Sci 46:250–261

Shang J, West LJ, Hencher SR, Zhao Z (2018a) Geological discontinuity persistence: implication and quantification. Eng Geol 241:41–54

Shang J, West LJ, Hencher SR, Zhao Z (2018b) Tensile strength of larger-scale incipient rock joints: a laboratory investigation. Acta Geotechnica 13:869–886

Shen WG, Zhao T, Crosta GB, Dai F (2017) Analysis of impact induced rock fragmentation using a discrete element approach. Int J Rock Mech Min Sci 98:33-38

Shen WG, Zhao T, Zhao J, Dai F, and Zhou GG (2018) Quantifying the impact of dry debris flow against a rigid barrier by DEM analyses. Eng Geol 241:86–96

Shi J, Guo P (2018) Fabric evolution of granular materials along imposed stress paths. Acta Geotech 13(6):1341–1354

Shreve RL (1968) Leakage and fluidization in air-lubricated avalanches. Geol Soc Am Bull 79(5):653–658

Silbert LE, Grest GS, Landry JW (2002) Statistics of the contact network in frictional and frictionless granular packings. Phys Rev E 66(6):061303

Singh M, Rao KS, Ramamurthy T (2002) Strength and deformational behaviour of a jointed rock mass. Rock Mech Rock Eng 35:45–64

Song ZY, Konietzky H, Herbst M (2019) Bonded-particle model-based simulation of artificial rock subjected to cyclic loading. Acta Geotech 14:955–971

Stead D, Eberhardt E, Coggan J (2006) Developments in the characterization of complex rock slope deformation and failure using numerical modelling techniques. Eng Geol 83:217–235

Sun Q, Zheng JX (2019) Two-dimensional and three-dimensional inherent fabric in cross-anisotropic granular soils. Comput Geotech 116:103197

Taberlet N, Richard P, Jenkins JT, Delannay R (2007) Density inversion in rapid granular flows: the supported regime. The European Physical Journal E: Soft Matter 22(1):17–24

Tang CL, Hu JC, Lin ML, Angelier J, Lu CY, Chan YC, Chu HT (2009) The Tsaoling landslide triggered by the Chi-Chi earthquake, Taiwan: insights from a discrete element simulation. Eng Geol 106(1):1–19

Tang C, Ma G, Chang M, Li W, Zhang D, Jia T, Zhou Z (2015) Landslides triggered by the 20 April 2013 Lushan earthquake, Sichuan Province, China. Eng Geol 187:45–55

Tang HM, Liu X, Hu XL, Griffiths DV (2015) Evaluation of landslide mechanisms characterized by high-speed mass ejection and long-run-out based on events following the Wenchuan earthquake. Eng Geol 194:12–24

Thompson N, Bennett MR, Petford N (2009) Analyses on granular mass movement mechanics and deformation with distinct element numerical modeling: implications for large-scale rock and debris avalanches. Acta Geotech 4:233–247

Thornton C, Yin KK, Adams MJ (1996) Numerical simulation of the impact fracture and fragmentation of agglomerates. J Phys D: Appl Phys 29(2):424–435

Tian YY, Xu C, Ma SY, Xu XW, Wang SY, Zhang H (2019) Inventory and Spatial Distribution of Landslides Triggered by the 8th August 2017 MW 6.5 Jiuzhaigou Earthquake. China J Earth Sci 30:206–217

Timár G, Blömer J, Kun F, Hermann HJ (2010) New universality class for fragmentation of plastic materials. Phys Rev Lett 104:095502

Turcotte DL (1986) Fractals and fragmentation. J Geophys Res Solid Earth 91(B2):1921–1926

Tyler SW, Wheatcraft SW (1992) Fractal scaling of soil particle size distributions: analysis and limitations. Soil Sci Soc Am J 56:362–369

Utili S, Nova R (2008) DEM analysis of bonded granular geomaterial. Int J Numer Anal Methods Geomech 32:1997-2031

Utili S, Zhao T, Houlsby GT (2015) 3D DEM investigation of granular column collapse: Evaluation of debris motion and its destructive power. Eng Geol 186(0):3–16

Vergara MR, Jan MVS, Lorig L (2016) Numerical model for the study of the strength and failure modes of rock containing non-persistent joints. Rock Mech Rock Eng 49(4):1211–1226

van der Baan M, & Chorney D (2019) Insights from micromechanical modeling of intact rock failure: Event characteristics, stress drops and force networks. Journal of Geophysical Research: Solid Earth, 124(12): 955 – 980.

Varela Valdez A, Morel S, Marache A, Hinojosa M, Riss J (2018) Influence of fracture roughness and micro-fracturing on the mechanical response of rock joints: a discrete element approach. Int J Fract 213:87-105

Virgo S, Abe S, Urai JL (2013) Extension fracture propagation in rocks with veins: insight into the crack-seal process using discrete element method modelling. J Geophys Res Solid Earth 118:5236–5251

Vora HB, Morgan JK (2019) Microscale Characterization of Fracture Growth and Associated Energy in Granite and Sandstone Analogs: Insights using the Discrete Element Method. J Geophys Res: Solid Earth 124:7993– 8012

Walton G, Alejano LR, Arzua J, Markley T (2018) Crack damage parameters and dilatancy of artificially jointed granite samples under triaxial compression. Rock Mech Rock Eng 51:1637-1656

Wang C, Tannant DD, Lilly PA (2003) Numerical analysis of the stability of heavily jointed rock slopes using PFC2D. Int J Rock Mech Min Sci 40(3):415–424.

Wang FW, Cheng QG, Highland L, Miyajima M, Wang HB. Yan CG (2009) Preliminary investigation of some large landslides triggered by the 2008 Wenchuan earthquake, Sichuan Province, China. Landslides 6:47–54

Wang J, Gutierrez MS, Dove JE (2007) Numerical studies of shear banding in interface shear tests using a new strain calculation method. Int J Numer Anal Meth Geomech 31(12):1349–1366

Wang J, Yan HB (2012) DEM analysis of energy dissipation in crushable soils. Soils Found. 52(4): 644–657

Wang TT, Huang TH (2009) A constitutive model for the deformation of a rock mass containing sets of ubiquitous joints. Int J Rock Mech Min Sci 46(3):521–530

Wang Y, Tonon F (2009) Modeling Lac du Bonnet granite using a discrete element model. Int J Rock Mech Min Sci 46:1124–1135

Wang Y, Tonon F (2010) Discrete element modeling of rock fragmentation upon impact in rockfall analysis. Rock Mech Rock Eng 44:23–35

Wang YF, Cheng Q, Zhu Q (2015) Surface microscopic examination of quartz grains from rock avalanche basal facies. Can Geotech J 52:167-181

Wang YF, Dong JJ, Cheng QG (2018) Normal stress-dependent frictional weakening of large rock avalanche basal facies: Implications for the rock avalanche volume effect. J Geophys Res Solid Earth 123:3270–3282

Wang YF, Cheng QG, Lin QW, Yang HF (2018) Insights into the kinematics and dynamics of the Luanshibao rock avalanche (Tibetan Plateau, China) based on its complex surface landforms. Geomorphology 317:170-183

Wang YF, Dong JJ, Cheng QG (2017) Velocity-dependent frictional weakening of large rock avalanche basal facies: Implications for rock avalanche hypermobility? J Geophys Res: Solid Earth 122:1648–1676

Wei J, Zhao Z, Xu C, Wen Q (2019) Numerical investigation of landslide kinetics for the recent Mabian landslide (Sichuan, China). Landslides 16:2287–2298

Wu J, Lin J, Chen C (2009) Dynamic discrete analysis of an earthquake-induced largescale landslide. Int J Rock Mech Min 46:397–407

Wu JH, Chen CH (2011) Application of DDA to simulate characteristics of the Tsaoling landslide. Comput Geotech 38:741–750

Wu JP, Huang, Y, Zhang, TZ, Ming, YH, Fang, LH (2009) Aftershock distribution of the MS 8.0 Wenchuan earthquake and 3-D P-wave velocity structure in and around source region. Chinese Journal of Geophysics 52(1):102–111

Wu H, Guo N, Zhao J (2018) Multiscale modeling and analysis of compaction bands in high-porosity sandstones. Acta Geotech 13(3):575–599

Xu C, Xu X, Shyu JBH, Gao MX, Tan XB, Ran YK, Zheng WJ (2015a) Landslides triggered by the 20 April 2013 Lushan, China, Mw 6.6 earthquake from field investigations and preliminary analyses. Landslides 12:365–385

Xu C, Xu XW, Shyu JBH (2015b) Database and spatial distribution of landslides triggered by the Lushan, China Mw 6.6 earthquake of 20 April 2013. Geomorphology 248:77–92

Xu GW, He C, Chen ZQ, Wu D (2018) Effects of the micro-structure and micro-parameters on the mechanical behaviour of transversely isotropic rock in Brazilian tests. Acta Geotech 13:887–910

Xu G, Li Z, Li P (2013) Fractal features of soil particle-size distribution and total soil nitrogen distribution in a typical water shed in the source area of the middle Dan River, China. Catena 101: 17–23

Xu T, Xu Q, Tang C, Ranjith PG (2013) The evolution of rock failure with discontinuities due to shear creep. Acta Geotech 8(6):567–581

Yang SQ, Huang YH, Jing HW, Liu XR (2014) Discrete element modeling on fracture coalescence behavior of red sandstone containing two unparallel fissures under uniaxial compression. Eng Geol 178(21):28–48

Yang XX, Kulatilake PHSW, Chen X, Jing HW, Yang SQ (2016) Particle flow modeling of rock blocks with nonpersistent open joints under uniaxial compression. ASCE Int J Geomech 16(6): 04016020

Yang XX, Qiao WG (2018) Numerical investigation of the shear behavior of granite materials containing discontinuous joints by utilizing the flat-joint model. Comput Geotech104:69-80

Yerro A, Pinyol Núria M, Alonso EE (2016) Internal progressive failure in deep-seated landslides. Rock Mech Rock Eng 49(6):2317-2332

Yuan RM, Tang CL, Hu JC, Xu XW (2014). Mechanism of the Donghekou landslide triggered by the 2008 Wenchuan earthquake revealed by discrete element modeling. Nat Hazards Earth Syst Sci 14:1195–1205

Yin Y, Wang F, Sun P (2009) Landslide hazards triggered by the 2008 Wenchuan earthquake, Sichuan, China. Landslides 6(2):139-152

Yin YP, Li B, Wang WP (2015) Dynamic analysis of the stabilized Wangjiayan landslide in the Wenchuan Ms 8.0 earthquake and aftershocks. Landslides 12(3):537- 547

Yuan RM, Tang CL, Hu JC, Xu XW (2014) Mechanism of the Donghekou landslide triggered by the 2008 Wenchuan earthquake revealed by discrete element modeling. Nat Hazards Earth Syst Sci 14:1195–1205

Yuan RM, Tang CL, Deng Q (2015) Effect of the acceleration component normal to the sliding surface on earthquake-induced landslide triggering. Landslides 12:335–344

Zhan WW, Fan XM, Huang RQ, Pei XJ, Xu Q, Li WL (2017) Empirical prediction for travel distance of channelized rock avalanches in the Wenchuan earthquake area. Nat Hazards Earth Syst Sci 17(6):833–844

Zhao S, Zhou X, Liu W (2015) Discrete element simulations of direct shear tests with particle angularity effect. Granular Matter 17(6):793–806

Zhao S, Zhou X (2017) Effects of particle asphericity on the macro- and micro- mechanical behaviors of granular assemblies. Granular Matter 19(2):38

Zhang HQ, Zhao ZY, Tang CA, Song L (2006) Numerical study of shear behavior of intermittent rock joints with different geometrical parameters. Int J Rock Mech Min Sci 43:802–816

Zhang M, Yin YP, McSaveney M (2016) Dynamics of the 2008 earthquake-triggered Wenjiagou Creek rock avalanche, Qingping, Sichuan, China. Eng Geol 200:75–87

Zhang, M, Wu L, Zhang J, Li L (2019) The 2009 Jiweishan rock avalanche, Wulong, China: deposit characteristics and implications for its fragmentation. Landslides 16 :893–906

Zhang M, McSaveney M (2017) Rock avalanche deposits store quantitative evidence on internal shear during runout. Geophys Res Lett 44:8814–8821

Zhang M, Yin YP, McSaveney M (2016) Dynamics of the 2008 earthquake-triggered Wenjiagou Creek rock avalanche, Qingping, Sichuan, China. Eng Geol 200:75–87

Zhang N, Evans TM (2019) Discrete numerical simulations of torpedo anchor installation in granular soils. Comput Geotech, 108:40-52

Zhang Q, Zhang X (2017) A numerical study on cracking processes in limestone by the b-value analysis of acoustic emissions. Comput Geotech, 92: 1-10

Zhang SH, Wu S C, Duan K (2019) Study on the deformation and strength characteristics of hard rock under true triaxial stress state using bonded-particle model. Comput Geotech, 112: 1–16.

Zhang XP, Wong L (2012) Cracking processes in rock-like material containing a single flaw under uniaxial compression: a numerical study based on parallel bonded-particle model approach. Rock Mech Rock Eng 45:711–737

Zhang YH, Fu XD, Sheng Q (2014) Modification of the discontinuous deformation analysis method and its application to seismic response analysis of large underground caverns. Tunnelling and Underground Space Technology 40: 241-250

Zhang Y, Wang J, Xu Q, Chen G, Zhao J, Zheng L, Han Z, Yu P (2015) DDA validation of the mobility of earthquake-induced landslides. Eng Geol 194:38-51

Zhao T, Crosta GB, Dattola G, Utili S (2018) Dynamic fragmentation of jointed rock blocks during rockslide-avalanches: insights from discrete element analyses. J Geophys Res: Solid Earth 123:1-20

Zhao T, Crosta GB, Utili S, and De Blasio FV (2017) Investigation of rock fragmentation during rockfalls and rock avalanches via 3-D discrete element analyses. J Geophys Res: Earth Surf 122:678–695

Zhao T, Crosta GB (2018) On the dynamic fragmentation and lubrication of coseismic landslides. J Geophys Res: Solid Earth 123:9914 – 9932

Zhao Y, Semnani SJ, Yin Q, Borja RI (2018) On the strength of transversely isotropic rocks. Int J Numer Anal Methods Geomech. 42:1917– 1934

Zhou C, Xu C, Karakus M, Shen, J (2019) A particle mechanics approach for the dynamic strength model of the jointed rock mass considering the joint orientation. Int J Numer Anal Methods Geomech. 43:2797– 281

Zhou GG, Sun QC (2013) Three-dimensional numerical study on flow regimes of dry granular flows by DEM. Powder Technol 239 :115–127

Zhou JW, Cui P, Yang XG (2013) Dynamic process analysis for the initiation and movement of the Donghekou landslide-debris flow triggered by the Wenchuan earthquake. Journal of Asian earth sciences 76(1):70-84

Zhou JW, Huang KX, Shi C, Hao MH, Guo CX (2015) Discrete element modeling of the mass movement and loose material supplying the gully process of a debris avalanche in the Bayi gully, Southwest China. J Asian Earth Sci 99:95-111

Zhou W, Lai Z, Ma G, Yang L, Chen Y (2016) Effect of base roughness on size segregation in dry granular flows. Granul Matt 18(4):83

Zhang N, Evans TM (2019) Discrete numerical simulations of torpedo anchor installation in granular soils. Computers and Geotechnics 108:40-52

Zhou W, Lai Z, Ma G, Yang L, Chen Y (2016) Effect of base roughness on size segregation in dry granular flows. Granul Matt 18(4):83

Zou ZX, Tang HM, Xiong CR, Su AJ, Criss ER (2017). Kinetic characteristics of debris flows as exemplified by field investigations and discrete element simulation of the catastrophic Jiweishan rockslide, China. Geomorphology 295:1-15